MEDICAL UNIVERSITY OF VIENNA

Bridging the gaps in Particle Therapy using Monte Carlo Codes

Doctoral thesis at the Medical University of Vienna
for obtaining the academic degree
Doctor of Philosophy

Submitted by
Mgr inż. Wioletta Kozłowska

Supervisor:
Univ. Prof. Dr. DI Dietmar Georg
Department of Radiation Oncology
Medical University of Vienna
Spitalgasse 23, Vienna, Austria

Doctoral thesis was carried out at CERN under the supervision of:
Dr. Vasilis Vlachoudis & Dr. Alfredo Ferrari
CERN, Esplanade des Particules 1, Geneva, Switzerland

Vienna, 09/2022

Declaration

Hereby, I declare:

- Chapter 2: the chapter is based on the article *The FLUKA code: An accurate simulation tool for particle therapy* published in a peer-reviewed journal Frontiers in Oncology; 6:116; 2016. The work was co-authored by the author of this thesis, and author was responsible mainly for development of the Flair interface for medical applications and production of text and figures in section 2.4; the work was performed at CERN.
- Chapter 3: the work presented in this chapter was published as a scientific article *FLUKA particle therapy tool for Monte Carlo independent calculation of scanned proton and carbon ion beam therapy* in a peer-reviewed journal Physics in Medicine and Biology; 64; 075012; 2019. It is presented as published; the study was performed at CERN in collaboration with CNAO and Trento Proton Facility, where author of this thesis was a main contributor.
- Chapter 4: the chapter is based on two manuscripts *First benchmarking of the BIANCA model for cell survival prediction in a clinical hadron therapy scenario*, published in a peer-reviewed journal Physics in Medicine and Biology 64 215008; 2019, and *In vivo validation of the BIANCA Biophysical Model: Benchmarking against Rat Spinal Cord RBE Data*, published in a peer reviewed journal International Journal of Molecular Sciences 21; 2020, both articles were co-authored by the author of this thesis, and author was responsible for integration of the BIANCA model with the FLUKA MC code and BIANCA simulations as described in section 4.4 and 4.5; the study was performed in collaboration with CERN, INFN and University of Pavia.
- Chapter 5: the work presented in this chapter was published as a scientific article *First application of the BIANCA biophysical model to carbon-ion patient cases* in a peer-reviewed Physics in Medicine and Biology; 67; 115013; 2022. It is presented as published; the study was performed in collaboration with CERN, INFN and University of Pavia, where author of this thesis was a main contributor.

Doctoral Candidate
Mgr inż. Wioletta Kozłowska

Supervisor
Univ. Prof. Dr. DI Dietmar Georg

Contents

List of Figures

List of Tables

Abstract

Charged particle therapy is well known for precise dose delivery to the tumour, while simultaneously increasing sparing of surrounding healthy tissues, compared to high energy photon beams. As a constantly evolving technology, new research challenges must be addressed in order to further optimize treatment outcomes. These challenges include improvement of dose calculation accuracy for treatment planning, development of independent quality assurance methods, as well as evaluation of the biological effectiveness of a treatment. A significant part of such research can be carried out using particle interaction and transport simulations. Monte Carlo (MC) codes, which are considered as the 'gold standard' in radiation therapy, can help bridge research gaps. As such an improvement, the development and application of MC codes for charged particle therapy are presented in this thesis. Specifically, this thesis is focused on the development and application of a Patient Specific Quality Assurance (PSQA) tool for scanned particle beam delivery, as well as benchmarking and application of a new radiobiological model for proton and ion beam therapy - BIANCA.

The general purpose MC code FLUKA was selected to pursue this research. FLUKA profits from its recent developments in charged hadron interactions an transport models, at the therapeutic energy range. During the course of this work, the code was upgraded and several new features were subsequently implemented. As a result, the code was able to simulate a full set of treatment beamlets for an active beam scanning technique for proton and ion beam therapies. The performed study was finalized with development of the FLUKA Particle Therapy Tool (FPTT), which enables simulation of realistic clinical treatment planning scenarios using a voxelized patient geometry. A next step for PSQA development involved an application and a validation of the FPTT, i.e., benchmarking studies were performed using data sets from two particle therapy facilities - Trento Proton Facility and CNAO. The beam parameters were modelled in FPTT and compared with commissioning data of the respective clinical Treatment Planning Systems (TPS). Further evaluation included simulations of four clinical treatment planning scenarios in FPTT: two proton chordoma cases (one from each facility), where small differences between FPTT calculations of dose deposition and TPS calculations were noticed; one proton head-and-neck case (using a range shifter), where significant differences between TPS and MC calculations were highlighted and discussed; and one chordoma carbon ion case, where biological dose calculations were performed using the clinical radiobiological model - LEM

I. In addition, a research application related to the dose-averaged Linear Energy Transfer (LET) was presented on a carbon ion case. Overall, the FPTT was proved to be reliable and well-integrated with the FLUKA MC code. It supported an import of particle therapy treatment planning data, adjustment to the user's requirements, and translation into FLUKA input file, without superior experience in the MC simulations. Finally, it proved its usability for a complex treatment plan scenarios in a PSQA simulations and research applications.

The second part of this thesis focuses on the radiobiological effectiveness of proton and ion beam therapies, presenting an upgrade and a benchmarking of a research biophysical model, BIANCA. An accurate description of underlying phenomena is crucial for evaluation of tumour control probability and normal tissue complication. First, the BIANCA model was expanded to new ion species, and various cells of interests. This was followed by an integration with the FLUKA MC code and the FPTT. Subsequently, BIANCA cell survival predictions were benchmarked against experimental data of Chinese Hamster Ovary Cells (CHO) irradiated by two opposed fields of proton or carbon ions. The results showed that the prediction of BIANCA and LEM I models were comparable, and the BIANCA model was in good agreement with the experimental data. The second benchmarking study compared the outcome of BIANCA modelling with cell survival of the rat spinal cord, following proton or carbon ion irradiation. In this case, the BIANCA model was again in a very good agreement with the data, well reproducing the trend of the RBE-dose and the RBE-LET dependence. This work provided a baseline for the first application of the BIANCA model to carbon-ion patient cases. Three cases from CNAO facility were chosen: a chordoma, a head-and-neck, and a prostate case. BIANCA Relative Biological Effectiveness (RBE) predictions were calculated, based on chordoma cell survival (RBE_{surv}), or on dicentric aberrations in peripheral blood lymphocytes (RBE_{ab}), which are indicators of late normal tissue damage. Simulation outcomes were compared with those provided by LEM I. Overall, results suggested that, if RBE_{surv} is used to evaluate the beam effectiveness at killing tumour cells, and RBE_{ab} is used to estimate (late) normal tissue damage, BIANCA provides lower RBE-weighted doses (with respect to LEM I) in the tumour and in the entrance channel; whereas in the Organs at Risk, BIANCA and LEM I provide very similar values. The presented work, and previous benchmarking studies, are encouraging, suggesting that BIANCA can be applied for radiobiological optimization of carbon ion treatment planning, using RBE database based on cell-specific tumour cell survival and RBE database based on normal tissue aberrations.

In summary, this thesis resulted in implementation of a MC-based tool for particle therapy, that can be used for clinical and research applications, supporting dose distribution calculation for PSQA purposes, and evaluation of the biological-weighted dose for ion beam therapy. In addition, the final chapter showed that MC codes can support the development of prototype accelerators, and its commissioning in a commercial TPS. As such, the research presented in this thesis bridges certain gaps in particle therapy by providing solutions using general-purpose MC code.

Publications

- **First application of the BIANCA biophysical model to carbon-ion patient cases [33]**
  W. Kozłowska, M. Carante, G. Aricò, A. Embriaco, A. Ferrari, G. Magro, A. Mairani, R. Ramos, P. Sala, D. Georg, F. Ballarini,
  published in *Physics in Medicine and Biology*; 67; 115013; 2022

- **In Vivo Validation of the BIANCA Biophysical Model: Benchmarking against Rat Spinal Cord RBE Data [28]**
  M. Carante, G. Aricò, A. Ferrari, C. Karger, **W. Kozłowska**, A. Mairani, P. Sala, F. Ballarini,
  published in *International Journal of Molecular Sciences*; 21; 2020

- **First benchmarking of the BIANCA model for cell survival prediction in a clinical hadron therapy scenario [20]**
  M. Carante, G. Aricò, A. Ferrari, **W. Kozłowska**, A. Mairani, F. Ballarini,
  published in *Physics in Medicine and Biology*; 64; 215008; 2019

- **FLUKA particle therapy tool for Monte Carlo independent calculation of scanned proton and carbon ion beam therapy [13]**
  W. Kozłowska, T. Böhlen, C. Cuccagna, A. Ferrari, F. Fracchiolla, G. Magro, A. Mairani, M. Schwarz, V. Vlachoudis, D. Georg,
  published in *Physics in Medicine and Biology*; 64; 075012; 2019

- **The FLUKA code: An accurate simulation tool for particle therapy [16]**
  G. Battistoni, J. Bauer, T. Böhlen, F. Cerutti, M.P.W. Chin, R. Dos Santos Augusto, A. Ferrari, P.G. Ortega, **W. Kozłowska**, G. Magro, A. Mairani, K .Parodi, P. Sala, P. Schoofs, T. Tessonnier, V. Vlachoudis,
  published in *Frontiers in Oncology*; 6:116; 2016

Abbreviations

ADAM - Applications of Detectors and Accelerators to Medicine an AVO company, Meyrin, Switzerland
AG01522 - Human Skin Fibroblast cell; cell line used for radiobiological experiments
ASTRO - American Society of Radiation Oncology
AVO - Advanced Oncotherapy plc, London, United Kingdom
BIANCA - BIophysical ANalysis of Cell death and chromosome Aberrations; radiobiological database
BME - FLUKA embedded low energy nucleus-nucleus event generator based on the Boltzmann Master Equation theory
CA - chromosomal aberration
CABOTO - CArbon BOoster for Therapy in Oncology; conceptual carbon therapy linac created by TERA
CERN - European Organization for Nuclear Research in Geneva, Switzerland
CHO - Chinese hamster ovary cells; cell line used for radiobiological experiments
CL - critical lesions created in DNA which disrupts the continuity of the chromatin fibre producing two main independent chromosome fragments
CNAO - Centro Nazionale di Adroterapia Oncologica, Italian Handrontherapy Center in Pavia, Italy
CNS - Central Nervous System
CSDA - Continuous Slowing Down Approximation
CT - Computerized Tomography. X-ray radiation imaging from different angles for obtaining a 3D view inside the human body
CTV - Clinical Target Volume; delineated tumour volume greater than GTV which covers regions of microscopic tumour spread
DNA - Deoxyribonucleic Acid; molecule composed of two strands in a form of double helix carrying genetical instruction
DSB - Double Strand Break in DNA
DTA - Distance to Agreement
DVH - Dose-Volume Histograms; histogram relating radiation dose to tissue volume in radiation therapy planning
ENEA - Italian National Agency for New Technologies, Energy and Sustainable Economic Development
ENIAC - Electronic Numerical Integrator and Computer
FBP - Filtered Back-Projection; 2D reconstruction algorithm used in Positron Emission Tomography
FDG - fluorodeoxyglucose; radiofarmaceutical used in Positron Emission Tomography
FLUKA - Monte Carlo particle transport and interaction code; originally named FLUktuerende KAskaden

FWHM - Full Width at Half Maximum
FPTT - FLUKA Particle Therapy Tool
GINC - Generalized IntraNuclear Cascade; physical model for hadron-nucleus interactions
GSI - Gesellschaft fur Schwerionenforschung, German National Laboratory for Heavy Ion Research in Darmstadt, Germany
GTV - Gross Target Volume; delineated tumour volume visible on clinical image
GUI - Graphical User Interface
HIMAC - Heavy Ion Medical Accelerator in Chiba, Japan
HIT - Heidelberger Ionenstrahl Therapiezentrum, Ion Therapy Center in Heidelberg, Germany
HU - Hounsfield Unit; transformation of the attenuation coefficient used in Computer Tomography
IAEA - International Atomic Energy Agency
IC - Ionization Chamber
ICRU - International Commission on Radiological Units and Measurements
IDD - Integrated Depth Dose
IDE - Integrated Development Environment
IMPT - Intensity Modulated Particle Therapy
INFN - Instituto Nazionale de Fisica Nucleare, Italian Institute for Nuclear Physics
ISO - Isocenter; the point through which the central beam passes
LBNL - Lawrence Berkeley National Laboratory
LEM - Local Effect Model; radiobiological database
LET - Linear Energy Transfer
LIGHT - LINAC for Image-Guided Hadron Therapy; linear accelerator developed by ADAM SA., Meyrin, Switzerland
LOR - Line Of Responses; the imaginary line that unites two coincidence events in Positron Emission Tomography
LQM - Linear Quadratic Model; model describing relation between cell survival and dose
LUT - Look-Up Table
MedAustron - Center for ion therapy and research in Wiener Neustadt, Austria
MC - Monte Carlo
MCS - Multiple Coulomb Scattering
MKM - Microdosimetric Kinetic Model; radiobiological Database
MLEM - Maximum-Likelihood Expectation-Maximization; 2D iterative reconstruction algorithm used in Positron Emission Tomography
MRI - Magnetic Resonance Imaging
MU - Monitor Units
NIRS - Japanese National Institute of Radiological Sciences in Chiba, Japan
NTCP - Normal Tissue Complication Probability
OAR - Organ At Risk; delineated volume of critical organ structure
OER - Oxygen Enhancement Ratio; level of radio-resistance due to lack of oxygen
PEANUT - Pre-Equilibrium Approach to Nuclear Thermalization; a pre-equilibrium Intra-Nuclear Cascade hadron interaction model

PET - Positron Emission Tomography
PIMMS - Proton and Ion Medical Machine Study
PMMA - Polymethyl methacrylate [CH2-C(CH3)COOCH3]n, Plexiglass
POI - Point of Interest
PSI - Paul Scherrer Institute
PSQA - Patient Specific Quality Assurance
PTCOG - Particle Therapy Co-Operative Group
PTV - Planned Target Volume; delineated expansion of the CTV volume covering possible uncertainties
QA - Quality Assurance
Renca - Renal Adenocarcinoma tumour cells
RBE - RadioBiological Effectiveness
RF - Radiofrequency
ROI - Region of Interest
ROS - Reactive Oxygen Molecules
rQMD - FLUKA embedded event generator based on the Cascade-Relativistic Quantum Molecular Dynamics model for nucleus-nucleus interactions
SAD - Source Axis Distance
SFUD - Single Field Uniform Dose
SNR - Signal to Noise Ratio
SOBP - Spread Out Bragg Peak
SPECT - Single Photon Emission Computed Tomography
SPHIC - Shanghai Proton and Heavy Ion Center, China
SSB - Single Strand Break in DNA
TCP - Tumour Control Probability
TDRA - Theory of Dual Radiation Action
TERA - Terapia con Radiazioni Adroniche, Italian Foundation for Therapy with Hadronic Radiations
TPS - Treatment Planning System
TRiP - TReatment planning for Particle, used in GSI
TULIP - TUrning LInac for Protontherapy, prototyped by TERA Foundation
voxel - a single data sample within a volume unit in a regular grid in three-dimensional space
V79 - Chinese hamster cell; cell line used in radiobiological experiments
xr5 - mutated Chinese hamster cell derived from the CHO type cell line; cell line used in radiobiology
U87 - Human Primary Glioblastoma cell; cell line used in radiobiological experiments
WED - Water Equivalent Depth

Acknowledgements

This work would not have been possible without my supervisors, with whom I had an honor to work with. I would like to thank my supervisor at the Medical University of Vienna - Prof. DI Dietmar Georg. Thank you for your support, deep knowledge, and for the guidance and advice during my research. Additionally for helping me to navigate the way to complete this thesis. Many thanks goes to my CERN supervisor Dr. Vasilis Vlachoudis, who supported me from the beginning. I am especially grateful for sharing your knowledge and dedication, patience in answering endless questions, hours of debugging sessions and being supportive thorough entire process. I would like to thank also my co-supervisor Dr. Alfredo Ferrari, for sharing your knowledge with me, a valuable time spent while developing ideas, resolving issues arisen from my ideas, and solving problems which I had never encounter before.

I would also like to express my gratitude to Dr. Andrea Mairani, Dr. Till Böhlen, Dr. Paola Sala, Dr. Giuseppe Magro, Dr. Francesco Fracchiolla, Dr. Marco Schwarz for their insightful comments and suggestions, and whose support was visible thorough my thesis. I would like to pay my special regards to Prof. Francesca Ballarini and Dr. Mario Carante, without whom the last part of the thesis would not be possible.

My personal greeting goes to all my CERN friends, and especially to my office comrades, with whom I spend many hours at work and conferences. Thanks goes to Ricardo dos Santos Augusto, for providing an invaluable amount of support, encouragement for growing more flowers and endless discussions about life, work and coffee quality at 864. Another special thanks goes to Giulia Aricò for kindness, excellent organization skills and many trips to Pavia, where a good coffee can be found. I thank also Caterina Cuccagna, with whom I shared the learning and problem solving experience. Another set of gratitude goes to my CERN 864 friends: Mohi, Barbara, Tobias, Maris, Adam, Jose, James, Joao, Francesc, Matteo, Francesca and the others, which made my stay at CERN an unforgettable experience.

Dziękuję moim rodzicom za to, że zawsze wierzyli we mnie i pozwalali mi iść wybraną drogą. Chciałabym również podziękować mojej siostrze, za nieustanne wsparcie i miłość, oraz małej Hani, za uśmiech jaki wywołuje codziennie.

Finalnie chcę podziękować moim przyjaciołom, którzy towarzyszyli mi i towarzyszą na różnych etapach mojego życia, za motywację oraz za to, że nigdy nie znudziło im się zadawanie pytania 'Jak ten doktorat?'.

Chapter 1

Introduction

While the main causes of cancer are late age and increased exposure to risk factors (such as pollution, sunlight, obesity, alcohol, and tobacco), the most of these factors cannot be avoided, and the number of cancer incidents in the world increases each year. With 29.5 million cases projected in 2040 [34], the 5-year survival rate for patients in the European Union between 15-75 years old, is above 50 % [35]. This improvement cannot be achieved without the continuous development of cancer therapies. Currently, cancer treatment involves a combination of different types of therapies, including surgery, chemotherapy, radiotherapy, immunotherapy, and hormone therapy. It is estimated that more than half of the cancer patients will undergo radiotherapy during their oncological treatment [3, 36, 37]. Aiming to irradiate and kill tumor cells while sparing normal tissues. In addition to radiotherapy, the combination of radiotherapy and immunotherapy has recently yielded promising outcomes [38].

Conventional radiotherapy began in 1895 [39, 40]. A few months after Wilhelm Röontgen discovered X-rays [41], the first patient in Chicago was irradiated (but without success) by Emil Grubbe from local relapse of breast carcinoma [42]. Leopold Freund in Vienna, a few months later, at 1896 [43] performed a successful treatment of *naevus pigmentosus piliferus* using X-rays. Hadrons were not used for medical purposes until 1946 when Robert Wilson proposed the use of accelerated protons for cancer treatment [44]. He reasoned that the peak in the depth-dose deposition profile discovered for alpha particles by William Bragg 33 years earlier (called the Bragg peak) could be advantageous for a fixed and controllable beam range. In conventional radiotherapy with X-rays, the maximum deposited dose is located at the patient's skin proximity, decreasing with depth, whereas for charged hadrons, the sharp dose deposition peak is placed at the end of the particle range (see figure 1.1). This depth-dose profile allows more precise targeting of deep-seated tumors, as well as better sparing of normal tissues, which decreases the risk of secondary malignancies. The first attempts of the clinical use of protons were made in 1954 at the Lawrence Berkeley National Laboratory (LBNL) in the USA [45]. Since then, several different ions have been tested, ranging from helium to argon [46, 47, 48]. At the beginning of particle therapy, patients with cancer were experimentally treated at the LBNL research institute for nuclear physics; however, the facility was not optimized for medical purposes. The first medical

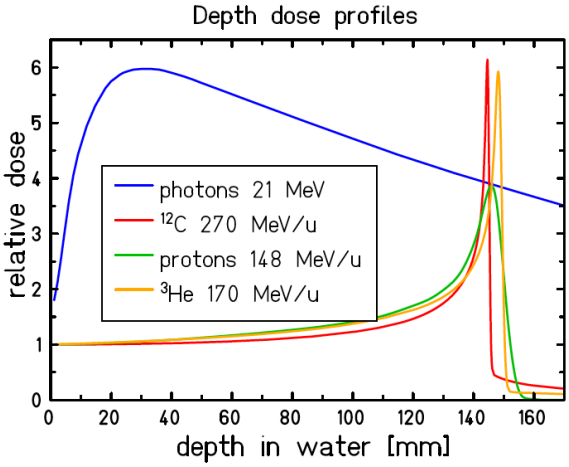

Figure 1.1: The Bragg peaks of proton, helium ions and carbon ion beams plus photon depth dose profile. *Reprinted from [1].*

hospital-based hadrontherapy [1] facility opened at the Loma Linda University Medical Center in 1991. Owing to the design provided by the Fermi National Accelerator Laboratory, the Medical Center was able to accelerate protons up to 250 MeV. The center has obtained satisfactory clinical outcomes [49, 50]. Next years brought several innovations, such as the development of the pencil beam scanning at Paul Scherrer Institute (PSI) [51] (which subsequently replaces passive scanning techniques) and the clinical implementation of carbon ion treatments, first at the Heavy Ion Medical Accelerator (HIMAC) facility (by Japanese National Institute of Radiological Sciences (NIRS)), Japan in 1994, and then in Europe at GSI in Darmstadt, Germany in 1997. Today almost 100 proton facilities and 13 carbon ion centres are in operation, 30 proton facilities and 6 carbon ion centres in construction, at the same time helium ions, are already implemented at HIT, Germany for patient treatment. As a result of favourable outcomes, particle therapy [2] became a popular cancer treatment technique, reaching currently over 250 thousand patients treated by protons, and over 40 thousand treated by different types of ions [52].

Nowadays, there are still several challenges in charged particle therapy, including the development of more precise and faster particle accelerators, improvement of calculation accuracy for delivered dose in treatment planning systems and its verification, determining the biological effectiveness of a treatment and advancement in imaging for radiotherapy, which overall will allow to decrease safety margins. A significant part of the research for these developments include particle interaction and transport simulations, since the research time in ion beam therapy facilities is limited. In other words, many solutions to these problems can be found with Monte Carlo Techniques. Therefore, the main aim of this thesis is to bridge the gaps in particle therapy using Monte Carlo methods, which are known for their superior and accurate modelling of particle interactions and transport in matter, in comparison to analytical modelling.

[1] Hadrontherapy - the term hadrontherapy was coined by Ugo Amaldi in 1992 to collect all non-conventional therapies with proton, ion, pions or neutron beams

[2] Particle therapy - refers to charged particle therapy, a non-conventional radiotherapy using charged particles such as protons or light ions

1.1 Monte Carlo Methods

Monte Carlo (MC) is a numerical method for calculating integrals based on random number sampling [53]. MC techniques are widely used in natural sciences because of their statistical approach, which is suitable for studying random phenomena such as radiation transport [54].
The idea of stochastic sampling was invented in 1943 by Stanisław Ulam, who further discussed it with John von Neumann. They worked together with Nicholas Metropolis at the Manhattan Project in the Los Alamos National Laboratory for theoretical calculations related to thermonuclear weapons research [55]. Von Neumann, inspired by Ulam's idea, implemented the method for the repetitive sampling generator, using an early computer ENIAC (Electronic Numerical Integrator and Computer) [56], to apply it for radiation transport calculations. The name Monte Carlo is derived from Ulam's uncle, who constantly borrowed money from relatives 'just to go to Monte Carlo' [57].

1.1.1 Mathematical basis of Monte Carlo

A general schematic of the Monte Carlo method applies [54]:

- determination of the problem in mathematical terms
- interpretation of the problem, where the searched quantity (expected value $\langle z \rangle$) is expressed as a parameter of a distribution $\mathcal{F}(x)$
- estimation of the expected value $\langle z \rangle$ via Equation 1.3 and its statistical uncertainty via Equation 1.4
- optimization of a calculation for reducing the computing time required to achieve a desired statistical uncertainty
- generation of sufficiently large random number samples (distribution) to achieve a satisfactory small level of uncertainty
- final estimation of a parameter $\langle z \rangle$ and its uncertainty

The Monte Carlo method is based on two fundamental statistical theorems: the Law of Large Numbers and the Central Limit Theorem [58].
The Law of Large Numbers allows obtaining an estimate of the expected value $\langle z \rangle$, which is:

$$\langle z \rangle = \int_a^b z(x)\mathcal{F}(x)dx, \tag{1.1}$$

where $\mathcal{F}(x)$ is the probability density function of the variable x.
$\bar{z}$ is the average of the N results $z(x)$, which is calculated as:

$$\bar{z} = \frac{1}{N}\sum_{i=1}^{N} z(x_i), \tag{1.2}$$

where x_i is sampled from $\mathcal{F}(x)$.
Finally, using the Law of Large Numbers:

$$\lim_{N\to\infty} \bar{z} = \langle z \rangle. \tag{1.3}$$

This implies that the average of the results obtained from a large number of samples should be close to the expected value $\langle z \rangle$ when $N \to \infty$.
The estimate of the uncertainty in the expected value can then be calculated using the Central Limit Theorem, which can be written as:

$$\lim_{N\to\infty} \mathcal{P}(\bar{z}) = \frac{1}{\sqrt{2\pi\sigma(z)^2/N}} e^{-\frac{(\bar{z}-\langle z \rangle)^2}{2\sigma(z)^2/N}}. \tag{1.4}$$

This indicates that for $N \to \infty$, the distribution of averages $\bar{z}$ of N identically distributed independent random variables tends to a normal distribution with a mean $\langle z \rangle$ and variance $\sigma(z)^2/N$ [59].
Random number samples are generated using a random number generator. The randomness of MC is suitable for mimicking the complexity of stochastic phenomena. In reality, these numbers are not truly random, which is why they are referred to as pseudorandom numbers. They must be uncorrelated, but reproducible [60]. Typically, they still exhibit periodicity and generate the same sequence of numbers, but nowadays it is possible to obtain a period that is sufficiently large for most applications.

1.1.2 Monte Carlo Methods for particle interaction with matter

Particle transport and interactions are typical representations of the stochastic processes. Setting an MC simulation for a particle physics simulation resembles the setting of a virtual experiment, with a particle source, a set of detectors in controlled conditions, and the possibility of iterating experiments as many times as necessary [59]. The *life cycle* of each particle is described individually, from its creation, through a set of undergoing interactions, modulating its parameters, until its destruction by i.e. absorption, discard, or any other user-defined condition.
The particle parameters are described by position (x, y, z), linear momentum (p_x, p_y, p_z) and time (t). Each particle is followed on its path through the matter with small steps [59]. At each step, in accordance with the modelled physical processes, the probability distribution, occurrence, and outcome of the interactions are determined, which leads to a direction change, momentum reduction, ionization process, fragmentation within the material, and production of secondaries. Subsequently, the next mean free path is calculated, and a step length is obtained. These steps are repeated until the particle reaches the energy threshold cut-off. Secondary particles created during the run are also placed in the simulation stack and treated in the same manner. According to Equation 1.3, more particle tracks are simulated, more precise description of its effects can be determined. Depending on the phase space and the quality to be evaluated, various estimators can be considered, such as boundary crossing estimators (i.e., fluence estimation on a surface), track length estimators (i.e., fluence in a region), pulse height estimators (i.e., a spectrum of the deposited energy in a region), scalar integral estimators (i.e., deposited energy and inelastic interactions in a region), and mesh/binning estimators (2D or 3D spatial distribution of a scalar quantity over a portion of a sub-volume in a region) [59].
The accuracy of the simulations depends on the implemented physical models, realistic experimental geometry description, energy cut-off values, and reasonable statistical accuracy. Depending on the complexity of the modelled problem, a large number of particle histories may be required to obtain more precise estimations. Although some methods, such as biasing (locally increased/decreased particle density), can speed up the convergence, they need to be used with care to avoid overestimating the impact of the occurring

phenomena [59]. MC methods also have the following drawbacks: particles do not interact with each other, but they interact with individual electrons, atoms, nuclei, and molecules; the material properties are not affected by the particle reaction; and particle transport is considered to be a Markovian process, meaning that the fate of the particle depends only on its current state, not on past or future events [59].
Several general purpose MC codes are currently used for particle transport and interaction simulations. FLUKA [61, 62, 63], GEANT4 [64, 65], and PENELOPE [66] are the most popular and provide sufficiently detailed radiation simulation models. Many MC codes have developed interfaces dedicated to particle therapy, including GATE [67], GAMOS [68], TOPAS [69], PTSIM [70](all based on GEANT4), and MCNP6 [71].

1.1.3 Monte Carlo in particle therapy

MC code entered the field of particle therapy in the late 70's [53]. Since then, they have gained popularity and are considered the gold standard owing to their dosimetric accuracy [72]. MC codes are particularly suitable when measurements are infeasible or unavailable. Although the calculation time is still the main drawback, they successfully found a niche in hadrontherapy applications such as [53]:

- development of accelerator and its beamline
- dose distribution calculations
- development of radiobiological models
- treatment planning validation and quality assurance
- detector development for image monitoring
- creation of databases for Treatment Planning Systems

For this thesis, the FLUKA MC code was selected because of its extensive use and validation at HIT and CNAO particle therapy facilities: commissioning, validation, and generation of physical databases for treatment planning systems [15, 16, 62, 73, 74, 75]. A more detailed description of the FLUKA code and implemented physics models (within the scope of particle therapy) is provided in Chapter 2.

1.2 Physical basis of proton and ion interactions with matter

The general advantage of charged particle therapy over conventional therapies (X-rays and photons) is more localized dose delivery and higher biological effectiveness. Low energy X-rays show a steep exponential dose-decrease with depth, and high energy photons reach the highest and widest dose peak a few millimeters from the patient's skin; however, with a further slow dose fall-off within the depth. Hadrons, on the other hand, with a very low entrance dose, a narrow dose peak (called Bragg peak) and practically zero dose at the exit can precisely target the desired depth in the tissue by changing their kinetic energy. The target tumor volume of any length and depth can be fully irradiated by delivering protons or ions with different energies and directions, creating Spread Out Bragg peak (SOBP), as shown in Figure 1.2. This section provides an overview of the physical basis for proton and ion beam therapies.

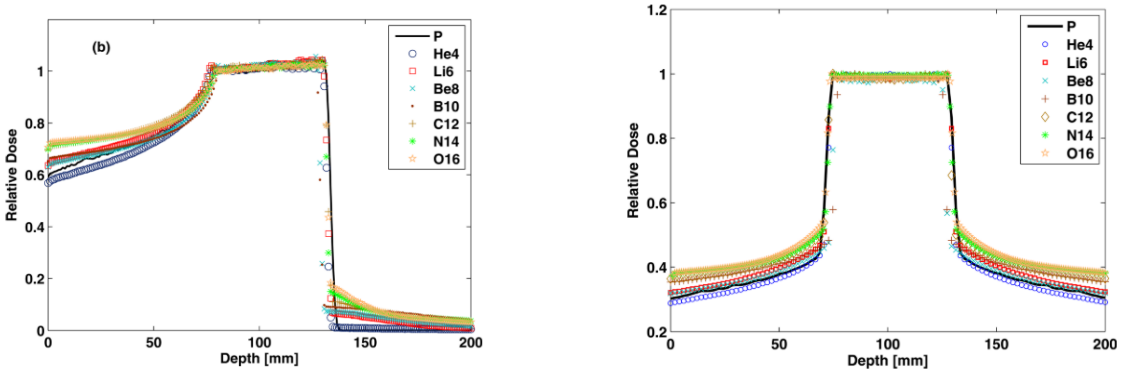

(a) Single field SOBP

(b) Two opposite field SOBP

Figure 1.2: Example of single field (a) and opposite fields (B) SOBPs of protons and ions such as He-4, Li-6, Be-8, B-10, C-12, N-14, and O-16. *Reprinted from [2].*

1.2.1 Energy loss

As the ion traverses through matter, its electromagnetic forces excite and ionize media atoms, leaving them in the excited state, while the particle loses its kinetic energy and slows down. In contrast to photons, X-rays, or neutrons (which produce secondary charged particles and do not ionize atoms by themselves, but only by secondary radiation), charged hadrons used in radiotherapy are capable of direct ionization of atoms of the medium through which they traverse.

The average energy loss of a charged particle dE per unit path length dx in a material is defined as the stopping power [76]:

$$S(E) = -\frac{dE}{dx}. \tag{1.5}$$

During the traverse, the energy deposition of ions can be described by three mechanisms [76]:

- energy losses due to inelastic collisions with atomic electrons (collision stopping power S_{col}) [3], see Figure 1.4
- energy losses due to energy transferred to the nuclei (nuclear stopping power S_{nucl}),
- energy losses due to the bremsstrahlung mechanism (radiative stopping power S_{brem}).

Particles heavier than electrons, with energies used in radiotherapy[4], typically lose most of their energy through S_{col} . S_{nucl} becomes significant for ions with energies lower than 10 keV/n, which means that at the end of their range, energy deposition to the nuclei, as well as S_{brem}, which is important for electrons, is negligibly small for protons and ions [76].

S_{col} of charged particles is described by the Bethe-Bloch formula for stopping power, first described by Hans Bethe in 1930 [78]. In the following years, it was further enhanced for a relativistic version and shell and density correction terms. For the scope of readability, the formula is described term-by-term. The general equation can be written as:

[3] For heavy charged particles, the collision stopping power S_{col} is often called electronic stopping power S_{el} [77]
[4] Energies below 500 MeV/n

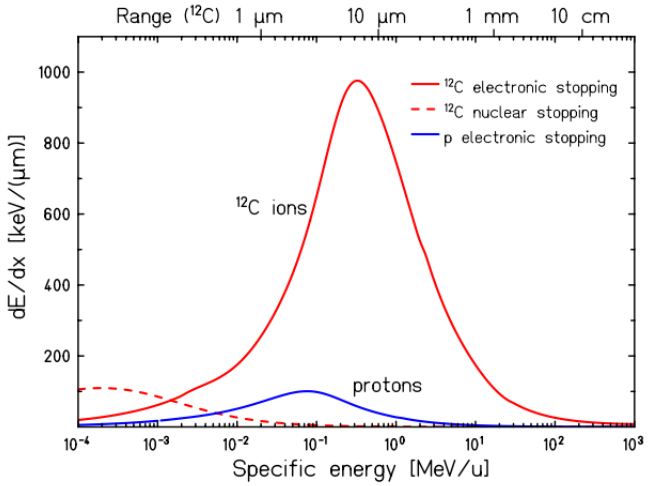

Figure 1.3: Proton and carbon ion energy losses in water target. *Reprinted from [3].*

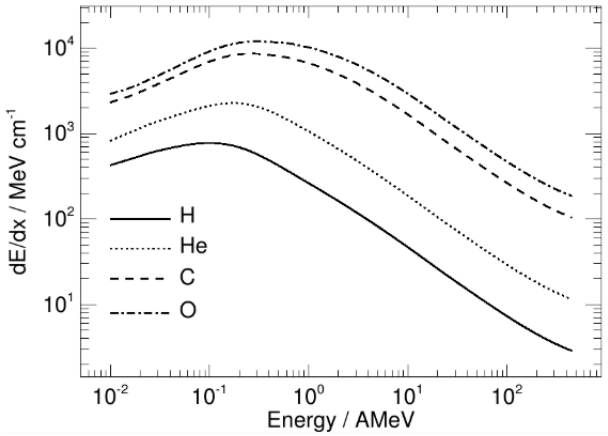

Figure 1.4: Electronic stopping power S_{el} in water as a function of energy for different ions. *Reprinted from [4].*

$$\frac{S_{col}}{\rho} = K\frac{Z}{A}\frac{z^2}{\beta^2}\left(\mathcal{L}+\mathcal{M}\right), \tag{1.6}$$

where:

$$K = 4\pi N_A r_e^2 m_e c^2 = 0.31[MeVcm^2/g], \tag{1.7}$$

in which: $N_A = 6.022 \cdot 10^{23}$ is Avogadro number, $r_e = e^2/4\pi\epsilon_0 m_e c^2 = 2.817 \cdot 10^{-15} m$ is a classical electron radius, $m_e = 511keV$ is the electron mass, $\beta = v/c$ is projectile particle velocity relative to the speed of light, Z is the atomic number of traversed medium, A is the atomic weight of traversed medium, ρ is the density of the absorbing material, z_e is the charge of the incident particle in units of e.

$\mathcal{L}$ and $\mathcal{M}$ correspond to various correction factors that are described below [76]:

$$\mathcal{L} = \mathcal{L}_0 + z_e\mathcal{L}_1 + z_e^2\mathcal{L}_2. \tag{1.8}$$

$\mathcal{L}_0$ is the Bethe term that includes the basic stopping power formula [79]:

$$\mathcal{L}_0 = ln\left(\frac{2m_ec^2\beta^2}{I(1-\beta^2)}\right) - \beta^2 - \frac{C}{Z} - \frac{\delta}{2}. \tag{1.9}$$

$\mathcal{L}_0$ includes the following factors:
I denotes the mean ionization energy of the target. For liquid water, the value was recently experimentally shown to be approximately ~ 78 eV [80].
C is the sum of the target shell corrections, which accounts for the effect of atomic bonds when the projectile velocity is not larger than the velocity of the atomic electrons. At such energies, the assumption that an electron is at rest is no longer valid. Hence, this correction is important for lower energy projectiles.
δ is the density correction resulting from polarization. Polarization shields the outer electrons from the electric field; therefore, collisions with these electrons do not significantly account for the total energy loss. This correction must be included in highly relativistic projectiles [79].
$z_e\mathcal{L}_1$ is a correction that considers the Barkas-Andersen effect [81]. This accounts for the smaller stopping power of a negatively charged particle in comparison to a positively charged particle with the same mass and velocity.
$z_e^2\mathcal{L}_2$ is the Bloch (z_e^4) correction factor added by Felix Bloch [82]. Significant at lower energies.
Finally, $\mathcal{M}$ is a correction valid for relativistic projectiles with medium or heavy mass, and is correlated to the electron-ion Mott cross-section [83].
At high velocities, the atomic electrons of the projectile are stripped off, and the charge of the particle equals the atomic charge number Z. For lower velocities ($\simeq 0.008c$), the projectile captures the electrons from the target, and the charge between the medium and the projectile is redistributed - a partial neutralization of the projectile charge takes place; thus, Z has to be replaced by z_{eff}, which is approximated empirically by Barkas *et al* [81] as:

$$z_{eff} = Z\left(1 - e^{-125\beta Z^{-\frac{2}{3}}}\right). \tag{1.10}$$

From the $1/\beta^2$ ratio in equation 1.6 it can be observed that the energy loss increases with decreasing particle energy. The maximum energy loss is reached for the particle energy:.

$$v = Z^{2/3}v_0, \tag{1.11}$$

where $v_0 = e^2/\hbar$ is the Bohr velocity and $\beta = e^2/\hbar c = 1/137$ [3]. This results in a characteristic peak in the last few millimeters of the particle path.

1.2.2 Energy loss straggling and range straggling

The distance travelled by the particle until it loses its kinetic energy is defined as the range. Assuming slowing down of the particle, as a continuous process, the continuous slowing down approximation (CSDA)

can be used [76] to determine the mean range of the particle based only on their stopping power and their initial energy E_0. Range can be then defined as:

$$R_{CSDA}(E) = \int_0^{E_0} \left(\frac{dE}{dx}\right)^{-1} dE. \tag{1.12}$$

All particles undergo statistical fluctuations in the energy loss within; thus, $R_{CSDA}(E)$ is an approximation. This phenomenon is called energy straggling and causes the Bragg peak to broaden.

The relative target thickness parameter k defines the ratio between the mean energy loss ΔE and maximum energy E_{max}, which can be transferred by the projectile in a single collision with atomic electrons. K is defined as:

$$k = \Delta E / E_{max}. \tag{1.13}$$

In 'thick targets' (when $k > 10$), the projectile undergoes numerous interactions, and loses small amount in every single collision with the target electrons. For multiple processes, the energy loss distribution can be modelled with a Gaussian distribution as follows:

$$f(\Delta E) = \frac{1}{\sigma\sqrt{2\pi}} e^{-\frac{\left(\Delta E - \overline{\Delta E}\right)^2}{2\sigma^2}}, \tag{1.14}$$

with a variance:

$$\sigma_E^2 = 4\pi N_A r_e^2 m_e^2 c^4 \rho z^2 \frac{Z}{A} \Delta x, \tag{1.15}$$

where Δx denotes the measured target thickness (mm).

For 'thinner targets, the Vavilov distribution [84] is used ($0.01 \leq k \leq 10$), and for even thinner targets ($k \leq 0.01$), the Landau distribution [85].

As a result of energy-loss straggling, range straggling occurs. As mentioned in Equation 1.14, for thick targets, energy-loss straggling is approximated by a Gaussian distribution. Thus, the range straggling variation σ_R^2 is closely related to σ_E^2 via:

$$\sigma_R^2 = \int_0^{E_i} \left(\frac{d\sigma_E^2}{dx}\right) \left(\frac{dE}{dx}\right)^{-1} dE. \tag{1.16}$$

The ratio of the distribution width σ_R is proportional to the mean range R and inversely proportional to the square root of the particle mass number as follows:

$$\frac{\sigma_R}{R} = \frac{1}{\sqrt{M}} f\left(\frac{E}{Mc^2}\right), \tag{1.17}$$

where f is a function that depends on the absorber, and E and M are the particle energy and mass, respectively. Thus, according to the approximation from [86]: for protons $\sigma_R = 0.012 R_0^{0.935}$ in water, for heavier ions, the straggling effect is smaller. In tissues, the range straggling is approximately 1% of the mean proton range, 0.5% of the mean helium ion range, and approximately 0.3% of the mean carbon ion range [87].

Although observable, range straggling in tissue targets has a small impact on the quality of the therapeutic beam and treatment itself. The impact of the beam production and delivery systems is often significantly

larger, as is the density inhomogeneities in patient tissues, which will be discussed further in Sections 1.4.2, 1.4.4 and 1.4.3. As a result of these drawbacks, in a typical treatment planning scenario, beam stopping just in front of the OAR should be avoided.

1.2.3 Lateral scattering

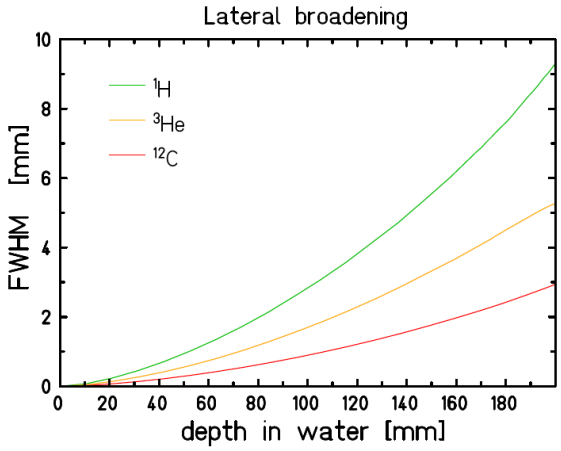

Figure 1.5: Broadening of charged hadron beam: proton, helium, carbon ion. *Reprinted from [1].*

Charged particles, apart from undergoing inelastic collisions (as described in Section 1.2.1), also undergo elastic Coulomb collisions, which deflect the projectile trajectory. For hadrons, small angle scattering has a higher probability than large-angle deflection, and the sum of tens of collisions creates a lateral spread of the beam and an angular divergence. This phenomenon is known as Multiple Coulomb Scattering (MCS). The lateral distribution and the scattering angle θ can be described by the Molière theory [88, 89]. For small angles ($\leq 10^o$), the angular distribution can be approximated by a Gaussian distribution with σ_θ [rad] given by Highland *et al* [90]:

$$\sigma_\theta = 14.1MeV\frac{Z}{\beta pc}\sqrt{\frac{x}{L_{rad}}}\left(1+\frac{1}{9}log_{10}\left(\frac{x}{L_{rad}}\right)\right)[rad], \tag{1.18}$$

where p is a projectile momentum, Z a projectile charge, and $v = \beta c$ a velocity, x is a penetration depth in the traversed medium, and L_{rad} is a radiation length (which can be found in Tsai *et al* [91]).
According to Linz *et al* [87], the lateral deflection of particles refers to the square-root function of the number of nucleons. Hence, the lateral spread of helium is half that of protons, and the carbon lateral spread is 0.3 of protons, as can be seen in Figure 1.5. The MCS increases significantly with a decrease in the energy of the particle owing to $1/\beta pc$ term. Moreover, it is worth mentioning that targets composed of heavier elements cause larger deflection angles than those consisting of lighter elements [3].
In proton or ion therapy, MCS can be observed in elements of the beam delivery and control systems, and in elements located in front of the patient (such as a range shifter and immobilization masks). Hence, for low energies, these elements must be thin, made of light materials, and located as close as possible to the

patient. For higher energies, the tissue with significant inhomogeneities can cause significant broadening of the beam.

1.2.4 Nuclear fragmentation

The probability of nuclear reactions is smaller than that of collisions with atomic electrons, although its importance generally increases with the particle energy (larger penetration depths), primary particle mass (heavier ions), and density of the medium. Nuclear collisions do not affect the position of the Bragg peak, as this is driven by Equation 1.6, although they are responsible for the loss of fluence of the primary particles, fragment production, and emerging secondary particles, which decrease, broaden, and create a tail in the Bragg curve.

In general, nuclear reactions result in an exponential decrease in the fluence distribution of projectiles $\Phi(x)$ with depth x, described as follows:

$$\Phi(x) = \Phi_0 e^{-N\sigma_R x}, \tag{1.19}$$

where Φ_0 is the initial fluence, σ_R is the total nuclear reaction cross section, and N is the atomic density. This attenuation causes a decrease in the energy delivered at the Bragg peak with increasing penetration depth.

The nuclear collisions in heavy ions differ depending on the projectile energy. For energies above 200 MeV/n, collisions are considered pure fragmentations, and their cross-sections are almost constant [3]. For lower energies, other processes take part, which increase the cross-section, such as Coulomb scattering, deep-inelastic collisions, or fusion reactions, for which a semi-empirical parameterization reproduces experimental data [92].

For particle therapy energies, in general, all nucleus-nucleus collisions can be described by a two-step abrasion-ablasion process, as shown in Figure 1.6. During the fast initial abrasion interaction, spectator nucleons of the projectile and the target change little momentum, and in the overlapping reaction zone, a fireball is created from the excited nucleons of the projectile and the target. Subsequently, the slower ablation process takes part, during which the fireball, remaining projectile-fragment, and target-fragment are de-excited by the evaporation of nucleons and clusters [3]. Owing to geometrical reasons, peripheral interactions are the most common; however, central collisions also occur, leading to the complete destruction of the target and projectile.

The secondaries created from the target fragment typically deposit their energy in proximity to the target itself [93]. On the other hand, the secondary nucleons, particles, and fragments of the projectile have a similar velocity and almost the same direction as the initial projectile. Hence, they travel beyond the Bragg peak, depositing the rest of their energy, producing a fragmentation tail, which is explicitly visible for ions [94, 95]. For protons, only target fragmentation is possible, which results in secondary protons, deuterons, tritons, helium ions, alfa, or neutrons. However, for heavier ions, projectile fragments cause the build-up of light fragments along their trajectory, which can cause further fragmentation reactions [96], see Figure 1.7. Moreover, secondary fragments, with charge and mass lower than those of the primary beam, have a longer range, which contributes to additional dose deposition visible in the Bragg peak tail. The heavier the ion, the more fragments are produced, and consequently, ions heavier than oxygen are not considered suitable

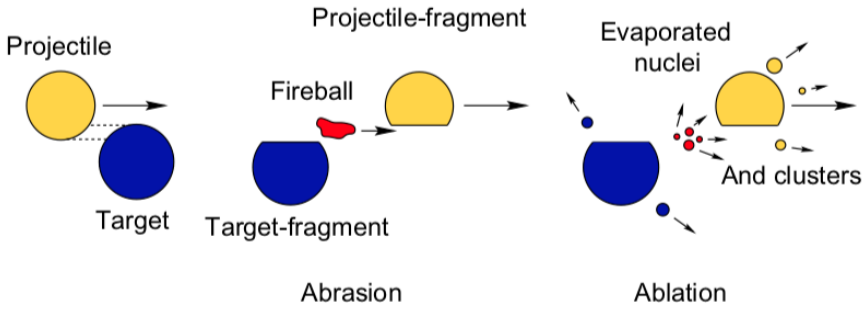

Figure 1.6: Abrasion - ablation process. *Reprinted from [5].*

for clinical use [97]. Helium is currently considered a good compromise between its biological effectiveness and relatively low fragmentation cross-section.

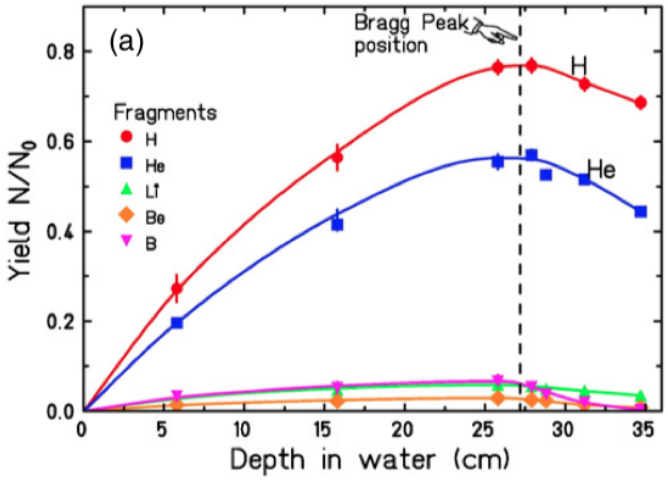

Figure 1.7: Build up of secondary fragments produced by 400 MeV/n carbon ion in water. *Reprinted from [6].*

Another consequence of the fragmentation of the shape of the Bragg curve is that fragments contribute to the lateral and longitudinal broadening of the beam [16]. In general, the angular spread of fragments is narrow; however, lighter fragments, such as protons or helium ions, may contribute significantly to the broadening of the beam at the distal part of the Bragg peak.

Due to the complexity, and lack of significant amount of measurements for ion fragmentation cross-sections, for the therapeutic energy range, Monte Carlo models can be a solution for a correct reproduction of the double differential cross-section for all emitted particles. MC can provide information on the expected impact of the target fragmentation, not only for proton therapy (where measurements are accurate enough [92]), but also for ion beam therapy, where projectile fragmentation with relatively high velocity becomes a major problem for the dose distribution in normal tissues located beyond the Bragg peak.

1.3 Biological basis of protons and ion beams in radiotherapy

Any tumor cell can be destroyed by radiation at a sufficiently high dose. This limitation comes from the radiation tolerance of healthy tissues located close to the tumor. Therefore, precise charged particle therapy has a clear advantage over conventional radiotherapy. It provides:

- better conformity of the target coverage with a high dose, which increases a Tumour Control Probability (TCP) - the probability that a given dose of radiation will provide a total control or eradication of the tumour [98],
- limitation of a dose delivered to the organ at risk (OAR), which reduces the Normal Tissue Complication Probability (NTCP) - the probability that a given dose of radiation will induce damage in healthy tissue organs [98],
- decrease in integral dose, which lowers the risk of secondary tumours.

This section provides an overview of the biological basis of proton and ion beam therapies.

1.3.1 Basis of radiobiology

Cell deoxyribonucleic acid (DNA) is the most sensitive cell component responsible for encoding the genetic instructions for cell function and development. It has a double-helix structure with two strands of nucleotides composed of three parts: a deoxyribose, a phosphate group, and a nitrogenous base. Four types of nitrogenous bases exist: adenine (A), guanine (G), cytosine (C), and thymine (T), which create pairs (A-T or G-C) and connect nitrogenous bases in opposite strands. Radiation therapy works mostly by damaging DNA, because cells with functional DNA damage cannot create viable daughter cells nor reproduce.

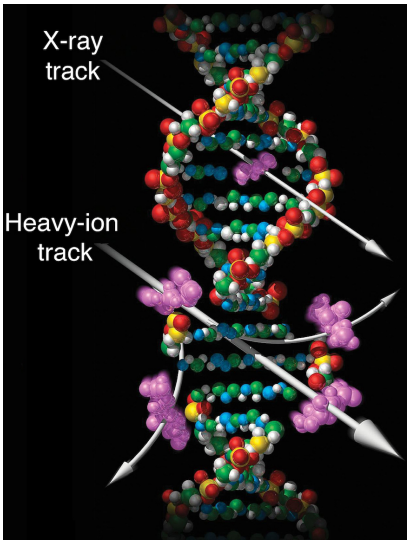

Figure 1.8: Different kinds of damage to the DNA caused by photons and ions. Credits NASA

The underlying reason for the different biological effectiveness of photons and ions is the density of the ionizing tracks crossing the cell. A denser ionization track is more effective for cell inactivation than a

few low-ionizing tracks. While photon beams generate rather low ionizing density radiation, hadron particle beams (especially ions) provide more direct hits, and thus more lesions to the cell's DNA. At the microscopic level, photons transfer most of their energy to secondary electrons via the Compton-effect, which loses their energy within a typical range of 1-3 cm, and as a consequence of a larger energy, spreads it over a large distance/radius from the interaction point. In the case of heavier particles, which undergo Coulomb interactions, they deposit most of their energy locally, creating a substantial number of secondary electrons but with smaller energies (100 eV); thus, smaller ranges (few μm) [99, 100]. The small mean free paths of electrons provide a higher probability of events being close to each other, and hence are closer to both strands of the DNA. Single and isolated DNA lesions can be easily repaired by the cell (based on nitrogenous base pairing), although clusters of DNA double-strand breaks (DSB) significantly lower the probability of cell repair and lead to apoptosis (programmed cell death).
In addition to direct primary DNA damage, indirect damage also occurs, which is related to the generation of reactive oxygen molecules (ROS), which are a result of water radiolysis in cells [9]. ROS also cause DNA damage as well as damage to cellular mitochondria, which may ultimately lead to cell apoptosis. However, for this indirect damage, the existence of oxygen in cell proximity is crucial. In the case of fast-growing tumors, it is very common that not enough new vessels are created to provide sufficient oxygen to the tumor core, which leads to the creation of poorly oxygenated (hypoxic) regions. These regions are highly radioresistant [101]. The level of radio-resistance due to a lack of oxygen is quantified by the Oxygen Enhancement Radio (OER) (see Equation 1.20). The OER plays a significant role in standard radiotherapy; however, for charged ions, the effect of oxygen levels is smaller. Therefore, ion particles are more efficient in decreasing OER and killing tumors with hypoxia. OER is defined as:

$$OER = \frac{D_{hypoxic}}{D_{aerobic}} \tag{1.20}$$

Radiation-induced DNA damage might also result in cell misrepair. A single-strand break may not be sufficient for cell apoptosis and can cause a malignant mutation during repair. In the case of double-strand breaks, chromosomal rearrangement may occur in a different form, causing an effect called chromosomal aberration [102]. Most aberrations lead to cell death; however, some cells survive, leading to increased radioresistance or secondary tumors [103].

1.3.2 Dose-to-water and Dose-to-medium

The absorbed dose is a basic quantity related to the physical, chemical, and biological effects of ionizing radiation. The dose absorbed in tissue is the quantity used to refer to the radiotherapy effects, and it is defined as [104]:

$$D = \frac{dE}{dm} Gy = \frac{J}{kg}, \tag{1.21}$$

where dE is the mean energy deposited by the ionizing radiation in mass dm.
Because of historical reasons and the fact that the human body is mainly composed of water, in dosimetry, water material is typically used as a tissue reference medium (dose-to-water - D_w). This simplified approach (used by analytical dose calculation treatment planning systems) models the patient's body as a set of water voxels with different densities, electron densities, or stopping powers. In reality, tissue composition varies

significantly, and Monte Carlo codes (i.e., FLUKA) allow the calculation of dose to tissue (dose-to-medium - D_m), which reflects particle interactions (especially nuclear interactions) more accurately. Nevertheless, the clinical experience gained through years of radiotherapy is based on the dose-to-water, and commissioning quality assurance procedures are also performed in water [105] thus, it is necessary to comply with the clinical approach and for dose calculations perform on-the-fly conversion from D_m to D_w. This is achieved by considering all elements of the mixed-radiation field produced by the primary beam, secondary particles, and fragments that undergo nuclear reactions in a patient voxel geometry. Hence, D_w is calculated as [74]:

$$\overline{D_w} = \sum_i \int \Phi_{m,i}(E) \frac{S_{w,i}(E)}{\rho_w} dE, \tag{1.22}$$

where $\Phi_{m,i}(E)$ is the particle fluence spectrum in a medium for all particle species i with kinetic energy E and $S_{w,i}(E)/\rho_w$ is the corresponding mass stopping power in water.

A patient model is typically obtained using a Computerized Tomography (CT) image. CT numbers - Hounsfield units (HU) represent the linear transformation of an effective X-ray attenuation coefficient. It is a CT-scanned dependent coefficient, with a typical range of -1000 $\leq$ HU $\leq$ 3500 and fixed values for distilled water at standard temperature and pressure conditions $HU = 0$, and air at approximately $HU = -1000$ [106]. The corresponding value for a specific tissue is given by:

$$HU = 1000 \frac{\mu - \mu_w}{\mu_w - \mu_{air}}, \tag{1.23}$$

where μ_w and μ_{air} are the linear attenuation coefficients of water and air, respectively, and μ is the linear attenuation coefficient obtained for the tissue.

It is known that, in approximation, each tissue has a different HU value, which allows the discrimination of voxels with a distinct material density, stopping power, or composition. For analytical dose calculation engines, the HU to stopping power (or density) conversion ratio is used. If the stoichiometric approach [107] is used for calibration, the accuracy of the calculated stopping power for tissue samples can be 1% for soft tissues and 2% for bone [108]. However, non-biological materials will typically not be transformed into the correct stopping power, which might have significant consequences when irradiating through patient immobilization materials. In addition, the influence of patient's metal implants is also noticeable with saturation of HU values (up to 3095 HU), which does not allow distinguishing between different types of metals (with different stopping powers) [7]. MC allows, on the other hand, the assignment of a mass density and detailed chemical composition of the patient's tissue, immobilization devices, and metal implants; hence, MC correctly calculates the stopping power for all materials. For biological tissues, the most popular approach uses a look-up-table (LUT), based on the work of Schneider *et al* [109], for HU tissue parameterization. Other materials can be manually defined.

1.3.3 Linear Energy Transfer (LET)

Different particles, although distributed at the same physical dose, can lead to different biological effects, see Figure 1.8. The absorbed dose is the average quantity of the deposited energy. Hence, it does not consider the random fluctuation of the interaction events and energy distribution at the microcellular level. For the same absorbed dose, the number of energy deposition events estimated in micro volumes is highly variable,

and stochastic averaging might not be meaningful [110]. Linear Energy Transfer (LET) $[keV/\mu m]$ expresses the beam quality at the microdosimetric level. It is defined in terms of the mean energy lost by charged particles due to electronic interactions dE_{el} while travelling dx distance along their track [111]:

$$LET_{\infty} = \frac{dE_{el}}{dx}[keV/\mu m] \tag{1.24}$$

LET_{∞} is known as an unrestricted LET, where energy deposition from all secondary electrons is considered. For charged particles heavier than the electrons, $LET_{\infty} = S_{el}$.

A certain amount of energy is absorbed in non-local, more distant positions in the material, and consequently, this energy does not contribute to the ionization density at the microscopic level. It is mainly derived from high-energy electrons with a long range (such as $\delta-rays$) and in small amounts from bremsstrahlung photons and Cerenkov radiation. To exclude their contribution, the energies above the threshold Δ for secondary electrons are settled [104] and the restricted LET term is defined as

$$LET_{\Delta} = \frac{dE_{\Delta}}{dx}[keV/\mu m] \tag{1.25}$$

Radiation can be divided into low-LET radiation (photons, protons) and high-LET radiation (carbon and oxygen ions). The LET of a monoenergetic proton beam at the entrance is approximately 1 $keV/\mu m$, reaching 100 $keV/\mu m$ at the end of its range, and the LET contribution is derived mostly from the primary particles. In contrast, for carbon ions, these values are 10 $keV/\mu m$ for the entrance and exceed 1000 $keV/\mu m$ at the end of their range. For ions, secondary particles created during nuclear reactions significantly influence the LET distributions.

Therefore, calculating the LET from monoenergetic beams with a single particle type, although straightforward, does not refer to the real treatment scenario. Determination of the total biological effect of multiple particle types with different energies is a significantly more complicated task [112]. Therefore, a mean LET value is introduced to account for the dose contribution of different LET components that create the radiation field [9]. The mean LET is calculated by averaging the stopping powers $S_{el}(E)$ of all particles i with a particle energy spectrum E at a specific position x along the beam trajectory.

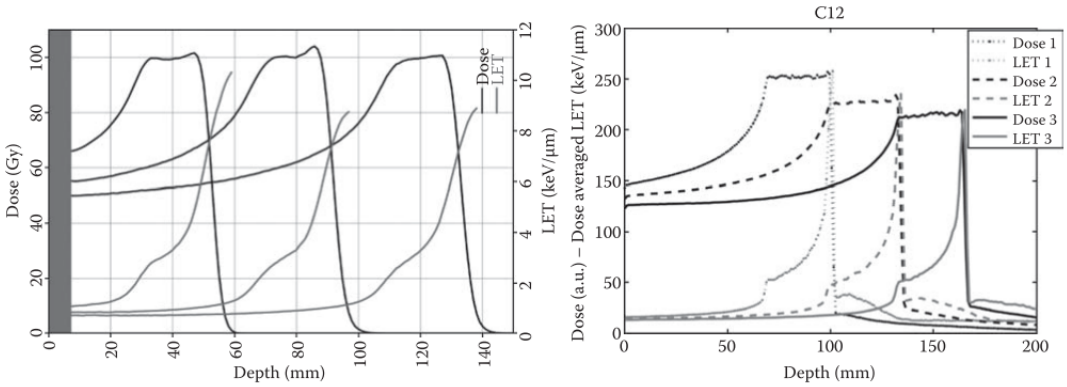

Figure 1.9: SOBPs and their LET_D profiles of a proton (left) and carbon ion (right). *Reprinted from [7].*

Two definitions of the mean LET are used: a fluence-averaged LET (LET_F) and a dose-averaged LET (LET_D) [111]. Both can be calculated for primary and secondary particles generated through nuclear interactions. LET_F can be defined as

$$\overline{LET}_F(x) = \frac{\sum_{i=1}^{N} \int_0^\infty S_{el}^i(E,z)\varphi_i(E,z)dE}{\sum_{i=1}^{N} \int_0^\infty \varphi_i(E,z)dE}[keV/\mu m], \tag{1.26}$$

and LET_D as follows:

$$\overline{LET}_D(x) = \frac{\sum_{i=1}^{N} \int_0^\infty S_{el}^i(E,x)D_i i(E,x)dE}{\sum_{i=1}^{N} \int_0^\infty D_i(E,x)dE} = \frac{\sum_{i=1}^{N} \int_0^\infty (S_{el}^i(E,x))^2\phi_i(E,x)dE}{\sum_{i=1}^{N} \int_0^\infty S_{el}^i(E,x)\phi_i(E,x)dE}[keV/\mu m], \tag{1.27}$$

where S_{el}^i is the stopping power, ϕ_i is the local particle spectrum, and D_i is the dose contribution from particle i with energy E at depth x.

Because the biological effectiveness of radiation depends mainly on high-LET particles, which contribute the most to the dose deposition per particle, $\overline{LET}_D(x)$ is typically used to relate the beam quality to its biological effect. Several clinical studies have attempted to determine the optimal values of $\overline{LET}_D(x)$ for a particle type to be used as a simplified indicator of the biological response of the tissue to irradiation [113, 114], but with mixed success. It is known that, with increased LET, the number of clustered (multiple damages) DNA lesions is also increasing [9], and with high LET radiation, the OER in hypoxic tumor cells decreases [110]. However, owing to the non-linear response of the cell survival to LET values, the only indication is to maintain the $\overline{LET}_D(x)$ as low as possible for the normal tissue, while targeting the tumor with a higher $\overline{LET}_D(x)$, but not higher than LET_{max} value, above which the overkill effect appears [3]. Currently no analytical systems for LET calculations are available on the clinical market, on the other hand, general purpose MC codes are suitable for determining the LET distribution.

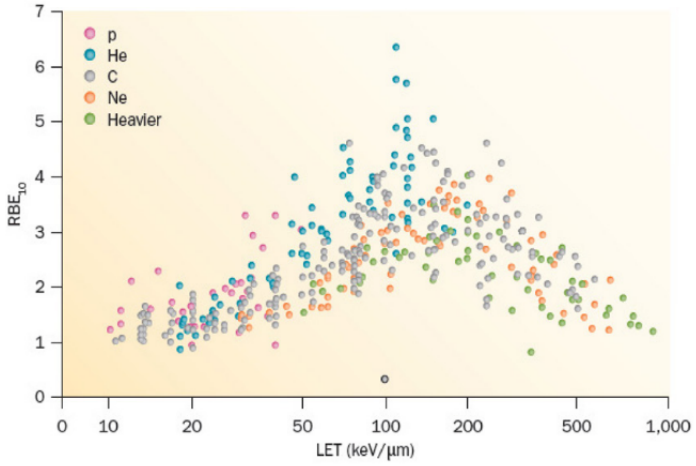

Figure 1.10: Radiobiological Effectiveness (RBE) at 10% survival compared with LET, for different ions from published experiments on in vitro cell lines. *Reprinted from [8].*

1.3.4 Radiobiological effectiveness

The biological effects of radiation depend on several factors. Such as an amount of the delivered dose, an energy or an LET of the penetrating particle, a particle type, as well as a radio-sensitivity of the irradiated cell, an oxygen supply and a treatment fractionation [115]. A few decades of clinical experience gained with photon radiotherapy has enabled the efficient determination of the planned dose with a reliable clinical outcome. Thus, the best way to determine the biological effectiveness of new radiation types is to estimate it in relation to effects obtained by radiation already known, using a weighting factor called Radiobiological Effectiveness (RBE), which is defined as:

$$RBE = \frac{D_{X-rays}}{D_{ions}}, \tag{1.28}$$

where D_{X-rays} is the ratio of the dose delivered by photons (typically 250 kV X-rays or cobalt-60 (Co-60)) to the dose from the new particle type, D_{ions} leading to identical biological effects [37]. Consequently, the isoeffective, clinically prescribed dose is calculated as $D_{bio} = RBE \cdot D_{ph}$ [Gy(RBE)] and is called an effective or biological dose.

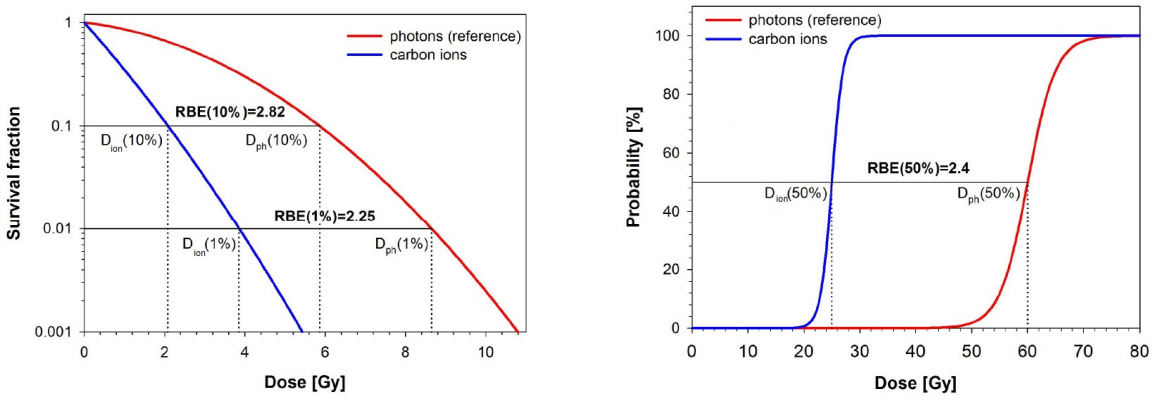

Figure 1.11: The most frequently used methods to determine the RBE: left - cell survival curves in vitro, where different survival levels are considered as different end-points, right - response curves dependent on NTCP or TCP in vivo. *Reprinted from [9].*

The RBE requires determination of a biological end-point (effect), as shown in Figure 1.11. For tumors, the important end-point is the TCP, and for normal tissue, the NTCP. In addition, cell survival is a parameter commonly used for in vitro experiments, and it can be estimated using a linear quadratic model (LQM) [116, 117, 118], defined as:

$$S(D) = e^{-\alpha D - \beta D^2}, \tag{1.29}$$

where $S(D)$ is the surviving fraction, D is the absorbed dose, α is linear, and β is a quadratic cell killing coefficient. α corresponds to cell death from lethal damage caused by a single particle, β defines death caused by the interaction of damages from different radiation tracks [119].

The concept of the RBE is simple, but shows dependency on many factors, typically in a non-linear manner,

see Figure 1.10. Mentioning i.e.:

- Dose - the RBE increases with lower dose [23], with a higher dose the difference between two types of radiations is smaller. For photons, the initial survival fall-off with respect to the dose is broader than that for ions (see Figure 1.11), hence the RBE increases with the increase of cell survival and dose decrease.
- Energy or LET - the RBE increases with higher LET, however reaching maximum value, above which the RBE decreases further [23]. For protons, this point is 31 $keV/\mu m$ [21], and for ions between 100 $keV/\mu m$ (helium) [21] up to approximately 200 $keV/\mu m$ (carbons) [10]. The reason for the overkilling effect is the contribution of the high-LET particles to the dose deposition. It is sufficiently large that a single particle may successfully limit cell survival. Thus the residual dose is wasted. This also limits the probability of hitting because of the lower number of particles required to acquire a certain dose, resulting in a lower RBE for cell killing.
- Particle type - for a given LET the RBE is higher for lighter ions. This can be explained by the fact that, for heavier ions, the maximum RBE is shifted towards a higher LET. At the LET corresponding to the RBE maximum of protons, the carbon ions are faster, resulting in a broader track with a reduced ionization density. Slower ions, with a smaller diameter of the ionization track, increase the ionization density and cell killing effect [3]. Moreover, for light ions, the difference between the proximal rise and the peak part for biological dose-depth curves is lower, whereas for heavier ions, the biological maximum increases more significantly, causing a risk to OARs in proximity to the target.
- Cell type (cell intrinsic radio-sensitivity) - the RBE depends on a repair capacity of the cell system after photon irradiation. The first approximation can be described using the α/β coefficient of the photon dose effect curve from the LQM [116], where the RBE increases with a decreasing α/β ratio [120]. For example, Weyrather *et al* [10] irradiated three different hamster cells (V79, CHO, and xr5) and noticed that for repair-proficient cells (V79, CHO), the RBE exhibited a maximum between 100-250 $keV/\mu m$; for a radio-resistant cell (xr5), there was no maximum, but a slight decrease above 100 $keV/\mu m$.

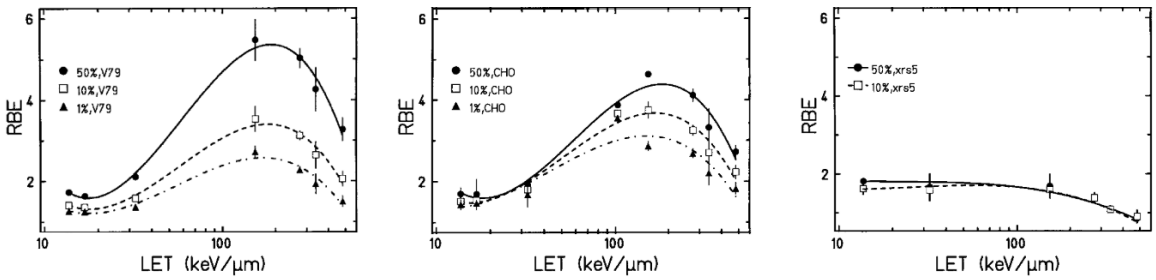

Figure 1.12: RBE at a survival level of 50%, 10% and 1% for V79, CHO and xrs5 cells. *Reprinted from [10].*

- Fractionation - the RBE increases with decreasing fractional dose [121]. Fractionation means that the dose is delivered to the tumor in several daily sessions depending on the clinical protocol. The reason for fractionation is that normal tissue recovers faster than tumor cells. Few studies have been

performed to determine the RBE with different fractionation schemes, to limit the number of fractions, and to increase the delivered dose, in order to lower the treatment cost [101, 122].

- Oxygen Enhancement Ratio (OER) (described in 1.3.1) - the RBE increases with the decrease of the OER [23].

1.3.5 Radiobiological models

Two strategies can be followed to determine the RBE: experimental and modelling approaches. An experimental approach requires a set of precise measurements for different irradiation conditions and various cells for in vitro studies [123, 124]. Non-existing values must be extrapolated or interpolated from experimental points. The direct transfer of measurements to an in vivo clinical scenario is not a trivial task [9]. The second approach requires creating a biophysical model, which would be able to predict an in vivo response of a biological material to the ionizing radiation, from the known response of the material irradiated by photons.

The recommendation from the ICRU [125] stated that proton $RBE = 1.1$ with respect to photons, and it is considered to be constant through their trajectory. This determined the same RBE value at all positions of the Bragg curve at all dose levels and for all tissues. However, a microdosimetric examination of the particle spectrum presented a small variation from 1.1 [93, 126], and recent discussions concerning the nonconstant value have been raised because of unexpected complications from proton treatment [127]. In reality, the RBE of the proton SOBP varies from RBE = 1.1 at the entrance, RBE = 1.15 at the center, RBE = 1.35 at the distal edge to RBE = 1.7 or even RBE = 4-6 in the fall-off [127]. The differences in RBE values are mainly derived from the dose level, an increase in the LET due to proton slowing down, fractionation, oxygenation, and tissue type (α/β ratio) [128, 129]. Owing to these constraints, the possibility of incorporating LET_D into treatment planning is being discussed [130, 131] and some phenomenological RBE models have been developed [132, 133].

Heavier ions with higher biological effectiveness have more complex RBE depth-dose distributions, which must be considered in more details [120, 121, 134, 135, 136, 137, 138]. RBE determination is not a trivial task in view of the variations in biological effectiveness between different ions and different tissues. For example, in the '80s at the Bevalac at Lawrence Radiation Laboratory, several patients were treated with neons, and long-term evaluation of the clinical trial presented unexpected side effects in normal tissues. These side effects are further associated with high-density ionizing radiation and elevated biological effectiveness [139]. Consequently, in 1994, it was decided to initiate patient irradiation with lower Z-ions - carbons [140, 141]. Currently, carbon ions are the most widely used ions, for which two radiobiological models are accepted for clinical purposes in scanned pencil beam facilities - Microdosimetric Kinetic Model (MKM) and Local Effect Model (LEM) [5]

MKM - Microdosimetric Kinetic Model

MKM [143, 144, 145] is based on the Theory of the Dual Radiation Action [117] and originates from cellular microdosimetry models. MKM estimates cell death in domains - micrometer-scale size partitions of the cell

[5]The phenomenological mixed-beam model developed and partially used at NIRS in Japan [142] will not be described, because it is used for passive beam scattering, which is not the scope of this thesis

nucleus. Cell damage is calculated on a microdosimetric spectrum of energy deposition. From this, the average number of lethal events after irradiation is derived in every single domain. Thus, the LQM is a function of the energy absorbed by a single domain. Finally, cell survival S(D) is calculated using Human Salivary Glands (HSG) cells response as an input parameter:

$$-ln(S(D)) = (\alpha_0 + \beta z_{1D}^*)D + \beta D^2, \tag{1.30}$$

where $\alpha_0 = 0.172Gy^{-1}$ [146] describes the initial slope of the surviving fraction curve, $\beta = 0.0615Gy^{-2}$ [147] is a term independent of the radiation type, and z_{1D}^* is the saturation-corrected dose-mean specific energy of the domain delivered in a single event, which depends on the energy z and the saturation-corrected energy z_{sat}.

The saturation-corrected energy determines the point of the over-killing effect, and is dependent on the radius of the cell nucleus R_n and the radius of the domain R_d. The RBE is then calculated [146] as:

$$RBE = D_{st}(S) / \left(\frac{-\alpha_0 + \sqrt{\alpha_0^2 - 4ln(S)\beta}}{2\beta} \right), \tag{1.31}$$

where $D_{st}(S)$ is the reference radiation dose for survival fraction S.

According to the NIRS protocol, $D_{bio} = D \cdot RBE$ is scaled by a factor $F_{clin} = 2.39$ to obtain a clinical dose $D_{clin} = D_{bio} \cdot F$ [148].

LEM I - Local Effect Model

LEM I was developed at GSI [149, 150, 151]. It uses microscopic dose depositions around ion tracks to determine the RBE with respect to photons. The critical target in the cell is uniformly distributed over the cell nucleus and is divided into infinitely small cellular sub-volumes. The damage depends on the amount of locally deposited energy (in sub-volumes) by different radiation track structures with different radial dose distributions. The damage is independent of the origin of energy deposition, that is, photons or ions. The cell survives only if none of the subvolumes receive lethal damage [9]. The survival curve is calculated:

$$-ln(S) = \begin{cases} \alpha D + \beta D^2 & D \leq D_t \\ \alpha D_t + \beta D_t^2 + (D - D_t)S_{max} & D > D_t \end{cases}, \tag{1.32}$$

where α and β are radiosensitivity parameters of a cell, D_t is the transition dose above which the dose-response curve from the linear-quadratic turns into a linear function, $S_{max} = \alpha_X + 2\beta_X D_t$ is the maximum of a slope occurring at D_t for α_X and β_X is the radiosensitivity parameter for photons.

The RBE is then calculated as follows:

$$RBE = \begin{cases} \left(\sqrt{\frac{-ln(S)}{\beta_X} + \left(\frac{\alpha_X}{2\beta_X}\right)^2} - \left(\frac{\alpha_X}{2\beta_X}\right) \right) / D & -ln(S) \leq -ln(S_t) \\ \left(\frac{-ln(S) + ln(S_t)}{S_{max}} + D_t \right) / D & -ln(S) > -ln(S_t) \end{cases} \tag{1.33}$$

where $-ln(S_t) = \alpha_X D_t + \beta_X D_t^2$.

Comparison and new RBE models

Different RBE dependencies and chosen biological end-points for biological models lead to different RBE-weighted doses for identical absorbed dose distributions. Therefore, the prescribed doses in GyRBE units cannot be considered isoeffective in clinical scenarios, and the transfer of radiobiological effect information between two models is complicated. According to Fossati *et al* [121] prescribing 3 GyRBE in Europe using LEM I and prescribing 3 GyRBE using MKM may provide treatments with DVH for RBE-weighted dose almost identical, while the two treatments will differ in the biological end-points (TCP or NTCP), and none of them might be isoeffective to 3 Gy of physical dose delivered by photons.
For helium ions, the development and application of the RBE models is currently under discussion [152]. Several phenomenological models have been developed to date [136, 143, 153]; however, they have not been applied clinically. The upgraded LEM model, LEM IV, has already been benchmarked extensively for carbon and helium ions, and it can predict the RBE for several other ion species [26]; however, it has not yet been applied clinically. The modified Microdosimetric Kinetic Model (mMKM) was selected for the first helium-4 ion therapy using active scanning at HIT [154]. Other radiobiological models have recently been presented, such as BIANCA (BIophysical ANalysis of Cell death and chromosome Aberrations), which supports proton, helium, and carbon ion treatments for calculation of cell survival and RBE, as well as allows calculation of the probability of chromosomal aberrations in normal tissue [102, 155, 156].
Monte Carlo codes are suitable for determining in detail the mixed radiation field from the treatment plan, where the analytical Treatment Planning System (TPS) provides only partial output data for RBE modelling. Considering both primary and secondary particles, through the ionization track, MC code allows the determination of the RBE in detail for complex situations. Moreover, it is possible to investigate treatment results from different institutions, simulate the RBE-weighted dose from treatment optimized for another RBE model, and determine differences.

1.4 Application of proton and ion beams in radiotherapy

The cost of charged particle therapy is typically 2-3 times higher than the cost of conventional therapy [157], meaning that access to non-conventional therapy is still limited. Protons are currently the most feasible option for delivering doses precisely. Light ions have a few advantages over protons in terms of physical and biological properties, such as reduced lateral scattering, higher LET, and higher RBE. However, at the same time, they presents physical drawbacks - as to include: fragmentation tail, which leads to a deposition of the residual dose, significantly affecting lateral dose distributions [95]. In recent years, there has been increasing interest in helium ions [158, 159, 160], owing to twice as low a lateral spread compared to protons, a sharper lateral penumbra, an intermediate RBE, and a lower cost (1.4 x cost of a proton facility) compared to carbon ions (2.6 x cost of a proton facility) [87].
After considering the demand for proton or ion therapy but before building a facility, a few factors have to be taken into consideration: determining which patients will benefit from this type of radiotherapy, defining a beam delivery system, choosing a treatment planning system, and providing quality assurance procedures. The cost, timeline to establish a facility, and efficacy vary between proton, helium, and carbon ion modalities, and there are questions, problems, and gaps in the clinical application, which require further insight.

This section provides an overview of clinically applied proton and ion therapies, describing each stage from the clinical rationale of particle therapy, beam production systems, transport and delivery systems, treatment planning, quality assurance, and possible treatment uncertainties. Some questions raised in this section may be answered with MC simulations.

1.4.1 Clinical rationales for proton and ion beam therapies

Considering the clinical rationale for proton and ion beam therapies, most patients benefit from a highly conformal dose distribution and a lower risk of secondary cancer incidence [161, 162]. ASTRO [163] indicated only a few cases when the use of a proton beam is not supported, when a clinical urgency is needed, with extensively moving targets or for a palliative treatment, where the normal tissue tolerance would not be strictly considered.

The main group of patients profiting from proton therapies are children, due to a reduced risk of radiation-induced normal tissue complications expected during their lifetime [164, 165]. Ions are avoided in pediatric cases owing to an unknown late effect of high-LET radiation. For adults, tumors frequently treated by protons are head-and-neck cases; certain types of tumors were found to respond better if treated with higher-LET radiation (ions) such as salivary glands [166], chondrosarcomas [167], and glioblastoma [168]. Finally, a superior inverse depth dose profile with a sharp gradient provides the advantage of delivering the dose to irregularly shaped target volumes or targets located close to critical structures [169].

Several ongoing clinical trials are trying to determine which tumors respond best to proton or ion treatment. Few clinical trials are currently studying various types of tumors [170] as well as the ion species to be used. Durante *et al* [157] presented five clinical trials in phase III, comparing protons with X-rays, two clinical trials comparing the effectiveness of light ions versus protons, and three comparing carbon ions and X-rays; however, to date, the results have not been conclusive [171, 172]. Further investigation of its biological effectiveness is required, especially if helium ions are being considered for radiotherapy.

1.4.2 Beam production

In a typical proton or ion beam therapy center, a beam production system should be capable of selecting and delivering beams with a 30 cm range in water, which corresponds to a maximum energy of 220 MeV for protons, 225 MeV/n for helium ions, and 430 MeV/n for carbon ions. The delivered beam should have a maximum energy spread of approximately 0.1% and energy changes must be performed relatively quickly (up to a few seconds) [11]. The accelerator beam production system delivers a dose at a rate of 2 Gy/min/l [173]. Finally, for operational reasons, the accelerator should be small, reliable, cheap, modular, and easy to operate.

As of 2022, all accelerators used in charged-particle therapy facilities were either isochronous cyclotrons (57 in operation), synchrocyclotrons (13 in operation), or slow-extracting synchrotrons (40 in operation) [52]. Linear accelerators dedicated to protons [174] or ion beam therapies are in the final construction phase. However, they are forecasted to be released into the market within the next few years [174].

The description of the main beam production systems used or planned for use in charged particle therapy is presented below.

Cyclotrons

Cyclotrons are circular accelerators in which particles follow a spiral path with a continuous duty cycle. The particles retain spiral trajectories using a strong magnet. They are accelerated repeatedly by a radiofrequency (RF) high-voltage electric field created between the two electrode plates of a cyclotron. Synchrocyclotrons are a type of cyclotron with superconducting magnets, in which the frequency of the RF electric field varies synchronously with the speed of the particle to account for relativistic effects of the particle mass. In contrast, isochronous cyclotrons compensate for an increase in particle mass by increasing the strength of the magnetic field, maintaining a constant frequency of the high-voltage RF [173].
Overall, cyclotrons are small, with a typical diameter between 5 and 2.5 m and a height of approximately 1.5 m, they have high reliability (few components, compactness, and ease of operation), and their cost is relatively low. Currently, cyclotrons are only used in proton therapy. They provide a continuous proton beam with a fixed energy value. Therefore, passive energy variation needs to be predicted through a reduction in the nominal energy. For this purpose, degraders of various thicknesses are placed along the beam path. The typical time needed for energy modulation (through insertion of the appropriate degrader) is 50-100 ms, meaning that the cyclotron provides a fast dose delivery, but with the drawback of beam quality and purity, due to MCS and range straggling. In addition, the activation of cyclotron materials and components near degraders is inevitable because of severe beam loss during beam collimation. Finally, the neutron background contribution to the patient should be considered while planning the treatment, which adds an additional advantage to MC simulations [96].
Currently, cyclotrons are provided by companies such as IBA, Varian, Mevion, and Sumitomo. Current development focuses on superconducting cyclotrons and cyclotrons for particles heavier than protons [11].

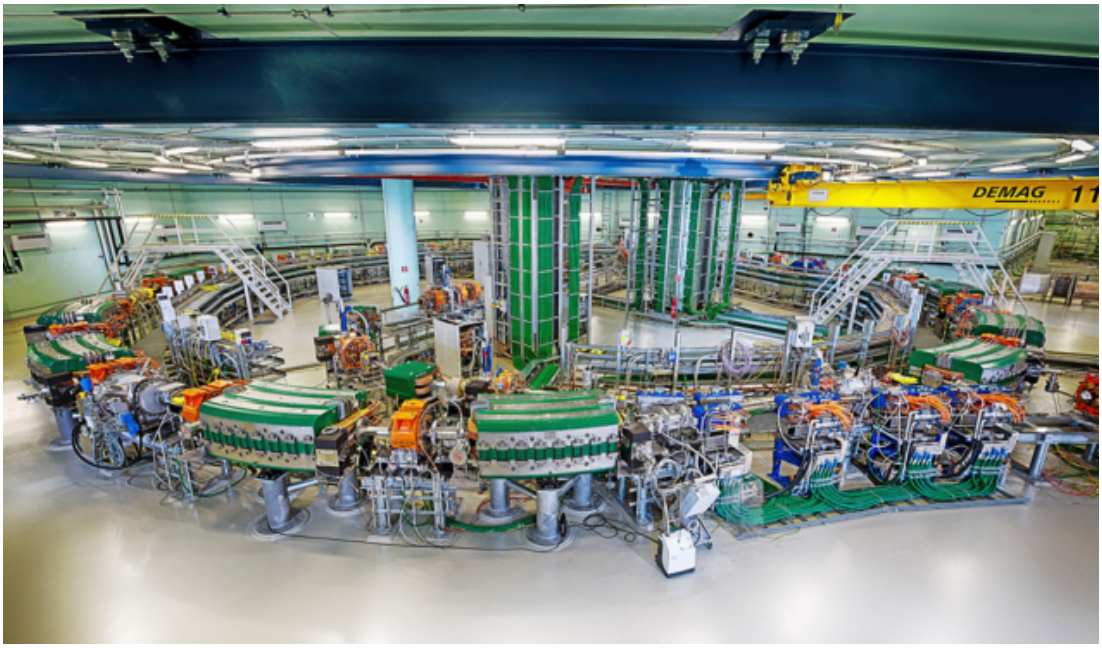

Figure 1.13: The MedAustron proton/carbon ion synchrotron. *Credits: MedAustron, Austria.*

Synchrotrons

Synchrotrons are circular accelerator rings that are usually linked with linear accelerators for the pre-acceleration of particles up to a few MeV. In synchrotrons, each particle repeatedly traverses the same path during the acceleration cycle. A magnetic field is used to bend the particles in a circular fixed orbit using a dipole magnet. An RF electric field, located in straight sections between bending magnets, is used to accelerate the particles and create an energy gain per turn. The particle trajectory is focused via quadrupole magnets and corrected using sextuplet magnets [173].
Overall, synchrotrons are larger than cyclotrons, with typical diameter of 8-10 m for protons and 20-25 m for carbon ion machines. They are also more complex and slow to operate. As mentioned previously, synchrotrons can accelerate protons and other types of ions (helium and carbon ions). They can actively vary energy within high-intensity spills delivered every few seconds (1-2 s). Synchrotrons provide excellent beam quality but at a slow rate.
Synchrotrons are currently provided by Siemens, Hitachi, ProTom, and Mitsubishi. In 1996, a conceptual medical synchrotron design (the study of the consortium between CERN and TERA) - the Proton and Ion Medical Machine Study (PIMMS [175, 176]) resulted in a proof of concept, which was partially adopted at CNAO (first proton patient in 2011) and MedAustron (first proton patient in 2016). The main upgrades for synchrotrons are an increase in the beam speed delivery, control of the extracted beam current, and multiple-energy extraction, which is currently possible at a few accelerator centers, such as HIMAC [11].

Linacs

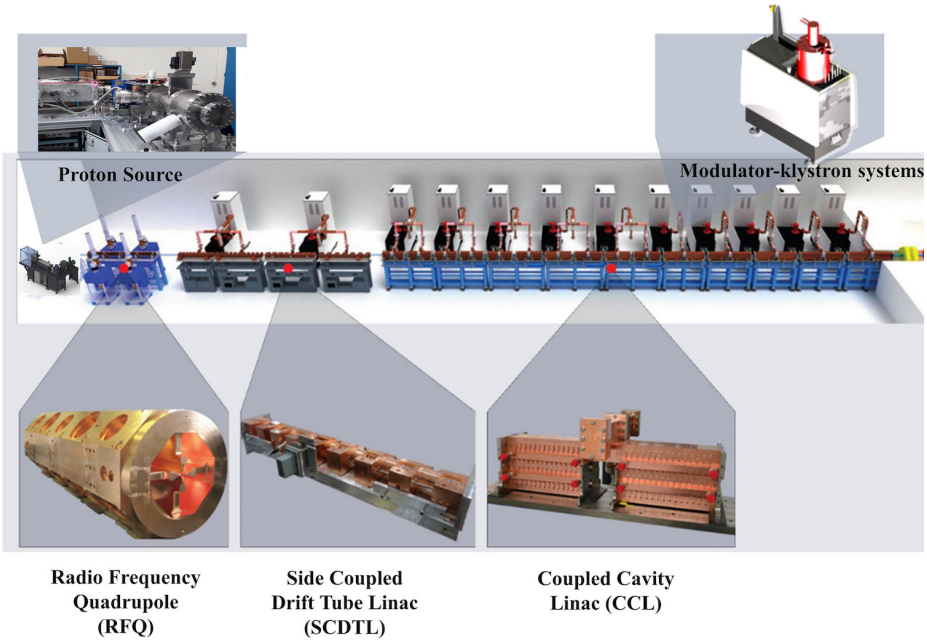

Figure 1.14: LIGHT system and its components under development by ADAM - AVO *Reprinted from [11]*

Linacs are linear accelerators, which are single-pass devices for accelerating charged particles. Particles increase their energy by passing through a series of RF cavities (klystrons) and maintaining their trajectory via magnets, such as quadruples and sextuplets [173].
Proton or ion linacs for clinical particle therapy are currently in the research and production phase. The rationale for linac development for charged particle therapy is their high flux and fast variation of energy from one pulse to another, which can yield a cycle as short as 5 ms [174]. A linac provides an excellent beam quality (small emittance, i.e. a small spot size) with less induced radiation, which reduces the shielding costs [11]. Finally, they are compact and modular, providing the advantages of installation, commissioning, moving location, transportation, maintenance, and dismantling.
The first idea of a clinical hadron linac was conceptually designed by TERA and CERN [177, 178]. This proof of concept was further extended to the concept design of a proton linac with a rotating gantry (TULIP-TUrning Linac for Protontherapy) [179] and carbon linac - CABOTO (CArbon BOoster for Therapy in Oncology) [180, 181]. Currently, CERN's spin-off company Advanced Oncotherapy (AVO-ADAM) is at the final construction stage of the proton LIGHT system-LINAC for Image-Guided Hadron Therapy [11]. The planned total length of the proton linac is estimated to be around 25 m from the source to the exit, and in reality depends on the accelerating potential of the cavities.

1.4.3 Beam delivery systems

Particle therapy aims to cover the target with high accuracy and precision, controlling beam characteristics such as the number of particles and the expected position with a defined spatial distribution. Charged particles leaving the accelerator are bunched in quasi-monoenergetic primary beams; in reality, their transverse profile has a sharp tail. However, after passing through several degraders or a nozzle structure, the beam can be approximated as a Gaussian shape. The obtained beam is too small and narrow compared to the tumor size. However, a set of primary beams must be delivered in a predefined way to cover the 3 dimensional target body with a high dose while tailoring sufficiently with patients' anatomical conditions (avoiding critical structures). The dose delivery system connects the accelerator with the patient and operates charged particles to provide the beam with clinical requirements. Two general dose delivery techniques are in use: passive scattering and active scanning, which are briefly described below.

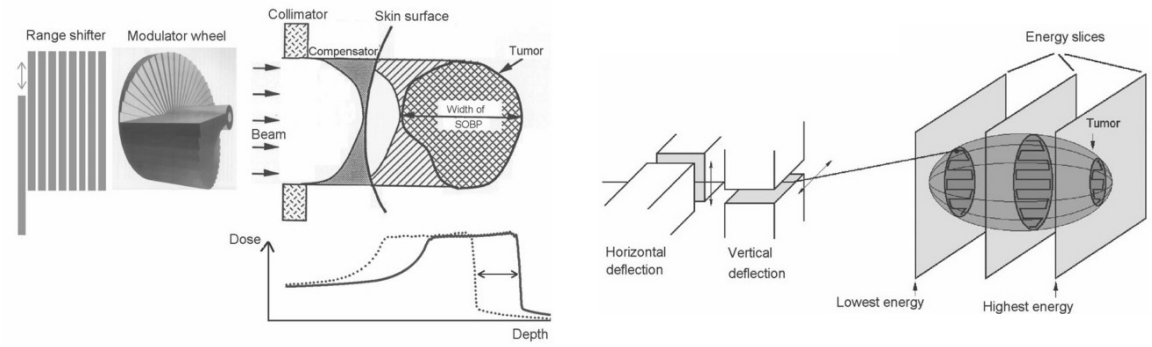

Figure 1.15: The passive scattering technique (left), and the active scanning technique (right). *Reprinted from [12].*

Passive Scattering technique

A passive scattering technique uses passive devices placed along the beam path that provide a degradation in energy and a scattering effect [182] to obtain a beam of a size corresponding to the longitudinal and lateral treatment target size. The narrow beam is broadened laterally with a scattering system that consists of a single, high-Z material layer (lead, tantalum) in the single-scattering technique. A secondary scatterer along the beamline is added to obtain a larger and more uniform dose in the double-scattering technique. Once the lateral spread is acquired, collimators are used to block the beam outside the planned target margins. The longitudinal profile is provided by a set of degraders placed before the scattering set, creating a superposition of pristine Bragg peaks - Spread Out Bragg Peak (SOBP). Degraders can be in the form of fixed wedges, insertable slabs, or fast-rotating range modulator wheels with varying thicknesses.
Overall, the passive scattering system is not optimal owing to a reduced beam intensity and quality and a smaller energy range, as well as an increase in the unintended dose delivered to the patient due to nuclear reactions (especially neutrons), which are responsible for adverse effects (especially for particles heavier than protons). Finally, beam blocking devices and boluses must be adapted for individual patients, which increases workload. In most clinical facilities, passive scattering techniques are replaced with active scanning systems. However, for specific treatments, such as ocular proton therapy, these techniques still provide excellent results and are used in more than 90% of ocular clinics [183, 184].

Active scanning technique

To cover the target volume, the active scanning technique uses a primary beam with actively varying energy and magnetic steering. First, the target is divided into thin range-equivalent layers, and each layer is covered in an arbitrary target shape. The active scanning technique allows the performance of Intensity Modulated Particle Therapy (IMPT), which is a scanning mode wherein the determination of each individual spot intensity can be defined by treatment optimization. Thus, the dose is delivered in a sequence of monoenergetic beamlets, each delivering a predetermined dose according to the planned spot intensity. A very high dose conformity is acquired by continuous irradiation from the most proximal to the distal tumor layer (or *vice versa*) by changing the energy step in a slice-by-slice manner. Transversal beam sweeping is performed by two dipoles, used for horizontal and vertical deflection, located at the end of the extraction line, a few meters upstream of the patient. In general, the tumor is irradiated in a 3D manner by superimposing sequences of spots.
The amount of material along the beam path is minimized, which reduces beam losses and secondary particles production (i.e. neutrons). The active scanning technique does not require a field or patient-specific hardware because the delivered dose can be varied from point to point, allowing conformity of the treatment. Of course, in the case of a shorter particle range (which the accelerator cannot provide), a modifying system (a range shifter) along the path can be added to absorb the particle energy upfront, thus decreasing the particle range; however, this solution results in a decrease in the beam quality. The main disadvantage of the spot-scanning method lies in the speed of the dose delivery, and another problem arises owing to the high conformity - the treatment has to be highly robust.
There are three active spot-painting methods. They determines the method for delivering the dose within one energy layer [173]. The choice between them is specified by the precision, treatment time, and repainting

capabilities (useful for robustness planning) [185]. These methods are:

- Discrete Spot Scanning - circular-shaped pencil beams deliver the dose with Gaussian profiles in discrete steps - spot by spot. After the one-spot dose delivery, the beam intensity is switched off, and the bending magnets fields are modified for the next spot position. The main drawback of this method is the dead time between switching off and switching on while delivering spots. The first spot-scanning system was developed at NIRS [186] for protons. However, the first patient application was installed at PSI [187] (also for protons).
- Raster Scanning - is a type of the spot-scanning method where the beam is not being switched off between delivery of two spots positioned close to each other. Raster scanning requires fast scanning magnets to reduce the dose delivered between spots. It was developed at GSI [188] and was further implemented at HIT [189], CNAO [190], MedAustron [191] and NIRS [192].
- Continuous Line Scanning - the dose is delivered with a steady velocity and a varying dose rate, while following the line segment which connects planned spot together. Constant movement allows re-painting, which was found to be a superior technique for minimizing errors due to organ motions [193]. This type of scanning is installed at PSI Gantry 2.

Wobbling

Wobbling method lays in between active and passive scanning, and the beam is first scattered and then scanned with magnets to a pre-defined spot position, with varying energy but without an intensity change. One successful design is currently used at NIRS for heavy-ion therapy [194].

1.4.4 Beam transport and beam monitoring systems

The treatment plan is typically composed of two or more irradiation fields, and in order to minimize the dose delivered to surrounding organs, the angles of the fields are determined during the treatment plan optimization. In the majority of facilities, the beam is delivered with fixed angle beam ports - horizontal, vertical, or other inclined directions such as - 45^o, in combination with a patient positioning system couch rotations (tilt, pitch, yaw). This solution is limited by the available angles, which can be overcome using the same technology as in standard radiotherapy - rotating gantries.
Gantry is a device used to change the direction of the beam and to deliver the dose to the target from an angle determined during treatment plan optimization, minimizing patient discomfort related to couch rotations. It is a complex, heavy, and costly device consisting of magnets, beam diagnostic monitors, collimators, and other instruments mounted on the frame. The beam transport line from the accelerator ends at the coupling point to the gantry. Downstream, the gantry transport system is mounted, which rotates 360^o or slightly more than 180^o around the patient. The size of the gantry depends on the particle mass and charge, maximum energy of the beam, field strength of the magnets, and the required rotation diameter. The proton gantry has a diameter of 3-5 m, weighs between 90 and 200 tons. The rigidity of carbon ions (of the same range as protons) is almost three times larger, though ion gantries are also larger - 10-11 m and/or use higher magnetic fields [11]. As an example, the HIT gantry for carbon ions weighs 570 tons, and consumes approximately 400 kW at the maximum field. Superconducting magnets installed in Japanese facilities, that

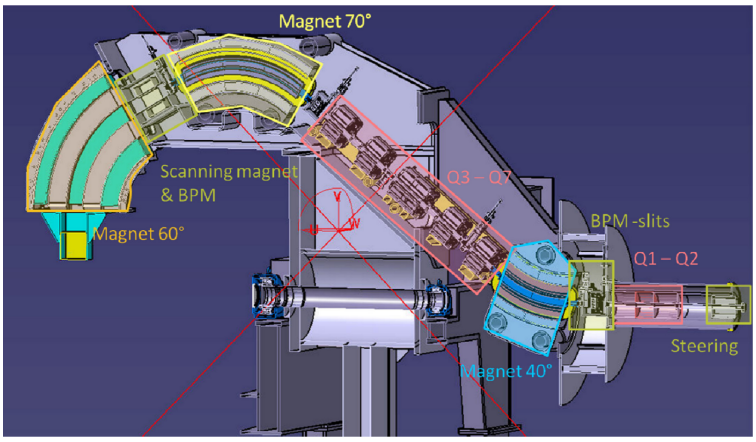

Figure 1.16: IBA Proteus One proton gantry. *Reprinted from [11].*

is, at HIMAC, allow higher magnetic fields and thus lower power and weight (300 tons). In the case of spot scanning, scanning magnets are located either upstream or downstream of the final bending magnet or the gantry, owing to the Source-Axis-Distance (SAD) impacting the skin dose in the case of non-parallel beam trajectories.

The final point of the beam delivery and transport system consists of the monitoring and interlock systems installed at the end of the beamline in the nozzle. The dose monitoring system allows the measurement of beam parameters - a beam flux (maximum 1-2% uncertainty), energy (1-2% uncertainty), shape (1 mm of uncertainty), and position (0.5 mm uncertainty) [173] and interlock systems can further interrupt irradiation when the beam parameters exceed the security limits. The beam position, particularly the beam intensity, is checked in real time owing to a redundant system of monitor chambers. The nozzle contributes significantly to the final beam size at the isocenter, and in the case of ion beam therapy, it can be used to smoothen the shape of the beam. For example, a ripple filter can be mounted on the nozzle to broaden the spot size to approximately 3 mm Full Width at Half Maximum (FWHM), which reduces the number of delivered spots and, thus, the delivery time. Finally, if a shorter particle range is required and the beam accelerator has limitations in terms of the minimum deliverable particle energy, the range shifter can be mounted on the nozzle in the form of PMMA slabs.

1.4.5 Treatment planning

Treatment planning task aims to create a plan that can deliver 100% of the planned dose to the target volume and spare normal tissue from any radiation. However, this balance cannot be achieved. Therefore, compromises must be made to provide a clinically acceptable plan. Because active scanning is becoming the most popular modality for charged particle therapy, a treatment planning procedure for this modality will be described briefly.

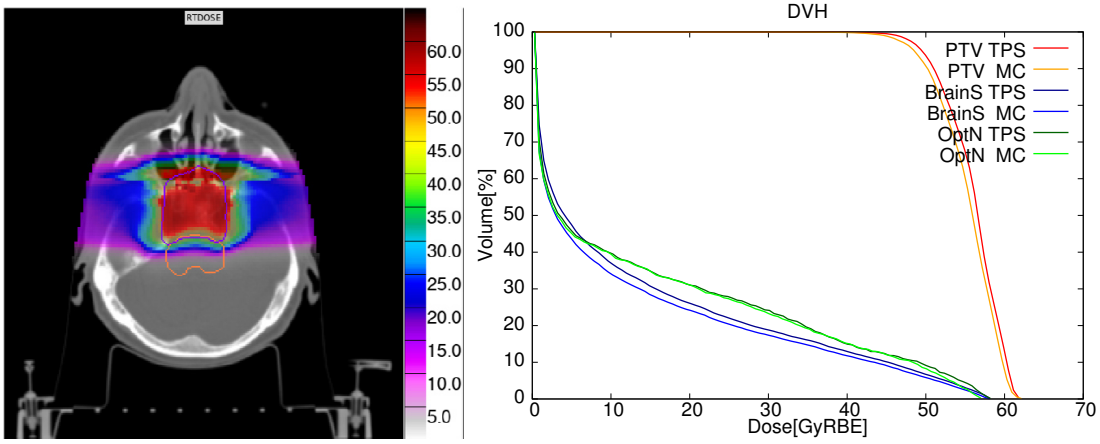

Figure 1.17: Dose deposition in the patient (left) and DVH (right) calculated for the proton treatment in [GyRBE] of the chordoma case from CNAO. Presented ROI on the left figure: PTV (violet), Brainstem (orange). *Published in [13].*

Patient immobilization

The treatment workflow begins with patient fixation and immobilization. The patient needs to be immobilized rigidly with a specified immobilizing device, which prevents changes over a long time scale between fractions (inter-fraction motions) and prevents short time-scale motions of the patient during delivery of a dose fraction (intra-fraction motions). Typical immobilization methods include vacuum cushions, which take the shape of a patient, thermoplastic masks, or bite-block systems [7]. All of these devices are built from thin, low-density materials so that their effect on the particle range and scattering is minimized.

Pre-treatment imaging

Immobilization must be performed before image data acquisition. The 3D or 4D acquisition of the patient anatomy is performed in order to have a reliable representation of the patient position, fixed in the immobilization devices, avoiding systematic errors. In practice, the most common imaging modality used for particle therapy is X-ray CT because HU is related to tissue density, which is a major determinant of the particle stopping power (as mentioned in section 1.3.2). To decrease the possibility of particle range uncertainties, the stopping power could be estimated using a dual-energy CT or measured directly with the support of a proton CT. Dual-energy CT [195], apart from the photon attenuation coefficient, can also determine Z_{eff} of the material, which is further used to calculate the tissue's stopping power. However, proton CT (currently under development, with promising results obtained by Johnson *et al* and Takabe *et al* [196, 197]) directly measures the proton attenuation coefficient, which can be further used in proton therapy planning. The main problems with both modalities are cost, accessibility, and low spatial resolution (proton CT).

Delineation of ROI

Other imaging techniques such as Magnetic Resonance Imaging (MRI), Single Photon Emission Computed Tomography (SPECT) and Positron Emission Tomography (PET) are supporting the delineation process. These images are further fused with the CT images to correctly define the target volume and to determine the soft tissue anatomy (relevant for MRI). Volumes of Regions of Interests (ROI) are delineated and defined as recommended by ICRU[125]: the Gross Tumor Volume (GTV), which is a tumor volume visible on the image, the Clinical Target Volume (CTV), a larger volume that includes expected regions of microscopic tumor spread, the Planning Target Volume (PTV), expansion of the CTV including a variability of the target position during the treatment, and possible uncertainties (for protons, 3% of the range + 1 mm,as recommended by Paganetti *et al* [198] and for carbon ions 2-3 mm, as mentioned by Vogin *et al* [199] however, the margin highly depends on the tumor type, moving organs, and patient itself). Critical structures - Organs at Risks (OARs) are delineated according to the individual clinics' procedures. Other structures on which the subsequent treatment volume will be based, such as couches and metal implants, are defined as Technical Volumes. It is important to reconsider biological volumes, that is, areas with poor blood perfusion or hypoxia, where boost treatments and high-LET radiation might overcome enhanced tissue OER.

Field selection

After contouring, the 3D patient geometry is constructed. Based on this model, a medical physicist defines the beam entrance fields to avoid the beam traversing through critical structures and to focus the beam on the target volume. Several principles must be followed. First, the dose should be delivered homogeneously, which could be in a single field direction. However, a multiple-field approach is recommended to expand the effects of uncertainties and low-dose regions. Second, it is crucial to spare normal tissues from the proximity of a steep dose fall-off to avoid the impact of range uncertainty. It is also recommended to take the shortest path to the target to reduce the integral dose to all normal tissues.
Medical physicists need to review the disadvantages of highly conformal beams as well as the effect of tissues with high heterogeneous density. The beam passing through areas of complex heterogeneity must be avoided in order to limit the distortion of the Bragg peak, in particularly high-gradient heterogeneities perpendicular to the beam direction. Other patient-related factors affecting the particle range have to be considered, such as positioning changes, patient weight loss [200] or changes in the internal anatomy (tumor shrinkage) [7].

Dose calculation and optimization

Subsequently, dose calculation and optimization is performed, following the conditions for sterilizing a malignant lesion and preserving normal tissues. A treatment planning system assigns energy, number of particles, and transverse position to every beamlet[6] to deliver the optimum dose distribution to the patient. Optimization is performed such that each field contributes to a uniform dose to the target (Single Field Uniform Dose (SFUD) or single-field-optimization), or that individual fields are inhomogeneous in order to spare organs at risk, while the combined plan delivers a homogeneous dose to the target (IMPT - intensity modulated particle therapy or multiple-field optimization) [201]. For scanned particle therapy, the most common approach is IMPT, in which the workflow leading to achieving an optimal dose is inversed.

[6]single monoenergetic proton or ion beam

The governing principles of the treatment planning in the IMPT are as follows: first, the desired dose distribution within ROIs is established by the medical treatment planner in the TPS; then, the objectives and constraints for the optimization must be created, which includes the specification of a weighting function for the desired target volume dose and the specification of weighting functions for the maximum allowed dose delivered to OARs; afterwards, the TPS determines cost functions, which quantify the dose distribution goals; further, the optimization algorithm is applied to all beamlets from all selected fields simultaneously, which iteratively determines the best field shapes, fluence profiles, and beamlet weights, while minimizing cost functions. The optimization process has many degrees of freedom, with the possibility of controlling the position, energy, and intensity of every beamlet. Each TPS software has a different method of pre-weighting and positioning beam spots before the minimization step, as well as a routine to minimize cost functions, which is why different TPSs may produce different treatment plans. Algorithms for calculating dose distributions are presented in more detail in Section 1.4.6.

Evaluation and robust planning

After optimization, dose distributions in ROIs were evaluated quantitatively based on dose volume histograms (DVH) for the target and organs at risk. The DVH represents the previously defined target and critical structure volumes receiving a certain dose. The aim is to obtain a specified DVH curve shape, evaluating points on the curve, that is, quantifying a certain percentage of the organ volume receiving a certain dose. While the tumor shall receive the planned dose to the entire volume uniformly, OARs have their limits in terms of the medium and maximum doses to be received, minimizing NTCP.
A high conformity of the treatment requires robust planning to estimate if the delivered dose distribution can differ from the planned one, owing to uncertainties in the particle characteristic. The most common sources of these uncertainties are setup errors, changes in the patient geometry, inter-fraction motions (between treatment fractionation, i.e., prostate), intra-fraction motions (during the treatment, i.e., lungs), and uncertainties in the dose calculations owing to the limitation in the dose calculation algorithms. In robust planning, different treatment scenarios are evaluated, considering a number of different error conditions from the nominal dose distribution. These calculations provided a spectrum of dose values [202] per voxel and a set of DVHs. Another step is to re-optimize the plan to obtain the most robust plan, which typically deteriorates the plan quality, but at the same time provides safer measures for the patient.

1.4.6 Dose calculation algorithms

Dose calculation is the primary task of a TPS. It is important to predict the 3D dose deposition in a patient with millimeter resolution and an absolute accuracy of a few percentages [7]. Depending on the physics models used and mathematical modelling, dose calculation algorithms can be divided into two main categories: analytical/semi-analytical dose calculation methods (Ray-Casting algorithm and Pencil beam algorithm) and Monte Carlo techniques. The most common TPSs currently used in clinical operation are RayStation from RaySearch [203], Eclipse from Varian Medical System [204], Pinnacle from Philips [205], and Monaco from Elekta [205].

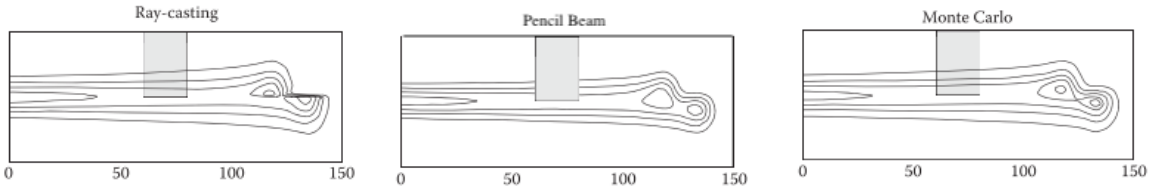

Figure 1.18: Ray-casting, Pencil beam and Monte Carlo dose calculation of a single proton pencil beam. The central axis passes through the area of high-gradient heterogeneity (water-to-bone). *Reprinted from [7].*

Ray-casting algorithm

The concept of the Ray-casting algorithm was introduced by Scheib *et al* [206]. It is based on the description of the depth-dose curve (integrated depth-dose curve (IDD)) for a single quasi-monoenergetic beam (or SOBPs) and the description of its lateral spread (as a function of the distance from the central axis). The IDDs for each energy can be derived from measurements (which is typical for SOBPs) or calculated analytically (i.e., using the Bethe-Bloch formula) and then validated with measurements. Lateral profiles, in the case of proton beams, are modelled using MCS theory, which results in a Gaussian beam profile with σ increasing as a function of depth. Each voxel has a defined water equivalent depth (WED) in the tissue material, as well as its lateral position relative to the central axis. Based on this, the dose deposition in each voxel is derived. The total dose is determined by adding the contributions from all individual spots.
In a homogeneous medium, the Ray-casting algorithm is sufficiently accurate. However, in the case of a heterogeneous medium, such as a patient, the algorithm may underperform. A high density at the entrance leads to the same change in the dose deposition at the Bragg peak, as the heterogeneity located just before the Bragg peak, which is nonphysical. This is because the heterogeneities of the tissue densities are corrected by scaling the depth of the dose calculation point into the WED, considering the integral of all relative stopping power values (coming from a CT scan) along the beam path (from the nozzle up to the calculation point). The nearer to the Bragg peak the heterogeneity is, the better is the Ray-casting algorithm. However, when heterogeneity is closer to the entrance, this solution tends to overestimate the sharp dose gradient effect of heterogeneity, which in reality will be smoothed out by particle scattering behind the heterogeneity and out-scattering from a high-density material [7]. See Figure 1.18.

Pencil beam algorithm

The most popular analytical algorithm is a Pencil beam algorithm [207]. Different variations of its implementation are in use, but they are generally based on the same physics principles as the Ray-casting algorithm. The input data for the beam modelling uses IDD profiles, and profiles of the lateral spread, both can be either measured and implemented using LUT [207], modelled analytically [86] or being based on the MC model [208]. Each physical pencil beam is decomposed into a set of elemental narrow pencil beams (beamlets), which are then transported into the patient's tissue along their central axis and react individually to materials encountered on its path. The dose calculation is then identical to that of the Ray-casting algorithm, except that dense heterogeneities are scaled only by the central axis of each beamlet. In contrast,

in the Ray-casting algorithm, the dose deposited by each spot is calculated at each grid point by adjusting the WED of that point. Specifically, the Pencil beam algorithm calculates the range of a beamlet based only on the target materials along the central axis. This means that the Pencil beam algorithm in the presence of complex geometries and a heterogeneous environment is not sensitive enough to lateral inhomogeneities and yields an inaccurate dose distribution. Moreover, while the Ray-casting algorithm performs better when heterogeneities are located near the end of the particle range, the Pencil beam algorithm performs better when the heterogeneity is closer to the surface [7]. Subsequently, doses from every beamlet are superimposed within the scoring grid, resulting in the final dose distribution.

Another shortcoming of the Pencil beam and Ray-casting algorithms is their inability to account for the production of secondary particles. Secondaries can have energies almost up to the energies of the initial primary particles, but with a much larger angular spread than the primary beam, leading to a low but significant halo of secondary particles (as mentioned in Section 1.2.3). Therefore, it can have a significant impact in small fields [187] and can sometimes lead to an additional accumulation of the dose in narrow dose fields. The halo shall be accounted for, and it is usually modelled as a second Gaussian distribution in a lateral profile that can be interfered with by experiments or MC [209]. The halo is mostly visible for beams passing through a range shifter and when treatment is performed with a large air gap between the beamline and the patient.

The final challenges for analytical/semi-analytical algorithms are the accurate description of nuclear interactions, fragmentation (for ion treatment), and biological planning. For this, the spectra of nuclear fragmentation must be pre-calculated, and the RBE must be modelled according to specific particle characteristics in an arbitrary place within the mixed radiation field.

MC TPS

Monte Carlo codes are the most accurate methods used to compute a dose for the radiation therapy, and they are considered to be the gold standard [13]. Monte Carlo simulations track the particle path and interaction from the source exit through the nozzle and any patient-specific beam modifier (aperture, compensator, range shifter), air gap, and finally, through the heterogeneous patient model. Particles are selected by random picking primary protons or ions according to the weighting of the spot in the treatment plan, and the parameters being based on the applied beam model. The beam model in MC differs from the analytical dose calculation algorithms because the particle transport and interactions along the particle track are entirely simulated, based on cross-section models in the target medium, either in the patient geometry (with real tissue material properties) or beam-modifying devices.

When comparing analytical algorithms with Monte Carlo codes, it can be observed that carefully commissioned Monte Carlo algorithms improve the handling of complex and lateral heterogeneities, and they are more accurate in predicting the particle range in this case. Multiple benchmarking studies have been performed to compare MC with an analytical algorithm, mentioning only a few of them [210, 211, 212, 213, 214]. However, analytical algorithms are considerably faster than MC and more practical for clinical use.

MC TPS calculations, until a few years ago, were using one of the research-based MC codes, which for a daily clinical routine is too slow. However, recent years have brought commercial solutions to the Monte Carlo dose calculation engines. The main challenge is to limit the computational time while simultaneously preserving

the reliability of the MC codes and providing usability for customers. Currently, RaySearch Laboratories AB (Stockholm, Sweden) and Varian Medical Systems (Palo Alto, CA, USA) offer commercial MC TPSs for proton spot scanning. The calculated speed incurs a high cost in terms of precision and accuracy. It is obtained by means of particle transport, which is evaluated based on a rectangular voxel grid. Therefore, tracking is more time-efficient, nuclear interaction modelling uses pre-computed cross-section libraries, and the transport and interactions are detached from the material and scoring grids, saving a significant amount of time, that is, MCS and range straggling calculations. Finally, the production of secondary particles is limited to a minimum. For example, the RaySearch MC algorithm does not track $\delta - rays$ nor does it track nonelastic nuclear reactions. Only the production of protons, deuterons, and alpha particles is considered, whereas all the other ions deposit energy locally. Neutrons and gamma do not deposit any energy and leak out, which is reviewed and corrected accordingly in the final energy balance [215].
Owing to the increased accuracy of analytical algorithms, MC dose calculation engines may become a new standard for proton or ion treatment planning. Another advantage is that MC codes can also be used for the validation or commissioning of the beam delivery system, for the quality assurance of the clinical beam, for the simulation of the beamline components, and to extract the phase space parameters for complex beam delivery systems. Sometimes pre-calculated Monte Carlo-based simulation outputs are used to commission an analytical TPS because MC code is capable of predicting the beam characteristic (based on the beamline geometry [216]) and the nuclear halo from beam scanning [217]. MC codes can also support the design of analytical algorithms, for instance, to model nuclear interactions [208], which are particularly important for ion therapy [15, 73]. The dose calculation in heavy ion therapy is, in general, more complex because of the need to incorporate biophysical models [73, 218].

1.4.7 Treatment plan verification

Sharp dose gradients, delivered spot by spot, render particle therapy very sensitive to planning and delivery uncertainties. Therefore, treatment plan verification is highly recommended to ensure that the dose delivered to the patient is consistent with the dose prescribed by the physician at every step of the treatment.

Patient Specific Quality Assurance

After approval of the treatment plan, patient-specific quality assurance (PSQA) is performed. Pre-treatment plan verification is required to confirm that the dose delivered to the patient is consistent with the dose calculated by the TPS. PSQA verifies several steps: correct modelling of the beam fluence (produced by the beam delivery system) by TPS, the performance of the beam delivery system (if it is within the acceptable limits), accuracy of the TPS calculation for a planned dose delivered to the patient, and correct transfer of the plan data between TPS and the beam delivery system [219].
PSQA is typically a dosimetric procedure that involves measuring the dose distribution independently for each treatment field and at selected depths with multidimensional (2D or 3D) detector arrays (i.e., ionization chambers) embedded in homogeneous phantoms [220, 221, 222]. Performed measurements are then evaluated against doses computed in a water phantom by the TPS using (typically) gamma analysis pass rate levels [223]. Verification of the beam fluence in a homogeneous environment (such as water or water-equivalent plastic phantoms) requires a significant time of working hours and beam time; however, it provides a reliable

check of the dose delivery system.
A challenge arises during the verification of the dose distribution in a patient model. Analytical algorithms perform acceptably well in many scenarios, although in the presence of heterogeneities (as mentioned in Section 1.4.6), a second check is necessary for patient-specific quality assurance (PSQA) [219]. Software, which performs dose and monitor unit (fluence) calculations independently, provides a second check without requiring any additional beam time. A few studies [219, 224] have proposed a solution in which the plan is exported from the TPS (in a DICOM format) and sent to an independent MC-based system for immediate dose re-calculation. Subsequently, the dose deposition calculated by MC is compared to the dose computed originally in TPS, and similarly, a gamma analysis pass rate estimates the level of agreement between doses [223]. MC codes, must first be validated [225, 226] and thoroughly benchmarked.
Last but not least solution used during PSQA is the use of the log-file analyzer [227]. While delivering the beam to the phantom or the patient, the beam delivery system creates log files that describe the spot parameters (i.e., position and fluence). Collected log-files are later transferred to the PSQA software to validate the delivered dose [224, 228]. Thus, either TPS is used to recalculate the dose from the sets of delivered spots or, again, an MC tool. Subsequently, as in the aforementioned cases, the gamma analysis pass rates [223] are used to determine the quality of the delivered treatment plan.
The three methods mentioned above for PSQA are complementary. While dosimetric measurements can verify the beam delivery performance, MC tools can validate the TPS calculation, and the use of log files can determine the dose actually delivered to the patient. The PSQA method depends on clinical regulations; thus, some vendors offer software that can combine all three methods and can choose freely depending on the needs of the clinic (i.e., MyQA Ion (IBA, Belgium)).

Online treatment monitoring

Another part of the verification process for treatment planning may include particle range verification. A technical complication arises due to the fact, that the beam is stopped within the patient. Therefore, only secondary particles can be used to acquire information regarding particle range. This technique requires dose calculations and MC to describe dose delivery and nuclear fragmentation. The two most promising methods for online treatment monitoring currently use β^+ emitters and prompt-γ emitters [14].
The measurements of β^+ emitters are based on PET scanners. While radioactive - β^+ emitting fragments are created (such as carbon-11, nitrogen-13, and oxygen-15), they annihilate with the material's electrons, a few millimeters after the incident point and not far from the Bragg peak, producing two 511 keV photons. These photons can be monitored using PET [229] for in vivo beam range verification in proton therapy [230, 231] and ion beam therapy [232, 233]. For carbon therapy, it is possible to use radioactive ion beams such as carbon-11 or oxygen-15 [234]. The results of PET imaging techniques are promising but are hampered by several issues. Mentioning only the limited correlation of the dose distribution and the β^+ emitter map, owing to the low activity of β^+ and a small signal-to-noise ratio (SNR), low efficiency of PET detectors, and limited spatial and time resolution. Finally, a biological washout further decreases the resolution because the activity of β^+ emitters in tissues changes over time due to perfusion. Therefore, PET measurements should be verified using MC simulations for a positron emitter distribution [230, 231] and corrected afterwards accordingly.

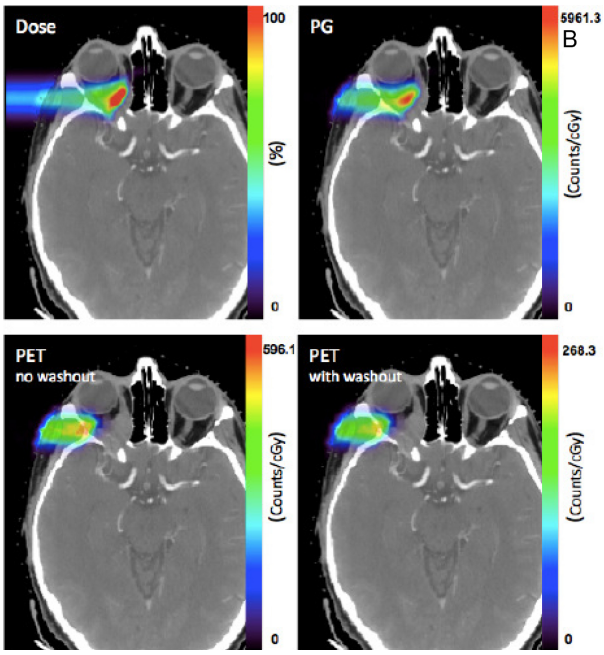

Figure 1.19: Dose verification on the CT image of a proton head-and-neck treatment. Top left, dose distribution; top right, prompt-γ counts; bottom left, PET counts without washout; bottom right, PET counts with washout. *Reprinted from [14].*

To overcome the low resolution of PET imaging, prompt-γ monitoring was introduced. Measurements of the prompt-γ are based on the instantaneous (few nanoseconds) de-excitations of the target nuclei along the particle path after nuclear reaction in a patient, which results in yielding 1-10 MeV γ photons, with no biological washout. Similar to PET, prompt-γ spectroscopy can be used for proton [235, 236] and carbon ion beams [237, 238]. The emitted energy is characteristic of the tissue, and the main peaks of prompt-γ can be distinguished for the oxygen and carbon reaction channels [96]. Moreover, the prompt-γ emitter results in a larger SNR. The main disadvantages are the lack of a two-photon coincidence signal for 3D reconstruction and the lack of an appropriate detector system to detect gammas with high efficiency and spatial resolution in a clinical setting. Similar to PET, prompt-γ range verification requires a comparison of the measured signal with an expected value, which can be obtained using MC simulations.

1.5 Thesis outline

This thesis investigates the application of Monte Carlo codes for proton and ion beam therapies, in order to bridge the gaps between research technologies and clinical needs. Charged particles provide an excellent treatment conformity in comparison to photon techniques. However, this advantage comes with its drawback. An accurate and precise modelling and validation of particle transport and interactions in the patient model, as well as along the beamline, is a prerequisite. The possibility of in vitro validations of performed treatments are restricted, the detailed treatment plan optimization is limited to the applied and known physics models, as well as measurements of the biological tissue response. Though, considering the limited research time in ion beam facilities, the application of MC simulations tools, which are claimed to be a gold standard in dosimetry, can successfully support these advancements.

In brief, this thesis is focused on the evaluation, development and application of MC techniques for charged particle therapy. Research is based on the general purpose FLUKA MC code. The first aim of the thesis was to develop and evaluate model and interface which enabled implementation of the FLUKA Particle Therapy Tool (FPTT) for clinical research purposes. The tool was then thoroughly validated using clinical beamline model and patient treatment data. Further focus was put on benchmarking of the new radiobiological research model BIANCA and its integration with the FLUKA MC code. This was finalized by application of the BIANCA model in the clinical treatment planning scenario and comparison against the clinically used radiobiological model. The thesis is organized as follows:

Chapter 1 provides a short overview of the history of particle therapy, physics and biological phenomena and currently used therapy concepts. The first section presents the main ideas of the MC simulations and its applications in particle therapy. The second and third sections gives an overview of the particle transport and interactions models and its physical and biological properties. The last section gives a short introduction of a current state in particle therapy, discussing rationales for hadrontherapy, providing a description of treatment planning procedures, currently used techniques and giving an overlook to future needs.

An application of the MC codes in particle therapy presented in this thesis is based on the FLUKA MC code. In Chapter 2, recent developments of the FLUKA MC code for particle therapy are shown. It starts from a presentation of recent advancements in physics models, applications and interface implementation for clinical usage. Special focus was put on the further development of the Flair Graphical User Interface for supporting needs in the proton or ion beam therapy. Based on that, the further development was supported and the rest of the presented research was pursued.

In the Chapter 3 a validation of the new FLUKA Particle Therapy Tool for MC based Quality Assurance procedure is presented. The tool was used to first commission two particle therapy facilities (Trento Proton Facility and CNAO), and afterwards to simulate realistic treatment planning scenarios. Thanks to the implemented framework, real proton, and carbon ion treatment planning scenarios were imported, calculated, and then dose distributions were compared with the results from commercial Treatment Planning Systems commissioned and used at these facilities, as well as with patient specific QA measurements. Good agreement was obtained between semi-analytical TPS and MC tool, for homogeneous cases. However, as expected, in heterogeneous cases, a significant disagreement was visible, as well as, some discrepancies were shown for the carbon ion treatment patient. An application of the biological models, and quantification of the dose-averaged LET in the carbon patient cases, were also simulated. The aim of this work was to thoroughly

validate and evaluate the FPTT for further application in particle therapy.
The Chapter 4 concentrates on recent developments in a new research radiobiological model for ion beam therapy - BIANCA. The BIANCA model, implemented in a form of MC code, supports an estimation of the RBE for proton and carbon ion beam therapies, as well as an evaluation of chromosomal aberrations. In this Chapter, recent developments and extensions of the BIANCA model are presented. A demonstrated integration with the FLUKA MC code, allowed to perform benchmarking studies against radiobiological data, previously used for evaluating the clinical model - LEM I. An initial study focused on predicting V79 cell survival, following two-field irradiation scenario using proton and carbon ion beams, imitating a clinical treatment scenario. The second benchmarking study used in vivo experimental data, from a proton and carbon ion beam irradiation of the rat spinal cord. These data has been historically applied to evaluate biological end-points for head-and-neck tumours treated with proton or carbon ions irradiation. The obtained results allowed to prepare the clinically relevant BIANCA database.
The Chapter 5 presents the first application of the upgraded BIANCA radiobiological model in a clinical scenario. The BIANCA model, was applied in realistic treatment planning scenarios for three carbon ion patient cases, and compared with the clinically applied model i.e. LEM I. The BIANCA database for the chordoma cell survival, as well as, database based on dicentric aberrations in peripheral blood lymphocytes, were used to calculate RBE of carbon ion treatment plans. Results, showed that, if RBE predictions, provided by BIANCA cell survival database is used for evaluation of the beam effectiveness at killing tumour cells, and database based on dicentric aberrations in peripheral blood lymphocytes is used to estimate (late) normal tissue damage, the BIANCA model provides lower RBE-weighted doses with respect to LEM I, in the PTV and in the entrance channel; whereas in the OARs, BIANCA and LEM I provide very similar values. Results were then discussed and placed in the context of clinical relevance. The work presented in this Chapter aimed to enhance the availability of different radiobiological models, taking into account the idea that none of the models was proved to estimate the tissue response to full extend. The robustness provided by the application of different models might support a better biological optimization of treatment plans for various ions.
The final Chapter 6 presents additional applications, limitations, and future work resulting from this thesis (i.e. virtual commissioning of the linear accelerator), as well as conclusions and an outlook on subsequent steps to fully exploit the potential of MC techniques in hadrontherapy.

Chapter 2

Development of the FLUKA Monte Carlo code for particle therapy

This Chapter presents a general overview of the application of FLUKA Monte Carlo code in particle therapy. It is based on the article *The FLUKA code: An accurate simulation tool for particle therapy*, published in *Frontiers in Oncology* 6; 2016, by the following authors (in alphabetical order, as commonly practiced for CERN publications):

Giuseppe Battistoni[1], Julia Bauer [2], Till Böhlen [3], Francesco Cerutti [4], Mary P.W. Chin [4], Ricardo Dos Santos Augusto [4,6], Alfredo Ferrari[4], Pablo Garcia Ortega [4], **Wioletta Kozłowska [4,7],** Giuseppe Magro [5], Andrea Mairani [5,8], Katia Parodi [6,8], Paola R. Sala [1,4], Philippe Schoofs [4], Thomas Tessonnier [2], Vasilis Vlachoudis [4]

[1] INFN Sezione di Milano, Italy; [2] Uniklinikum Heidelberg, Genrmany; [3] EBG MedAustron GmbH, Austria; [4] CERN – European Organization for Nuclear Research, Switzerland; [5] CNAO, Italy; [6] Ludwig-Maximilians-Universität München, Germany; [7] Medizinische Universität Wien, Austria; [8] HIT Heidelberg Ion-Beam Therapy Center, Germany

Wioletta Kozłowska Contribution: Development of the Flair interface for medical applications, with the possibility of importing, displaying and processing of radiotherapy DICOM files. Validation of the higher-level interface, simulation of treatment plans for clinical scenarios, and optimization of treatment plans for validation of the FLUKA PET Tools. Production of text and figures for Section 2.4 - *Flair and its applications to radiation therapy* .

2.1 Introduction

FLUKA [61, 62] is a general purpose Monte Carlo code capable of describing the particle transport and interaction with matter of approximately 60 different particle species and heavy ions, with an energy range from 1 keV to 20 PeV. All particles are tracked with high accuracy within the complex geometries created by the combinatorial geometry package. The history of the FLUKA code starts between 1962-1967 with the work of Johannes Ranft for calculations of the hadron cascades in shielding materials at CERN [239], with the original name, derived from FLUktuierende KAskade. The FLUKA code gained importance at CERN during the next decades and underwent general refactoring and development in terms of architecture and physical models, leading to the current generation design written in FORTRAN.
FLUKA supports a variety of applications, including shielding to target design in accelerators, calorimetry, activation and dosimetry studies, detector design, space application, neutrino physics, and radiotherapy. It supports the simulation with magnetic fields, low-energy neutron interactions, high-energy effects, and incorporating specialised routines that provide flexibility to users. FLUKA is a fully integrated code with a built-in superior quality physical models that track down particle interactions to the single event level, with no tuning on integral data. In recent years, FLUKA development and validation have focused on the medical application area, enhancing the description of ion fragmentation for ion beam treatments, secondary particle emission for QA imaging, and incorporation of biological models and voxel-based geometries. The work presented below shows enhanced models describing ionizing energy losses, particle scattering, and mixed radiation fields found in the therapeutic energy range. The benchmarking studies presented in the latter part of this chapter resulted in an outstanding agreement between the calculated depth-dose and lateral profiles for both proton and ion beams against measurements performed in particle therapy centers.
The FLUKA code benefits from a graphical user interface called Flair [240, 241]. It is an integrated development environment (IDE), that enables the creation, editing, and online debugging of FLUKA input files. In addition, Flair supports the creation and compilation of user routines, launching simulations, post-processing of data, editing geometry with a user-friendly tool, and plot generation. Recently Flair was enhanced with a new DICOM module, which can handle medical data in a well-organized way. As such, it is possible to export CT DICOM images into voxel-based geometry that is compatible with the FLUKA combinatorial geometry package. The user can also import DICOM RT data, which introduces higher-level usability to the treatment plan simulation process. Therefore, apart from patient voxel generation and material assignment for different ROIs, a treatment plan can be translated to FLUKA proprietary functions using a simple Graphical User Interface (GUI). In addition, Flair supports the semi-automated creation of PET scanner geometry and counting of coincidence events.

2.2 Dose and Biological Dose

The interaction of charged particles with matter, as described in more detail in Section 1.2.1, is dominated by Coulomb scattering with atomic electrons and nuclei. In the therapeutic energy range, protons and ions lose their energy mainly by inelastic collisions with atomic electrons (S_{el} - electronic stopping power), whereas the contribution of elastic collisions with atomic nuclei to energy losses is negligible (S_{nucl} - nuclear stopping power). As a result, particles continuously slowing down deposit energy and create a specific dose-depth

shape called the Bragg peak. The particle is also scattered, deflecting from the original trajectory; if due to inelastic collisions with atomic electrons, their angular deflection is proportional to the atomic number Z; if due to elastic interactions with nuclei, it is proportional to Z^2.
The following paragraphs present a summary of the physics models implemented in FLUKA for charged particles in the therapeutic energy range, describing energy losses, energy loss straggling, $\delta-ray$ production, Multiple Coulomb Scattering (MCS), and nuclear reactions. A more detailed description can be found in the original version of this article [16].

2.2.1 Electronic stopping power

In FLUKA, the average energy loss of charged particles, which are heavier than electrons, is represented by Equation 1.6 (relevant for spin 0 and spin 1/2 particles). The formalism of Bethe-Bloch [242, 243, 244] was implemented to account for all higher-order corrections mentioned in Section 1.2.1. Several improvements have been made to obtain high precision for particles in the therapeutic energy range, following (with modifications and revisions) the formulas presented in ICRU Report [76] and refined by Ziegler *et al* [245, 246, 247] for lower energies.
For the ionization potential value I, FLUKA uses the data from ICRU Report [76], which uses the value $I_{water} = 75$ eV, which (if needed) can be easily overwritten by the user. δ correction (density correction) is computed as in Sternheimer *et al* [248], C shell corrections, which are important at low energies, are extracted from proton stopping power values as presented in ICRU and NIST [76, 77]. The Barkas and Bloch corrections are taken into consideration according to ICRU [76] and Ashley *et al* [249, 250]. The Mott correction factor, which is rarely considered in stopping power calculations, although important for medium-heavy projectiles, is defined in FLUKA as a parameterized factor because of the high computational cost of on-the-fly calculations for Mott cross sections, following the work of Lijian *et al* and Jun *et al* [251, 252]. As mentioned in Equation 1.10 the projectile effective charge $z_{eff} = z$ is used for very light ions (such as protons and alpha particles) or particles with larger velocities; otherwise, z_{eff} is calculated in FLUKA, as proposed in Hubert *et al* [253], although with different parameters, to detach the impact from higher correction factors, not considered by Hubert *et al*.

2.2.2 Secondary electrons and energy loss fluctuations

The energy straggling fluctuations mentioned in Section 1.2.2 define the shape and position of the Bragg peak. The standard approach, which considers the Landau-Vavilov distribution, is difficult to implement in MC code. Instead, FLUKA uses an alternative implementation [254] that determines the statistical properties of the cumulants of distributions [255]. This approach considers the threshold for secondary electron production (δ -rays) with defined interaction step lengths to account for fluctuations in energy loss due to distant collisions [254]. The influence of Mott corrections is also included in this model. The production and transport of secondary electrons in FLUKA can be described by down to 1 keV threshold.

2.2.3 Multiple Coulomb Scattering

Concerning the MCS formalism presented in Section 1.2.3, in the FLUKA MC code, a dedicated implementation of MCS was developed [256, 257]. In this implementation, the user can apply very small as well as very large steps without compromising the resulting angular distribution. As an option, the Single Scattering mode can also be turned on; however, this is computationally expensive. Examples of benchmarking can be found in Parodi *et al* [209].

2.2.4 Nuclear interaction models

Section 1.2.4 points out that nuclear reactions degrade the hadron beam quality and conformity in both the longitudinal and lateral directions. The primary ion beam intensity is reduced along its path, meaning that the dose deposited by the primaries decreases with depth (see Equation 1.19). At the same time, the projectile fragments are lighter, but with the same energy as the primary beam, travel further, and deposit a dose beyond the Bragg peak. The lateral spread, particularly visible at the distal part of the Bragg peak, is affected mainly by secondary nucleons, particles, and fragments produced in nuclear reactions; therefore, the spatial distribution of the dose is also affected.
In the FLUKA MC code, nuclear interactions for the therapeutic energy range, are treated with several different models. A short overview is provided below, with a more detailed description, to be found in the full version of the article [16].
The nuclear reaction models considered in FLUKA account for the following:

- hadron-nucleus interactions, which are treated by the PEANUT model [258, 259, 260, 261]. This model handles collisions along the steps of the Generalized IntraNuclear Cascade (GINC). This is followed by a subsequent pre-equilibrium emission state models, in which the excited nucleus emits secondary particles and light fragments until an equilibrium state is achieved. The nuclei created from this interaction establish a thermally equilibrated system with a determined excitation energy and residual excitation that can undergo further de-excitation processes.
- nucleus-nucleus interactions, which are treated by the following models:
  - RQMD-2.4 - if a projectile has an energy in range of few [GeV/n] down to $\sim$ 100 [MeV/n]. This model is based on a modified version of the Relativistic Quantum Molecular Dynamics Model (RQMD) [262]. RQMD covers only the fast abrasion stage of the nuclear reaction; excited fragments are processed in the next step using the PEANUT model.
  - BME - if the projectile has an energy below 150 [MeV/n]. This model is based on the Boltzmann Master Equation (BME) [263], which describes thermalization processes originating from the complete or incomplete fusion of two ions. For a more peripheral collision, as described in Section 1.2.4, the same three body reaction model is implemented. The PEANUT model is used for the pre-equilibrium state and for the de-excitation phase. In the boundary energy range, FLUKA continuously switches from RQMD to BME.

The final step in the PEANUT model involves de-excitation after a precedent collision and pre-equilibration emission. Depending on the residual nuclei, they can undergo either:

- evaporation (for nuclei with $A \geq 17$), which means the emission of nucleons and light fragments (deuterons, tritons, and alpha particles) with a low kinetic energy. It is handled by a modified Weisskopf-Ewing formalism [258, 264].
- fission (for nuclei with $A \geq 17$), when the energy is higher than fission barrier and it can cause a significant deformation of the nuclei. However, it has a low probability of occurrence in particle therapy. The fission in FLUKA is also based on a statistical approach [258, 264].
- fragmentation (for nuclei with $A \leq 16$), when the energy is higher than the total binding energy. For this purpose, a statistical Fermi Break-up model is implemented in FLUKA [62, 265, 266].
- γ de-excitation, which occurs as the ultimate stage of the de-excitation. The emission of $\gamma - rays$ cascades is produced with the remaining excitation energy below the particle emission threshold. Their energies and ratios are sampled in FLUKA from the RIPL database [267].

2.2.5 FLUKA benchmarking against depth-dose curves and lateral-dose profiles

The FLUKA MC code has been thoroughly benchmarked against experimental data for particle therapy in various proton and ion therapy facilities. The beam characteristics of various accelerators were measured and benchmarked against FLUKA MC code simulations. These measurements include depth-dose data measurements performed with parallel-plate ionization chambers placed in water targets [15, 75, 268] and lateral-dose profile measurements performed using small ionization chambers placed also in a water targets [268, 269]. Currently, a few particle therapy centers use the FLUKA MC code for independent dose calculations in phantoms and patient geometries. Some clinical TPSs use FLUKA to produce cross-section databases for transport and interaction models [188]. This procedure includes incorporating an MC-calculated IDD profiles, lateral depth dose profiles fitted to Gaussian distributions, and generating a database for carbon ion fragment spectra used in RBE calculations [15, 74, 75, 209, 221]. Selected benchmarking results are presented in this chapter, and more information can be found in the full version of the article [16].

Figure 2.1 shows exemplary depth-dose profiles of proton and carbon ions in water, simulated in FLUKA and compared to measurements from the Heidelberg ion therapy center (HIT) (using PeakFinder, PWT) [15], for the nominal energies (before the beamline): 54.19, 142.66, 221.05 MeV for protons, and 200.28, 299.94, 430.10 MeV/n for carbon ions. The obtained results showed very good agreement with the measurements of the Bragg peak positions for both beams. On average, it is proven that FLUKA can reproduce the measurement data within experimental uncertainties of ~ 100 μm. In addition, the average dose-weighted dose difference, described as $\overline{\Delta D}/\overline{D}$ was less than 1% for protons and under 1.5% for carbon ions [16].

Figure 2.2 presents the depth-dose curves of other ions simulated in FLUKA and compared against measurements performed at HIT. Depth-dose profiles were acquired using PeakFinder for the beam energies before the beamline: 54.19, 79.78, 200.28, 300.13 MeV/n, for protons, helium, carbon, and oxygen ions, respectively. The obtained chi-square agreement for proton and carbon ion beams is 5.8 x 10^{-5} and 1.1 x 10^{-4} [270], where the smaller the chi-square difference, the higher the agreement between measurements and simulations. In addition, the helium ion chi-square differences was of 2.1 x 10^{-4} and oxygen ion 5.6 x 10^{-5}. Finally, the average dose-weighted dose difference presented low values of 0.6% for protons, 1.6% for helium ions, 0.8% for carbon ions, and 1.3% for oxygen ions [16].

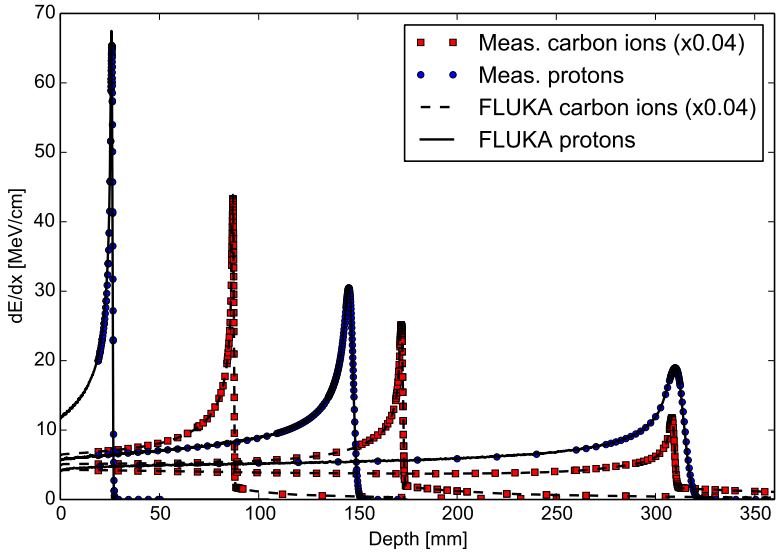

Figure 2.1: Depth-dose profiles of protons and carbon ions, simulated with FLUKA and compared against measurement data at HIT [15]. *Published in [16].*

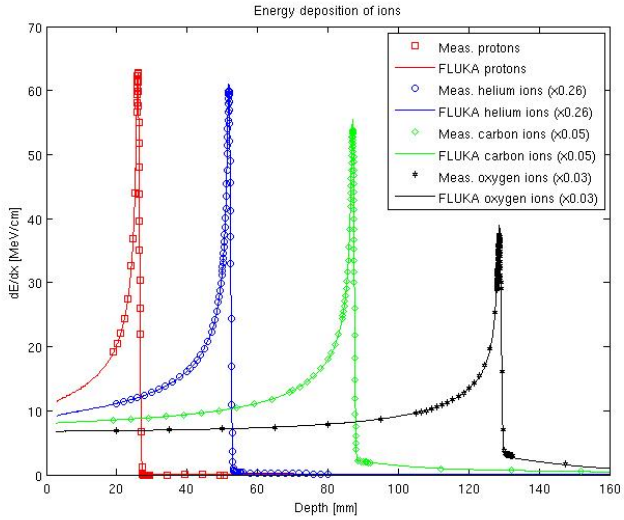

Figure 2.2: Depth-dose profiles of protons, helium, carbon and oxygen ions, simulated with FLUKA and compared against measurement data at HIT. *Published in [16].*

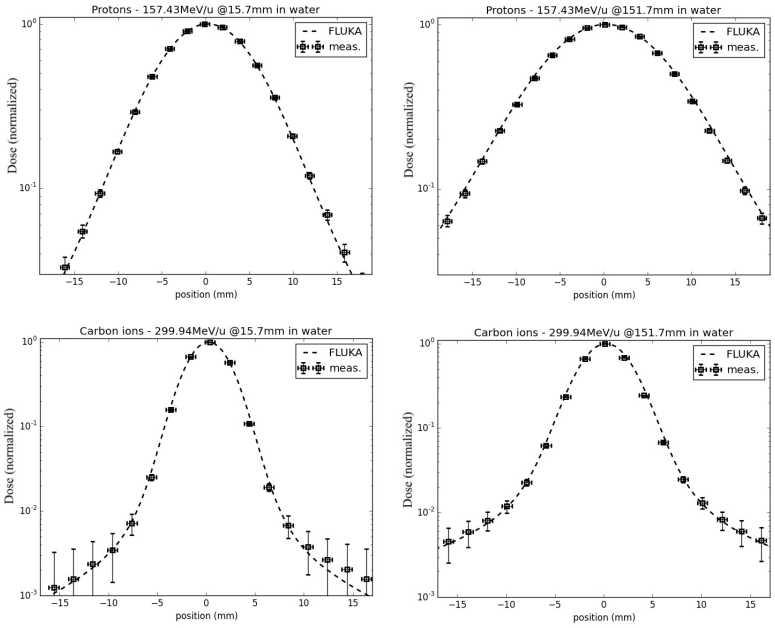

Figure 2.3: Lateral-dose profiles of protons (top) and carbon ions (bottom) in water, at the entrance region (left) and shortly before the Bragg peak (right), FLUKA simulations benchmarked against measurement data at HIT. *Published in [16].*

Figure 2.3 shows an example of lateral-dose profiles benchmarking studies, between FLUKA simulations, and measurements of proton and carbon ion beam - with nominal energy before the beamline - 157.43 MeV and 299.94 MeV/n, respectively. Lateral beam profiles were sampled at water at two depths: at the entrance level at a depth of $\sim$ 16 mm, and in front of the Bragg peak at a depth of $\sim$ 152 mm. The obtained agreement is satisfactory, considering that low-dose region measurements are associated with higher uncertainties, and cylindrical ionization chambers used in measurement average the dose in a volume instead of considering the dose gradient [269]. Additional comparisons and evaluations of FLUKA simulations against experimental lateral dose data for various energies and depth doses can be found in Tessonnier *et al* [271].

2.2.6 Radiobiological calculations

As mentioned in Section 1.3, ion beams provide an increased biological effect; therefore, the RBE must be considered while evaluating and planning ion treatment. The FLUKA MC code was coupled with a few external radiobiological databases, either model or phenomenological/experiment-based. This approach was first used for the physical and biological characterization of proton beams [272, 273]. Then to study the chromosome aberration induction in human cells [274, 275].

The Theory of the Dual Radiation Action (TDRA [276]) was implemented in FLUKA and describes the nonlinear response of the cell material due to mixed radiation fields. TDRA was used to interface the first LEM models for carbon ion therapy [73, 151]. Subsequently, a general interface was developed using Linear Quadratic Model (LQM) (Equation 1.29). In the FLUKA interface, a user is responsible for providing

their own radiobiological database, which includes α and β as a function of energy per nucleon or LET, for different components of the mixed radiation field. To calculate the RBE, the FLUKA MC code uses the dose-weighted averages $\overline{\alpha}_j$ and $\overline{\beta}_j$:

$$\overline{\alpha}_j = \frac{\sum_i \Delta d_{i,j} \cdot \alpha_{i,j}}{\sum_i \Delta d_{i,j}} \quad \text{and} \quad \sqrt{\overline{\beta}_j} = \frac{\sum_i \Delta d_{i,j} \cdot \sqrt{\beta_{i,j}}}{\sum_i \Delta d_{i,j}}, \tag{2.1}$$

where $\Delta d_{i,j}$ is the dose deposited in voxel j by the i-th charged particle with the related $\alpha_{i,j}$ and $\beta_{i,j}$ parameters. This is calculated for all i particles included in the mixed radiation field, which deposited the dose in voxel j. Then, RBE and D_{bio} can be determined, as presented by Mairani *et al* [73] for the LEM model (Section 1.3.5) and [218] for the MKM model (Section 1.3.5).

2.3 in vivo verification

According to the information presented in Section 1.4.7, MC codes can be essential for verifying the obtained distribution maps of β^+ or prompt-γ emitters. MC codes are also important for the design and optimization of detectors and in vivo setups suitable for clinical use [277, 278]. While using MC code simulation, users must rely on their accurate description of physics processes, with a particular focus on the complex nonelastic nuclear reaction history leading to β^+ or prompt-γ emissions.
The development of physics models describing prompt-γ emission and β^+ emitter production for the in vivo verification of proton and ion beams is not the main scope of this thesis. Therefore, only a brief description of the models used in the FLUKA MC code is presented here, where more information concerning benchmarking studies for in vivo verification is available in the full version of this article [16]. On the other hand, the development of the interface for FLUKA PET tools is mentioned in the following section to indicate author's contribution to the development and validation.

2.3.1 FLUKA model developments for in vivo verification

The probability of prompt-γ and β^+ emitter production is affected by many factors, such as the residual excitation energy in the system, balance of binding energy, and level structure of the excited and residual nuclei [16]. Considering proton or ion beam therapies, an accurate description of low energy nuclear models is particularly important because of the low projectile energy level in the Bragg peak region. For these models, the FLUKA MC code is constantly upgraded.
In proton therapy for PET monitoring systems, interesting reactions include O-16(p,x)O-15 and C-12(p,x)C-11 [279], which can produce ejectiles such as deuterons, tritons, helium-3, or α particles. In FLUKA, the process of ejectile emission is described by the coalescence algorithm in the first phase, followed by the equilibrium phase, which describes the evaporation process of the created fragments. During model development, particular interest was placed on energies below a few tens of MeV, where colaescence no longer reproduces the experimental data, owing to the increased impact of binding energies. As such, an appropriate deuteron formation mechanism was implemented, improving the description of the (p,d) reaction [16]. FLUKA simulations were compared with experimental data using the experimental PET system, as presented in Rosso *et al* [280], and using a full phantom with a standard PET setup, as presented in Sommerer

et al [281].

Electromagnetic models, which play a significant role in PET simulations are included in FLUKA to precisely reproduce an annihilation distribution map. FLUKA reproduces the decreasing positron energy before the annihilation process occurs, and it describes the electron binding energy effects and the final (possibly acollinear) motion of the two emitted photons. This model, implemented in FLUKA, was verified experimentally, as presented by Böhlen *et al* [282].

During the last stage of the evaporation process, the PEANUT model (Section 2.2.4) takes over, describing the emission of the residual excitation energy by $\gamma - rays$ cascades. Their angular distribution follows the formalism presented in Tolhoek *et al* [283], and whenever the data are incomplete or nonexistent, they are sampled according to Ferrari *et al* [265].

Finally, to reproduce the prompt-γ production, it is important to determine the excitation functions of single γ lines in the various reaction channels and the γ de-excitation flow [16]. An example of benchmarking data for the FLUKA MC code is presented in Figure 2.4.

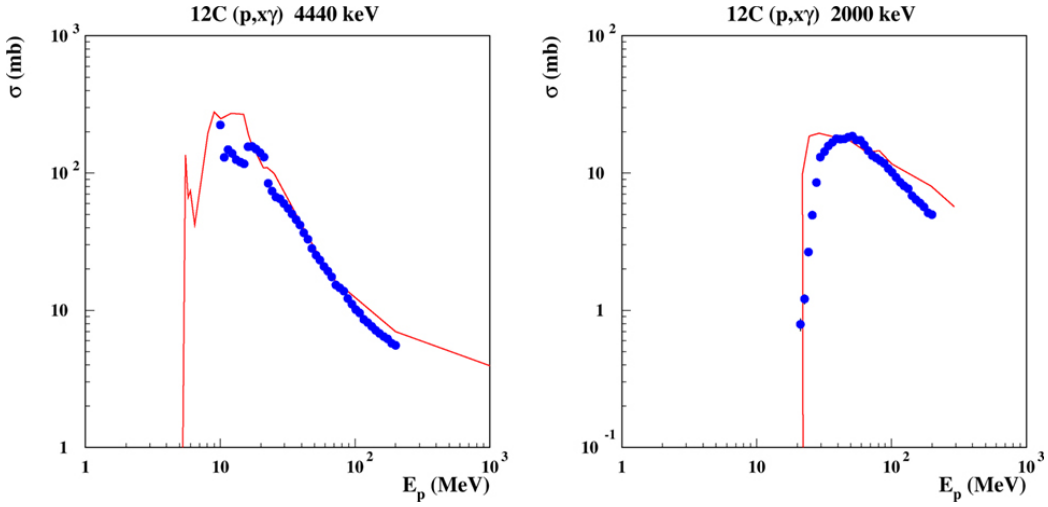

Figure 2.4: Excitation function for the emission of discrete γ lines from proton reactions on carbon. Left: the 4.44 MeV line - de-excitation of the 1st excited level in C-12, the 2nd excited level in B-11, and 2nd excited level in C-11. Right: the 2.0 MeV line -the 1st excited levels of C-11 and B-11. Lines are FLUKA predictions and dots are evaluated data from Kozlovsky *et al* [17]. *Published in [16].*

2.3.2 Model comparison with integral measurements

The study of integrated data, including all single interactions, allows for a better assessment of the model for therapeutic applications, such as conceptual and design detector studies. Profiting from several prompt-γ measurements using ion beams on PMMA or water targets, the FLUKA MC code was benchmarked for γ emission profiles as a function of depth and prompt-γ energy spectra. More detailed information on the experimental setups simulated in the FLUKA MC code and the implemented prompt-γ formalism verification can be found in the full version of this article [16]. It is worth mentioning that overall agreements between

the simulated photon spectra and experimental data were found to be within 10% for energies above 2 MeV, and for the in-depth profile studies, qualitatively FLUKA reproduced the relative shapes of the profiles, as well as it can be noticed a good absolute agreement for different experimental setups.

2.4 Flair and its applications to radiation therapy

2.4.1 Introduction

Building FLUKA input files is supported by a graphical user interface, Flair [240, 241] presented in Figure 2.5. The Integrated Development Environment (IDE), provided by Flair, assists the user in all steps during FLUKA simulations, from creating input files and geometries, through debugging and input error detection, implementation of user-specific routines, running simulations with progress monitoring, output data post-processing, and plotting the results. In general, Flair provides a gentle learning curve for beginners and greatly increases user productivity.

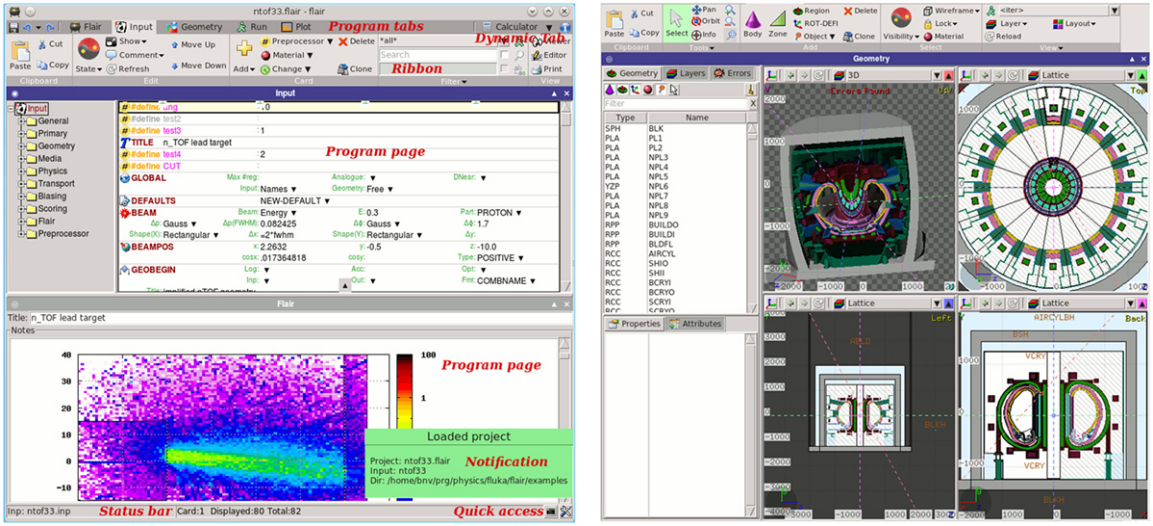

Figure 2.5: Flair graphical user interface (left), Geoviewer - geometry editor (right). *Published in [16].*

One of the main advantages of Flair is a 2D/3D graphical editor and debugger [240] used for building FLUKA geometries. The graphical editor supports the creation of complex layouts with rapid real-time 3D ray-trace rendering. Visualization is performed by a dynamic customized layering mechanism, with the possibility of overlaid views on the created geometry.

Recently, two new modules were implemented and attached to the Flair GUI: one supporting DICOM file handling, and the second supporting automatic PET geometry generation. The DICOM module is responsible for the import, display, processing, export, and conversion of DICOM files into FLUKA propriety functions used in the MC simulations. The PET geometry generator simplifies the modelling of the PET detector geometry with a graphical template, which facilitates parameter definition, or by using predefined

templates of commercial PET scanners available in the module.
This section presents the status of medical tools already functional inside Flair as presented by Battistoni *et al* [16]. This study is based on version 2 of the Flair program [284].

2.4.2 DICOM processing in Flair

Digital Imaging and Communications in Medicine (DICOM) is the standard for the communication and management of medical imaging information and related data [285]. DICOM is used worldwide in various fields of medicine including radiology, radiation oncology, nuclear medicine, cardiology, pathology, and dentistry.
Currently, Flair is capable of interpreting DICOM file modalities for which separate functional classes are implemented:

- CT - Computed Tomography imaging, represented by a single or a multiple files with 2D sliced images,
- MR - Magnetic Resonance imaging, represented by a single or multiple files with 3D representation,
- RT DOSE - Radiotherapy Dose distribution
- RT PLAN - Radiotherapy Plan for treatment
- RT STRUCT - Radiotherapy Structure Set describing ROIs.

DICOM handling is performed using Pydicom [286] and NumPy [287] libraries, both of which are dedicated to the Python programming language. Pydicom is an open source package for interpreting all standard DICOM files from image-based matrices (i.e., found in CT or MRI) through various data tags and nested sequences (found in DICOM RT). The NumPy library is a numerical Python package that is used for image and data processing.
Imported DICOM files can be viewed in Flair using either a tree structure text browser, where the user can inspect DICOM fields, or using a Slice Viewer (Figure 2.6). A graphical representation in the Slice Viewer is capable of displaying CT, MR, and RT DOSE modality images using a 2D slice format directly from DICOM files. For the RT STRUCT modality, ROIs structures and points of interest are visualized as an overlaid layer on the respective CT/MR slice. To enhance usability, it is possible to perform simple image modifications such as cropping and re-scaling.
Recent developments include improvements in the visualization of simulation outputs for medical applications, particularly dose calculation representation. The new DICOM module RTViewer (see Figure 2.7) can represent 2D cross-sectional CT images for three planes (axial, coronal, and sagittal) with an overlaid dose representation from the RT DOSE file or FLUKA calculations. It also allows visualization of the difference between the planned dose calculated by the TPS and MC based re-calculation. Upcoming features will include embedding graphical representation of ROIs (from RT STRUCT) onto the RTViewer plans and providing automatic DVH plots for the referenced dose maps.
Computed tomography (CT) is a typical patient geometry representation used for radiotherapy. As mentioned in Section 1.3.2, CT images contain integer HU values reflecting the X-ray attenuation coefficient for a specific tissue composition. Assigning a detailed material description for each HU value is neither memory- nor time-efficient for simulation purposes. Therefore, following the proposition presented by Schneider *et al* [109], HU values are divided into groups with specified intervals for particular organ compositions. FLUKA

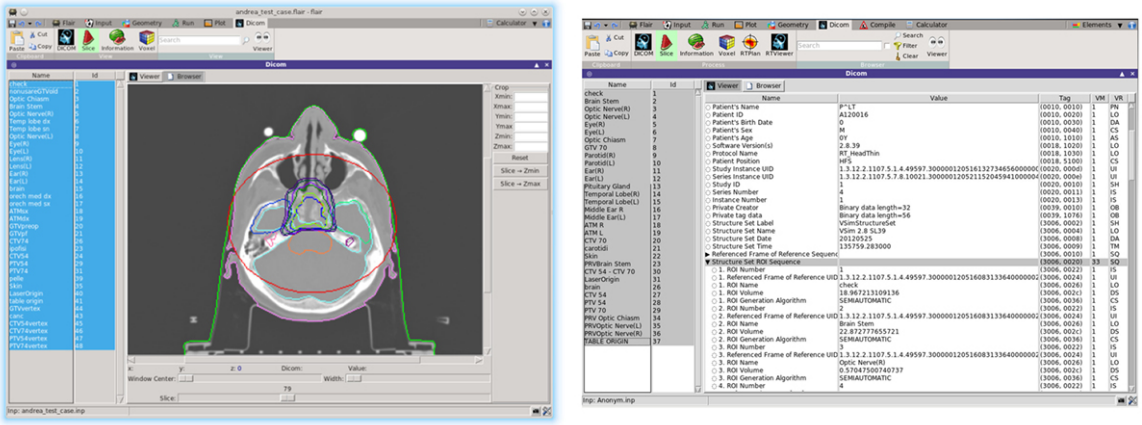

Figure 2.6: Flair RT DICOM viewer, with RT STRUCT superimposed (left); DICOM tree browser (right). *Published in [16].*

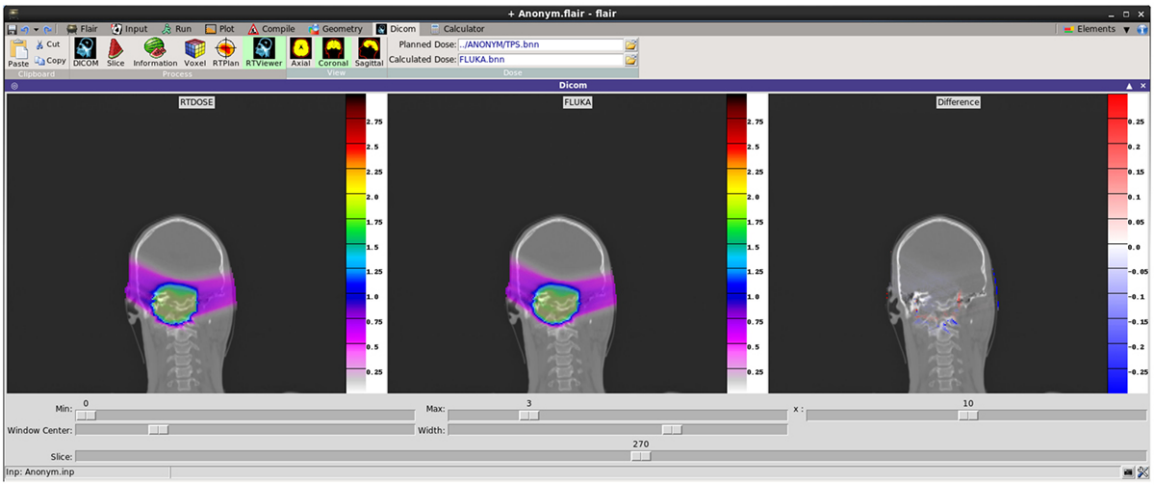

Figure 2.7: New DICOM RT interface. Coronal CT plane with mapped physical dose [Gy] from RT DOSE and FLUKA calculations. On the right, the differences between the obtained values [Gy]. *Published in [16].*

handles group (or groups) of voxels with the same tissue material composition as one organ region. The organ is an internal FLUKA representation of a geometry region, defined similarly to the standard (non-voxel) FLUKA regions, modelled by the user.

Flair segments CT scans into 24 tissue materials, with a nominal elemental composition (based on human CT scans) and pre-defined mean tissue density at the center of the HU interval [161, 230, 288]. In reality, an HU interval within an organ represents a continuous range of densities and properties of the same tissue. FLUKA provides a scaling mechanism to interpolate material properties within HU intervals. The 24 material description set is divided into smaller intervals (41 in total), allowing further scaling correction. The same materials are used for organs with identical material composition; however, other parameters

such as density and electronic stopping powers are scaled with respect to the real HU value to account for proper interaction processes. The FLUKA voxel file was recently refined to embed all input cards describing supplementary data on the materials, assignments, and correction factors.

RT STRUCT

The RT STRUCT file is used to transfer defined patient structures and related data between the software, devices, and radiotherapy departments. It includes geometrical data of ROIs structures defined on CT scans and points of interest (POI) created during treatment planning (e.g., dose reference points). Structures are used during treatment planning simulation for dose scoring on an organ basis and for calculating the DVH. In RT STRUCT, ROIs are typically represented by sets of points (defined in 2D coordinates for each CT/MR slice image) belonging to a closed polygon.
The user can select and embed ROIs from the RT STRUCT file in the voxel file. For each internal voxel cube, Flair determines the ROI to which it belongs, considering the situation in which the voxel belongs to more than one ROIs. Created correspondence matrix between voxels and ROIs is embedded into the FLUKA voxel file. Flair uses this matrix for 2D/3D plotting and/or DVH calculations (Figure 2.5).
Because the structure point positions (by which ROIs are defined) are not rounded to the CT/MR image grid, Flair provides additional information on the structure volumes. It calculates ROIs volumes interpolating points using true polygonal information or their discrete version (adapted to voxel grid), which typically results in a difference of a few percent.

RT DOSE

RT DOSE is used to transfer 2D or 3D radiation dose maps generated from treatment planning systems or similar software/devices [285]. Flair enables conversion of all DICOM files containing a PixelData tag (i.e., CT, MR, and RT DOSE) into a FLUKA USRBIN 3D mesh file.
The FLUKA proprietary USRBIN file can be used for graphical representation of the results and analysis. For example, in RTViewer (Figure 2.6), the output data from the TPS can be imported, and the chosen field, fraction, or the entire treatment dose can be compared with FLUKA simulations and visualized, overlaying CT scans. The created USRBIN files may also be used as particle source generators, for example, for scoring delivered doses from PET/CT radioactive tracers (Figure 2.8).

RT PLAN

An RT PLAN file is typically generated by a TPS and contains essential information for the treatment delivery system. In the Tag fields, RT PLAN describes the i.a. treatment fractions, patient position, accessories, external beam parameters, and planning CT. In spot scanning particle therapy, each single beam spot is stored in a beam sequence with enumerated control points. Every beam sequence provides information on the particle type, planned isocenter position, gantry, patient, and table angles. In addition, the control points cover spot-specific data, that is, particle energy, spot position at the isocenter, and the number of monitor units/particles.
To simulate treatment planning delivery, the user can export typical spot beam parameters into an external file using a Flair DICOM interface. While exporting RT PLAN data, Flair can also account for rotations

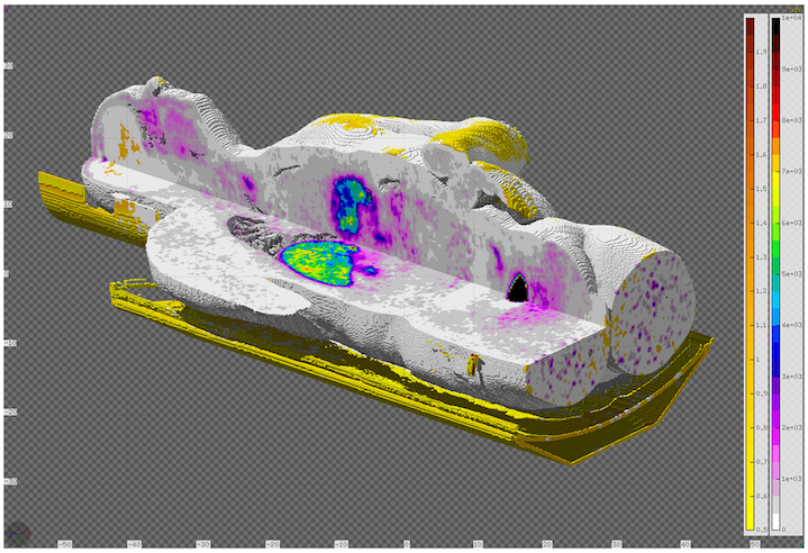

Figure 2.8: Voxel representation of DICOM CT data together with superimposed RT DOSE data. Displayed using a Flair geometry editor. *Published in [16].*

and translations of the patient included in the RT PLAN coordinate systems. Consequently, Flair updates the basic FLUKA input file, creating a fully functional, ready-to-run input for MC simulations of each beam field. The export of the DICOM data is fully controlled by Flair, which also performs validation checks using the available control sequence variables.

The following steps include the compilation of a predefined source routine for RT PLAN, which reads and generates the beam spot source data for FLUKA simulations. Finally, post-processing allows the creation of a fractional dose file based on the combined beam sequence outputs, which can then be visualized in RTViewer. Further work will focus on simplifying the process of treatment plan simulation and including less frequent treatment plan parameters.

2.4.3 PET scanner simulation tools for FLUKA

Positron Emission Tomography (PET) is a medical imaging technique used to measure the biochemical and physiological activity of body tissues. The PET scanner measures, in coincidence, a pair of photons created during the positron-electron annihilation process. Positrons are obtained from the decaying β^+ emitter, typically injected into the patient's body via a radio-pharmaceutical drug. In clinical applications, the most frequently used radio-pharmaceutical is fluorodeoxyglucose ($_{18}$ FDG). It is a glucose analog coupled with the F-18 radioactive isotope used to measure in vivo glucose uptake in body cells and search for an abnormal metabolism of diseased organs and tissues.

In addition to nuclear medicine, PET is increasingly used in charged-particle therapy. Online and offline monitoring of dose delivery and range verification can be supported by this noninvasive technique. Commercial PET scanners, as mentioned in Section 2.3, need to fulfil additional requirements for proton or ion

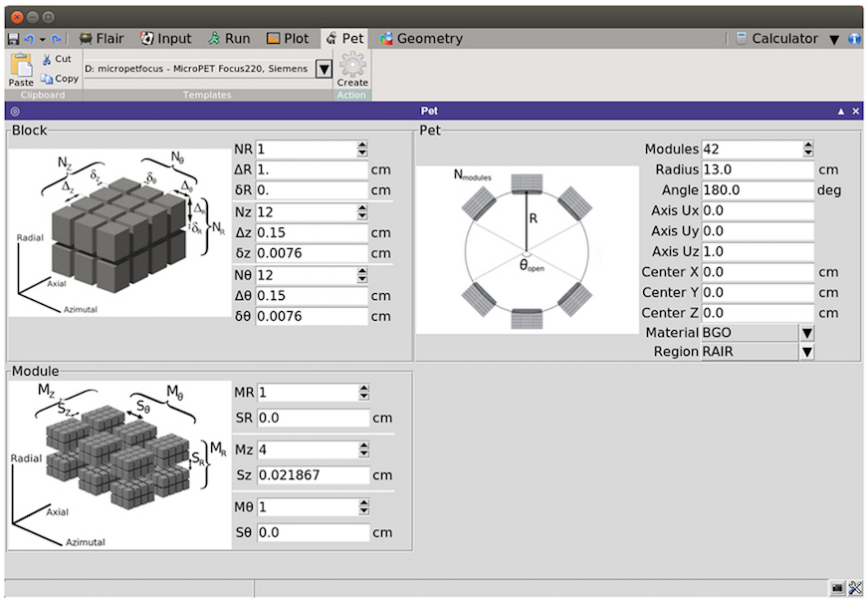

Figure 2.9: PET geometry tool in Flair. *Published in [16].*

beam monitoring, which challenges current designs. Monte Carlo codes can support performance evaluation and redesign studies because MC is capable of estimating an accurate dose map for the simulated β^+ emitter distribution. FLUKA PET Tools assist with the MC simulations of the PET scanners by allowing a step-by-step configuration of the new PET geometry and provide improved physics models for β^+ production.

A typical PET scanner is composed of a set of scintillator detectors merged into modules, which are mounted on a closed or open gantry structure, allowing the detection of collinear photons derived from the annihilation process. The creation of the PET scanner geometry, with multiplied rectangular parallelepiped detectors, can be easily parameterized and quickly replicated into the FLUKA geometry. As presented in 2.9, FLUKA PET Tools support a user at every step, visualizing and explaining specification details. The user describes parameters starting from the level of blocks, through an array of blocks called modules, and finally on the ring level, where one defines the scintillator material, radius of the ring, center coordinates of the scanner, and opening angle. Closed PET rings are typically used for standard imaging purposes; however, partial rings with an opening angle θ_{open} are an interesting solution for in-beam PET, where the scanner must be incorporated into the radiation room [289].

Users can start modelling the PET geometry with a set of predefined templates from commercial PET providers, such as Siemens (Ecat HRRT, Hi-Rez, MicroPET Focus 220), Phillips (Allegro, Mosaic), GE (GE Advance), and Concorde (MicroPET P4). Subsequently, all predefined parameters can be modified and further optimized according to user needs. The basic PET geometry and input data for FLUKA are automatically generated using FLUKA PET tools. Additional elements should be modified or added manually, including the phantom target definition, radioisotope distribution, and beam structure (see Figure 2.10).

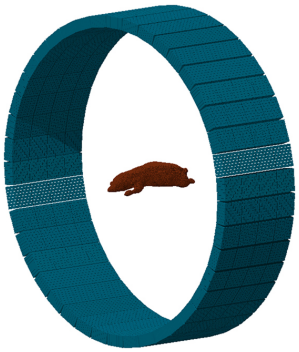

(a) Example of a MicroPET P4 scanner with a high-quality voxelized mouse phantom [290, 291]. *Published in [16].*

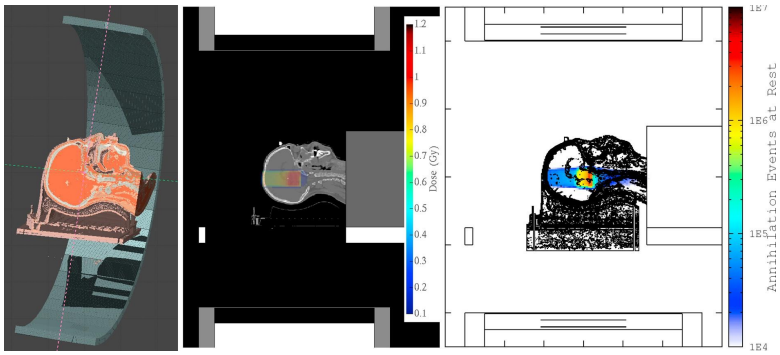

(b) 1 Gy SOBP irradiation with an O-15 beam (center), in an anthropomorphic voxelized phantom (left) imported into geoviewer and the total annihilation events at rest, time integrated (right). *Publlished in [234].*

Figure 2.10: Example or geometries and simulation set-ups created using FLUKA PET Tools

The final 3D PET image is reconstructed from tomographic sliced images created from a set of 2D projections at different angles. Annihilation events create a pair of collinear photons, whose tracks are delineated into a set of parallel lines of responses (LOR). All detected events are then integrated along each LOR into a single pixel in the projection of a specific angle, forming a Sinogoram image (Figure 2.11). The sinogram is used as an input data matrix for the PET reconstruction algorithms. The two most popular algorithms used in PET are Filtered Back-Projection (FBP) and Maximum-Likelihood Expectation-Maximization (MLEM). The FBP provides a fast and simple solution using a Fourier Transform of each 2D projection, with additional interpolation in the Fourier space. By contrast, MLEM is based on an iterative approach of maximizing a likelihood function that estimates the mean number of radioactive decays, which fits and improves the estimate of the sinogram [16].

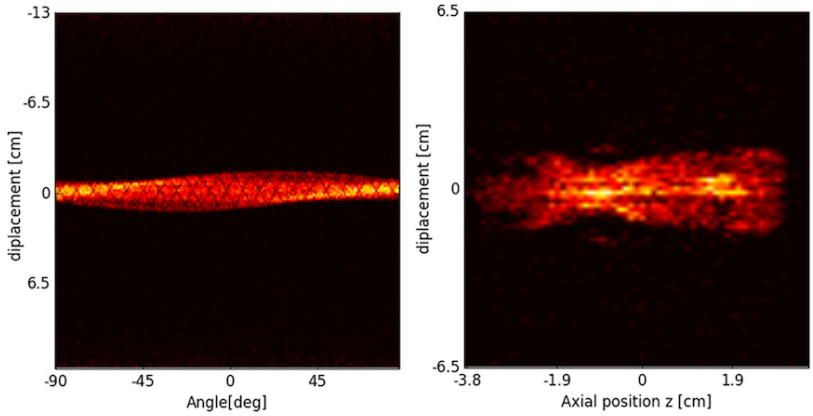

Figure 2.11: Sinogram (left) and projection image (right) of the segmented mouse phantom of Figure 2.10(a), using a MicroPET P4 scanner. *Published in [16].*

FLUKA provides a set of scoring routines suited for acquiring data on energy deposition events in PET

detectors and the pairing of individual events into coincidence events. In standard simulations, two steps are required: simulation of nuclear interactions and tracks of decaying particles in the target phantom geometry up to the PET scanner and post-processing of the obtained data into a sinogram. In the first step, the portion of energy deposited in the scintillator detectors is identified as an individual event, and all related data are stored in the output file. The sensitivity of event tracking can be adjusted according to the desirable energy windows, minimum scoring time, time resolution, and dead time of the detector. Accordingly, with each FLUKA run one output file is generated. In the second step, a set of output files is processed, and coincidence events are determined and saved in another coincidence output file. This output file is further organized into a sinogram and exported to the Interfile 3.3 format, a binary format standardized for nuclear medicine image data [292]. In addition, a created singoram file can be parameterized to customize the scoring using Arc Correction, Maximum Ring Difference, Number of Segments, Span and Mashing Factors.
With the new updates presented by Augusto *et al* [234], the aforementioned reconstruction algorithms were implemented in Flair. While the FBP reconstruction time is synchronized with the generation of the output sinogram file, MLEM reconstruction requires significantly more time; however, it yields a higher image quality. Finally, the generated reconstructed image can be stored in the USRBIN file and further used in the Flair and FLUKA simulations.

2.5 Application of the FLUKA code for clinical calculations at HIT and CNAO

This section provides a brief summary of the clinical application of FLUKA, which was applied prior to the presented extension of the Flair functionality for DICOM objects (Section 2.4). In the past HIT and CNAO facilities developed home-made frameworks, for automated FLUKA MC simulations of clinical treatment plans for scanned proton and carbon ion beams [74]. The results of these simulations were benchmarked against clinically commissioned TPSs, which provided a baseline validation database for the development of RT functionalities in Flair. More detailed information on application and verification studies can be found in the full version of this article [16] and the further extension of Flair for spot-scanning applications can be found in Kozłowska *et al* [13], as shown in Chapter 3 of this thesis.
HIT developed a GUI for FLUKA clinical calculations using a MeVisLab environment [293] and the CNAO GUI is based on MATLAB ®. Calculations of the physical and RBE-weighted dose distributions for particle therapy treatment are performed individually for each field. The RBE dose is obtained by weighting the physical dose using an RBE value of 1.1 for proton beams, or calculated using a dedicated LEM I framework implementation for carbon ion beams (also used in the TPS [73, 151, 294]). The dose-to-medium ratio is converted automatically into a dose to water (Section 1.3.2). Optionally, it is also possible to obtain LET_D values for proton beams. To ensure compliance with the clinical TPS database, the FLUKA physics settings are set according to the parameters used during the production of the TPS physics database [15, 209, 221]. The patient model is based on CT scans and created using the standard FLUKA approach with stoichiometric calibration [109, 231]. Each facility-based CT scanner has individually adjusted CT-range calibration curves (which are also defined in the TPS); therefore, adjustments of the electromagnetic and nuclear parameters, as presented in Jiang *et al* [295], are needed in the FLUKA calibration files for consistency with all CT protocols.

In addition, at CNAO, a separate interface has been developed for conversion of the FLUKA outputs into an RT DOSE DICOM file, which can be imported to local TPS installation, RaySearch RayStation®. In general, this solution facilitates the fast visualization of MC simulation output within the clinical routine for physicists and physicians.

2.6 Conclusions

This Chapter presents the latest improvements to the electromagnetic and nuclear models of FLUKA. Upgraded models were benchmarked against measurements of depth-dose and lateral profiles in water for different ions of clinical interest. Satisfactory and accurate results proved usability and made FLUKA the code of choice for the generation of the TPS database at leading European centers [16].

A particular effort was made to progress within nuclear interaction models. The particle production and interaction cross-section models for proton and ion beams were enhanced in the therapeutic energy range. As such, both primary particles and produced fragments (including electromagnetic particles) are transported and treated reliably, profiting from the latest upgrades in the evaporation, fragmentation, and de-excitation models.

Studies of in vivo verification techniques require accurate low energy nuclear models. In the FLUKA production models, β^+ emitters were successfully benchmarked for the therapeutic energy range, reproducing production by protons within experimental error bars, and by carbon projectiles with accuracy equal to or lower than 25%. New prompt-γ production models in FLUKA, refined after the last revision of the experimental data, improved discrete line cross sections and integral energy spectra, and yield-versus-depth data for proton and carbon ion beams. Agreement with the experimental yield depth data was within 15%-20% of the absolute yields. Energy spectra benchmarking studies for prompt-γ monitoring and spectroscopy (above 2 MeV) during proton irradiation showed an agreement within 10%. Currently, FLUKA development is focused on improving nuclear interaction models, focusing on light ion beams, such as carbon, nitrogen, and oxygen ions.

Upgraded and thoroughly benchmarked FLUKA models with a flexible DICOM interface of the Flair GUI comprise a powerful and simple interface to perform Monte Carlo simulations for particle therapy and medical imaging. The DICOM files are read and processed using the Flair DICOM module. Users can create patient voxel geometry from CT/MRI files, add information on ROI structures based on RT STRUCT, visualize dose from RT DOSE, and perform simulation of the PET scanner using an automatic PET geometry generator. Future work will focus on improving RT PLAN exports and developing a Monte Carlo-based optimizer for treatment planning.

The FLUKA MC calculations supported the development of commercial analytical TPSs, with the main focus on dose calculation algorithm enhancements. In addition, institution based home-made solution i.e. at HIT, and CNAO, automated the MC based re-calculations, supporting the extensive studies on the analytical algorithm shortcomings for the particle therapy planning. Reported implementations add more information on the biological effectiveness of the treatment and provide a flexible tool to address scientific questions aiming for higher-quality treatment.

Chapter 3

FLUKA particle therapy tool for Monte Carlo independent calculation of scanned proton and carbon ion beam therapy

In this Chapter, the development and validation of a specific proton and ion therapy interface - the FLUKA Particle Therapy Tool is presented. This tool was created to support the application of the FLUKA MC code in hospital based research environments.
The Chapter is a presentation of the article *FLUKA particle therapy tool for Monte Carlo independent calculation of scanned proton and carbon ion beam therapy* published in *Physics in Medicine and Biology*, 64, 075012; 2019 [13] by following authors:

Wioletta Kozłowska [1,2], Till Böhlen [3], Caterina Cuccagna [4,5], Alfredo Ferrari [1], Francesco Fracchiolla [6], Dietmar Georg [2,7], Giuseppe Magro [8], Andrea Mairani [8,9], Marco Schwarz [6,10], Vasilis Vlachoudis [1]

[1] CERN – European Organization for Nuclear Research, Switzerland;
[2] Medical University of Vienna, Austria;
[3] PSI – Paul Scherrer Institute, Switzerland;
[4] TERA Foundation, Switzerland;
[5] Université de Genève, Switzerland;
[6] Protontherapy Department, Trento, Italy;
[7] Christian Doppler Laboratory for Medical Radiation Research - MUW/AKH, Austria;
[8] CNAO, Italy;
[9] Heidelberg Ion-Beam Therapy Center, Germany;
[10] TIFPA-INFN, Italy

IOP Publishing Phys. Med. Biol. 64 (2019) 075012 (12pp) https://doi.org/10.1088/1361-6560/ab02cb

Physics in Medicine & Biology

IPEM Institute of Physics and Engineering in Medicine

OPEN ACCESS

CrossMark

RECEIVED
9 October 2018

REVISED
14 January 2019

ACCEPTED FOR PUBLICATION
29 January 2019

PUBLISHED
29 March 2019

PAPER

FLUKA particle therapy tool for Monte Carlo independent calculation of scanned proton and carbon ion beam therapy

Wioletta S Kozłowska[1,2], Till T Böhlen[3], Caterina Cuccagna[4,5], Alfredo Ferrari[1], Francesco Fracchiolla[6], Giuseppe Magro[7], Andrea Mairani[7,8], Marco Schwarz[6,9], Vasilis Vlachoudis[1] and Dietmar Georg[2,10]

[1] CERN—European Organization for Nuclear Research, Geneva, Switzerland
[2] Medical University of Vienna, Vienna, Austria
[3] PSI—Paul Scherrer Institute, Villigen, Switzerland
[4] TERA Foundation, Geneva, Switzerland
[5] University of Geneva, Geneva Switzerland
[6] Proton Therapy Center, Trento, Italy
[7] CNAO, Pavia, Italy
[8] HIT – Heidelberg Ion-Beam Therapy Center, Heidelberg, Germany
[9] TIFPA-INFN, Trento, Italy
[10] Christian Doppler Laboratory for Medical Radiation Research—MUW/AKH, Vienna, Austria

E-mail: wioletta.kozlowska@cern.ch

Keywords: Monte Carlo, FLUKA, quality assurance, particle therapy, treatment planning

Abstract

While Monte Carlo (MC) codes are considered as the gold standard for dosimetric calculations, the availability of user friendly MC codes suited for particle therapy is limited. Based on the FLUKA MC code and its graphical user interface (GUI) Flair, we developed an easy-to-use tool which enables simple and reliable simulations for particle therapy. In this paper we provide an overview of functionalities of the tool and with the presented clinical, proton and carbon ion therapy examples we demonstrate its reliability and the usability in the clinical environment and show its flexibility for research purposes. The first, easy-to-use FLUKA MC platform for particle therapy with GUI functionalities allows a user with a minimal effort and reduced knowledge about MC details to apply MC at their facility and is expected to enhance the popularity of the MC for both research and clinical quality assurance and commissioning purposes.

1. Introduction

Hadron beams have been in the focus of radiation oncology for over 60 years, due to their superior physical and biological properties compared to conventional high-energy photon beams (Jäkel *et al* 2008, Durante and Loeffler 2010). Protons are currently used in 80 facilities around the world, with 27 centers in clinical operation in Europe, and several are under construction. Motivated by the excellent clinical results achieved with carbon ion beams in Japan, four centers for carbon ion therapy were established in Europe during the last decade. More recently, the researchers focused also on particle species other than protons and carbon ions, i.e. helium and oxygen (Fuchs *et al* 2015, Mairani *et al* 2016, Knäusl *et al* 2016, Tessonnier *et al* 2017a, 2017b). The clinical outcome of particle therapy depends, besides the various clinical aspects, on the dosimetric accuracy including accurate dose calculations and beam delivery, respectively. So far most of the clinical experience in particle beam therapy has been obtained with radiotherapy treatment planning and dose calculations based on semi-analytical pencil beam algorithms (Hong *et al* 1970).

Regarding the dosimetric accuracy, general purpose Monte Carlo (MC) codes are considered, as the 'gold standard' (Rogers 2006). However, their complexity leads to a long learning-curve for a typical user. On top of it, in most cases they are not able to efficiently support DICOM standard (DICOM 2018), optimization processes, and evaluation of dose distributions as required for clinical treatment planning. As a partial solution to this problem, commercial MC treatment planning systems (TPS) are being introduced in the clinical routine (Widesott *et al* 2018). Apart from their advantages, such as: typically good integration with the standard pencil-beam TPS, as well as, a relatively short time of calculations, they are not as flexible as the research tools; not all types of par-

ticles are transported and implemented interaction models are limited. This restricts the usage of commercial, simplified MC TPS with respect to novel ion species, scoring of non-standard quantities (i.e. LET_D, experimental and new *RBE* models) and accurate dose estimation in non-biological materials.

General purpose MC Codes have a full flexibility to support the above mentioned problems. They have demonstrated a potential as a tool for independent dose recalculation for patient specific QA, or for benchmarking for dose calculation algorithms of commercial TPS (IAEA and ICRU 2007, Parodi *et al* 2012, Grevillot *et al* 2012, Bauer *et al* 2014). Several institutions succeeded to develop their own customized solutions based on MC Codes, mainly for research purposes (Trento—(Fracchiolla *et al* 2015) (also clinical), CNAO—(Molinelli *et al* 2013), HIT—(Parodi *et al* 2012)). Future systematic and user-friendly utilization of the general purpose MC tools for quality assurance (QA) and research, requires reliable and at the same time generally applicable interfaces to connect and embed MC tools in the radiation oncology workflow. One of the general purpose MC Code that has been continuously developed with a focus on medical application is FLUKA (Ferrari *et al* 2005, Böhlen *et al* 2014, Battistoni *et al* 2016, Augusto *et al* 2018).

The purpose of the current manuscript is to present first, an easy-to-use particle therapy platform based on FLUKA and to demonstrate its potential for clinical applications on selected examples for proton and carbon ion beams, i.e. beam modelling or patient specific treatment plan QA. Furthermore, with the new FLUKA release, the platform currently supports biological dose calculations as well as calculations of dose-averaged LET distributions for treatment plans. These new developments are scheduled for release in 2019 and will hence become widely available.

2. Materials and methods

Recent developments of the FLUKA particle therapy tool aim at supporting current research challenges. The first section provides general information about its functionalities. The subsequent sections present its usage for the following applications:

- Patient specific treatment plan QA for proton therapy in clinical setting (section 2.3)
- Biological dose scoring for carbon ion therapy (section 2.4)
- Dose-averaged LET determination on the basis of treatment plans generated with a commercial TPS for carbon ion therapy (section 2.5)

2.1. FLUKA Monte Carlo code and its GUI Flair for particle therapy

The FLUKA particle therapy tool is based on the established general purpose MC code FLUKA, which includes the state-of-the-art physics models (Ferrari *et al* 2005, Böhlen *et al* 2014). FLUKA has been thoroughly benchmarked against depth-dose data and lateral profiles from research and clinical particle-beam therapy accelerators, for protons, carbon and various other light ions with therapeutic potential (Battistoni *et al* 2016, Parodi *et al* 2012, Mirandola *et al* 2015), as well as supported a beam characterization for the design of TULIP (TUrning LInac for Protontherapy) (Cuccagna *et al* 2018). To provide a flexibility in designing simulations for particle therapy as well as to improve the usability, FLUKA was enhanced with several new functionalities.

The FLUKA particle therapy tool is integrated with Flair (Vlachoudis 2009, Vlachoudis and Sinuela-Pastor 2014)—a graphical user interface (GUI) and an integrated development environment (IDE). Flair enables creating and editing error-free FLUKA input files, writing and compiling user routines, executing simulations, data processing and plot generation. It is based on Python and thanks to its modular design the RTmodule for particle therapy was implemented to enhance the use of the new FLUKA functionalities for medical applications.

For particle therapy applications of FLUKA described in this study, the predefined simulation default settings—HADROTHErapy is always chosen to guarantee a reasonable simulation time and reliable accuracy. Particle transport thresholds are set down to 100 keV, except low energy neutrons, which are transported down to 10^{-5} eV.

Atomic physics models handle continuous energy loss, energy loss straggling, delta-ray production (production cut at 100 keV) and the multiple Coulomb scattering of charged particles. Nuclear interaction models for hadrons, photons, muons and neutrinos are described using PEANUT model (Battistoni *et al* 2006). For ions, in the range down to 0.1 GeV n^{-1}, FLUKA uses a modified version of relativistic quantum molecular dynamics (RQMD-2.4) model (Andersen *et al* 2004) implementation, below 150 MeV n^{-1} nuclear reactions are handled by Boltzman master equation (BME) (Cerutti *et al* 2006), while smoothly transiting from one model to another in the overlapping range of energies.

Typical input and output standards used in the clinical experience is recognized by the platform, and the exported data readable by other software. The RTmodule uses the DICOM (digital imaging and communications in medicine (DICOM 2018)) standard for the data exchange with imaging tools or TPS. More specifically, it can process computer tomography (CT) files into the voxelized patient geometry and translate and embed

regions of interest (ROI) from DICOM RTSTRUCT file into patient-voxel files readable by FLUKA. The module imports information from each pencil beam spot described in the DICOM RTPLAN file. It processes the DICOM RTDOSE file into the FLUKA format and provides a tool for direct comparison with the FLUKA output. The obtained FLUKA data can be then exported to the DICOM RTDOSE format. For treatment plan calculations, the FLUKA particle therapy tool enables handling a multiple-field treatment at once or performing individual treatment field analysis with possibility of merging data from individual fields. Furthermore, for the sake of the compatibility with clinically used and commissioned TPS, on-the-fly conversion of dose-to-medium to dose-to-water can be performed for both physical and biological calculations (Bauer *et al* 2014).

The standard patient model for stoichiometric calibration of voxelized CT-based geometry is based on a published Hounsfield unit (HU) calibration procedure (Schneider *et al* 2000). Creation of a voxel geometry requires two files. The individual assignment of HU (or any other arbitrary unit) to tissue material, and the composition of tissue components. It is important to emphasize that if the individual stopping power (dE/dx) determined by FLUKA does not match exactly the stopping power used for clinical TPS (due to minor differences in the defined material composition), there will be a systematic deviation in the particle ranges. Correction factors for stopping powers can be added to overwrite FLUKA-calculated values.

The beam source can be generated directly from clinical treatment plans. The DICOM RTPLAN file contains the essential information of each pencil beam spot (i.e. energy, position, rotation), which are then translated to FLUKA-proprietary functions. Specific beam model information is treated as supplementary data; details for selected key energies needs to be provided in a separate file, and the values between key energies are interpolated using a spline algorithm. This supplementary information encompasses: beam size, angular spread, momentum spread and other data specific to the treatment and gantry/beamline facility, such as the normalization of monitor units (MU) to the number of primary particles. In the other words, each defined pencil beam spot has its assigned individual set of modifiable parameters. This eases and accelerates the facility-specific beam model creation and verification.

While importing DICOM information into the FLUKA input RTmodule, scoring parameters (such as: voxel size, dose binning and patient/image orientation) are automatically determined to simplify subsequent dosimetric assessment. The RTmodule determines the scoring resolution based on the DICOM RTDOSE file, however, on top of the standard dose scoring, it is possible to modify the pre-generated settings or to specify additional scoring estimators.

Finally, for biological dose (D_{RBE}) computation as presented here, a radiobiological database for the local effect model (LEM) (Scholz *et al* 1997) is used for FLUKA simulations (Mairani *et al* 2010). In the respective FLUKA input file it is possible to include external files that describe alpha and beta parameters within the linear quadratic formalism, of different tissue components of the mixed radiation field as a function of energy per nucleon and ion. This allows to interface easily external RBE models with the FLUKA computation. At the end of the simulation, dose-weighted averages of α_D^{mixed} and β_D^{mixed} are obtained for each voxel using the formalism from (Krämer and Scholz 2006), followed by the calculation of the survival curve and dose-weighted RBE (see appendix).

2.2. Commissioning of the FLUKA particle therapy tool for independent dose calculations

For testing and illustrating the versatility of the FLUKA particle therapy tool on clinical cases, the tool was first commissioned for two particle therapy facilities, i.e. the synchrotron based facility CNAO for proton and carbon ion therapy and the cyclotron based proton facility at Trento. For these two facilities two different levels of commissioning were performed, which is described briefly in the following. Then the commissioned data were handled via the RTmodule functionalities.

Commissioning for the CNAO facility: The geometry of the CNAO horizontal beam-lines was modelled, including the vacuum window, the beam monitoring system and the air gaps. For each proton and carbon ion beam within the clinically relevant energy range, both the momentum spread and the size of the beam before the nozzle were adjusted to match the commissioned measured values. Furthermore, for carbon ion beams, ripple filters were embedded into the geometrical description as additional 'lattice' layers. A previously determined facility-specific CT calibration curve was provided. FLUKA-based stopping powers for different materials were slightly adapted to match the predetermined TPS-based dE/dx values.

Commissioning for the Trento facility: For the modelling of the Trento proton facility, no detailed information concerning the beam delivery system was available, thus the methodology presented in Fracchiolla *et al* (2015) was used. Original beam data used for the MC model in Fracchiolla *et al* (2015) was retrieved and described in the supplementary beam model file. Simulations for 16 key energies (between 70 MeV and 200 MeV in steps of 10 MeV) were performed and compared with commissioning measurements in terms of range and spot size. The range was defined as the position of the 90% of the maximum of the curve in the Bragg peak's distal fall-off (R_{90}) for integral depth dose curves measured in water, while spot size was defined as sigma obtained for a single Gaussian fit in transversal planes for measurements in air at five distances from the isocenter (−19.8 cm, −10 cm, 0 cm, +10 cm, +20 cm). For treatment simulations, the beam energy delivered for the Trento cyclotron

Table 1. Input parameters for LEM I for chordoma cells.

Input parameter	Value
$\alpha_X(\mathrm{Gy}^{-1})$	0.1
$\beta_X(\mathrm{Gy}^{-2})$	0.05
D_t (Gy)	30

was assumed to be continuous in the range from 70 MeV to 226 MeV. Values for the energies in between were interpolated using a spline algorithm. For the commissioning of the facility, a specific CT calibration curve and two phantoms were used to adjust the default HU-tissue calibration within the FLUKA particle therapy tool. The first phantom consisted of two material blocks with significantly different densities (two plates substituting tissues—lung 0.3 g cm^{-3} and bone 1.819 g cm^{-3}), while the second one was an anthropomorphic lung phantom.

2.3. Application 1: patient specific treatment plan QA in particle therapy

Representative clinical treatment plans were selected at the two different particle therapy treatment centers. These were generated using commercial and fully commissioned TPS (Syngo at CNAO, RayStation version 6i in Trento). At both sites dose distributions resulting from treatment plans are calculated with pencil beam algorithms implemented in the TPS.

Based on this data, FLUKA input files were built using the RTmodule. Pencil beam scanning data (particle species, position, rotation, intensity and spot size at the isocenter) were extracted from treatment plans. For both cases supplementary beam model file with the additional, commissioned beam source information were used. In the case of CNAO simulations, the model of the beam nozzle was designed using FLUKA combinatorial geometry, however the model, once created, can be easily re-adapted for further simulations.

Two proton chordoma patient cases were selected from each of the facilities. The cases are representative for rather homogeneous tissue conditions. Each treatment plan consisted of three fields. As third proton example, a head-and-neck cancer case, representative for more heterogeneous tissue conditions, was selected. In addition, in this setting a 4 cm thick range shifter was used and modeled in FLUKA geometry. The last clinical case was a chordoma patient, treated with carbon ions using a two field arrangement.

Standard dose scoring in terms of dose-to-water was applied, as well as dose-to-medium. For proton simulations 1% of the planned number of particles was used, while for the carbon ion 10% of planned particles was used to obtain error below 1% for values above 25% of the maximum dose. All calculated dose distributions were evaluated in terms of Dose-Volume-Histograms and several DVH parameters were extracted and compared (D_5 and D_{95} for PTV, D_5, $D_{7.5}$ and D_{10} for OAR). As in clinical practice a fixed proton RBE of 1.1 was used.

2.4. Research application 2: biological dose calculation

For biological dose calculation, a carbon ion treatment plan of a chordoma patient case was selected. Biological dose calculations with FLUKA were performed using the LEM I model with the parameter set, given in table 1.

2.5. Research application 3: dose-averaged linear energy transfer scoring

The final research application presents the possibility of extracting an unrestricted dose-averaged linear energy transfer (LET_d) distribution from TPS files, which can serve as a simplified indicator for future approaches of treatment plan optimization or radiobiology oriented research.

The scoring of the LET_d (ICRU 1970) was performed with external FLUKA user routines, which will be added as a standardized estimator in the future. This external routine was designed to derive the total LET_d, which takes into account the contribution from primary and secondary particles from each beam spot, calculated through scoring separately the numerator and denominator of the equation (1) from (Wilkens and Oelfke 2003):

$$L_d(z) = \frac{\sum_{i=1}^{N} \int_0^\infty S_i^2(E,z)\varphi_i(E,z)dE}{\sum_{i=1}^{N} \int_0^\infty S_i(E,z)\varphi_i(E,z)dE}, \quad (1)$$

where S_i is the is the stopping power of the beam spot i with energy E at depth z, and φ_i is a local particle spectrum of the beam spot i with energy E at depth z.

3. Results

3.1. Commissioning

Since the commissioning of the CNAO facility with FLUKA was previously performed and the related results can be found in Molinelli *et al* (2013), Mirandola *et al* (2015), Parodi *et al* (2013) and Mairani *et al* (2013), we

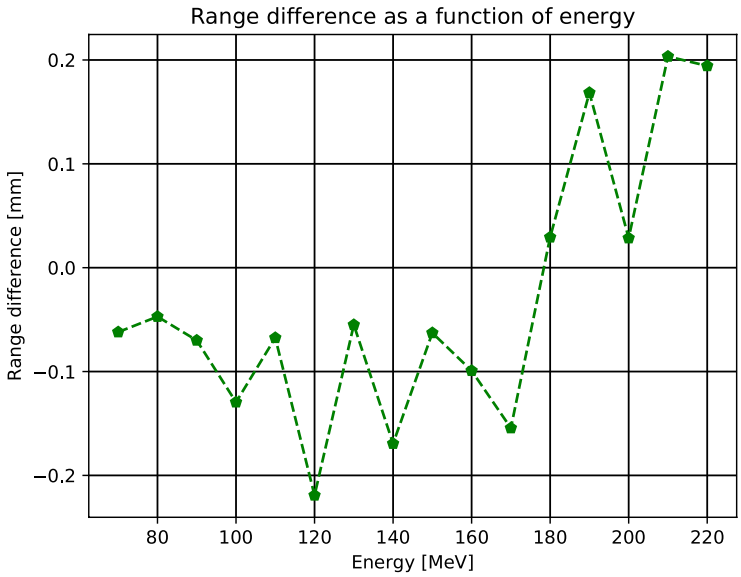

Figure 1. Comparison of measured and simulated IDD in water presented as a range difference. Lines are presented only for better readability.

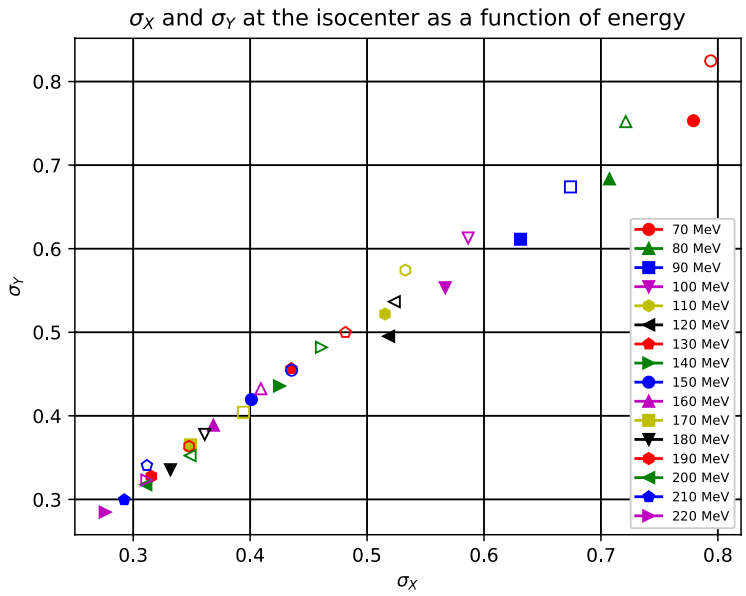

Figure 2. Comparison of σ_X and σ_Y; ●—measurements, ◯—simulations.

retrieved the required beam and calibration data. This information were directly used in FLUKA particle therapy tool for the presented CNAO clinical cases.

However, the commissioning of the Trento beam model required model validation in FLUKA. Simulations of pencil beams with selected energies showed a very good agreement with integrated depth doses (IDD) measured in water (figure 1) and Bragg peak shape. The spot size differences in air for x and y axis at the isocenter between measurements and simulations are less than 10% (figure 2), while for all five distances, the mean difference does also not exceed 10% for any of the key energies. This difference is considered to be adequate from a clinical perspective because it is comparable with the spot size fluctuations for each energy as a function of spot position and gantry angle (Schwarz *et al* 2016). Concerning the CT calibration curve, the discrepancies between the dose distributions obtained with FLUKA and the clinically used TPS were negligible, therefore it was decided not to correct and overwrite stopping powers calculated by MC. A more detailed approach would require calibration

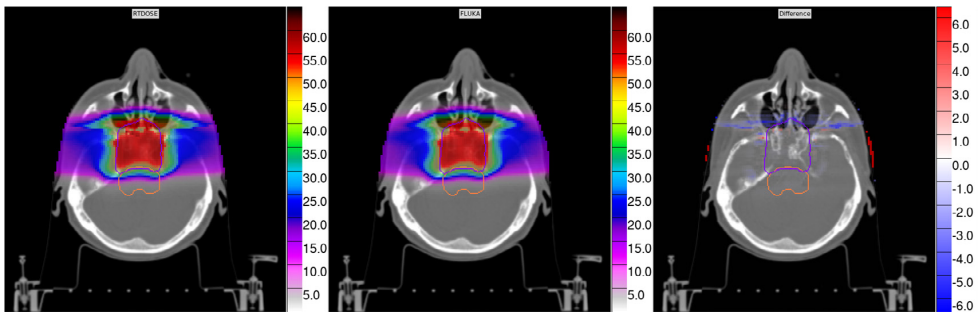

Figure 3. RTViewer representation of dose deposition for TPS (a), FLUKA (b), and Difference (FLUKA-TPS) (c) in [GyRBE] of chordoma CNAO case. Presented ROI—PTV (violet), Brainstem (orange).

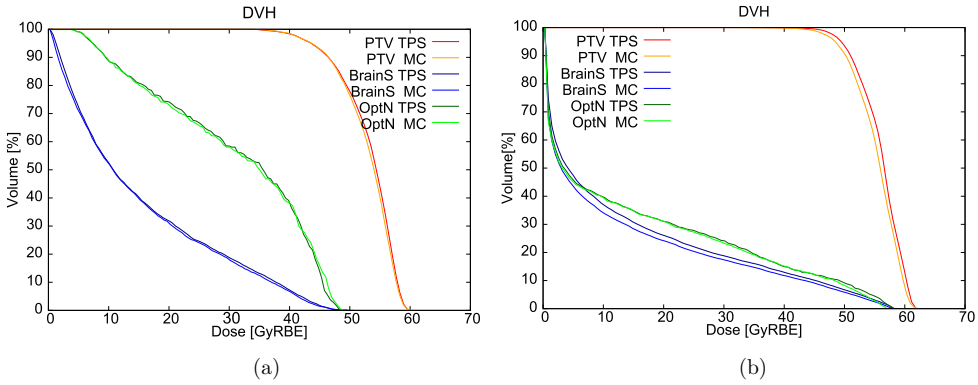

Figure 4. DVH's for TPS and MC simulations for full plans for chordoma cases. Presented OAR—brainstem (BrainS), optic nerve (OptN). (a) ChordomaCN. (b) ChordomaTR.

with a tissue characterization phantom, composed of several materials of known elemental composition and electron density.

Based on the commissioned data we tested the functionality and verified our automatized approach on the proton and carbon case presented in this article.

3.2. Application 1: patient specific treatment plan QA in particle therapy

Chordoma cases (three field arrangements): figure 3 shows the comparison of dose calculation results (at the isocenter plane) obtained with the respective clinical TPS (a), with the FLUKA particle therapy tool (b) for the clinical chordoma case at CNAO (*ChordomaCN*), as well as the absolute difference (c). As expected, for this relatively homogeneous case, a good consistency was found for dose-to-water calculation.

Figure 4 shows the corresponding DVH, and table 2 summarizes respective DVH parameters. For this chordoma case at CNAO the difference in selected DVH parameters for the PTV did not exceed 0.4% and for OAR the maximum difference of DVH parameters was 3%.

Similar results were obtained for the chordoma case at Trento proton facility (*ChordomaTR*), although these results were found to be slightly less accurate, with a difference in the DVH parameters up to 1.6% for the PTV and 4% for OAR.

Head and neck (2 fields arrangement): figure 5 shows the comparison of dose calculation results obtained with the respective clinical TPS and those obtained with the FLUKA particle therapy tool for the head and neck case at Trento proton facility, in the principal planes ((a)–(c) axial, (d)–(f) coronal, (g)–(l) sagittal) covering the isocenter. The right column figures show the absolute dose difference at the isocenter. The TPS overestimated the dose in empty cavities up to 16% and thus underestimated the particle ranges. The resulting differences in the DVH are shown in figure 6. Table 3 summarized the most essential DVH parameters. $D_{95\%}$ exceed 14% for PTV1 and $D_{95\%}$ 21% for PTV2. For OAR these values were respectively: 7% for $D_{5\%}$ at brainstem, 22% for $D_{10\%}$ at optic nerve, 8% for $D_{10\%}$ at thyroid.

Table 2. DVH evaluation for two chordoma cases [GyRBE].

		PTV		Brainstem			Optic nerve		
		$D_{5\%}$	$D_{95\%}$	$D_{5\%}$	$D_{7.5\%}$	$D_{10\%}$	$D_{5\%}$	$D_{7.5\%}$	$D_{10\%}$
ChordomaCN	TPS	58.5	43.6	42	39.8	37.8	45.5	45.7	46.4
	MC	58.3	43.7	41.3	39.3	37	46.2	46.5	46.9
ChordomaTR	TPS	60.8	49.4	53.2	48.9	45.2	54.4	51.6	49.1
	MC	60.4	48.6	52.1	47.4	43.4	53.1	50.7	48.3

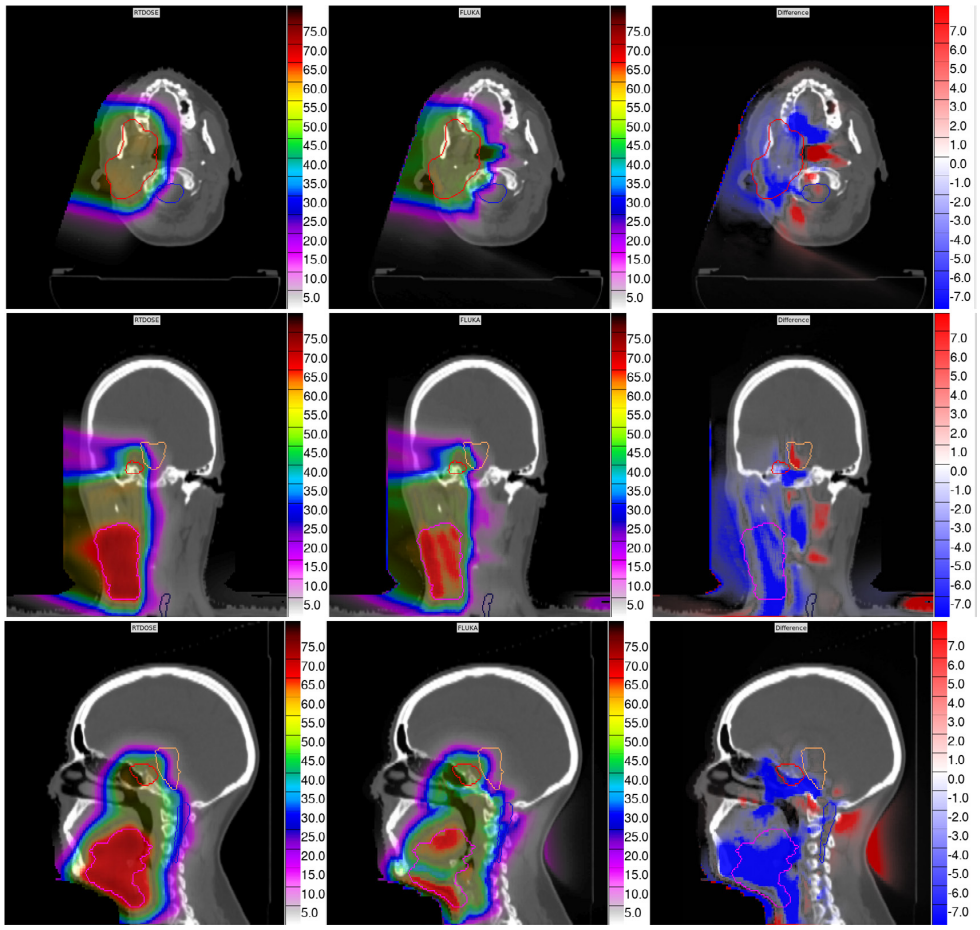

Figure 5. RTViewer representation of dose deposition for TPS, FLUKA, and Difference (FLUKA-TPS) in [GyRBE] of HeadNeckTR case in three planes (top (a)–(c)—axial, middle (d)–(f)—coronal, bottom (g)–(i)—sagittal). Presented ROI—PTV1 (red), PTV2 (pink), brainstem (orange), thyroid (dark blue), spinal cord (blue).

These significant differences were first associated with the range shifter modelling in TPS. To test this hypothesis, patient specific QA measurements were retrieved from IBA MAtriXX and compared with MC simulations performed at three depths in a homogeneous Gammex phantom: at 2 cm, 3 cm and 5 cm. The calculated doses were subsequently compared to measurements and a gamma index analysis was performed with a dose tolerance (DT) of 3%, distance-to-agreement (DTA) of 3 mm and lower dose threshold of 1% of the maximum measured dose. In case the gamma evaluation is performed with MC simulations, potential artifacts, due to statistical noise, need to be considered (Low and Dempsey 2003). The average score for gamma index analysis at all three depths and for both fields was 96%. Consequently the range shifter model used in MC was ranked as acceptable and the dose differences between MC and TPS calculations were associated rather with shortcomings of pencil beam algorithm modelling for the primary beam interaction in the range shifter and lateral inhomogeneities (Saini *et al* 2017, Widesott *et al* 2018).

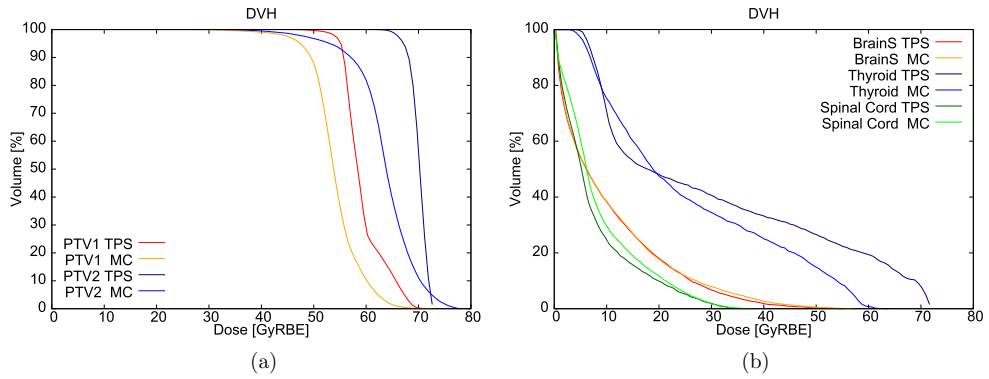

Figure 6. DVH's for HeadNeckTR case for PTVs and selected OARs. (a) PTVs. (b) OARs.

3.3. Research application 2: biological dose scoring in ion therapy

The biological dose scoring for the chordoma case treated with carbon ion therapy at CNAO is presented in figure 7. The right hand figure is the physical dose distribution after recalculation with the FLUKA particle therapy tool, while the left hand side figure shows the resulting biological dose. As mentioned previously, for the scope of this comparison the LEM I was used, as it is the standard clinical radiobiological model employed for carbon ion therapy in Europe.

The scored RBE-weighted dose was compared with the results obtained in the TPS, and good agreement is observed in 2D cross-section presented in figure 7 as well as for the DVH comparison shown in figure 8.

3.4. Research application 3: scoring of dose-averaged LET

Figure 9 shows the dose-averaged LET distribution (LET_D) in the isocenter plane of the carbon ion case, and the resulting LET_D-volume histograms (LVH). When studying the LVH the pronounced variation of the LET_D across the target and OAR can be noticed. While 95% of the PTV received values of 55 keV μm^{-1}, for the 'most exposed 5%' of the PTV volume the LET_D almost doubles to 102 keV μm^{-1}. The highest LET_D values above 100 keV μm^{-1} were found to be located at the PTV edges. For the selected OARs, i.e. brainstem and optic nerve, 10% of the respective volumes received LET_D of at least 67 keV μm^{-1} and 47.5 keV μm^{-1}.

4. Discussion

Particle therapy is a growing field within radiation oncology that faces a number of challenges. Starting from the beam delivery, passive scattering is being eclipsed by pencil beam scanning technology, for which much less experience has been gathered so far (Lomax 2008a, 2008b). The biological quantification of particle beams and the assessment of treatment plans are re-discussed, this includes the clinically used constant RBE for proton beams, as well as radiobiological models in general. In addition there is and ongoing discussion about novel ions species beyond proton and carbon ions (Mairani *et al* 2016, 2017). This manuscript illustrates the potential of the FLUKA particle therapy tool in this context, ranging from QA purposes in clinical particle therapy environment to clinical radiobiology oriented research.

The FLUKA particle therapy tool has been specifically designed to support independent dose verification for particle therapy, as a recommended part of the QA procedure (IAEA and ICRU 2007). For fluence modulated radiotherapy techniques, for both photon and particle therapy, the current best practice is to perform experimental treatment plan verification as part of the patient specific QA program. This procedure is beam time and workload intensive, and inefficient in detecting errors (Lomax *et al* 2004, Arjomandy *et al* 2010, Furukawa *et al* 2013). Thus, independent dose calculation (supported by log-file recalculations) is an alternative procedure for patient specific QA, but also for systematic investigations of dose calculation uncertainties or uncertainties in the beam model of commercial TPS based on studies using (anthropomorphic) phantom or patient cases. Modelling of the primary beam interaction within the range shifter or the poorly modelled multiple Coulomb scattering in complex geometries were identified as shortcomings of dose calculation algorithms in commercial TPS (Tourovsky *et al* 2005, Paganetti 2012, Verburg and Seco 2013, Grassberger *et al* 2014, Taylor *et al* 2017, Saini *et al* 2017, Widesott *et al* 2018).

When aiming to apply general-purpose MC codes for verifying TPS, and its integration into the clinical research, workflow is key—implying smooth and flexible data import from the TPS and imaging systems. With the proton and carbon ion therapy cases exemplified above, the FLUKA particle therapy tool demonstrated such functionality and usability in a clinical setting. The current implementation allows fast export of the TPS

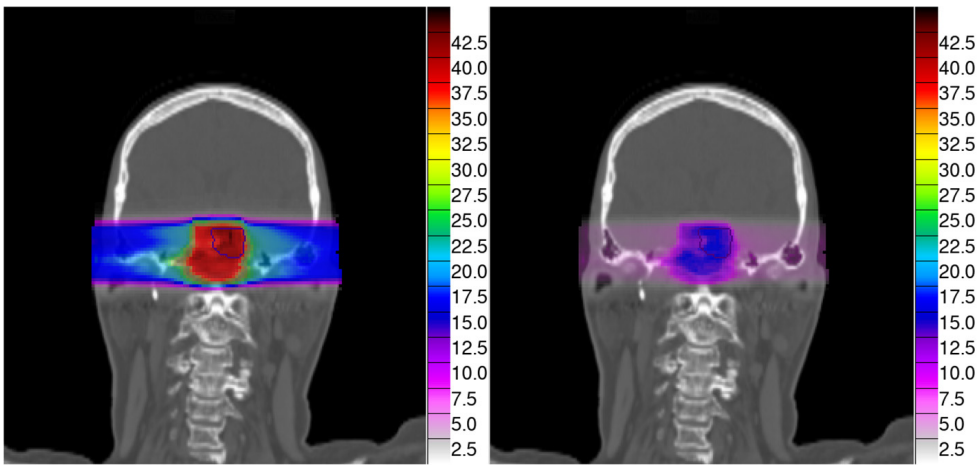

Figure 7. RTViewer representation of biological (left) and physical (right) dose deposition for FLUKA in [GyRBE]/[Gy] of carbon case. Presented ROI—PTV (dark blue).

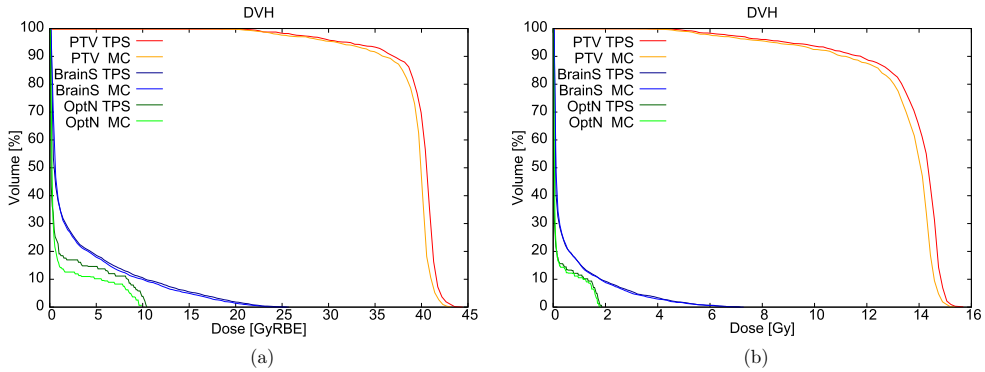

Figure 8. DVHs for carbon case for carbon ion case. (a) DVH for biological dose. (b) DVH for physical dose.

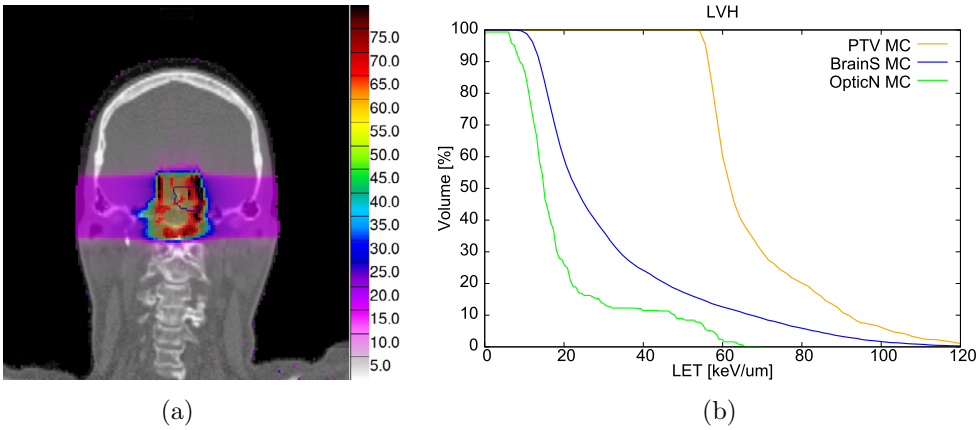

Figure 9. Dose-averaged LET scoring for carbon case. (a) RTViewer representation of LET_D (keV μm^{-1}). Presented ROI—PTV (dark blue). (b) LET_D volume histogram.

radiotherapy plan files, which was tested on two different TPSs. The Flair geometry editor allows adapting the simulations into the specific treatment scenarios, and if needed supports modelling of the range shifter, ripple filter or other devices used during treatment. Finally it is possible to export the results into DICOM standard files, readable by most clinical and research software.

Table 3. DVH evaluation for head and neck case [GyRBE].

	PTV1		PTV2	
	$D_{5\%}$	$D_{95\%}$	$D_{5\%}$	$D_{95\%}$
TPS	67.3	55.2	72.3	67.1
MC	62.2	47.4	72.5	53

	Brainstem			Thyroid			Spinal cord		
	$D_{5\%}$	$D_{7.5\%}$	$D_{10\%}$	$D_{5\%}$	$D_{7.5\%}$	$D_{10\%}$	$D_{5\%}$	$D_{7.5\%}$	$D_{10\%}$
TPS	32.8	29	26.1	70.9	70.2	68.9	25.4	22.6	19.8
MC	35.1	30.8	27.2	57.1	55.8	53.9	25.8	23.4	21.3

A limitation of some of the above-presented clinical cases, lays mostly in the not fully exploited commissioning measurements and applied simplifications. Obviously commissioning and beam modelling of the FLUKA particle tool itself has an impact on the achievable dose calculation accuracy. For example, the differences in the chordoma case from the Trento proton facility showed slightly higher differences compared to the CNAO case. This was inevitable due to less rigorous beam modelling as well as the HU-tissue calibration, which was on purpose not exploited fully to illustrate that the FLUKA particle tool can be setup easily, with acceptable results, even if the detailed geometry of the beam delivery system or the HU calibration curve is not known. Consequently, this affected insignificantly the ranges of the primary beam spots, resulting in marginally higher differences in the selected DVH for the Trento cases. On the other hand, HU calibration has also an inherent uncertainty around 2%–3% (Schuemann *et al* 2014). However, even with a rather generic HU calibration curve and no detailed beam line information the FLUKA particle therapy tool can be used for clinically motivated and oriented research.

One of these applications is the systematic exploration of helium or oxygen ions, which FLUKA can support due to its benchmarked interaction models. Especially helium ions have become a research focus during the last years and it is generally agreed that they are a promising alternative to proton therapy due to their favorable physical and biological properties (Fuchs *et al* 2015, Mairani *et al* 2016, Knäusl *et al* 2016, Tessonnier *et al* 2017a, 2017b). The versatility of FLUKA for helium ion beam research was recently demonstrated for brain and ocular meningiomas (Tessonnier *et al* 2018). Despite the promising result achieved so far, further studies for different tumor entities are still needed to investigate the clinical potential of helium ions.

Moreover, the radiobiological modelling of helium remains a major challenge in the light of the limited number of experimental data. Based on the pioneering work at the Heidelberg ion therapy facility it can be expected that other European synchrotron based particle therapy facilities will follow and more radiobiological data will become available in the coming years. Thorough benchmarking of the applied FLUKA model for RBE-weighted dose calculations based on the LEM model was already demonstrated for protons and carbon ions (Bauer *et al* 2014, Mairani *et al* 2008). The FLUKA interface for biological calculation based on the linear-quadratic (LQ) formalism allows to apply biological calculations of the plan with several different models, such as LEM IV (Elsässer *et al* 2010) and microdosimetric kinetic model (MKM) used by NIRS (National Institute for Radiological Sciences, Japan) (Magro *et al* 2017). Thus the FLUKA particle therapy tool can further serve as support for comparison between different biological models and for exploring novel ions species.

The uncertainties in radiobiological models motivated to explore the dose average LET (LET_D) as additional descriptor for characterizing dose distributions in particle beam therapy. It is well known that high-LET results in higher cell-killing per absorbed dose, and can overcome radio resistance (Schlaff *et al* 2014) of tumor cells, but it is also well known that high-LET causes higher toxicity when delivering doses with high RBE to OAR. The significant difference between the RBE-weighted DVH and LVH exemplified above in section 3.4 underlines the importance of LET assessment (Cao *et al* 2018). In the new clinical era of particle beam therapy that has been initiated with the widespread implementation of pencil beam scanning, such additional scoring of treatment plans becomes essential. The FLUKA particle therapy tool can support such clinical research related to LET_D or can be used to benchmark or validate LET calculation modules in commercial TPS.

5. Conclusion

In this study the performance of the FLUKA particle therapy tool in the clinical environment was presented. The application was tested in the scope of two different facilities and against their commissioned TPS for QA purposes, RBE-weighted dose and dose-averaged LET scoring, for proton and ion treatment plans. Presented work is encouraging and it is planned to be applied in the clinical environment in the near future.

To conclude, the FLUKA MC code using well benchmarked physics models provides good accuracy for clinical purposes, and the newly developed RTmodule in GUI Flair supports user during the simulation workflow.

FLUKA particle therapy tool is reliable and well integrated with the code itself, it allows to import data, tailor it according to the user's needs and arrange the simulation input file with no detailed knowledge of the MC code. The user can share the results and export the output for further analysis in external software. Due to its flexibility it is easily applicable also for research purposes.

Current work is focused on improving the usability of the particle therapy tool and extending the range of applications for the clinical and research environment.

Acknowledgments

W S Kozłowska acknowledge the financial support of the CERN–KT funding. C Cuccagna sincerely thanks Prof. Ugo Amaldi for support and advice.

Appendix

Biological scoring

$$-\ln(S) = \begin{cases} \alpha_D^{mixed} \cdot D + \beta_D^{mixed} \cdot D^2 & D \leqslant D_t \\ \alpha_D^{mixed} \cdot D_t + \beta_D^{mixed} \cdot D_t^2 + (D - D_t) S_{max} & D > D_t, \end{cases} \tag{A.1}$$

where α_D^{mixed} and β_D^{mixed} are dose weighted averaged for the mixed radiation field and S_{max} is $S_{max} = \alpha_X + 2\beta_X D_t$ with coefficients from table 1.

$$D_{RBE} = \begin{cases} \sqrt{-\ln(S)/\beta_X + (\alpha_X/(2\beta_X))^2} - (\alpha_X/(2\beta_X)) & -\ln(S) \leqslant -\ln(S_t) \\ (-\ln(S) + \ln(S_t))/S_{max} + D_t & -\ln(S) > -\ln(S_t) \end{cases} \tag{A.2}$$

$$RBE = D_{RBE}/D, \tag{A.3}$$

where D is the total absorbed dose (to medium or water) and $-\ln(S_t) = \alpha_X D_t + \beta_X D_t^2$

ORCID iDs

Wioletta S Kozłowska https://orcid.org/0000-0002-4899-1910
Till T Böhlen https://orcid.org/0000-0001-7408-0187
Caterina Cuccagna https://orcid.org/0000-0002-7259-4958

References

Andersen V *et al* 2004 The fluka code for space applications: recent developments *Adv. Space Res.* **34** 1302–10 (Space life sciences: radiation risk assessment and radiation measurements in low earth orbit)
Arjomandy B, Sahoo N, Ciangaru G, Zhu R, Song X and Gillin M 2010 Verification of patient-specific dose distributions in proton therapy using a commercial two-dimensional ion chamber array *Med. Phys.* **37** 5831–7
Augusto R S *et al* 2018 An overview of recent developments in FLUKA PET TOOLS *Phys. Med.* **54** 189–99
Battistoni G *et al* 2016 The FLUKA code: an accurate simulation tool for particle therapy *Frontiers Oncol.* **6**
Battistoni G, Cerutti F, Engel R, Fass A, Ferrari A, Gadioli E, Garzelli M V, Ranft J, Roesler S and Sala P R 2006 Recent Developments in the FLUKA nuclear reaction models *Proc. 11th Int. Conf. on Nuclear Reaction Mechanisms* pp 483–95
Bauer J *et al* 2014 Integration and evaluation of automated Monte Carlo simulations in the clinical practice of scanned proton and carbon ion beam therapy *Phys. Med. Biol.* **59** 4635–59
Böhlen T T, Cerutti F, Chin M, Fassò A, Ferrari A, Ortega P, Mairani A, Sala P, Smirnov G and Vlachoudis V 2014 The FLUKA code: developments and challenges for high energy and medical applications *Nucl. Data Sheets* **120** 211–4
Cao W, Khabazian A, Yepes P, Lim G, Poenisch F and Grosshans D 2018 Linear energy transfer incorporated intensity modulated proton therapy optimization *Phys. Med. Biol.* **63** 015013
Cerutti F, Battistoni G, Capezzali G, Colleoni P, Ferrari A, Gadioli E, Mairani A and Pepe A 2006 Low energy nucleus–nucleus reactions: the BME approach and its interface with FLUKA *Proc. 11th Int. Conf. on Nuclear Reaction Mechanisms (Varenna, Italy)*
Cuccagna C *et al* 2018 Beam parameters optimization and characterization for a TUrning LInac for Protontherapy *Phys. Med.* **54** 152–65
DICOM NEMA PS3 / ISO 12052 Digital Imaging and Communications in Medicine (DICOM) Standard (Rosslyn, VA: National Electrical Manufacturers Association) (http://medical.nema.org/)
Durante M and Loeffler J S 2010 Charged particles in radiation oncology *Nat. Rev. Clin. Oncol.* **7** 37–43
Elsässer T *et al* 2010 Quantification of the relative biological effectiveness for ion beam radiotherapy: direct experimental comparison of proton and carbon ion beams and a novel approach for treatment planning *Int. J. Radiat. Oncol. Biol. Phys.* **78** 1177–83
Ferrari A, Sala P, Fasso A and Ranft J 2005 FLUKA: a multi-particle transport code *Technical Report* CERN-2005-10, INFN/TC 05/11, SLAC-R-773 CERN, INFN, SLAC, Menlo Park, CA
Fracchiolla F, Lorentini S, Widesott L and Schwarz M 2015 Characterization and validation of a Monte Carlo code for independent dose calculation in proton therapy treatments with pencil beam scanning *Phys. Med. Biol.* **60** 8601–19
Fuchs H, Alber M, Schreiner T and Georg D 2015 Implementation of spot scanning dose optimization and dose calculation for helium ions in Hyperion *Med. Phys.* **42** 5157–66
Furukawa T, Inaniwa T, Hara Y, Mizushima K, Shirai T and Noda K 2013 Patient-specific QA and delivery verification of scanned ion beam at NIRS-HIMAC Patient-specific quality assurance method for VMAT treatment delivery Patient-specific QA and delivery verification of scanned ion beam at NIRS-HIMAC *Med. Phys.* **40** 121707–4530

Grassberger C, Daartz J, Dowdell S, Ruggieri T, Sharp G and Paganetti H 2014 Quantification of proton dose calculation accuracy in the lung *Int. J. Radiat. Oncol. Biol. Phys.* **89** 424–30
Grevillot L, Bertrand D, Dessy F, Freud N and Sarrut D 2012 GATE as a GEANT4-based Monte Carlo platform for the evaluation of proton pencil beam scanning treatment plans *Phys. Med. Biol.* **57** 4223–44
Hong L, Goitein M, Bucciolini M, Comiskey R, Gottschalk B, Rosenthal S, Serago C and Urie M 1970 A pencil beam algorithm for proton dose calculations *Phys. Med. Biol.* **217** 1305–30
IAEA and ICRU 2007 IAEA-TECDOC-1560. Dose reporting in ion beam therapy *Proc. of a Meeting Organized Jointly by IAEA and ICRU, Inc. (Ohio, USA, March 2006)* pp 18–20
ICRU 1970 Report 16. Linear Energy Transfer *J. Int. Comm. Radiat. Units Meas.* **os9**
Jäkel O, Karger C P and Debus J 2008 The future of heavy ion radiotherapy *Med. Phys.* **35** 5653–63
Knäusl B, Fuchs H, Dieckmann K and Georg D 2016 Can particle beam therapy be improved using helium ions? A planning study focusing on pediatric patients *Acta Oncol.* **55** 751–9
Krämer M and Scholz M 2006 Rapid calculation of biological effects in ion radiotherapy *Phys. Med. Biol.* **51** 1959–70
Lomax A J 2008a Intensity modulated proton therapy and its sensitivity to treatment uncertainties 1: the potential effects of calculational uncertainties *Phys. Med. Biol.* **53** 1027–42
Lomax A J 2008b Intensity modulated proton therapy and its sensitivity to treatment uncertainties 2: the potential effects of inter-fraction and inter-field motions *Phys. Med. Biol.* **53** 1043–56
Lomax A J *et al* 2004 Treatment planning and verification of proton therapy using spot scanning: Initial experiences *Med. Phys.* **31** 3150–7
Low D A and Dempsey J F 2003 Evaluation of the gamma dose distribution comparison method *Med. Phys.* **30** 2455–64
Magro G, Dahle T J, Molinelli S, Ciocca M, Fossati P, Ferrari A, Inaniwa T, Matsufuji N, Ytre-Hauge K S and Mairani A 2017 The FLUKA Monte Carlo code coupled with the NIRS approach for clinical dose calculations in carbon ion therapy *Phys. Med. Biol.* **62** 3814–27
Mairani A, Böhlen T T, Schiavi A, Tessonnier T, Molinelli S, Brons S, Battistoni G, Parodi K and Patera V 2013 A Monte Carlo-based treatment planning tool for proton therapy *Phys. Med. Biol.* **58** 2471–90
Mairani A, Brons S, Cerutti F, Fassò A, Ferrari A, Krämer M, Parodi K, Scholz M and Sommerer F 2010 The FLUKA Monte Carlo code coupled with the local effect model for biological calculations in carbon ion therapy *Phys. Med. Biol.* **55** 4273–89
Mairani A *et al* 2017 A phenomenological relative biological effectiveness approach for proton therapy based on an improved description of the mixed radiation field *Phys. Med. Biol.* **62** 1378–95
Mairani A *et al* 2016 Biologically optimized helium ion plans: calculation approach and its *in vitro* validation *Phys. Med. Biol.* **61** 4283–99
Mairani A, Parodi K, Brons S, Cerutti F, Ferrari A, Gadioli E, Scholz M and Sommerer F 2008 Clinical calculations of physical and biological effective dose distributions in proton and carbon ion therapy using the FLUKA Monte Carlo code *2008 IEEE Nuclear Science Symp. Conf. Record* (IEEE)
Mirandola A *et al* 2015 Dosimetric commissioning and quality assurance of scanned ion beams at the Italian National Center for Oncological Hadrontherapy *Med. Phys.* **42** 5287–300
Molinelli S, Mairani A, Mirandola A, Freixas G V, Tessonnier T, Giordanengo S, Parodi K, Ciocca M and Orecchia R 2013 Dosimetric accuracy assessment of a treatment plan verification system for scanned proton beam radiotherapy: one-year experimental results and Monte Carlo analysis of the involved uncertainties *Phys. Med. Biol.* **58** 3837–47
Paganetti H 2012 Range uncertainties in proton therapy and the role of Monte Carlo simulations *Phys. Med. Biol.* **57** 1199–11117
Parodi K, Mairani A and Sommerer F 2013 Monte Carlo-based parametrization of the lateral dose spread for clinical treatment planning of scanned proton and carbon ion beams *J. Radiat. Res.* **54** i91–6
Parodi K, Mairani A, Brons S, Hasch B G, Sommerer F, Naumann J, Jäkel O, Haberer T and Debus J 2012 Monte Carlo simulations to support start-up and treatment planning of scanned proton and carbon ion therapy at a synchrotron-based facility *Phys. Med. Biol.* **57** 3759–84
Rogers D 2006 Fifty years of Monte Carlo simulations for medical physics *Phys. Med. Biol.* **51** R287–R301
Saini J, Maes D, Egan A, Bowen S R, St James S, Janson M, Wong T and Bloch C 2017 Dosimetric evaluation of a commercial proton spot scanning Monte-Carlo dose algorithm: Comparisons against measurements and simulations *Phys. Med. Biol.* **62** 7659–81
Schlaff C D, Krauze A, Belard A, O'Connell J J and Camphausen K A 2014 Bringing the heavy: carbon ion therapy in the radiobiological and clinical context *Radiat. Oncol.* **9** 88
Schneider W, Bortfeld T and Schlegel W 2000 Correlation between CT numbers and tissue parameters needed for Monte Carlo simulations of clinical dose distributions *Phys. Med. Biol.* **45** 459–78
Scholz M, Kellerer A M, Kraft-Weyrather W and Kraft G 1997 Computation of cell survival in heavy ion beams for therapy: The model and its approximation *Radiat. Environ. Biophys.* **36** 59–66
Schuemann J, Dowdell S, Grassberger C, Min C H and Paganetti H 2014 Site-specific range uncertainties caused by dose calculation algorithms for proton therapy *Phys. Med. Biol.* **59** 4007–31
Schwarz M, Algranati C, Widesott L, Farace P, Lorentini S, Righetto R, Ravanelli D and Fracchiolla F 2016 Clinical pencil beam scanning: present and future practices *Particle Radiotherapy* (New Delhi: Springer India) pp 95–110
Taylor P A, Kry S F and Followill D S 2017 Pencil beam algorithms are unsuitable for proton dose calculations in lung *Int. J. Radiat. Oncol. Biol. Phys.* **99** 750–6
Tessonnier T, Böhlen T T, Ceruti F, Ferrari A, Sala P, Brons S, Haberer T, Debus J, Parodi K and Mairani A 2017a Dosimetric verification in water of a Monte Carlo treatment planning tool for proton, helium, carbon and oxygen ion beams at the Heidelberg ion beam therapy center *Phys. Med. Biol.* **62** 6579–94
Tessonnier T, Mairani A, Brons S, Haberer T, Debus J and Parodi K 2017b Experimental dosimetric comparison of 1 H, 4 He, 12 C and 16 O scanned ion beams *Phys. Med. Biol.* **62** 3958–82
Tessonnier T, Mairani A, Chen W, Sala P, Cerutti F, Ferrari A, Haberer T, Debus J and Parodi K 2018 Proton and helium ion radiotherapy for meningioma tumors: a Monte Carlo-based treatment planning comparison *Radiat. Oncol.* **13** 1–10
Tourovsky A, Lomax A J, Schneider U and Pedroni E 2005 Monte Carlo dose calculations for spot scanned proton therapy *Phys. Med. Biol.* **50** 971–81
Verburg J M and Seco J 2013 Dosimetric accuracy of proton therapy for chordoma patients with titanium implants *Med. Phys.* **40** 071727
Vlachoudis V 2009 FLAIR: a powerful but user friendly graphical interface for FLUKA *Proc. Int. Conf. on Mathematics, Computational* pp 1–11
Vlachoudis V and Sinuela-Pastor D 2014 Numerically robust geometry engine for compound solid geometries *SNA + MC 2013—Joint Int. Conf. on Supercomputing in Nuclear Applications + Monte Carlo* pp 1–6
Widesott L, Lorentini S, Fracchiolla F, Farace P and Schwarz M 2018 Improvements in pencil beam scanning proton therapy dose calculation accuracy in brain tumor cases with a commercial Monte Carlo algorithm *Phys. Med. Biol.* **63** 145016
Wilkens J J and Oelfke U 2003 Analytical linear energy transfer calculations for proton therapy *Med. Phys.* **30** 806–15

Chapter 4

Development of a radiobiological model BIANCA

This Chapter presents an overview of recent developments and benchmark studies for the BIANCA radiobiological model. It is based on the article *First benchmarking of the BIANCA model for cell survival prediction in a clinical hadron therapy scenario*, published in *Physics in Medicine and Biology* 64 215008; 2019, by following authors:

Mario P. Carante[1,2], Giulia Aricò [3], Alfredo Ferrari[3], **Wioletta Kozłowska[3,5]**, Andrea Mairani[6,7], Francesca Ballarini[1,2]

and article *In vivo validation of the BIANCA biophysical Model: Benchmarking against Rat Spinal Cord RBE data* , published in *International Journal of Molecular Sciences* 21; 2020 by the following authors:

Mario P. Carante[1,2], Giulia Aricò [3], Alfredo Ferrari[3], Christian P. Karger[4], **Wioletta Kozłowska[3,5]**, Andrea Mairani[6,7], Paola R. Sala[8], Francesca Ballarini[1,2]

[1] INFN, Sezione di Pavia, Italy; [2] Physics Department, University of Pavia, Italy;
[3] CERN – European Organization for Nuclear Research, Switzerland;
[4] Department of Medical Physics in Radiation Oncology, DKFZ, Germany;
[5] Medizinische Universität Wien, Austria; [6] CNAO, Italy; [7] Heidelberg Ion-Beam Therapy Center, Germany;
[8] INFN, Sezione di Milano, Italy

Wioletta Kozłowska Contribution: Integration of the BIANCA model with the FLUKA MC code and FLUKA Particle Therapy Tool, as presented in detail in Section 4.4. Extension of the BIANCA model to different cells of interest, validation, and benchmarking of the BIANCA model against experimental data and comparison with clinical radiobiological models using FLUKA simulations, as presented in Section 4.5.

4.1 Introduction

BIANCA (BIophysical ANalysis of Cell death and chromosome Aberrations) [296] is a biophysical model that models cell death and chromosome damage caused by different charged particles used in hadrontherapy, such as protons, helium ions (He-ions), and carbon ions (C-ions). The initial BIANCA model was specific to radiation-induced chromosomal aberrations [275, 297, 298] and was later extended to the prediction of cell death [18, 102, 155, 296, 299, 300]. Implementation of the BIANCA model is based on a Monte Carlo (MC) code, which links the amount of energy deposited in the cell nucleus by different ion types to damage cell DNA, chromosome aberrations, and eventually, cell death. The biophysical properties of various cells are described using two adjustable BIANCA parameters.

Recently, with increased interest in other ion species in radiation therapy, the BIANCA model has been expanded to oxygen ions (O-ions). The upgraded model was benchmarked against experimental data on the LET-dependence of RBE for reference V79 cells irradiated by ions with Z in the range from 1 to 8. A reference database of V79 cells is the basis for the creation of other RBE databases for various cell lines of interest. Another significant milestone was achieved by integrating the BIANCA model with FLUKA MC code [13, 16, 61, 301]. This integration allowed the performance of benchmarking studies for the BIANCA model in clinically relevant scenarios. In one of the presented studies, two opposing fields of corresponding range beams of protons or C-ions were simulated in FLUKA, and cell survival rates were calculated using the integrated BIANCA model. The obtained results were then compared with experimental data from HIT, as presented by Elsässer *et al* [26].

Further work evaluated the performance of the BIANCA model against radiobiological experimental data for the rat spinal cord after C-ion and proton irradiation [32]. The rat spinal cord model is a well-established standard for investigating late reactions of the central nervous system (CNS)[302] because human-based data for CNS radiation tolerance are scarce. For skull based tumors treatment, this is a major biological end-point and critical dose limit. Rat spinal cord data were applied to determine RBE values for C-ions [27, 29, 31, 30] and proton therapy [32] and were employed for the LEM I model and the more recent LEM IV [26] model.

4.2 The BIANCA model

As previously mentioned, the BIANCA model is implemented in the form of Monte Carlo code. The subsequent sections provide an overview of recent developments in the BIANCA model. A more detailed discussion of the assumptions used for the BIANCA model can be found in [18, 296]; only a few key issues are presented in this Chapter.

In Chapter 1, Section 1.3 discusses the impact of ionizing radiation on biological materials. It was mentioned that, with a certain probability, ionizing radiation can cause severe damage to the double helix of a cell's DNA, producing two independent chromosome fragments. This type of damage, by definition, is called a Critical Lesion (CL). CLs are likely to be double-strand break (DSB) clusters [303], but their detailed features remain an open question in radiobiological research. Therefore, no theoretical definition of critical lesions was presented in this study. CL yield expresses the amount of initial damage, with respect to their severity and biological impact, which causes the chromosome to break into two large (visible in metaphase)

independent chromosome fragments. The CL yield is defined as the mean number of CLs per Gy per cell, and in the case of ions, it is converted into CLs per unit length of the particle track. The resulting chromosome fragment joining can lead to lethal or non-lethal chromosomal aberrations. CL yield is highly dependent on the radiation type and particle energy, as well as biological criteria, such as cell-specific repair proficiency. It increases within LET (up to a certain level, when the overkill effect starts to manifest itself), and with cell radiosensitivity. The CL yield value affects the absolute number of surviving cells at various doses without modulating the shape of the survival curve. In the BIANCA model, CL yield is the first adjustable parameter.

An independent chromosome fragment, created by CL, will then attempt to reconnect (end-join) with another fragment. Two chromosome free ends with an initial distance smaller than d will undergo end-joining with a certain probability, whereas two fragments with an initial distance larger than d will never undergo end-joining. This process is well described by a step function with a threshold distance d defined as the mean distance between two adjacent chromosome territories. Not all chromosome fragments located within a threshold distance d from each other undergo a re-joining process, and with a certain probability f, some fragments might remain unrejoined. Probability f is not dependent on the particle type and energy; however, it is determined by the cell line characteristics. More radiosensitive cells present a higher probability of remaining unrejoined chromosome fragments than normal radioresistant cells. Probability f is the last modifiable parameter of the BIANCA model. The step function, which describes the rejoining process, works well for predicting cell death [20, 102, 155, 156, 296]. On the other hand, if the aim is to distinguish between different chromosome aberration types, recent works have proposed an exponentially decreasing function. In particular, this function has been proven to differentiate well between inter- and intra-arm exchanges [304, 305], leading to potential lethal aberrations.

Subsequently, the ratio between lethal and non-lethal chromosomal aberrations was determined based on experimental observations. It defines the ratio between the logarithm of the surviving fraction and the mean number of lethal aberrations per cell (i.e., dicentrics, rings, and deletions) visible during metaphase [306, 307].

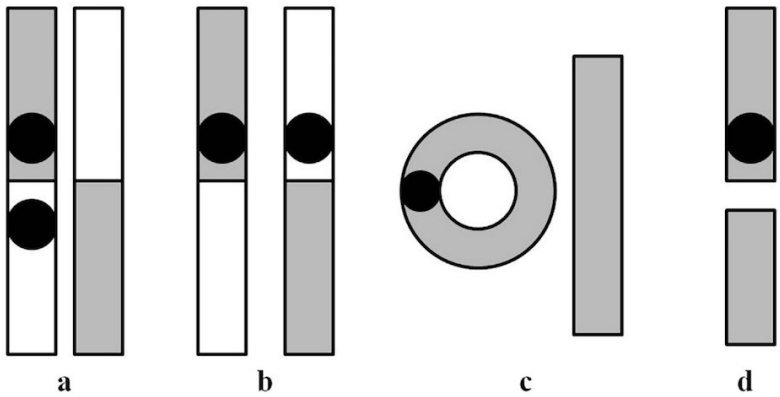

Figure 4.1: Chromosome aberration schematic (a) dicentric, (b) translocation, (c) centric ring, (d) terminal deletion. *Reprinted from [18].*

Simulations of chromosome aberrations in the BIANCA model [156, 296, 308] require several initial parameters, describing the cell specification, CL yield, f parameter, cell nucleus size and shape (spherical or cylindrical), irradiation parameters - particle species (photons, light ions, or heavy ions), LET, and finally an absorbed dose. The simulation model defines a chromosome territory as an (irregular) intranuclear region composed of a set of cubic voxels allocated within the cell nucleus. Extracting the value of CLs for each cell depends on the radiation type. If the cell is irradiated with a given dose of photons, CLs are evenly distributed in the cell nucleus, and the exact number of CLs is determined by the Poisson distribution. However, if the cell is irradiated with a given dose by a certain ion type of a specified LET, first, the number of particles travelling through the cell nucleus is extracted from the Poisson distribution, and the exact number of CLs is derived from the Poisson distribution for each traversing primary ion. Depending on the ion type, CLs are allocated either along the straight line of the traversing particle path (proton and He-ions) or within a certain radial distance from the primary-ion trajectory. This takes into account that half of the deposited energy originates from interactions taking place along the main particle path, whereas the second half is derived from ionization induced by $\delta - rays$, found mainly in the penumbra [309].
In the final step, the position of each CLs, is determined and compared with the coordinates of the voxels representing the chromosome territory. After defining chromosomes and chromosome arms hit by CLs, end-joining or un-rejoining fragments are simulated to estimate the surviving fraction. Lethal aberrations are identified and accounted for cell death; otherwise, the cell is marked as surviving. MC simulations for the BIANCA model are performed for all considered dose levels to obtain dose-response curves for cell death and aberrations, and they are repeated until a certain statistical significance is obtained. More detailed information regarding simulations of interphase chromosome territories and arm domains can be found in Tello *et al* [304, 305].

4.3 BIANCA database for different ions and cell types

4.3.1 RBE calculation for different ion types

In recent years, the BIANCA model has been shown to be capable of reproducing experimental survival curves for V79 and AG01522 cells irradiated by monochromatic protons, C-ions, or He-ion beams [156]. This section presents a summary of a method used for the adjustment of the CL yield parameter to extend the BIANCA model for the new ion type - oxygen (O-ion). More detailed information and a more profound discussion of these results can be found in the original version of the article [20].
Simulated survival curves for oxygen irradiation were benchmarked against experimental data for V79 data from Stoll *et al* [19]. As the un-rejoining probability parameter f is not dependent on the radiation type, it was fixed to 0.08 value, hence the CL yield was the only adjusted parameter.
Figure 4.2 shows the BIANCA simulation results for V79 cells obtained for five O-ion beam exposures with LET values of 18, 46, 238, 276, and 754 keV/μm, and compared with the experimental data from Stoll *et al* [19]. It can be noticed that the mean number of CLs per unit track length [CL/μm], for O-ions is comparable to the C-ion results presented in [156] for the same LET values. As shown in Table 4.1, the presented ion species demonstrate a similar LET dependence; higher LET values lead to an increase in CL yield.
Although the mean number of CLs per unit dose and DNA mass [$CL \cdot Gy^{-1} \cdot cell^{-1}$], reached a maximum

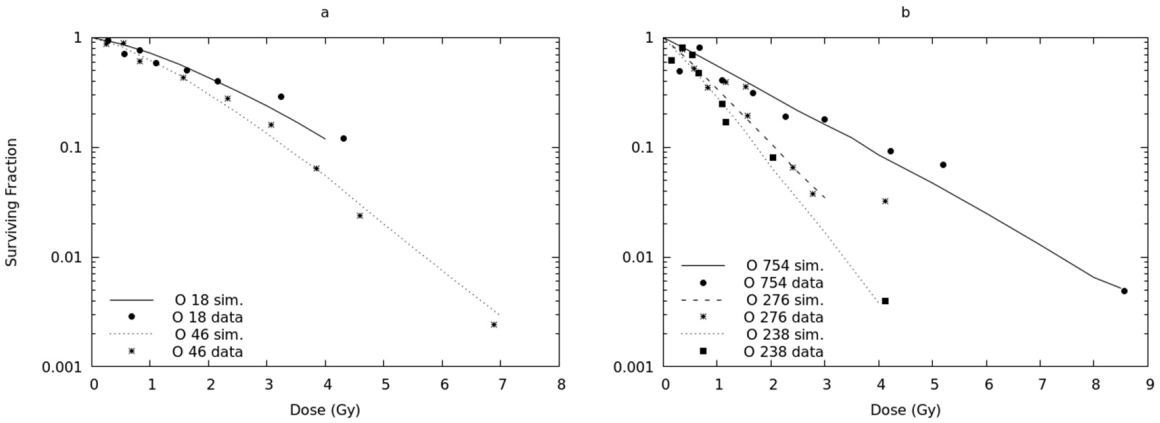

Figure 4.2: Survival of V79 cells exposed to O-ion beams of 18, 46 keV/μm (a), 238, 276, 754 keV/μm (b). Lines are the simulation outcomes, and points are the experimental data [19]. *Published in [20].*

Ion	**18 keV/μm**	**46 keV/μm**	**238 keV/μm**	**276 keV/μm**	**754 keV/μm**
O-ion	0.009	0.031	0.389	0.384	0.678
C-ion	0.007	0.034	0.343	0.385	0.657

Table 4.1: CL yield expressed as mean number of CLs/μm for O-ion and C-ion at different LET values. *Published in [20].*

value at 238 keV/μm, and a further decrease for higher LET, as expected for RBE (see figure 4.3(b)), a similar situation was also found for C-ions [156]. The difference between the LET-dependence curves of CL/μm and $CL \cdot Gy^{-1} \cdot cell^{-1}$ is related by the following Equation:

$$\frac{CL}{Gy \cdot cell} = 6.25 \cdot \frac{CL}{\mu m} \cdot \frac{V}{L}, \tag{4.1}$$

where L is the LET [keV/μm], and V is the cell nucleus volume [μm^3].

After adjustment of the CL yield to selected LET values, it is possible to fit the LET-dependence curve to the CL yield for the selected ion type, resulting in a full prediction of cell survival dose-response for, in theory, any LET value and any particle involved in the irradiation process.

Simulation of the BIANCA model for V79 cells irradiated by protons, He-ions, and C-ions of different LET values estimated the full survival curves for these three ion species for different LET values. For protons (LET: 2.5-30 keV/μm), 12 survival curves were created for He-ions (LET: 5-90 keV/μm) 18 curves, and 29 curves for C-ions (LET: 10-500 keV/μm). The linear and quadratic coefficients of the Linear Quadratic Model (LQM) (see Equation 1.29) were fitted for each survival curve. Subsequently, the following expression provides a means of calculating the RBE values for different ions at different LET values [73]:

$$RBE = \frac{2\beta_i \left[-\alpha_X + \sqrt{\alpha_X^2 - 4\beta_X lnS}\right]}{2\beta_X \left[-\alpha_i + \sqrt{\alpha_i^2 - 4\beta_i lnS}\right]}, \tag{4.2}$$

where α_X and β_X are photon coefficients, α_i and β_i are ion coefficients (at a given LET), and S is the chosen

survival level.

Below, a short overview of the benchmarking results for RBE prediction with different ion types for V79 cells is presented. Although the BIANCA application reported in Chapter 5 is concentrated on C-ion treatments, proper evaluation of ions with $Z < 6$ is essential to account for the biological impact of all ion fragments created during irradiation.

A comparison between the BIANCA model and experimental data for the RBE at 10% survival ($RBE_{10\%}$) for V79 cells is presented in Figure 4.3. Figure 4.3 (a) represents BIANCA predictions for protons and He-ions (line) compared to experimental data from [21, 22] (protons), and data from [23] (He-ions represented as He-3), plus the Li-7 point taken from [24]. Regarding heavier ions, Fig 4.3 (b) shows BIANCA predictions for C-ions benchmarked against experimental C-ion data from [23], as well as O-ion points [19], B-ion points [25], and N-ion point [25].

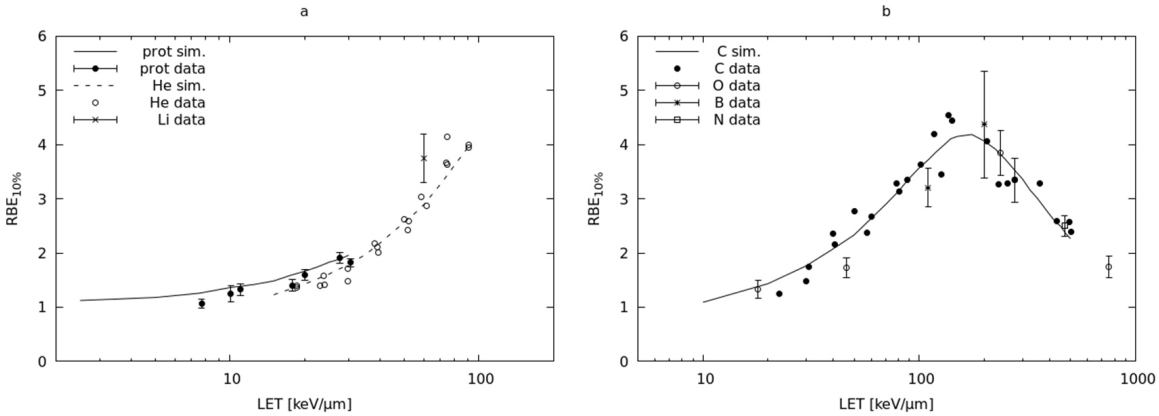

Figure 4.3: $RBE_{10\%}$ for V79 exposed to: (a) protons and He-ions with data for protons [21, 22], He-ions [23], Li-ion [24]. (b) C-ions with data points for C-ions [23], O-ions [19], B-ions [25], N-ions [25]. Error bars, represent one s.d. *Published in [20].*

In general, the BIANCA model predictions for $RBE_{10\%}$ for V79 cells well reproduced the LET-dependence curve, and the results were in good agreement with the data for protons and He-ions, as well as C-ions. The presented results suggest that the BIANCA model can also be applied to ions with *Z=5*, *Z=8*, and *Z=7*, which is expected to have an in-between behaviour of *Z=6* and *Z=8*.

Benchmarking studies were also performed for 50% survival ($RBE_{50\%}$). Figure 4.4 (a) presents the results for light ion irradiation and figure 4.4 (b) for heavy ion irradiation of the V79 cells. The same experimental data, as mentioned above, were used for comparison with BIANCA predictions.

It can be observed that the effectiveness of the proton beam at approximately 30 keV/μm is underestimated by the BIANCA model. The reason of the mentioned above underestimation, can be explained by the overestimation of the surviving cells at low doses. This expected behaviour of the BIANCA model, discussed further in Carante el al. [156], is most likely related to the selection of the step function, which describes the probability of chromosome fragment rejoining. Aside from this exception, light-ion predictions were in good agreement with the data, which proved that BIANCA is able to reproduce the $RBE_{50\%}$ for V79 cells irradiated by protons, He-ions, and ions with *Z=3*with high probability. This limitation was not found for

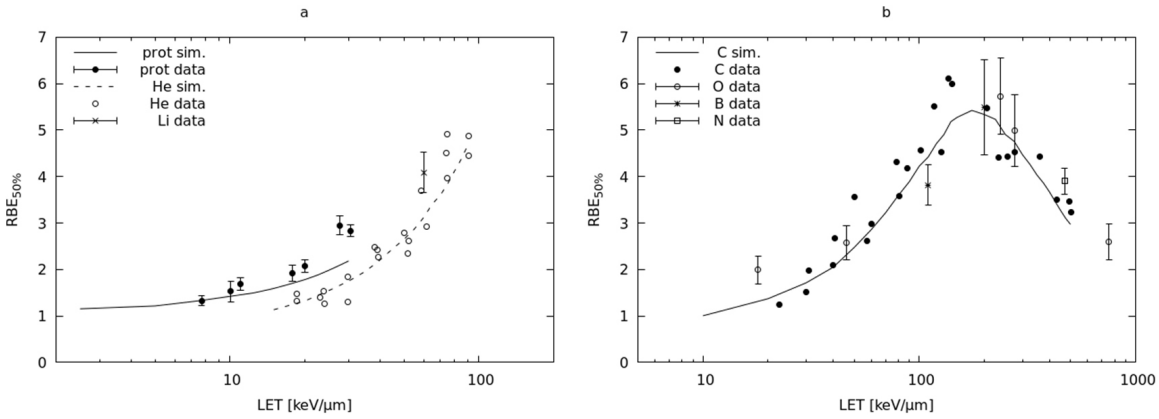

Figure 4.4: $RBE_{50\%}$ for V79 exposed to: (a) protons and He-ions with data for protons [22, 21], He-ions [23], Li-ion [24]. (b) C-ions with data points for C-ions [23], O-ions [19], B-ions [25], N-ions [25]. The error bars, represent one s.d. *Published in [20].*

$RBE_{10\%}$, where higher doses were applied, and it can be stated that these LET values for low doses are not likely to have a significant role in proton therapy, including in the distal region of the SOBP. In terms of the C-ion beams for $RBE_{50\%}$ predictions, good agreement was achieved with the BIANCA model. The presented results suggest that C-ion estimations can also be used for prediction with ions *Z=5*, *Z=8*, and *Z=7*.

4.3.2 RBE calculation for chosen cell lines

BIANCA model assumptions consider the CL yield parameter as dependent not only on radiation quality (i.e., particle type and energy) but also on the target tissue characteristics. The BIANCA model operates independently on databases created for separate cell lines. This section presents a formula used to predict the survival of the chosen cell line after ion irradiation. The formula uses parameters of the ion survival of a known cell line and photon responses for known/referenced and newly selected cell lines. The formula is based on the work presented by Carante *et al* [156], where this approach was proven to reproduce the survival of AG01522 and U87 cells irradiated by proton beams with different LET.
The CL yield for a selected cell line irradiated with beams of a specified quality is calculated as follows:

$$\frac{CL}{\mu m} = \left(\frac{CL}{\mu m}\right)_{ref} \cdot \left[\left(\frac{CL}{Gy \cdot cell}\right) / \left(\frac{CL}{Gy \cdot cell}\right)_{ref}\right] \cdot \frac{V_{ref}}{V}, \tag{4.3}$$

where $CL/\mu m$ is the CL yield for a selected cell line, $(CL/\mu m)_{ref}$ is the CL yield of the known cell line, both of which are exposed to identical radiation quality. $(CL \cdot Gy^{-1} \cdot cell^{-1})$ and $(CL \cdot Gy^{-1} \cdot cell^{-1})_{ref}$ are the photon irradiation related CL yields used for the cell line of interest and the reference cell line, respectively. The cell parameters are described by V_{ref} and V, which define the nucleus volume of the known and selected cell lines, respectively.
Chinese Hamster Ovary (CHO) cells were selected as the first cell line of interest. The experimental data used to adjust the BIANCA model were based on the photon CHO survival curve presented by Elsässer *et al*

[26]. BIANCA parameters were fitted to the LQM with $\alpha = 0.105\ Gy^{-1}$ and $\beta = 0.025\ Gy^{-2}$. The CL yield value for photon CHO survival was fixed at 1.2 $CL \cdot Gy^{-1} \cdot cell^{-1}$ and an unrejoining parameter f at 0.08. The reference cell line, V79, was considered to have the same cell nucleus volume as the CHO cells. The obtained parameters were further applied to Equation 4.3 to derive the CL yields of CHO cells exposed to different ion types and energies. Subsequently, CHO survival curves were created using obtained CL yields, for various monochromatic beams (12 proton beams with LET = 2.5-30.0 keV/μm, 18 He-ion beams with LET = 5-90 keV/μm, and 29 C-ion beams with LET = 10-500 keV/μm). Every survival curve was then fitted to the LQM, obtaining linear α and quadratic β coefficients for different ion types and LET values. The simplified approach used the He-ion coefficient for ions with *Z=3*, whereas for *Z=4*, *Z=5*, *Z=7*, and *Z=8* coefficients derived for C-ions were applied.

4.4 BIANCA and the FLUKA Monte Carlo code

The created BIANCA database tables were applied to the FLUKA Monte Carlo code. Two FLUKA code versions were used for the benchmarking studies presented in Section 4.5: the development version 2018.1 (for two-field irradiation of CHO cells) and the release version 2020.0 [310] (for rat spinal cord simulations). FLUKA simulations used the predefined settings option, PRECISIOn. C-ion simulations required launching coalescence and evaporation functions, as well as linking the external event generator - Relativistic Quantum Molecular Dynamic (RQMD-2.4, Section 2.2.4) for accurate modelling of nucleus-nucleus collisions above 125 MeV/n. FLUKA calculated the required data, that is: particle species and energy, and deposited the dose within target voxels. During simulations, when a particle deposits a certain amount of energy in a voxel, FLUKA reads the referenced α and β coefficients from the BIANCA database based on the particle type and its LET value. Subsequently, considering the effects of mixed radiation fields and with respect to the Theory of Dual Radiation Action [276], the mean value of α and the mean value of β in the target voxel are calculated as described by Mairani *et al* [73], that is:

$$\alpha_D^{mix} = \frac{\sum_{i=1}^{n} \alpha_i D_i}{\sum_{i=1}^{n} D_i} \tag{4.4}$$

$$\sqrt{\beta_D^{mix}} = \frac{\sum_{i=1}^{n} \sqrt{\beta_i} D_i}{\sum_{i=1}^{n} D_i}, \tag{4.5}$$

where D_i is the absorbed dose within the voxel deposited by the i-th particle, α_i and β_i are the corresponding radiobiological coefficients from the BIANCA database, and α_D^{mix} and β_D^{mix} are their mean values. The survival level, RBE-weighted dose, and RBE values were calculated using the following equations:

$$-lnS = \alpha_D^{mix} \cdot D + \beta_D^{mix} \cdot D^2, \tag{4.6}$$

$$D_{RBE} = \left(\sqrt{\alpha_X^2 - 4\beta_X \cdot lnS} \right) / 2\beta_X - \alpha_X / (2\beta_X), \tag{4.7}$$

$$RBE = \frac{D_{RBE}}{D}, \tag{4.8}$$

where α_X and β_X are photon parameters reported by BIANCA.

4.5 BIANCA benchmarking

4.5.1 Two opposed field irradiation

For this study, an experiment, as described by Elsässer *et al* [26], was modelled and simulated using the BIANCA model integrated with the FPTT. Elsässer *et al* [26] reported irradiation experiments performed at HIT with CHO cells, which used two opposed beam fields, as typically found in a clinical scenario. Before the experiment, the target CHO cells were grown on plastic plates. Immediately before irradiation, they were inserted into an acrylic glass container ($5 \times 10 \times 16 cm^3$) with a 5 mm distance between the plates. Two particle types were used for the opposed-field irradiation: protons (with energies of 90-120 MeV), and C-ions (with energies of 175-230 MeV/n). Treatment plan, performed with TRiP98 TPS [311] and LEM I model, used prescription for 5.3 Gy (with protons) or 3.9 Gy (with C-ions) delivered to the target region, while preserving 1.5 Gy in the entrance channel for both particle irradiations. The main goal was to obtain a homogeneous cell survival level in the 4 cm wide target, located between 6 and 10 cm water-equivalent depth. More information regarding the experiment can be found in Elsässer *et al* [26], which also presents the outcome of LEM IV cell survival predictions.

The simulations performed in FLUKA modelled the experimental setup. The beam data model, derived from HIT, was used to describe the irradiation beam parameters: a C-ion beam in the energy range of 175-230 MeV/n, and a proton beam in the energy range of 90-120 MeV. Homogeneous target dose coverage was obtained by optimizing the opposed input beam weights using an in-house written routine, resulting in a 4 cm wide SOBP deposited in a water target.

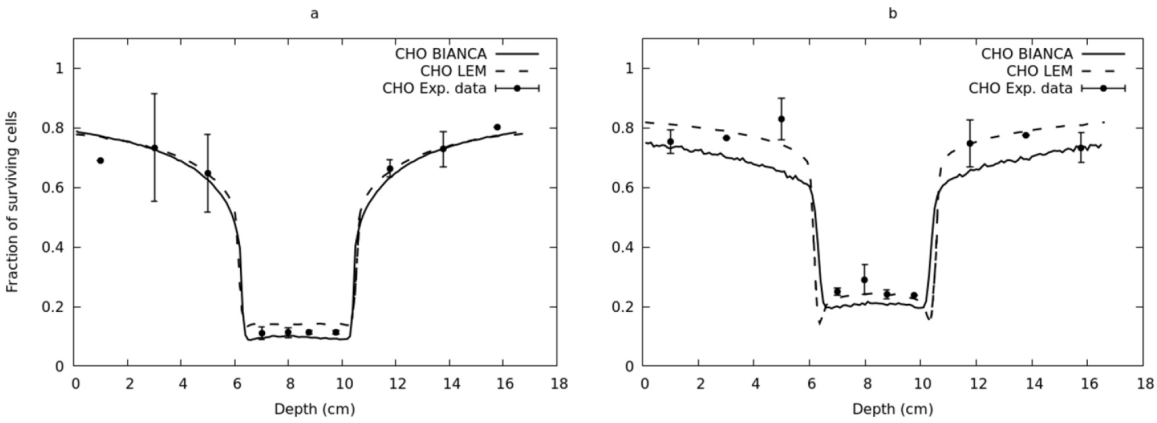

Figure 4.5: Surviving fraction for CHO cells in a two-field irradiation with C-ions (a) and protons (b). Solid lines: BIANCA predictions interfaced with FLUKA; points: experimental data [26]; dashed lines: LEM predictions interfaced with TRiP98 [26]. *Published in [20].*

Figure 4.5 reports C-ion beam (Figure 4.5 (a)) and proton beam (Figure 4.5 (b)) experimental data (points) and LEM IV predictions (dashed line) [26], compared with predictions provided by BIANCA interfaced with FLUKA (solid line). Experimental data, as well as LEM IV predictions obtained using TRiP98, were derived from Elsässer *et al* [26] and digitised using an online software called WebPlotDigitizer [312].

It can be observed that, in Figure 4.5 (a), for C-ion case, BIANCA predictions are consistent with the

experimental data, as well as they are very close to LEM IV predictions. Quantitatively, the difference between BIANCA predictions and the experimental data is $\leq 17\%$, with a 2.2 (reduced) chi-square value. For proton simulations, as reported in 4.5 (b), similar results are observed, although in this case BIANCA overestimated cell death at the entrance channel, predicting a higher RBE in comparison to LEM IV. In the target area, BIANCA is in good agreement with the data and LEM IV predictions.
Overall, the results from the BIANCA model interfaced with the FLUKA MC code suggest that BIANCA can provide accurate predictions of cell survival and radiobiological effectiveness in both C-ion and proton irradiation clinical scenarios. In addition, the method presented in Section 4.3.2, can be used to extend BIANCA model to, in theory, any chosen cell line of interest.

4.5.2 Rat Spinal Cord Data

For clinical applications, benchmarking studies of the BIANCA model against experimental data from the rat spinal cord were performed. The main reason for this study is that the clinical LEM I model was initially applied to skull based tumors, where the main dose constraint is based on late reactions of the central nervous system (CNS), which also applies to head-and-neck tumors. In 1974, Van der Kogel *et al* [302] reported in detail the late effects (functional damage) in rat CNS after irradiation of the spinal cord. Absolute values from these experiments might not be directly applicable to patient studies, although relative values such as RBE and the impact of treatment parameters on RBE might be used [27]. The reported data were applied to evaluate the RBE values for C-ion [27, 29, 31, 30] and proton [32] beam therapies. The LEM I model, as well as the more recent LEM IV version, presented in vivo data for benchmarking their predictions for chordoma patients for both tumor and normal tissues. The present study aims to repeat benchmarking studies using the BIANCA model. Below, only a summary can be found and a more detailed discussion is reported in the original version of the article [28].
In this study, the approach described in Section 4.3.2 was used to define a radiobiological database for chordoma cells. The nucleus of the target cell is defined as a 6-μm height cylinder with 6μm radius. LEM I authors assumed $\alpha_X = 0.105\ Gy^{-1}$ and $\beta_X = 0.05\ Gy^{-2}$, obtaining α_X/β_X ratio of 2 Gy; currently, more recent data for chordoma tumors are available (i.e., in vitro data [313, 314] and in vivo data [315]), BIANCA used the $\alpha_X = 0.159$ and $\beta_X = 0.065$ values proposed by Henderson [315]. Considering the fact, that chordoma database is used for both tumour and normal tissues, the α_X/β_X ratio of 2.45 Gy is a good estimation for photon irradiation of chordoma tumour in vivo, and comparable to LEM I estimations, which minimized a possible normal tissue damage, observed in years of clinical experience. Further optimization of the CL yield value was performed to reproduce the photon survival curve from the experimental data. The obtained CL yield for photon irradiation was used in Equation 4.3 to obtain the CL yields for many particle species and different energies. Subsequently, to obtain values for the BIANCA database, fitting of each survival curve in terms of α and β coefficients in LQM (see Equation 4.2) was performed as a function of the particle species and LET.
Figure 4.6 compares the RBE values simulated with the BIANCA model and experimental data of the rat spinal cord cells RBE value for C-ions [27, 316] for different dose values at different positions of the SOBP. The spinal cord was placed either at the entrance channel of a 270 MeV/n beam (LET_D: 13 keV/μm) or at the center of a 1-cm SOBP of a 140 MeV/n beam (LET_D: 125 $\pm$ 25 keV/μm). Few fractionation schemes

were used:1, 2, 6, or 18 fractions, obtaining RBE values, with respect to 15 MV photons, ranging from 1.33 to 1.44 (entrance) or 1.77 to 5.04 (peak). Further experimental details can be found in Karger *et al* [27] and Debus *et al* [316].

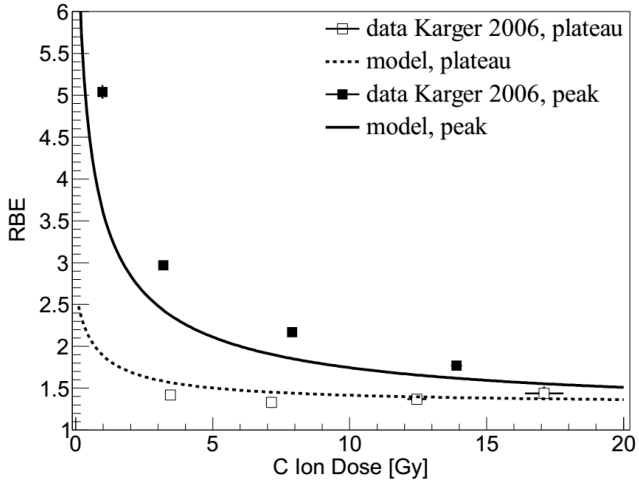

Figure 4.6: Rat spinal cord irradiation for C-ion beam. RBE dose dependency in the SOBP (upper line and filled data points) or entrance plateau (lower line and open data points). Lines: BIANCA predictions; points: experimental data [27]. *Published in [28].*

A very good agreement was obtained between the BIANCA predictions and experimental data in the entrance plateau region (see Figure 4.6, lower line). The observed discrepancies were small and the BIANCA model followed the data trend. These results indicate that the BIANCA model can successfully predict late side effects in the CNS. Estimations of the BIANCA model for the SOBP region for the RBE-dose dependency (see Figure 4.6, upper line) were underestimated; however, they successfully reproduced the data tendency. It can be noticed that, the maximum underestimation can be found for lower doses, and discrepancy decreases with higher values, suggesting, that BIANCA may predict lower RBE for the distal SOBP region, where the highest LET is observed. However, it is worth mentioning a follow-up work by Saager *et al* [29], where Saager *et al* reported that the experimentally measured doses were lower than the TPS predictions by $\leq$ 10%. This suggested a shift in the experimental data towards the left side of the RBE-dose dependency plot, but subsequently RBE values might be increased in this situation. In addition, according to Karger *et al* [27], for the same data, the LEM model presents an underestimation of 25% of the biologically effective dose in the SOBP region and a small overestimation for the plateau region.

More recent publications by Saager *et al* [29, 30, 31] investigated the RBE for rat spinal cord experimental data at different LET values (16, 21, 36, 45, 66, and 99 keV/μm). Animals were located at six different positions along a 6-cm SOBP, and were irradiated with one fraction (reported in [29, 30]) or two fractions (presented in [31]). Similar to previous studies, the obtained RBE values were relative to the 15 MV photon beam. Figure 4.7 shows the predictions of the BIANCA model benchmarked with the experimental data.

For the single fraction and two fraction cases, the RBE increase was lower than that of the experimental data. As a result, the RBE is slightly overestimated for lower LET values and underestimated for higher LET values, especially for lower doses (two fractions). Evaluation of the presented results with comparison

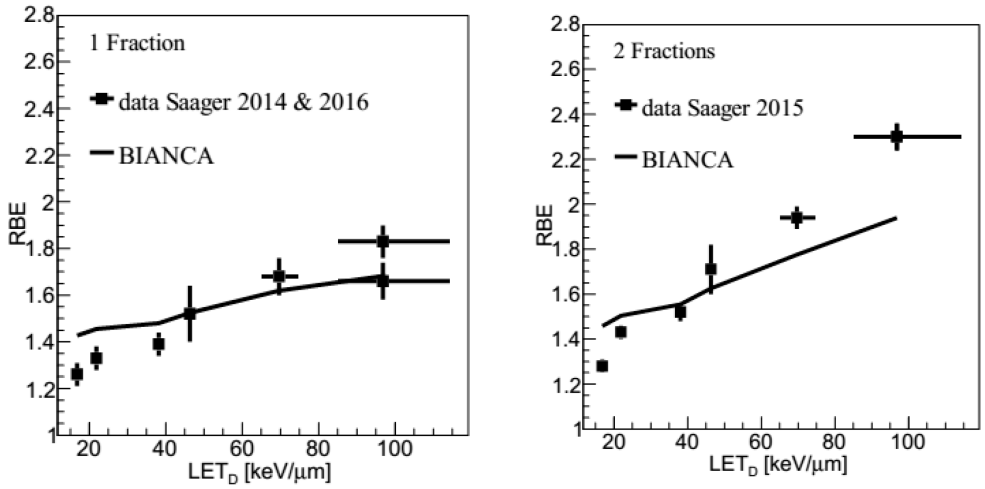

Figure 4.7: Rat spinal cord irradiation for C-ion beam. RBE-LET_D dependency for single-fraction (a) and two-fraction (b) irradiation at different positions within the C-ion SOBP. Lines: BIANCA prediction; points: experimental data [29, 30] (a), or [31] (b). In panel (a), at 99 keV/μm, the higher experimental value is obtained from a repetition experiment [30] and it is considered to be more reliable. *Published in [28].*

to the dose-dependence plots presented in Figure 4.6 can raise the question of consistency for BIANCA performance in a lower LET region (where BIANCA is in a very good agreement for the lower LET region, see Figure 4.6). However, the comparison between the two studies is nonetheless complex: two different beam configurations resulted in different RBE values; afterward, RBE was compared with the data from two independent experiments, where two different dose ranges were used (i.e., approximately 15-27 Gy for the LET study, 1-17 Gy for the dose study). This indicates that BIANCA overestimates biological effectiveness for lower LET and high doses, at the therapeutic dose range, which is in good agreement with experimental data. Evaluating the higher LET values, it was already noticed that BIANCA underestimated the RBE for lower doses, whereas for higher dose values, the discrepancy between BIANCA predictions and experimental data was relatively small. Further investigation of this issue is discussed in patient case studies [33] and it is presented in Chapter 5.

Saager *et al* [31] compared the LEM I model with the experimental data. The clinical LEM I model presented lower RBE values for the entire range of considered LET values. On the other hand, the BIANCA model overestimated the data for lower LET and underestimated the data at higher LET. In general, a quantitative comparison showed a smaller relative discrepancy between the predictions and experimental data for the BIANCA model than for the LEM I model (as reported in [31]). For the lowest LET data point (16 keV/μm), the BIANCA discrepancy was higher, about 13% for a single fraction (1 fx) or 14% for two fractions (2fx), whereas LEM I was 9% (1 fx) or 5% (2 fx), respectively. For other LET values, BIANCA reproduced the experimental data better than LEM I. For example, in the mid-SOBP region (45 keV/μm), the difference for BIANCA is as low as 0% for 1 fx or 4% for 2 fx, whereas for LEM I, the difference reaches 19% for 1 fx or 18% for 2 fx; in the distal part with high LET (99 keV/μm), the values for BIANCA are 8% for 1

fx or 15% for 2 fx, whereas for LEM I, it is 29% for 1 fx or 28% for 2 fx. Saager *et al* [31] also reported benchmarking studies of the (non-clinical C-ion) LEM IV model predictions. It can be observed that LEM IV improved the predictions, especially for 99 keV/μm data points (both 1 fx and 2 fx) and 66 keV/μm (2 fx), where a smaller difference can be seen in comparison to the BIANCA model. However, for all other data points, BIANCA exhibited a superior performance.

Further work focused on proton irradiation studies of the rat spinal cord as presented by Saager *et al* [32]. These experimental data were used to evaluate the performance of the BIANCA for proton beams. Figure 4.8 shows the RBE predictions of the BIANCA model compared to the data. Similarly to previous studies, the rat spinal cord was irradiated, with one or two fractions, using 6-cm proton SOBP (at 7-13 cmm WEQ depth), and a spinal cord was placed at different locations (3.5, 10, 12 and 12.7 cm, referenced 1.4, 2.7, 3.9 and 5.5 keV/μm LET values). Further experimental details can be found in Saager *et al* [32].

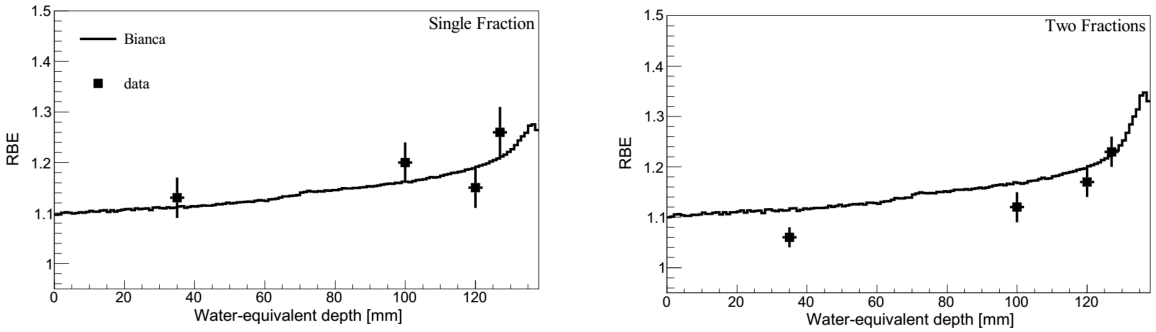

(a) (b)

Figure 4.8: Rat spinal cord irradiation for proton beam. RBE as a function of depth for single fraction (panel (a)) or two fractions (panel (b)). Lines: predictions by BIANCA; points: experimental data [32]. *Published in [28].*

It can be noticed that BIANCA reproduced the data trend for single- and split dose irradiations: RBE increased with the LET (thus depth). More specifically, in the case of single fraction irradiation, the BIANCA prediction is within the experimental error bars. However, the BIANCA simulation outcomes for the split-dose data were overestimated for lower LET values. On the other hand, it can be noticed, that results presented by Saager *et al* [32] for the split dose, reported lower RBE values than that of the single fraction data. According to the authors, the two-fraction experiment verified the results obtained for the single fraction data, and the split dose data were not expected to differ significantly from a single fraction. In addition, it is worth mentioning that the discrepancy between experimental data of up to 5-7% is acceptable for biological experiments [32].

In summary, the BIANCA model reproduces well the RBE data for the rat spinal cord irradiated by protons or C-ions and can successfully estimate the late effect in the CNS.

4.6 Conclusions

Recent upgrades to the BIANCA model, followed by integration with the FLUKA MC code, are presented in this Chapter. BIANCA simulations were compared against in vitro data for V79 cell survival and against in vivo data for rat spinal cord irradiation. In both cases, proton and carbon irradiations were evaluated. The respective radiobiological databases were created for cells of interest, which finalized the creation of α β parameter tables for different particle types and LET values read by the FLUKA MC code. Successful benchmarking studies have resulted in the creation of the BIANCA database for chordoma cell survival, which is a basic cell used in the LEM I model, mainly for RBE prediction in head-and-neck C-ion treatments. Further evaluation of patient cases is presented in Chapter 5 and suggests that BIANCA can successfully estimate the RBE of normal tissue in the CNS for both carbon and proton treatment. An evaluation study of proton cases aimed to challenge the discussion of a fixed RBE value of 1.1, as suggested by ICRU [125], and its future revisions [126, 317].

Further steps for BIANCA development are focused on creating an RBE table for normal tissue damage [275, 318] based on dicentric aberrations in blood lymphocytes, as presented by Embriaco *et al* [319]. Another step is to apply the BIANCA model to patient cases for C-ion treatment, as presented in Kozłowska *et al* [33] in Chapter 5.

Chapter 5

First application of the BIANCA biophysical model to carbon-ion patient cases

In this Chapter, the first application of the BIANCA biophysical model to a patient based treatment planning scenario is presented and discussed. Integration of BIANCA model with the FLUKA Particle Therapy tool allowed the assessment of three carbon ion patient cases, which further allowed the comparison of results with the clinically used model in carbon ion therapy.
This Chapter presents the article *First application of the BIANCA biophysical model to carbon ion patient cases* published in *Physics in Medicine and Biology*, 67, 115013; 2022 [33] by the following authors:

Wioletta Kozłowska[1*], Mario P. Carante[2,3], Giulia Aricò, Alessia Embriaco [3,4] Alfredo Ferrari[5,6], Giuseppe Magro[8], Andrea Mairani[7,8], Ricardo Ramos[3], Paola Sala[9], Dietmar Georg[1], Francesca Ballarini[2,3]

[1] Medizinische Universität Wien, Austria;
[2] University of Pavia, Physics Department, Pavia, Italy;
[3] INFN (Italian National Institute for Nuclear Physics), Sezione di Pavia, Italy;
[4] ENEA-Casaccia, Roma, Italy;
[5] University Hospital Heidelberg, Heidelberg, Germany;
[6] Gangneung-Wonju National University, Gangneung 25457, Korea;
[7] CNAO (Centro Nazionale di Adroterapia Oncologica), Italy;
[8] HIT (Heidelberg Ion-beam Therapy Center), Germany;
[9] INFN (Italian National Institute for Nuclear Physics), Sezione di Milano, Milano, Italy
[*] currently - ADAM an Advanced Oncotherapy company, Meyrin, Switzerland;

IOP Publishing Phys. Med. Biol. 67 (2022) 115013 https://doi.org/10.1088/1361-6560/ac702b

Physics in Medicine & Biology

IPEM Institute of Physics and Engineering in Medicine

RECEIVED
17 January 2022

REVISED
5 May 2022

ACCEPTED FOR PUBLICATION
16 May 2022

PUBLISHED
27 May 2022

PAPER

First application of the BIANCA biophysical model to carbon-ion patient cases

Wioletta S Kozłowska[1,*], Mario P Carante[2,3], Giulia Aricò[4], Alessia Embriaco[3,5], Alfredo Ferrari[6,7], Giuseppe Magro[8], Andrea Mairani[8,9], Ricardo Ramos[3], Paola Sala[10], Dietmar Georg[1] and Francesca Ballarini[2,3]

[1] Medical University of Vienna, Vienna, Austria
[2] University of Pavia, Physics Department, Pavia, Italy
[3] INFN (Italian National Institute for Nuclear Physics), Sezione di Pavia, Pavia, Italy
[4] Optimization of Medical Accelerators, Warrington, United Kingdom
[5] ENEA-Casaccia, Roma, Italy
[6] University Hospital Heidelberg, Heidelberg, Germany
[7] Gangneung-Wonju National University, Gangneung 25457, Republic of Korea
[8] CNAO (Centro Nazionale di Adroterapia Oncologica), Pavia, Italy
[9] HIT (Heidelberg Ion-beam Therapy Center), Heidelberg, Germany
[10] INFN (Italian National Institute for Nuclear Physics), Sezione di Milano, Milano, Italy
[*] Author to whom any correspondence should be addressed.

E-mail: wioletta.kozlowska@cern.ch

Keywords: RBE, BIANCA, carbon ion, heavy ion, particle therapy

Abstract

Objective. The main objective of this work consists of applying, for the first time, the BIANCA (BIophysical ANalysis of Cell death and chromosome Aberrations) biophysical model to the RBE calculation for C-ion cancer patients, and comparing the outcomes with those obtained by the LEM I model, which is applied in clinics. Indeed, the continuous development of heavy-ion cancer therapy requires modelling of biological effects of ion beams on tumours and normal tissues. The relative biological effectiveness (RBE) of heavy ions is higher than that of protons, with a significant variation along the beam path. Therefore, it requires a precise modelling, especially for the pencil-beam scanning technique. Currently, two radiobiological models, LEM I and MKM, are in use for heavy ions in scanned pencil-beam facilities. *Approach.* Utilizing an interface with the FLUKA Particle Therapy Tool, BIANCA was applied to re-calculate the RBE-weighted dose distribution for carbon-ion treatment of three patients (chordoma, head-and-neck and prostate) previously irradiated at CNAO, where radiobiological optimization was based on LEM I. The predictions obtained by BIANCA were based either on chordoma cell survival (RBE_{surv}), or on dicentric aberrations in peripheral blood lymphocytes (RBE_{ab}), which are indicators of late normal tissue damage, including secondary tumours. The simulation outcomes were then compared with those provided by LEM I. *Main results.* While in the target and in the entrance channel BIANCA predictions were lower than those obtained by LEM I, the two models provided very similar results in the considered OAR. The observed differences between RBE_{surv} and RBE_{ab} (which were also dependent on fractional dose and LET) suggest that in normal tissues the information on cell survival should be integrated by information more closely related to the induction of late damage, such as chromosome aberrations. *Significance.* This work showed that BIANCA is suitable for treatment plan optimization in ion-beam therapy, especially considering that it can predict both cell survival and chromosome aberrations and has previously shown good agreement with carbon-ion experimental data.

1. Introduction

Charged particle therapy is a fast growing branch within radiation oncology. Currently, more than 95 proton facilities and 12 carbon-ion centres are in operation, and their number is growing, with 32 proton facilities and 6 carbon-ion centres under construction (www.ptcog.ch).

The physical selectivity of charged particle beams and their different radiobiological characteristics provide better control over dose distribution, with respect to photons. However, especially for heavy ions like carbon, these advantages come hand-in-hand with the requirement for a precise description of the relative biological effectiveness (RBE), which, by definition, describes the biological effectiveness of a given ion in relation to photon beams. While until now it was agreed that a fixed value of 1.1 has to be assigned to proton beams (Paganetti 2002), heavier ions (such as carbon) are characterized by a higher RBE, with significant differences in the proximal, plateau, and distal regions of the spread out bragg peak (SOBP). This higher effectiveness is likely related to a higher yield of DNA damage clusters, which are less probable to be repaired by the cell (Karger and Peschke 2017, Schuemann *et al* 2019), thus causing cell death or non-lethal intracellular damage. Although such damages are likely to consist of two or more DSBs at local or regional scale, it cannot be excluded that also other DNA lesions (e.g. one DSB associated to a SSB and/or base damage) play a role. The higher probability of killing tumour cells also relates to a higher probability of complications in normal tissues, including the induction of secondary tumours. Therefore, a carbon-ion biophysical model coupled to a physical dose prescription is required to precisely predict the RBE variation along the beam for RBE-weighted dose calculations and optimizations.

Currently, two different radiobiological models are in use for active scanning carbon-ion beam facilities: the Local Effect Model I (LEM I) (Scholz *et al* 1997, Elsässer *et al* 2010) in Europe (i.e. at Centro Nazionale di Adroterapia Oncologica (CNAO), Italy, and the Heidelberg Ion-beam Therapy center (HIT), Germany) and at the Shanghai Proton and Heavy Ion Center (SPHIC); the Microdosimetric Kinetic Model (MKM) (Inaniwa *et al* 2010, 2015) in Japan (at the National Institute of Radiological Sciences (NIRS)). LEM I assumes that the critical target in the cell is uniformly distributed over the cell nucleus, which is divided into nano-meter level cellular sub-volumes. The damage in each sub-volume only depends on the amount of the (locally) deposited energy and is independent of the energy-deposition origin, which can be photons or ions. The cell survives only if it does not receive any lethal damage (Karger and Peschke 2017). With LEM, the cell survival probability is calculated based on the photon survival curve. Although LEM and MKM share some conceptual similarities, a direct comparison between these two models is not straightforward, also considering that at NIRS a scaling factor is introduced to rescale the (carbon-equivalent) biological dose to a clinical dose level. To face this issue, a specific tool was developed at CNAO to support the comparison between the NIRS clinical dose and the LEM dose specification (Magro *et al* 2017, Fossati *et al* 2018).

Another approach to RBE modelling is provided by the BIANCA (BIophysical ANalysis of Cell death and chromosome Aberrations) biophysical model recently developed at the University of Pavia, Italy, and the Italian National Institute for Nuclear Physics (INFN) (Carante *et al* 2018, 2019). BIANCA predicts chromosome damage and cell death caused by different monochromatic ion beams, as well as photons. According to the basic assumptions of BIANCA, radiation-induced cell death originates from a subset of DNA damages called *Critical Lesions* (CLs). Within CLs, independent chromosome fragments are produced that, following distance-dependent mis-rejoining (or un-rejoining), lead to chromosome aberrations. Finally, some aberration types lead to clonogenic cell death, whereas others can be related to late normal tissue damage, including secondary cancers (Rabbitts 1994).

Since it was developed, the BIANCA model has been systematically benchmarked against several experimental data sets, analyzing the dependence of RBE on LET (Linear Energy Transfer), particle type and dose. Additionally, BIANCA has been interfaced with the FLUKA Monte Carlo (MC) code (Ferrari *et al* 2005, Ballarini *et al* 2006, Böhlen *et al* 2014, Battistoni *et al* 2016), and subsequently tested against *in vitro* cell survival data, as well as *in vivo* data on the rat spinal cord damage after C-ion or proton irradiation (Saager *et al* 2018). Most recently, BIANCA predictions were evaluated for cell survival after He-3 and He-4 ion irradiation, and the results have been benchmarked against *in vitro* data on Chinese Hamster Ovary (CHO) cells and Renal Adenocarcinoma (Renca) tumour cells (Carante *et al* 2021). An evaluation of normal tissue damage was presented in Embriaco *et al* (2021), which reports the development of a radiobiological database describing the induction of dicentric chromosomes in peripheral blood lymphocytes. Chromosome aberrations in lymphocytes are considered as indicators of hematologic toxicity, which in turn is a major limiting factor for radiotherapy, both for acute morbidity and for secondary cancer risk, since CAs are well correlated to late cancer incidence (Durante *et al* 2000). In particular, the authors (Durante *et al* 2000) found a reduced level of PBL aberrations in patients treated with C-ions with respect to those treated with x-rays, suggesting a reduced risk of bone marrow morbidity.

In the present work, for the first time BIANCA was applied to re-calculate the beam radiobiological effectiveness for three carbon-ion treatment plans of patients treated at CNAO, where the original radiobiological optimization was performed by LEM I. To evaluate different treatment scenarios for BIANCA, plans were selected which differed regarding the fractionation dose, LET distribution, and beam energy. The BIANCA RBE was calculated both for tumour cell survival (called RBE_{surv}) and for peripheral blood lymphocyte chromosomal aberrations (called RBE_{ab}). Both predictions were then compared with the cell survival RBE

predictions obtained by LEM I. Finally, the suitability of the BIANCA model for treatment plan optimization in ion beam therapy was evaluated, considering that, in contrast to clinically used models (LEM I and MKM), BIANCA can predict RBE for both cell survival and chromosome aberrations, and good agreement has already been reported with carbon ion experiments (Carante *et al* 2018, 2019, 2020, Embriaco *et al* 2021).

2. Materials and methods

The basic principles of the BIANCA model, the interface with the FLUKA MC code and the clinical patient cases are briefly described below.

2.1. The BIANCA model

BIANCA is implemented in the form of a Monte Carlo simulation code and it is based on the following assumptions: (i) ionizing radiation can induce DNA Critical Lesions (CLs), defined as breaks in the chromatin fibre producing two (main) independent chromosome fragments, where 'main' refers to fragments that are visible with Giemsa/FISH when chromatin is condensed (that is, with minimum dimensions in the Mega-base-pair order); (ii) distance-dependent mis-rejoining of these chromosome fragments, or fragment un-rejoining, gives rise to chromosome aberrations; (iii) certain aberration types (dicentrics, rings, and deletions; see below) lead to clonogenic cell death. Only a brief discussion of these assumptions will be presented below. More detailed information can be found in Ballarini and Carante (2016), Carante and Ballarini (2016).

Clusters of double-strand breaks, that is two or more DSBs in proximity, are good candidates as critical lesions (Ballarini *et al* 2015, Schuemann *et al* 2019). However, a consensus on the definition of such proximity has not been reached yet: while some works suggest that clustering at the nm level plays a major role, others show that also higher-level clustering, up to the Mega-base-pair level, can be important. Therefore, the molecular characteristics of the model CLs are not defined, and their yield (mean number of CLs per unit dose and unit DNA mass) is an adjustable parameter.

The distance-dependence of chromosome fragment end-joining is described either by a step function, if the primary goal is to model cell death (Ballarini *et al* 2014, Carante *et al* 2015, Carante and Ballarini 2016, Carante *et al* 2018, 2019), or by an exponentially-decreasing function, if the goal is to predict specific aberration categories (Tello Cajiao *et al* 2017, 2018). When adopting the step function, each chromosome fragment is assumed to have a certain probability, f, to remain un-rejoined even if possible rejoining partners there exist within the threshold distance d, which is assumed to be equal to the mean distance between two adjacent chromosome territories. The value of f is the second, and last, adjustable parameter and represents the repair capacity of the specific cell type. On the other hand, if it is required to determine one or more specific aberration categories, the following exponentially decreasing function is used (Tello Cajiao *et al* 2017, 2018):

$$P(r) = \exp(-r/r_0), \tag{1}$$

where r is the initial distance between the two considered fragments and r_0 depends on the considered cell type. For lymphocytes, r_0 has been fixed to 0.8 μm.

The assumed relationship between cell death and chromosome aberrations is derived from experimental observations indicating a one-to-one relationship between the logarithm of the cell surviving fraction and the mean number of *lethal aberrations* per cell (i.e. dicentrics, rings, and deletions) visible in metaphase (Carrano 1973, Cornforth and Bedford 1987). A typical simulation of chromosome aberrations and cell survival (Carante and Ballarini 2016, 2017, Carante *et al* 2018) requires input data such as radiation type (photons, light ions or heavy ions), CL yield, f value, and cell nucleus size and shape (which can be spherical or cylindrical), as well as the irradiation parameters like LET and absorbed dose. During a simulation, a chromosome territory is modelled as an (irregular) intra-nuclear region consisting of the union of adjacent cubic voxels within the cell nucleus. If the cell is irradiated by a given dose of photons, an actual number of CLs is extracted from a Poisson distribution, and these CLs are uniformly distributed in the cell nucleus. In contrast if the dose is delivered by a certain ion type of given LET, an actual number of primary ions traversing the cell nucleus is first extracted from a Poisson distribution and then, for each of these nucleus traversals, an actual number of CLs is also extracted from a Poisson distribution. If the primary ion is a proton or a He-ion, these CLs are then uniformly distributed along parallel straight lines representing the primary-particle trajectory. In contrast, if the primary particle is a heavy ion (such as a carbon-ion or oxygen-ion), each CL has a 50% probability of being induced at a certain radial distance from the primary-ion path (as a consequence of *delta rays* (Chatterjee and Schaefer 1976)), and a 50% probability to occur within the track core. Afterwards, the chromosomes and chromosome-arms hit by each CL are determined, by comparing the coordinates of each CL with the coordinates of the voxels constituting the various chromosome territories. The process of chromosome fragment end-joining (or lack thereof) is then simulated, and the scoring of different aberration categories is reproduced. The cell is considered

as dead if it contains any *lethal aberration*, otherwise it is counted as a surviving cell. For each considered dose level, the process is repeated until the required statistical significance is obtained. The repetition for different dose values provides simulated dose-response curves for chromosome aberrations and cell survival. More details can be found in (Carante *et al* 2019).

2.2. Creation of a cell survival radiobiological database with BIANCA

In previous studies (Carante and Ballarini 2016, 2017, Carante *et al* 2018), the model parameters (CL yields and f) for cell survival curves obtained at different LET values of different ion types were adjusted to experimental data available in the literature for V79 cells, considered as a reference cell line. In moving towards the possible clinical use of BIANCA, the LET-dependence of both parameters was fitted for each ion type, and full predictions of survival curves at many different LET values were performed. Each of these curves was then fit by the well known linear-quadratic expression:

$$S(D) = exp(-\alpha D - \beta D^2). \tag{2}$$

This allowed construction of a radiobiological database describing V79 cell survival, consisting of pairs of α and β coefficients as a function of ion type and LET, as well as the two photon coefficients.

In order to predict the survival of, in principle, any cell line of interest based on the V79 reference database, the CL yield used to simulate the survival of the cell of interest (following exposure to a given ion type of given LET) was derived from the following equation (Carante *et al* 2018):

$$\frac{CL}{\mu\mathrm{m}} = \left(\frac{CL}{\mu\mathrm{m}}\right)_{V79} \cdot \left(\left(\frac{CL}{\mathrm{Gy}\cdot\mathrm{cell}}\right) \Big/ \left(\frac{CL}{\mathrm{Gy}\cdot\mathrm{cell}}\right)_{V79}\right) \cdot \frac{V_{V79}}{V}, \tag{3}$$

where $(CL/\mu\mathrm{m})_{V79}$ is the CL yield used for V79 cells exposed to the same radiation quality, whereas $(CL\cdot\mathrm{Gy}^{-1}\cdot\mathrm{cell}^{-1})$ and $(CL\cdot\mathrm{Gy}^{-1}\cdot\mathrm{cell}^{-1})_{V79}$ are the CL yields used to simulate photon exposure for the cell line of interest and V79 cells, respectively. Finally, V_{V79} and V are the nucleus volumes used for V79 cells and for the cell line of interest, respectively.

Concerning parameter f, its value was derived from this equation:

$$f = f_{V79} + f_X + f_{(X,V79)}, \tag{4}$$

where f_{V79} is the f value used for the V79 reference cell line exposed to the same radiation quality, whereas f_X and $f_{(X,V79)}$ are the f values used to simulate the photon survival curve of the cell line of interest and the reference cell line, respectively. This way, knowing the photon response of an arbitrary cell line of interest, the two equations above provide the CL yields and the f value to predict cell survival curves following irradiation of that cell line with different ion types over a wide LET range.

This implies that, for a given radiation quality, the different response of different cell types is related to a different number of induced CLs, as well as a different value of parameter f. While the yield of CLs is related to the cell sensitivity with respect to the induced DNA damage, the f value depends on the capability of the cell of repairing such damage or leaving it as un-repaired.

The cell survival database applied in this work is based on chordoma cells, the same cell type as considered by LEM I (Carante *et al* 2020). In LEM I, at the time of the clinical introduction, an α_X/β_X ratio of 2Gy was applied, with $\alpha_X = 0.10\ \mathrm{Gy}^{-1}$ and $\beta_X = 0.05\ \mathrm{Gy}^{-2}$. For BIANCA, a more recent patient data reported in Henderson *et al* (2009) was considered, which indicates a α_X/β_X ratio of 2.45 Gy.

Specifically, to create the cell survival database applied in this work, the photon survival curve for chordoma was reproduced with BIANCA by adjusting the CL yield. Subsequently, many survival curves for different ion types and LET values were simulated based on equation (3), and linear-quadratric fitting of such curves provided pairs of α and β coefficients as a function of particle type and LET.

2.3. Creation of a chromosomal aberration radiobiological database with BIANCA

The database for late normal tissue damage was based on chromosomal aberrations in peripheral blood lymphocytes. As previously reported in Durante *et al* (2000), an increase of the chromosome aberration yield in the hematopoietic tissue is an indicator of hematologic toxicity. In particular, the reduced number of aberrant lymphocytes in patients treated with carbon-ions compared to patients treated with x-rays was interpreted as suggestion of a reduced risk of bone marrow morbidity. Since many experimental data are available in the literature on lymphocyte dicentrics (Bauchinger and Schmid 1998, Ohara *et al* 1998, Di Giorgio *et al* 2004, Kowalska *et al* 2019), this aberration category was considered to create the normal tissue damage database applied in this work.

Analogous to what was done for cell survival, the CL parameter was adjusted to reproduce experimental dose-response curves available in the literature for dicentrics in lymphocytes exposed to different ion types at different LET values, as well as photons as a reference. Subsequently, for each ion type, the LET-dependence of

the CL yield was fitted, allowing derivation of the CL yields to predict dicentric dose-response at any LET value. Finally, each (simulated) dicentric curve was fit by the following linear-quadratic expression:

$$Y(D) = aD + bD^2, \tag{5}$$

where $Y(D)$ is the mean number of dicentrics per cell, D is the absorbed dose and a and b are fitting coefficients, stored in a table that constitutes a radiobiological database describing the induction of lymphocyte dicentrics as a function of ion type and LET. More details can be found in Tello Cajiao *et al* (2017, 2018), Embriaco *et al* (2021).

2.4. Interface between BIANCA and the FLUKA Particle Therapy Tool

In the current study, the tables produced by BIANCA, containing the linear and quadratic coefficients describing cell survival and lymphocyte dicentrics, were read by the FLUKA general-purpose MC Code, which includes state-of-the-art physics models (Ferrari *et al* 2005, Ballarini *et al* 2006, Böhlen *et al* 2014, Battistoni *et al* 2016). The FLUKA version 2020.0 (Ferrari *et al* 2005 FLUKA INFN distribution) was used for the simulations, together with the FLUKA Particle Therapy Tool (Kozłowska *et al* 2019). The predefined simulation default HADROTHErapy was chosen to guarantee reliable accuracy and reasonable computing time. For carbon ion treatment planning simulations, the external event generator—relativistic Quantum Molecular Dynamics (rQMD-2.4) (Andersen *et al* 2004) was linked to assure accurate modelling of nucleus-nucleus collisions above 125MeV/u, whereas below 150 MeV/u nuclear reactions were handled by the Boltzman Master equation (BME) approach, smoothly transitioning from one model to another in the overlapping range of energies. In addition, coalescence and evaporation of heavy ions were activated by using two PHYSICS cards.

The beam source was generated directly from the clinical treatment plans (DICOM RTPLAN), and the essential information of each pencil beam spot (i.e. energy, position, rotation) was translated into FLUKA-proprietary functions. The source beam was targeting (through the previously modelled nozzle (Kozłowska *et al* 2019)) a voxelized patient geometry, derived from computer tomography (CT) scans. The necessary information (particle type and energy, and absorbed dose) were calculated on a voxel-by-voxel basis, with determination of the scoring resolution based on the DICOM RTDOSE file. More details on the specific procedures for treatment planning simulation in the FLUKA Particle Therapy Tool can be found in Kozłowska *et al* (2019).

Concerning the radiobiological scoring, whenever (according to FLUKA) a certain amount of energy is deposited in a target voxel by a given particle type of given energy (and thus given LET), FLUKA reads the corresponding α and β coefficients from the tables produced by BIANCA. Subsequently, to take into account that a mixed radiation field is present in the voxel, the dose-averaged values of α and β in that voxel are calculated according to the *Theory of Dual Radiation Action* (Zaider and Rossi 1980) as described in Mairani *et al* (2010), i.e.:

$$\alpha_D^{mix} = \frac{\sum_{i=1}^{n} \alpha_i D_i}{\sum_{i=1}^{n} D_i} \tag{6}$$

$$\sqrt{\beta_D^{mix}} = \frac{\sum_{i=1}^{n} \sqrt{\beta_i} D_i}{\sum_{i=1}^{n} D_i}, \tag{7}$$

where D_i is the dose absorbed from the ith particle (i.e. given particle type of given energy) according to FLUKA, α_i and β_i are the corresponding radiobiological coefficients provided by BIANCA, and α_D^{mix} and β_D^{mix} are their mean values. After calculating α_D^{mix} and β_D^{mix} as described above, the cell survival level and the corresponding RBE-weighted dose in the voxel were calculated as follows:

$$-lnS = \alpha_D^{mix} \cdot D + \beta_D^{mix} \cdot D^2 \tag{8}$$

$$D_{RBE_{surv}} = \sqrt{-ln(S)/\beta_X + (\alpha_X/(2\beta_X))^2} - \alpha_X/(2\beta_X). \tag{9}$$

In parallel, the RBE-weighted dose for lymphocyte dicentric induction was calculated as follows:

$$D_{RBE_{ab}} = \sqrt{Y/b_X + (a_X/(2b_X))^2} - a_X/(2b_X). \tag{10}$$

In equation (9), α_X and β_X represent the photon coefficients provided by BIANCA for tumour cell survival following irradiation with 6 MV x rays; in equation (10), $_{aX}$ and b_X are the photon coefficients for lymphocyte dicentrics, which refer to Cs-137 gamma rays.

2.5. Simulation of carbon-ion patient treatment plans with the BIANCA RBE models

Three clinical carbon-ion treatment plans (optimized for LEM I) from the CNAO hadron therapy centre were analyzed in this study: a chordoma case, a head-and-neck (HN) tumour case, and a prostate tumour case, with FLUKA MC simulations performed for each case, with a simulation settings as presented in Kozłowska *et al* (2019). For BIANCA radiobiological calculations, the original treatment plans with the same energy distributions were simulated.

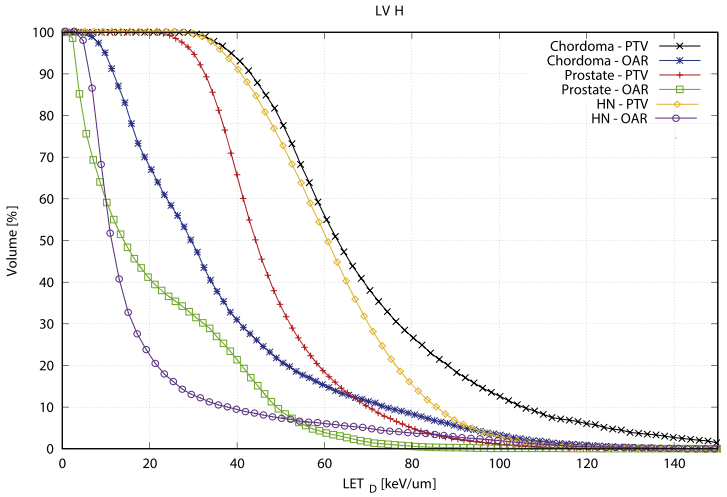

Figure 1. LET_D volume histograms. Prostate case (PTV and rectum), Chordoma case (PTV and brainstem) and HN case (PTV and brain stem).

While the chordoma case was irradiated by two opposite fields, one field was used for the HN case, and a partial plan (one field) was presented for the prostate case. In all three cases, the dose was delivered by an active scanning technique. The particle energies used in the treatments were 157–241 MeV/u for chordoma, 136–249 MeV/u for HN, and 304–397 MeV/u for prostate. In parallel to BIANCA, the LEM I model was applied, adopting the methods presented in Mairani *et al* (2010) for the LEM I database. The values of the RBE-weighted dose were multiplied by the number of planned fractions (9, 32, and 9, respectively), and that is how the results will be presented below.

3. Results

As mentioned above, in this work the RBE calculated by BIANCA was compared with that calculated by LEM I for three carbon-ion patient cases (chordoma, prostate and HN) irradiated at CNAO, where the treatment plan radiobiological optimization was performed by LEM I. To interpret the results, it is useful to first analyze the corresponding LET-volume histogram shown in figure 1, both for the planned target volume (PTV) and for the organs at risk (OARs), i.e. brainstem for chordoma and HN, and rectum for prostate.

In the PTV, the LET distribution for chordoma and HN is rather similar (although the chordoma case includes higher LET values compared to HN), whereas the distribution for the prostate case is shifted towards substantially lower values. For instance, the value of $LET_{D95\%}$ was 39 keV μm^{-1} for chordoma and HN, whereas it was 29 keV μm^{-1} for prostate. The difference is even more pronounced looking at $LET_{D5\%}$, which is about 125 keV μm^{-1} for chordoma, 95 keV μm^{-1} for HN, and 80 keV μm^{-1} for prostate. In contrast, concerning the selected treatment plans, chordoma still shows higher LET values, whereas HN shows lower values, and the prostate case seems to have an intermediate behaviour. All these differences are due to many factors, including a different depth of the three tumour types (which implies different energy ranges), different positions of the OARs with respect to the PTV, and different irradiation schemes (two opposing fields for chordoma, one single field for prostate and HN).

Simulated distributions of the RBE-weighted dose, calculated by the considered biophysical models are presented in the axial cross-section plots shown in figures 2(a)–(c), 3(a)–(c) and 4(a)–(c) for chordoma, prostate, and HN, respectively. In all three figures, panel (d) reports the corresponding RBE-weighted dose volume histograms, as well as the physical dose histograms, and bottom panels (e)–(f) represent the absolute difference of the RBE-weighted dose distributions between LEM I and BIANCA RBE_{surv} (e) and LEM I and BIANCA RBE_{ab} (f).

For all considered cases, in the entrance channel, both BIANCA approaches (cell survival or chromosome aberrations) show a lower RBE-weighted dose with respect to LEM I. This is particularly true for RBE_{surv}, whereas RBE_{ab} tends to show an intermediate behaviour between $BIANCA_{surv}$ and LEM I.

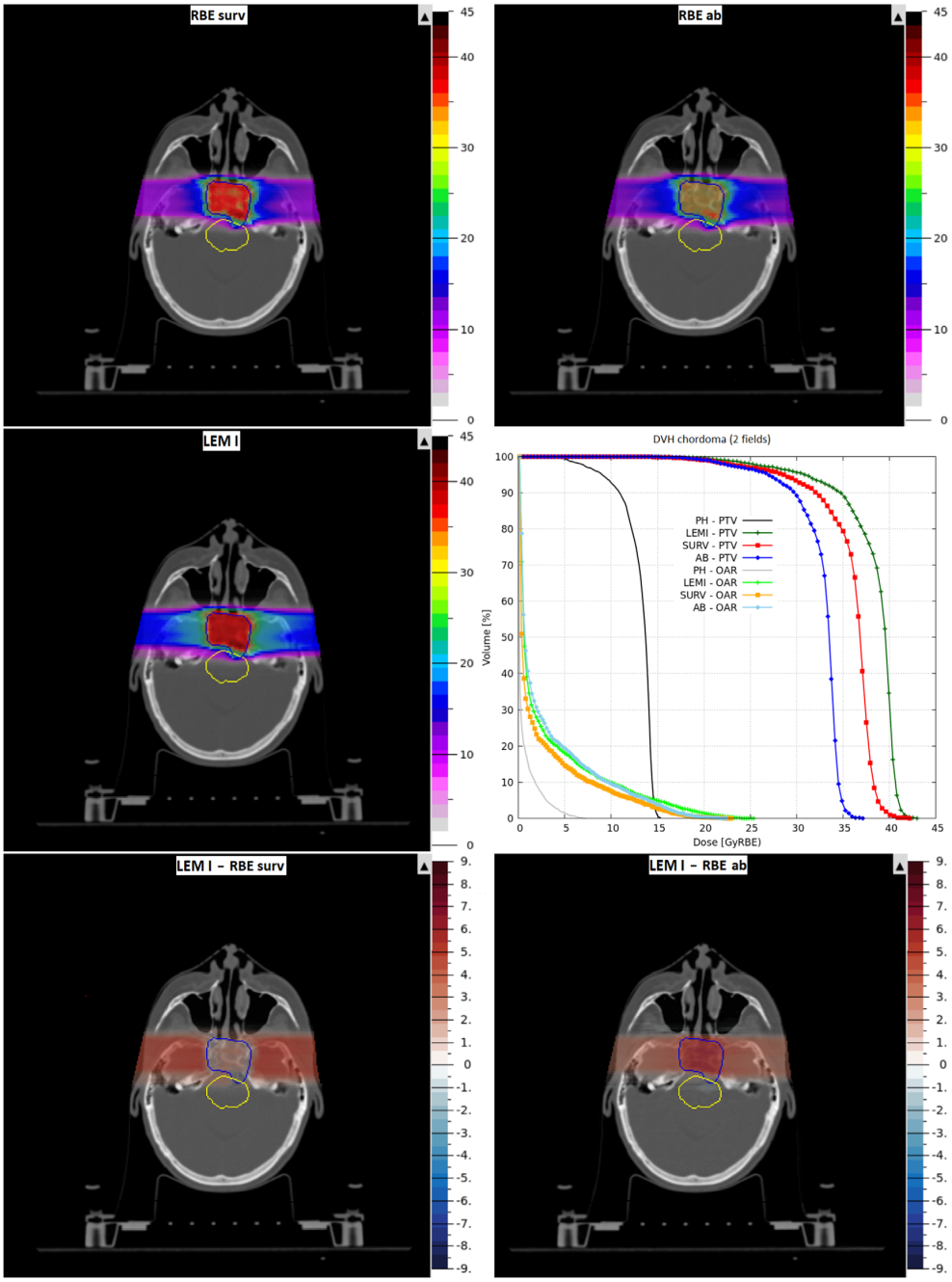

Figure 2. Chordoma case. RTViewer representation of RBE-weighted doses [GyRBE] using different models: (a) top left: BIANCA RBE_{surv}; (b) top right: BIANCA RBE_{ab}; (c) middle left: LEM I; the absolute dose difference [GyRBE] between models: (e) bottom left: LEM I—BIANCA RBE_{surv}; (f) bottom right: LEM I—BIANCA RBE_{ab}. (d) Middle right: RBE-weighted dose-volume histograms for LEM I, BIANCA RBE_{surv} and BIANCA RBE_{ab} [GyRBE], with physical-dose (PH) [Gy].

Also for the PTV, LEM I provides higher values with respect to BIANCA. However, for chordoma, $BIANCA_{ab}$ is lower than $BIANCA_{surv}$, whereas for prostate and HN, the opposite behaviour is observed. In particular, for the prostate case, the values of $BIANCA_{ab}$ are very similar to those of LEM I.

Finally, concerning the considered OARs, the values provided by BIANCA (especially by $BIANCA_{ab}$, whereas $BIANCA_{surv}$ tends to show lower values) are very similar to those obtained by LEM I.

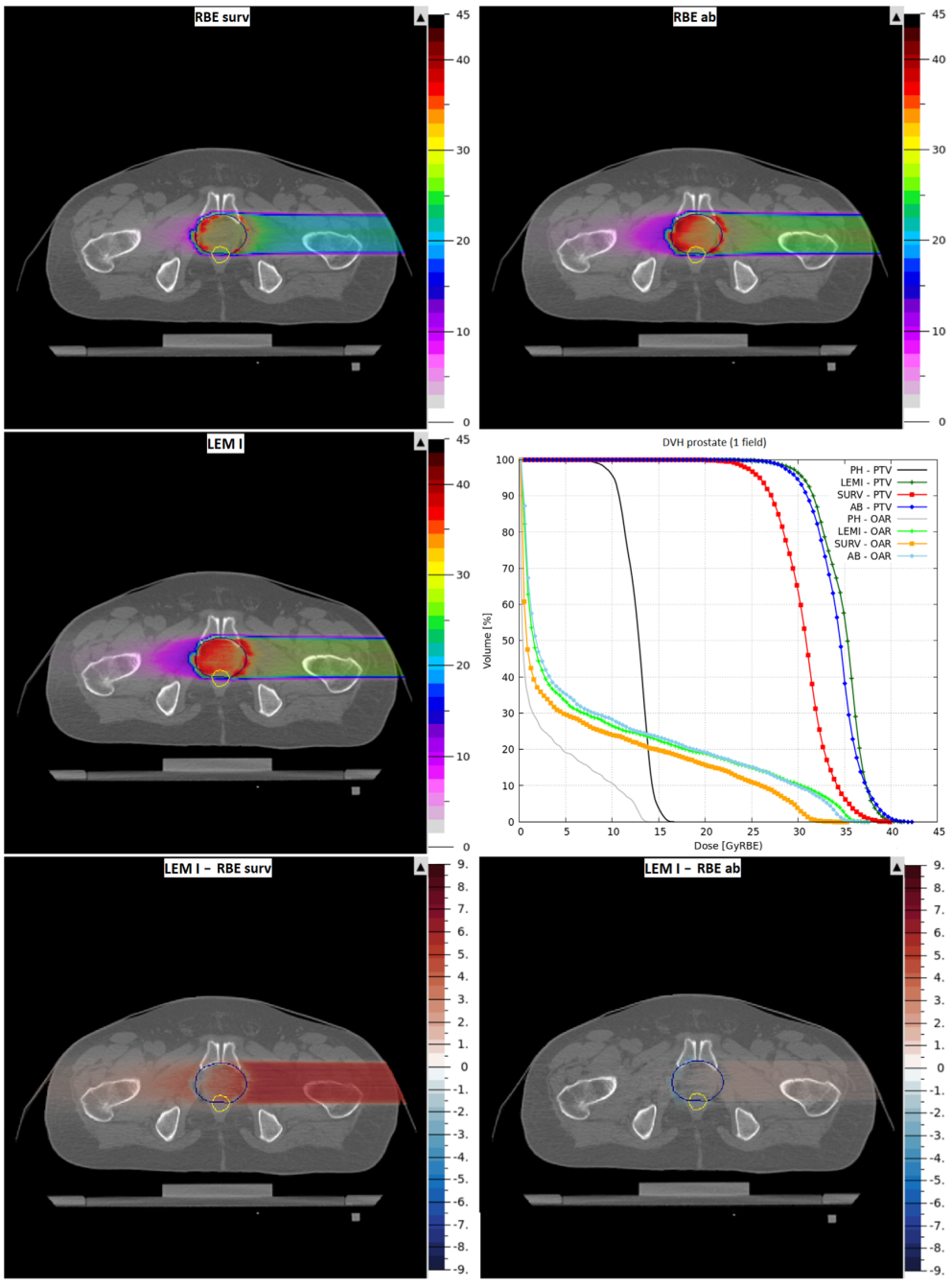

Figure 3. Prostate case. RTViewer representation of RBE-weighted doses [GyRBE] using different models: (a) top left: BIANCA RBE_{surv}; (b) top right: BIANCA RBE_{ab}; (c) middle left: LEM I; the absolute dose difference [GyRBE] between models: (e) bottom left: LEM I—BIANCA RBE_{surv}; (f) bottom right: LEM I—BIANCA RBE_{ab}. (d) Middle right: RBE-weighted dose-volume histograms for LEM I, BIANCA RBE_{surv} and BIANCA RBE_{ab} [GyRBE], with physical-dose (PH) [Gy].

4. Discussion

The clinical experience of carbon-ion therapy in Japan and Europe, and the satisfactory results in cancer patients obtained within in recent years (Fossati *et al* 2018), reflects the fact that carbon ions are currently the preferred clinically-used ions with $Z > 1$ for charged particle therapy. The RBE models used in clinics for carbon-ion therapy, that is LEM I and MKM, are based on well-established radiobiological data sets, which show relatively

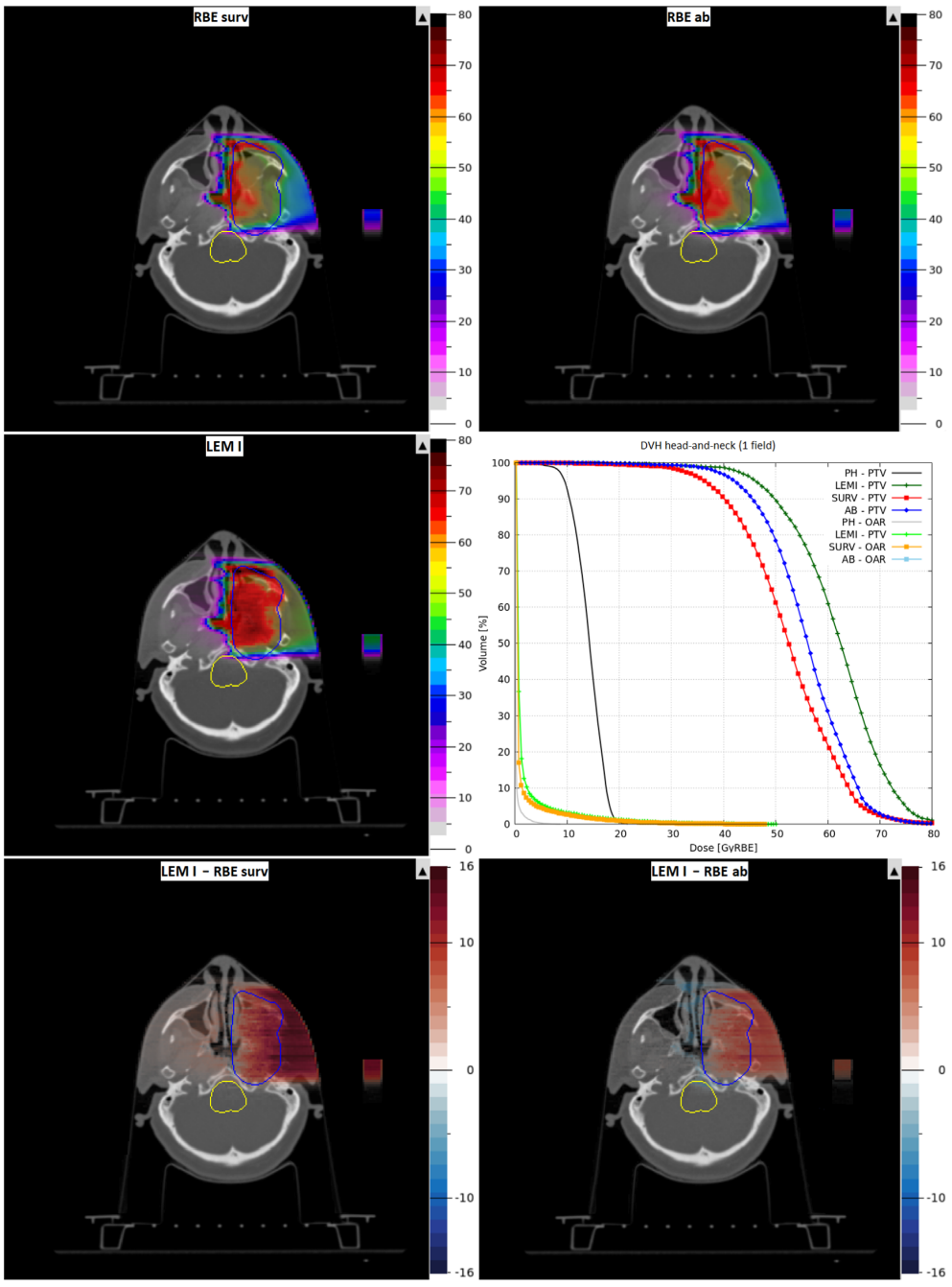

Figure 4. HN case. RTViewer representation of RBE-weighted doses [GyRBE] using different models: (a) top left: BIANCA RBE_{surv}; (b) top right: BIANCA RBE_{ab}; (c) middle left: LEM I; the absolute dose difference [GyRBE] between models: (e) bottom left: LEM I—BIANCA RBE_{surv}; (f) bottom right: LEM I—BIANCA RBE_{ab}. (d) Middle right: RBE-weighted dose-volume histograms for LEM I, BIANCA RBE_{surv} and BIANCA RBE_{ab} [GyRBE], with physical-dose (PH) [Gy].

good agreement with experimental *in-vitro* and *in-vivo* data. In this study, we present another biophysical model, called BIANCA, which potentially can be used for clinical RBE predictions.

The general assumption of the BIANCA model states that radiation-induced cell death derives from certain types of chromosomal aberrations, which in turn are generated by DNA CLs. BIANCA has been benchmarked against several available experimental data sets, including the survival of V79 cells irradiated by protons, helium ions, carbon ions and oxygen ions at different energies and doses (Carante *et al* 2019). A recent study presented BIANCA predictions for rat spinal cord *in vivo* data following carbon-ion or proton irradiation (Carante *et al* 2020).

Except for an underestimation of the carbon ion data at the higher LET values, those results showed that the RBE predictions provided by BIANCA were in line with the experimental data (Karger *et al* 2006, Saager *et al* 2014, 2015, 2016, 2018), suggesting that BIANCA can be applied for the evaluation of late side effect in the CNS when treating HN tumours (Carante *et al* 2020).

The present work was designed to apply the BIANCA model to clinical patient cases (chordoma, prostate and HN tumours) irradiated with carbon-ions at CNAO, and to asses its use in clinical scenarios. The predictions of BIANCA were compared with those provided by LEM I, which is used at CNAO for treatment plan optimization. While the LEM I database is specific for tumour cell survival, with BIANCA, the RBE was calculated both in terms of tumour cell survival, and in terms of lymphocyte dicentric aberrations, which are indicators of hematologic toxicity.

In the PTV, BIANCA provided lower values with respect to LEM I. The possible reasons for this difference may be related to the fact that LEM I, when compared with *in vitro* data, tends to overestimate the RBE at low and intermediate LET values (Elsaesser and Scholz 2007, Scholz and Elsaesser 2007), and the latter provide an important contribution to the LET distribution in the PTV region. Although tumour cell survival is the most important endpoint in the PTV, it is instructive to briefly discuss the observed differences between $BIANCA_{surv}$ and $BIANCA_{ab}$. While for the chordoma case, $BIANCA_{ab}$ was lower than $BIANCA_{surv}$, for the prostate and HN cases the opposite behaviour was observed. In particular, for the prostate case, the values of $BIANCA_{ab}$ were very similar to those of LEM I. The differences between $BIANCA_{surv}$ and $BIANCA_{ab}$ may be explained by taking into account that, qualitatively, at the same LET (as it happens for the PTV of chordoma and HN), at lower doses (like for HN, which got a fractional dose of 0.7 Gy), the RBE_{ab} tends to be higher than the RBE_{surv}; in contrast, at higher doses (like for chordoma, where the fractional dose was 1.7 Gy) the RBE_{ab} is smaller than the RBE_{surv}. This may explain why the $BIANCA_{surv}$ is higher than $BIANCA_{ab}$ in the chordoma PTV, whereas the opposite occurs in the HN PTV. Furthermore, comparing the chordoma with the prostate case, the different behaviour of $BIANCA_{surv}$ and $BIANCA_{ab}$ may depend on the fact that the prostate PTV is characterized by lower LET values with respect to the chordoma PTV; this would imply that the large quadratic coefficient of dicentric dose-response plays here a minor role.

Concerning the relevant OARs (brain stem for chordoma and HN; rectum for prostate), the values provided by $BIANCA_{ab}$, which is related to the risk of secondary tumours, are very similar to those obtained by LEM I. On the contrary, $BIANCA_{surv}$, which can be considered as an indicator of early damage, tends to show lower values.

For all considered cases, in the entrance channel $BIANCA_{ab}$ showed a lower RBE-weighted dose with respect to LEM I. Even lower values were found with $BIANCA_{surv}$. The higher values shown by LEM I may be interpreted by taking into account that, as mentioned above, LEM I tends to overestimate the RBE at the lower LET values when focusing on doses of a few Gy (Elsaesser and Scholz 2007, Scholz and Elsaesser 2007). The difference between $BIANCA_{surv}$ and $BIANCA_{ab}$ may be explained by considering that lymphocyte dicentrics dose-response curves are characterized by a much lower linear coefficient (and, in some cases, also a higher quadratic coefficient) with respect to cell survival curves, resulting in a lower alpha/beta ratio. As a consequence, at relatively low doses, like those involved in the entrance channel, the RBE for dicentric aberrations tends to be higher than that for cell survival.

Overall, our results suggest that, if $BIANCA_{surv}$ is used to evaluate the beam effectiveness at killing tumour cells and $BIANCA_{ab}$ is used to estimate (late) normal tissue damage, BIANCA provides lower RBE-weighted doses with respect to LEM I, both in the PTV and in the entrance channel; on the contrary, BIANCA and LEM I provide very similar values in the organs at risk. As a consequence, if one defines a certain RBE-weighted dose to the OARs, BIANCA would predict lower RBE-weighted doses in the PTV and in the entrance channel. This would imply a lower risk of damage to the healthy tissues before the tumour, but also a lower probability of tumour control. Conversely, if the starting point consists of obtaining a certain RBE-weighted dose in the PTV, and thus a certain tumour control probability, then the application of BIANCA would imply an overall enhancement of the physical dose, which in turn might imply an increased damage to the OARs, and thus a higher probability of complications to normal tissues. In any case, it must be taken into account that, at the moment, it is not possible to draw clear-cut conclusions on the clinical implications of using BIANCA for treatment plan optimization, because in the current study we directly applied BIANCA to the physical-dose distributions that had been previously obtained after plan optimization by LEM I.

More generally, having another model beyond those already available might provide additional information regarding the RBE complexity, particularly regarding the RBE dependence on the considered endpoint, thanks to the BIANCA capability of predicting both cell survival and chromosome aberrations. Furthermore, with BIANCA, it is possible to produce a cell-survival radiobiological database that is specific for the tumor type of interest and to provide the radiobiological database for lymphocyte dicentrics, which are indicators of damage to the hematopoietic tissue, which in turn is a major limiting factor of radiotherapy total dose.

Finally, the results presented in Carante *et al* (2020) and in Carante *et al* (2021) indicated that BIANCA can provide RBE predictions not only for carbon ions but also for protons and for helium-ions, which very recently

started being used at HIT and will be also used in other centers including CNAO. Concerning protons, although at the moment a constant RBE of 1.1 is applied in clinical practice, a debate is ongoing regarding the possibility to take into account the proton RBE increase in the distal SOBP, which requires radiobiological modelling. In this framework, BIANCA offers the advantage of having one single model that works for all three ion species, also considering that both protons and helium-ions are involved even for carbon ion treatments, since they are produced by primary-ion nuclear interactions.

5. Conclusions

Our current study presents the first application of the BIANCA biophysical model, interfaced with the FLUKA Particle Therapy tool, in a clinical treatment planning scenario for three carbon-ion patient cases. In the PTV and in the entrance channel, BIANCA showed lower values of RBE-weighted dose with respect to LEM I, whereas in the OARs the two models provided very similar outcomes. The presented work shows that BIANCA can be applied for the radiobiological optimization of carbon-ion treatment planning, using a radiobiological database based on cell-specific tumor cell survival, as well as a database for lymphocyte aberrations, to be considered as indicators of normal tissue damage.

In the future, we plan to apply the current version of BIANCA to a larger number of patient cases, both for the RBE recalculation of already optimized plans (as we did in the present work), and for performing treatment plan optimization by BIANCA. This will allow us to check whether the differences between BIANCA and LEM I shown in this work (lower RBE values in the entrance channel and the PTV, and similar values in OARs) can be generalized. A subsequent step may be the RBE recalculation in case of proton treatments, to investigate the differences between applying a variable RBE instead of the constant 1.1 value currently adopted in clinics, as well as the application to helium-ion patient cases, considering that He-ion therapy has restarted at HIT (Fuchs *et al* 2015, Knäusl *et al* 2016, Tessonnier *et al* 2018).

Afterwards, tumor-specific radiobiological databases may be developed, to avoid using the same database for different tumour types.

Acknowledgments

This work was supported by INFN (project 'MC-INFN/FLUKA'), the Italian University and Research Ministry ('MIUR Dipartimenti di Eccellenza 2018-2022 project F11I18000680001'), and the INSpIRIT project by Regione Lombardia, ID 1161 908, co-funded on resources POR FESR 2014-2020-Asse 1.

ORCID iDs

Wioletta S Kozłowska https://orcid.org/0000-0002-4899-1910
Paola Sala https://orcid.org/0000-0001-9859-5564
Francesca Ballarini https://orcid.org/0000-0002-6629-3382

References

Andersen V *et al* 2004 *Adv. Space Res.* **34** 1302–10
Ballarini F, Altieri S, Bortolussi S, Carante M P, Giroletti E and Protti N 2014 *Radiat. Environ. Biophys.* **53** 525–33
Ballarini F, Altieri S, Bortolussi S, Carante M P, Giroletti E and Protti N 2015 *Radiat. Prot. Dosim.* **166** 75–9
Ballarini F and Carante M P 2016 *Radiat. Phys. Chem.* **128** 18–25
Ballarini F *et al* 2006 *J. Phys.: Conf. Ser.* **41** 151–60
Battistoni G *et al* 2016 *Front. Oncol.* **6** 116
Bauchinger M and Schmid E 1998 *Int. J. Radiat. Biol.* **74** 17–25
Böhlen T T, Cerutti F, Chin M P W, Fassò A, Ferrari A, Ortega P G, Mairani A, Sala P R, Smirnov G and Vlachoudis V 2014 *Nucl. Data Sheets* **120** 211–4
Carante M, Embriaco A, Arico G, Ferrari A, Mairani A, Mein S, Ramos R, Sala P and Ballarini F 2021 *Phys. Med. Biol.* **66** 195009
Carante M P, Aimè C, Tello Cajiao J J and Ballarini F 2018 *Phys. Med. Biol.* **63** 075007
Carante M P, Altieri S, Bortolussi S, Postuma I, Protti N and Ballarini F 2015 *Radiat. Environ. Biophys.* **54** 305–16
Carante M P, Aricò G, Ferrari A, Karger C P, Kozlowska W, Mairani A, Sala P R and Ballarini F 2020 *Int. J. Mol. Sci.* **21** 3973
Carante M P, Aricò G, Ferrari A, Kozlowska W, Mairani A and Ballarini F 2019 *Phys. Med. Biol.* **64** 215008
Carante M P and Ballarini F 2016 *Front. Oncol.* **6** 1–10
Carante M P and Ballarini F 2017 *AIMS Biophys.* **4** 465–90
Carante M P, Tello Cajiao J and Ballarini F 2019 *Radiat. Prot. Dosim.* **183** 111–5
Carrano A V 1973 *Mutation Res./Fundam. Mol. Mech. Mutagenesis* **17** 341–53
Chatterjee A and Schaefer H J 1976 *Radiat. Environ. Biophys.* **13** 215–27
Cornforth M N and Bedford J S 1987 *Radiat. Res.* **111** 385–405

Di Giorgio M et al 2004 Radiat. Prot. Dosim. 108 47–53
Durante M, Yamada S A K, Furusawa Y, Kawata T, Majima H and Nakano T T H 2000 Int. J. Radiat. Oncol. 47 793–8
Elsaesser T and Scholz M 2007 Radiat. Res. 167 319–29
Elsässer T et al 2010 Int. J. Radiat. Oncol. Biol. Phys. 78 1177–83
Embriaco A, Ramos Rand Carante M, Ferrari Sala P, Vercesi V and Ballarini F 2021 Int. J. Mol. Sci. 22 10877
Ferrari A, Sala P R, Fassò A and Ranft J 2005 FLUKA: A Multi-Particle Transport Code (Menlo Park, CA: Stanford Linear Accelerator Center (SLAC)) (https://doi.org/10.5170/CERN-2005-0100)
Fossati P, Matsufuji N, Kamada T and Karger C P 2018 Radiobiological issues in prospective carbon ion therapy trials 45 e1096–110
Fuchs H, Alber M, Schreiner T and Georg D 2015 Med. Phys. 42 5157–66
Henderson F C, McCool K, Seigle J, Jean W, Harter W and Gagnon G J 2009 Neurosurgery 64 A44–53
Inaniwa T, Furukawa T, Kase Y, Matsufuji N, Toshito T, Matsumoto Y, Furusawa Y and Noda K 2010 Phys. Med. Biol. 55 6721–37
Inaniwa T, Kanematsu N, Matsufuji N, Kanai T, Shirai T, Noda K, Tsuji H, Kamada T and Tsujii H 2015 Phys. Med. Biol. 60 3271–86
Karger C P and Peschke P 2017 Phys. Med. Biol. 63 01TR02
Karger C P, Peschke P, Sanchez-Brandelik R, Scholz M and Debus J 2006 Int. J. Radiat. Oncol. Biol. Phys. 66 1488–97
Knäusl B, Fuchs H, Dieckmann K and Georg D 2016 Acta Oncol. 55 751–9
Kowalska A, Nasonova E, Czerski K, Kutsalo P, Pereira W and Krasavin E 2019 Production and distribution of chromosome aberrations in human lymphocytes by particle beams with different let Radiation and Environmental Biophysics 58 99–108
Kozłowska W S et al 2019 Phys. Med. Biol. 64 075012
Magro G, Dahle T J, Molinelli S, Ciocca M, Fossati P, Ferrari A, Inaniwa T, Matsufuji N, Ytre-Hauge K S and Mairani A 2017 Phys. Med. Biol. 62 3814–27
Mairani A, Brons S, Cerutti F, Fassò A, Ferrari A, Krämer M, Parodi K, Scholz M and Sommerer F 2010 Phys. Med. Biol. 55 4273–89
Ohara H, Okazaki N, Monobe M, Watanabe S, Kanayama M and Minamihisamatsu M 1998 Adv. Space Res. 22 1673–82
Paganetti H 2002 Phys. Med. Biol. 47 747–64
Rabbitts T 1994 Nat. Cell Biol. 372 143–9
Saager M, Glowa C, Peschke P, Brons S, Grün R, Scholz M, Huber P E, Debus J and Karger C P 2015 Radiother. Oncol. 117 358–63
Saager M, Glowa C, Peschke P, Brons S, Grün R, Scholz M, Huber P E, Debus J and Karger C P 2016 Acta Oncol. 55 1512–5
Saager M, Glowa C, Peschke P, Brons S, Scholz M, Huber P E, Debus J and Karger C P 2014 Int. J. Radiat. Oncol. Biol. Phys. 90 63–70
Saager M, Peschke P, Brons S, Debus J and Karger C P 2018 Radiother. Oncol. 128 115–20
Scholz M and Elsaesser T 2007 Adv. Space Res. 40 1381–91
Scholz M, Kellerer A M, Kraft-Weyrather W and Kraft G 1997 Radiat. Environ. Biophys. 36 59–66
Schuemann J et al 2019 Radiat. Res. 191 76–92
Tello Cajiao J J, Carante M P, Bernal Rodriguez M A and Ballarini F 2017 DNA Repair 58 38–46
Tello Cajiao J J, Carante M P, Bernal Rodriguez M A and Ballarini F 2018 DNA Repair 64 45–52
Tessonnier T, Mairani A, Chen W, Sala P, Cerutti F, Ferrari A, Haberer T, Debus J and Parodi K 2018 Radiat. Oncol. 13 1–10
Zaider M and Rossi H H 1980 Radiat. Res. 83 732

Chapter 6

Summary and Outlook

6.1 Summary

To summarize, the presented thesis aimed to support advancements in charged particle therapy by using Monte Carlo (MC) techniques. This thesis focuses on the development and application of the MC based tool for particle therapy, which resulted in two published first-author manuscripts (Chapter 3 and Chapter 5) and three co-authored publications (Chapter 2 and Chapter 4).

In the framework of this thesis, upgrades to the FLUKA MC code and the development of the FLUKA Particle Therapy Tool (FPTT) were presented. Advancements in the general purpose MC codes for particle therapy applications have been demonstrated, with exemplary clinical and research applications. The initial studies allowed the simulation of the proton treatment plan using basic extensions to the FLUKA MC code. Further work focused on a clinically oriented implementation of the new radiotherapy module, incorporated in the FLUKA MC code and its GUI - Flair, called the FLUKA Particle Therapy Tool. Comprehensive validation of this MC framework was demonstrated by calculating proton based patient data from two particle therapy facilities. To extend its usage, research applications for this tool have been proposed, such as RBE-weighted dose calculations and dose-averaged LET calculations for carbon ion patient case.

Another research application presented in this thesis are RBE-weighted dose calculations for carbon ion beam therapy. The radiobiological model BIANCA, which is suitable for proton and ion beam therapies, was extended and thoroughly benchmarked against experimental in vivo and in vitro data. Subsequently, two radiobiological BIANCA databases were created: one based on the prediction of chordoma cell survival (RBE_{surv}) [28], as presented in Chapter 4, and the second, created by Embriaco *et al* [319], which estimates the occurrence of dicentric aberrations in the peripheral blood lymphocyte RBE_{ab}. These databases were further applied to estimate the RBE-weighted doses in carbon ion patient cases, as presented in Chapter5. The results obtained from the BIANCA RBE-weighted dose predictions were compared with the predictions obtained with the clinical RBE model LEM I. This work leads to the conclusion that the research biophysical model BIANCA, in principle, can support an increase in robustness in the RBE-weighted dose calculations.

The following sections discuss in detail the additional applications, limitations, and future work resulting from this thesis, mainly focusing on the research gaps in particle therapy, which can be addressed by MC

techniques.

6.2 Beam Model Commissioning in TPS

This section presents the development and application of the MC code, not reported in this thesis, for commissioning the conceptual design of the proton linac system - TULIP (TUrning LInac for Protontherapy) [320]. Work was performed in collaboration with Caterina Cuccagna [321].

During the acceptance of new clinical accelerators, there are two situations, where MC simulations are preferable to direct commissioning measurements. First, when the total amount of data required to commission a system requires an excessive amount of time, and second, when physical limitations in commissioning measurements make it difficult to obtain the required data. For example, when a commissioning procedure based on measured data is not physically feasible because of the early phase of an accelerator design, MC codes are recommended to substitute measurements.

Linear accelerators are a state-of-the-art technology for conventional radiotherapy with photons, although clinical linac solutions are not yet available in the market for charged particle therapy, and the first machine is in the final phase. The linear accelerator TULIP [180, 181] is one of the first clinical proposals conceptually designed by TERA and CERN. The TULIP accelerator is based on a high-gradient linac accelerating system mounted on a rotating gantry [322]. Its design is based on two main sections: the first fixed part, which accelerates the proton beam up to 70 MeV, and the second part, which is mounted on a rotating gantry frame and provides a final beam directly to the isocenter, with a maximum energy of 230 MeV. The general advantage of the TULIP system is that it is fast and has an active energy change between 70 and 230 MeV, which is particularly useful for 3D dose repainting and is suitable for the treatment of moving targets. A more detailed discussion of this design can be found in Cuccagna *et al* [320].

The aim of this study was to examine the feasibility of the TULIP machine for proton treatment planning. For that scope, it was necessary to virtually commission the machine in the commercial TPS. The Phillips TPS *Pinnacle*^{3} was selected for this study. During the design, the TULIP machine parameters for the spot scanning delivery system were fixed, and these data were used as accelerator commissioning data. The Nominal Source-Axis Distance (SAD) was fixed at 196.30 cm (average SAD for the X plane at 216.3 cm and SAD for the Y plane at 176.3 cm), available gantry angles were set from -20 to 200 degrees, and the maximum deflection from the z axis to the isocenter was set up to 17.5 cm, for the X axis and 19 cm for the Y axis. With a fixed set of required measurement data, the TULIP beam model was commissioned for a designed energy range (70-230 MeV), and a pencil beam model was created using the TPS. The exemplary result for 145 MeV beamlet is presented in Figure 6.1 and 6.2.

Very good agreement was obtained for the entire energy range; no significant differences were observed between the pencil beam model created in *Pinnacle*^{3} and the simulation provided by the FLUKA MC code. For the IDDs, a maximum error value of 6 % was obtained for the 110 MeV beam, in close proximity to the Bragg peak. For spot profiles, it was noticed that the beam had a moderately elliptical shape, and lateral profiles for the X-and Y axis required separate models. However, the maximum error for the beam at the isocenter was always less than 2% for both planes. Finally, for the dose per Monitor Unit (MU) density simulations, which were measured at distances of 1.5 or 2 cm from the entrance, the MU in *Pinnacle*^{3} for each energy was calibrated with a maximum error of 1%.

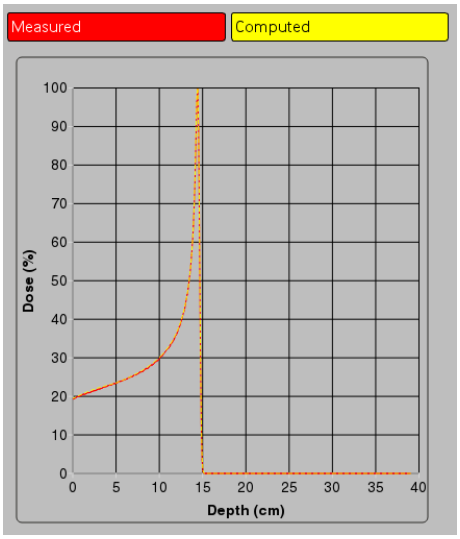

Figure 6.1: Integrated Depth Dose profile for 145 MeV beam, measured/simulated in the FLUKA MC code (red) and modelled by the $Pinnacle^3$ TPS (yellow).

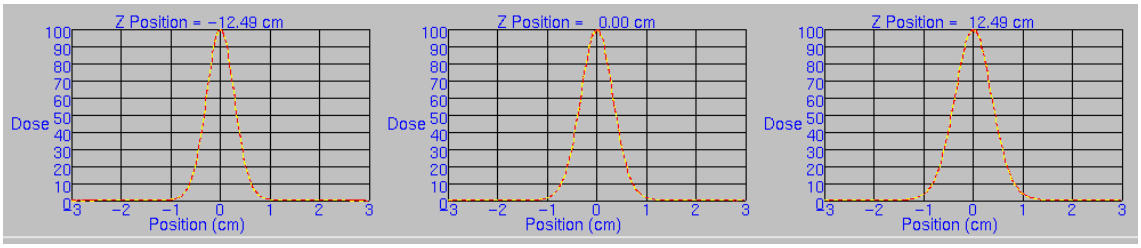

Figure 6.2: Spot lateral profile for 145 MeV beam, measured/simulated in the FLUKA MC code (red) and modelled by the $Pinnacle^3$ TPS (yellow).

After commissioning the pencil beam model in the TPS, the model is typically verified by physical measurements or, as in the presented case, by MC simulations. Verification requires the creation of a variety of plans with TPS (mainly SOBP in a water phantom) and mock-patient fields. Subsequently, verification of the dose model is typically performed by comparing the outcome of irradiation (as in our case, the MC model) and TPS simulation. As such, a simple SOBP treatment plan, using a water phantom, was created with $Pinnacle^3$, which was then exported to the DICOM format and imported into the FLUKA Particle Therapy Tool. The plan was then simulated using a TULIP nozzle and its beam model. The MC results were then exported to the $Pinnacle^3$ TPS for validation. The exemplary results are shown in Figure 6.3.
In general, a good agreement was obtained - the computed range and the width of the SOBP are aligned with the data measured/simulated by MC code; a distance-to-agreement never exceeds 1 mm for all measurement points, which is within clinical requirements. The discrepancy between the validation measurements and computed values in the deposited dose is noticeable. However, the shape of the field was followed correctly, and the error did not exceed a reasonable value of 5% (computed as $(ComputedValue - MeasuredValue)/(MaxDoseValue)$). Because the IDDs, Spot Profiles, and MU density calibrations were

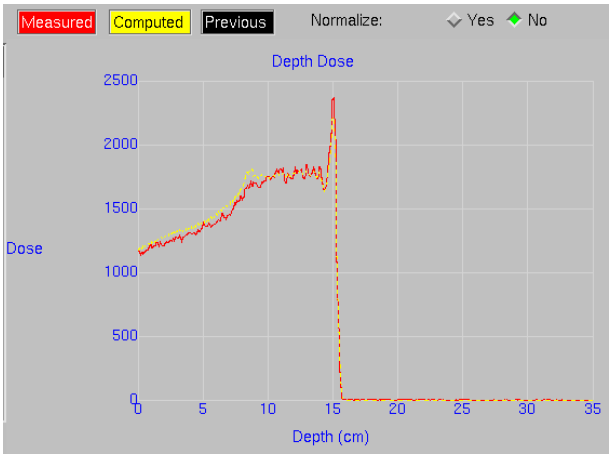

Figure 6.3: Beam model commissioning verification using exemplary plan, *Pinnacle*^{3} computed dept-dose distribution (yellow) and FLUKA simulations as measurements (red)

in a good agreement with TPS, the presented error underwent an additional evaluation to assess the Pencil beam algorithm performance for similar situations. The work plan aims to validate the model using a mock-patient model with treatment plans created by the TPS and to compare the TPS prediction with the full-MC simulation.

In principle, the tool and process presented above can be simply applied to model other conceptual accelerator designs using different TPS and other beam model phase spaces. As clinical proton linacs are currently being designed, some designs even reach the assembly point ([174]). MC based commissioning using the tool presented in this thesis may be beneficial for evaluating the proposed design for clinical and business requirements. At the same time, it may further improve beam modelling in the TPS, overcoming the measurement device limitations during the commissioning process.

MC simulations can be used for additional scaling of the commissioning measurements, owing to their increased accuracy. For example, IDDs measurements are typically performed using large-diameter, parallel plate, and ionization chamber (IC) detectors, with an active cross-section of up to 12 cm. Depending on the beam lateral dimension, energy, and depth of measurements, the area of the ionization chamber may or may not be sufficiently large to acquire the entire beamlet dose. Thus, MC is commonly used to assess this situation and correct the data, if needed [323]. A similar situation can be found while evaluating lateral Spot Profiles measurements when large-angle scattering and secondary products arise from nuclear interactions in water, resulting in a low dose halo, which is hardly assessed with films or scintillation detectors.

6.3 Treatment Planning and Quality Assurance

General purpose MC codes, if properly validated, are accepted as a more accurate method for calculating dose distribution. However, when considering the treatment planning process itself, the problem lies in its speed, which is a crucial parameter in the optimization process. As such, MC simulations based on general purpose codes are seldom implemented in clinical practice and are often found in the research environment [301]. Nonetheless, patient specific quality assurance using DICOM based data, provided by TPS, seems to be an applicable solution, which was one of the aims of the FLUKA Particle Therapy Tool (FPTT), as presented in Chapter 3.

On the other hand, recently, commercial vendors have started to incorporate MC engines into their products, trying to overcome the speed problem. RaySearch Laboratories and Varian Medical Systems provide MC dose calculation engines in their TPS for proton spot scanning based on GPU solutions. The governing principle of the design was to achieve a fast executing code while preserving adequate accuracy for the treatment planning application. Therefore, the question arises whether general purpose MC codes should still be considered, while commercial systems provide clinically acceptable performance with fast MC codes. The answer lies in precision - the computation speed is gained from several contributing and limiting implementation factors, which are described below.

For fast MC codes, dose calculations and particle transport are performed within a rectilinear voxel grid instead of the mean free path for each particle (general MC codes), which is a time consuming procedure. In addition, the tracked particle species, energy range, and materials are limited to modelling, and some physical models are simplified, allowing a speed gain. This is completely different in general MC codes, where each particle can contribute to dose deposition, unless restricted by the user or internal models. For example, it allows the assessment of the neutron dose in patients. Finally, general purpose MC codes are currently the only solutions that can be used for novel ion species.

As mentioned above, although general purpose MC codes might not be suitable for treatment planning, they can support patient-specific quality assurance. The full scope of the available physics models and the possibility of tracking each particle down to the selected energy threshold make them, if properly validated, a suitable tool for an accurate quality check of the treatment plan, saving time in a clinical room. One solution (clinically specific), with home-made software, was implemented at the Massachusetts General Hospital (MGH), Boston [216]. In this thesis Chapter 3 presents, not a facility specific, but an open solution, which can be used, in principle, at any clinical environment with a spot scanning system. The presented FLUKA Particle Therapy Tool is based on the user friendly GUI, allowing re-calculation of treatment plans delivered by the TPS to provide a validation of dose planning calculations. It also allows for checking whether the TPS accurately models the fluence of the beam delivery system, thereby increasing the accuracy of the planning itself. In addition, general purpose MC codes can also be used for log-file recalculation in patient geometry, as presented in Section 1.4.7. This kind of work was already presented by a group in PSI [224], and it is planned to be implemented in FPTT.

6.4 RBE models

RBE modelling is a complex and vividly discussed problem in the particle therapy community. The biological dose is an ambiguous quality, varying on many factors such as dose, particle type, energy spectra, LET, and tissue type, yielding conflicting results in vitro and in vivo [324], with uncertainty of the order of 20-30% [325]. In proton therapy, a fixed value of the RBE 1.1 is used, disregarding its variation at the distal part of the Bragg peak. Two RBE models are used clinically for carbon ions, and one is planned to be used clinically for helium ions [154]. Since their beginning, several versions and upgrades have been presented; however, most of RBE models remain research tools and are not referenced for clinical use.

The RBE varies along the Bragg peak with changes in the LET, and varies between ions. Increased RBE is generally attributed to high LET; however, the underlying mechanisms require further investigation. Numerous studies provided clinical evidence in vitro [326] and in vivo [327] for RBE dependence on LET in proton therapy. Few studies have investigated the dependence of the RBE-LET on other particle types [123, 328]. The recent spotlight is placed on providing variable RBE models in proton therapy, considering LET as an additional biological effectiveness indicator (LET-painting method). Nevertheless, if novel ion species are considered, where in vitro and in vivo experimental results have not yet been fully exploited for RBE estimation, LET estimation might also provide an indication for model improvements. As a result, it may increase the TCP outcome, as it is known that for hypoxic tumor cells irradiated with high LET-particles, TCP increases; however, it may limit NTCP, making it possible to localize hot LET spots in normal tissues, causing late-effect complications. For this purpose, a tool that can track LET within mixed radiation fields is required. The application presented in Chapter 3, which is based on the general purpose MC code FLUKA, can recalculate the distribution of fluence and dose-averaged LET in a patient geometry.

Another important point in the RBE discussion is the probable origin of secondary tumours, where radiation-induced chromosomal aberrations play a significant role. The biophysical model BIANCA, mentioned in Chapters 4 and 5, can estimate chromosomal aberrations caused by radiation. In principle, it can predict cell death based on lethal aberrations, as well as distinct non-lethal aberrations, causing malicious late effects such as dicentrics in peripheral blood lymphocytes. To evaluate new models such as BIANCA as well as to update clinically used models, it is advisable to compare their RBE predictions against the already used and validated clinical RBE models. However, it is not possible to evaluate the performance of the new models and compare the predicted RBE-weighted doses between different models in TPS. The main reason is that the radiobiological effectiveness also depends on the radiation quality, which is not easily accessible in the TPS database, limiting the interaction output data to a minimum. Therefore, the results must rely on MC simulations, as presented in Chapter 5.

Finally, it is possible to apply the selected clinical end-points to different ROIs. For example Fossati *et al* [121] mentioned end-points such as: an acute toxicity, late toxicity, and local control (lack of local recurrence), and tumour response (shrinkage or change of functional properties). All these end-points have different α/β ratios, which depend on the irradiation parameters. Various biological models work better with selected biological end-points than others do. As such, the possibility of including different models in different ROIs should be reviewed, upgraded to the currently used clinical models (and new ones), and various cell databases should be considered.

6.5 Novel ion species

Protons are the most common and cost-effective charged particles used in radiotherapy. However, they exhibit drawbacks in their physical and biological properties, such as augmented MCS and range straggling (causing a wider lateral penumbra and Bragg peak), along with a relatively low RBE, which is only 10% higher than that of photons. Consequently, carbon ions provide a significantly higher RBE with a reduced MCS and range straggling but produce a fragmentation tail in the lateral part of the Bragg peak. In addition, carbon ions require more complex and larger accelerators, which are associated with a higher cost of facility development. Instead, helium ions are considered to be an effective intermediate solution between two clinically used particle species, compensating for the wider Bragg peak and lateral spread of protons, minimizing the fragmentation tail of carbon ions, and providing a potential for tumour control similar to that of carbon ions [329]. This new area of charged particle therapy requires precise research tools for proper evaluation of particle interactions and biological effectiveness. As proven in this thesis, general purpose MC codes can successfully support both requirements.

Starting with the new requirements for helium-ion accelerators, there is a requirement to provide a machine with a smaller cost and footprint. The methods presented by Cuccagna *et al* [320] and Section 6.2 can be incorporated to evaluate the clinical requirements for new accelerator proposals. Moreover, while new commercial TPS for helium ions are being approved for clinical use, there is still a limited possibility to evaluate the advantages of new ions without comparison with other ion species. As such, the FPTT may provide an answer for dosimetric comparison between proton, helium, and carbon ions for various treatment scenarios. Detailed modelling of the helium ion beam in TPSs must be provided and validated. Therefore, a number of studies investigating the physical properties of helium ions have to be performed based on radiation transport simulations, mainly through MC methods. Finally, new biological models for helium ion beams must be incorporated in TPS predictions. The applications presented in Chapters 4 and 5 are advantageous for evaluating performance, and further enhanced toward helium ions by Carante *et al* [330].

It is worth mentioning that the choice of an optimal ion species for treatment is determined by patient parameters (age, general health condition) and tumour characteristics (type and localization), which must be evaluated clinically in detail. In some cases of complex tumors located close to healthy tissues, a more adaptive approach is required. For example, Multi-Ion radiotherapy is being considered, which enables profit from each ion simultaneously, according to their beneficial physical and/or biological characteristics. The development of a dose-LET-optimized treatment plan containing various ion species allows the optimization of LET delivery to provide a high TCP and low NTCP. As a result, Multi-Ion radiotherapy may allow the delivery of lower-LET beams (proton or helium ions), with sharp margins at tumour regions located close to normal tissue, and higher LET irradiation (carbon, oxygen ions) into radioresistant and hypoxic tumour regions [331]. However, as mentioned above, LET and RBE dependence is complex; therefore, direct translation of LET into biological effectiveness requires further development of RBE models.

Finally, radioactive ion beams such as carbon-11 or oxygen-15 may be of interest if the scope is to provide ion treatment, where the range of the delivered particles can be verified online or offline using PET scanners. Therefore, as Augusto presented [332], for this kind of study, the general purpose MC code plays a significant role in support benchmark prediction of experimental values.

6.6 Conclusion and Outlook

The use of Monte Carlo codes may support research in particle therapy in many ways, starting with the development and validation of the new accelerator design by providing input databases for TPS and supporting QA procedures, improving the description of radiobiological models, and supporting treatment innovation with novel-ion species in clinical practice. However, it seems clear that general purpose MC codes are currently not, and will hardly be used in clinical practice in the upcoming years. Unless proper GPU-based implementations are fully exploited, the problem of low speed can be solved. Currently, some intermediate solutions have to be utilized, as such TPSs may use simplified and faster MC codes, reaching a reasonable dose calculation accuracy within a reasonable time frame for clinical workflows.

On the other hand, general purpose MC codes will be, and are currently used for research purposes, with the main focus being on the modelling of radiation transport interactions. Obviously, MC codes without a thoroughly validated physics model cannot be of any support for this research; therefore, additional experimental studies on particle interaction cross-sections within the therapeutic energy range are required. This must be followed by MC benchmarking studies and code upgrades. In addition, further radiobiological studies are of the same importance, and comparisons between various models, creating new ones, and upgrading currently used ones should be continued.

The outcome presented in this thesis, which focuses on bridging the gaps in particle therapy with MC codes, can be used for clinical and research applications, supporting dose distribution calculation for PSQA purposes, and evaluation of the biological-weighted dose for ion beam therapy, as well as novel radiobiological models. In view of these results, future work is planned, which will include improvement of the user experience for FPTT and enhancement with new features, such as treatment plan recalculations based on the log-files, gamma evaluations for dose comparison, and embedded easy-to-use RBE-based dose calculations. In addition, the BIANCA model will be evaluated and benchmarked with more patient cases, and treatment plan optimization will be performed using BIANCA RBE databases.

To summarize, to fulfill the growing interest in particle therapy, MC codes supported by the abovementioned advantages must be utilized and promoted within the research community. First, for the scope of creating accurate and precise physics models, access to research beam time in clinical accelerators should be increased, which will support the creation and validation of physical and radiobiological models. In addition, cost-effective accelerator designs can support the building of more particle therapy centers, as well as in lower-income regions, where the initial investment costs play a crucial role. The exchange of knowledge among various research centers will provide all the information necessary to select the optimal treatment. This will bring radiation therapy another step closer towards personalized medicine and may help to improve treatment outcomes and reduce treatment side effects.

Bibliography

[1] M. Krämer, E. Scifoni, C. Schuy, M. Rovituso, W. Tinganelli, A. Maier, R. Kaderka, W. Kraft-Weyrather, S. Brons, T. Tessonnier, K. Parodi, and M. Durante, "Helium ions for radiotherapy? Physical and biological verifications of a novel treatment modality," *Medical Physics*, vol. 43, pp. 1995–2004, mar 2016.

[2] I. Kantemiris, P. Karaiskos, P. Papagiannis, and A. Angelopoulos, "Dose and dose averaged LET comparison of 1H, 4He, 6Li, 8Be, 10B, 12C, 14N, and 16O ion beams forming a spread-out Bragg peak," *Medical Physics*, vol. 38, no. 12, pp. 6585–6591, 2011.

[3] D. Schardt, T. Elsässer, and D. Schulz-Ertner, "Heavy-ion tumor therapy: Physical and radiobiological benefits," *Reviews of Modern Physics*, vol. 82, no. 1, pp. 383–425, 2010.

[4] A. Mairani, *Nucleus-nucleus interaction modelling and applications in ion therapy treatment planning*, vol. 1. 2008.

[5] K. Gunzert-Marx, H. Iwase, D. Schardt, and R. S. Simon, "Secondary beam fragments produced by 200 MeV u-1 12C ions in water and their dose contributions in carbon ion radiotherapy," *New Journal of Physics*, vol. 10, 2008.

[6] E. Haettner, H. Iwase, M. Krämer, G. Kraft, and D. Schardt, "Experimental study of nuclear fragmentation of 200 and 400 MeV/u 12C ions in water for applications in particle therapy," *Physics in Medicine and Biology*, vol. 58, no. 23, pp. 8265–8279, 2013.

[7] C.-M. C. Ma, *Proton and Carbon Ion Therapy*. Boca Raton: CRC Press, oct 2012.

[8] J. S. Loeffler and M. Durante, "Charged particle therapy–optimization, challenges and future directions.," *Nature reviews. Clinical oncology*, vol. 10, no. 7, pp. 411–424, 2013.

[9] C. P. Karger and P. Peschke, "RBE and related modeling in carbon-ion therapy," *Physics in Medicine and Biology*, vol. 63, p. 01TR02, dec 2017.

[10] W. K. Weyrather, S. Ritter, M. Scholz, and G. Kraft, "RBE for carbon track-segment irradiation in cell lines of differing repair capacity," *International Journal of Radiation Biology*, vol. 75, no. 11, pp. 1357–1364, 1999.

[11] J. B. Farr, J. B. Flanz, A. Gerbershagen, and M. F. Moyers, "New horizons in particle therapy systems," *Medical Physics*, vol. 45, no. 11, pp. e953–e983, 2018.

[12] O. Jäkel, C. P. Karger, and J. Debus, "The future of heavy ion radiotherapy," *Medical Physics*, vol. 35, no. 12, pp. 5653–5663, 2008.

[13] W. S. Kozłowska, T. T. Böhlen, C. Cuccagna, A. Ferrari, F. Fracchiolla, D. Georg, G. Magro, A. Mairani, M. Schwarz, V. Vlachoudis, and D. Georg, "FLUKA particle therapy tool for Monte Carlo independent calculation of scanned proton and carbon ion beam therapy," *Physics in Medicine and Biology*, vol. 64, p. 075012, mar 2019.

[14] M. Moteabbed, S. España, and H. Paganetti, "Monte Carlo patient study on the comparison of prompt gamma and PET imaging for range verification in proton therapy," *Physics in Medicine and Biology*, vol. 56, pp. 1063–1082, feb 2011.

[15] K. Parodi, A. Mairani, S. Brons, B. Hasch, F. Sommerer, J. Naumann, O. Jäkel, T. Haberer, and J. Debus, "Monte Carlo simulations to support start-up and treatment planning of scanned proton and carbon ion therapy at a synchrotron-based facility," *Physics in Medicine and Biology*, vol. 57, pp. 3759–3784, jun 2012.

[16] G. Battistoni, J. Bauer, T. T. Böhlen, F. Cerutti, M. P. W. Chin, R. Dos Santos Augusto, A. Ferrari, P. G. Ortega, W. Kozłowska, G. Magro, A. Mairani, K. Parodi, P. R. Sala, P. Schoofs, T. Tessonnier, and V. Vlachoudis, "The FLUKA Code: An Accurate Simulation Tool for Particle Therapy," *Frontiers in Oncology*, vol. 6, may 2016.

[17] B. Kozlovsky, R. J. Murphy, and R. Ramaty, "Nuclear Deexcitation Gamma-Ray Lines from Accelerated Particle Interactions," *The Astrophysical Journal Supplement Series*, no. 141, pp. 523–541, 2002.

[18] F. Ballarini and M. P. Carante, "Chromosome aberrations and cell death by ionizing radiation: Evolution of a biophysical model," *Radiation Physics and Chemistry*, vol. 128, pp. 18–25, nov 2016.

[19] S. E. Stoll U, Schmidt A and K. J, "Killing and mutation of chinese hamster v79 cells exposed to accelerated oxygen and neon ions," *Radiat. Res.*, vol. 142, p. 288, 1995.

[20] M. P. Carante, G. Aricò, A. Ferrari, W. Kozlowska, A. Mairani, and F. Ballarini, "First benchmarking of the BIANCA model for cell survival prediction in a clinical hadron therapy scenario," *Physics in Medicine and Biology*, vol. 64, p. 215008, oct 2019.

[21] R. Belli, F.and Cera, M. Cherubini, and M. Dalla, "RBE-LET relationships for cell inactivation and mutation induced by low energy protons in V79 cells: further results at the LNL facility," *International Journal of Radiation Biology*, vol. 74, pp. 501–509, jan 1998.

[22] M. Folkard, K. M. Prise, B. Vojnovic, H. C. Newman, M. J. Roper, and B. D. Michael, "Inactivation of v79 cells by low-energy protons, deuterons and helium-3 ions," *Int. J. Radiat. Biol.*, vol. 69, p. 729, 1996.

[23] Y. Furusawa, K. Fukutsu, M. Aoki, H. Itsukaichi, K. Eguchi-Kasai, H. Ohara, F. Yatagai, T. Kanai, and K. Ando, "Inactivation of aerobic and hypoxic cells from three different cell lines by accelerated (3)He-, (12)C- and (20)Ne-ion beams.," *Radiation research*, vol. 154, pp. 485–96, nov 2000.

[24] S. A. Pathak R, Dey S K and K.-B. A. R, "Genotoxic effects in m5 cells and chinese hamster v79 cells after exposure to 7li-beam (let: 60 kev/microm) and correlation of their survival dynamics to nuclear damages and cell death," *Mutat. Res.*, vol. 628, p. 56, 2007.

[25] G. D. T. Cox R, Thacker J and M. R. J, "Mutation and inactivation of mammalian cells by various ionising radiations," *Nature*, vol. 267, p. 425, 1977.

[26] T. Elsässer, W. K. Weyrather, T. Friedrich, M. Durante, G. Iancu, M. Krämer, G. Kragl, S. Brons, M. Winter, K. J. Weber, and M. Scholz, "Quantification of the relative biological effectiveness for ion beam radiotherapy: Direct experimental comparison of proton and carbon ion beams and a novel approach for treatment planning," *International Journal of Radiation Oncology, Biology, Physics*, vol. 78, no. 4, pp. 1177–1183, 2010.

[27] C. P. Karger, P. Peschke, R. Sanchez-Brandelik, M. Scholz, and J. Debus, "Radiation tolerance of the rat spinal cord after 6 and 18 fractions of photons and carbon ions: Experimental results and clinical implications," *International Journal of Radiation Oncology, Biology, Physics*, vol. 66, pp. 1488–1497, dec 2006.

[28] M. P. Carante, G. Aricò, A. Ferrari, C. P. Karger, W. Kozlowska, A. Mairani, P. R. Sala, and F. Ballarini, "In Vivo Validation of the BIANCA Biophysical Model: Benchmarking against Rat Spinal Cord RBE Data," *International Journal of Molecular Sciences*, vol. 21, p. 3973, jun 2020.

[29] M. Saager, C. Glowa, P. Peschke, S. Brons, M. Scholz, P. E. Huber, J. Debus, and C. P. Karger, "Carbon ion irradiation of the rat spinal cord: Dependence of the relative biological effectiveness on linear energy transfer," *International Journal of Radiation Oncology, Biology, Physics*, vol. 90, pp. 63–70, sep 2014.

[30] M. Saager, C. Glowa, P. Peschke, S. Brons, R. Grün, M. Scholz, P. E. Huber, J. Debus, and C. P. Karger, "The relative biological effectiveness of carbon ion irradiations of the rat spinal cord increases linearly with LET up to 99 keV/μm," *Acta Oncologica*, vol. 55, pp. 1512–1515, dec 2016.

[31] M. Saager, C. Glowa, P. Peschke, S. Brons, R. Grün, M. Scholz, P. E. Huber, J. Debus, and C. P. Karger, "Split dose carbon ion irradiation of the rat spinal cord: Dependence of the relative biological effectiveness on dose and linear energy transfer," *Radiotherapy and Oncology*, vol. 117, pp. 358–363, nov 2015.

[32] M. Saager, P. Peschke, S. Brons, J. Debus, and C. P. Karger, "Determination of the proton RBE in the rat spinal cord: Is there an increase towards the end of the spread-out Bragg peak?," *Radiotherapy and Oncology*, vol. 128, pp. 115–120, jul 2018.

[33] W. S. Kozłowska, M. P. Carante, G. Aricò, A. Embriaco, A. Ferrari, G. Magro, A. Mairani, R. Ramos, P. Sala, D. Georg, and F. Ballarini, "First application of the BIANCA biophysical model to carbon-ion patient cases," *Physics in Medicine Biology*, vol. 67, p. 115013, jun 2022.

[34] WHO, "Global cancer observatory: Cancer today." `https://gco.iarc.fr/today`, 2018. Accessed: 2019-10-29.

[35] "European cancer information system." `https://ecis.jrc.ec.europa.eu`, 2019. Accessed: 2019-10-29.

[36] G. Delaney, S. Jacob, C. Featherstone, and M. Barton, "The role of radiotherapy in cancer treatment: Estimating optimal utilization from a review of evidence-based clinical guidelines," *Cancer*, vol. 104, no. 6, pp. 1129–1137, 2005.

[37] *Relative Biological Effectiveness in Ion Beam Therapy.* No. 461 in Technical Reports Series, Vienna: International Atomic Energy Agency, 2008.

[38] Y. Wang, W. Deng, N. Li, S. Neri, A. Sharma, W. Jiang, and S. H. Lin, "Combining immunotherapy and radiotherapy for cancer treatment: Current challenges and future directions," *Frontiers in Pharmacology*, vol. 9, no. mar, pp. 1–11, 2018.

[39] H. Kogelnik, "Inauguration of radiotherapy as a new scientific speciality by Leopold Freund 100 years ago," *Radiotherapy and Oncology*, vol. 42, pp. 203–211, mar 1997.

[40] U. Amaldi, *Particle Accelerators: From Big Bang Physics to Hadron Therapy*. Cham: Springer International Publishing, 2015.

[41] W. Röntgen, "Ueber eine neue Art von Strahlen," *Annalen der Physik*, vol. 300, no. 1, pp. 12–17, 1898.

[42] E. P. Pendergrass, "The life and times of emil h. grubbe. paul c. hodges," *Isis*, vol. 56, no. 3, pp. 395–395, 1965.

[43] L. Freund, "Ein mit Röntgenstrahlen behandelter Fall von Naevus pigmentosus piliferus," *Wiener Medizinische Wochenschrift*, vol. 47, no. 10, pp. 428–434, 1897.

[44] R. R. Wilson, "Radiological Use of Fast Protons," *Radiology*, vol. 47, no. 5, pp. 487–491, 1946.

[45] M. L. M. Boone, J. H. Lawrence, W. G. Connor, R. Morgado, J. A. Hicks, and R. C. Brown, "Introduction to the use of protons and heavy ions in radiation therapy: Historical perspective," *International Journal of Radiation Oncology, Biology, Physics*, vol. 3, pp. 65–69, 1977.

[46] J. R. Castro, G. T. Y. Chen, and E. A. Blakely, "Current Considerations in Heavy Charged-Particle Radiotherapy: A Clinical Research Trial of the University of California Lawrence Berkeley Laboratory, Northern California Oncology Group, and Radiation Therapy Oncology Group," *Radiation Research*, vol. 104, no. 2s, pp. S263–S271, 1985.

[47] C. A. Tobias, J. T. Lyman, A. Chatterjee, J. Howard, H. D. Maccabee, M. R. Raju, A. R. Smith, J. M. Sperinde, and G. P. Welch, "Radiological Physics Characteristics of the Extracted Heavy Ion Beams of the Bevatron," *Science*, vol. 174, no. 4014, pp. 1131–1134, 1971.

[48] P. H. Fowler and D. H. Perkins, "The Possibility of Therapeutic Applications of Beams of Negative π-Mesons," *Nature*, vol. 189, no. 4764, pp. 524–528, 1961.

[49] J. M. Slater, D. W. Miller, and J. O. Archambeau, "Development of a hospital-based proton beam treatment center," *International Journal of Radiation Oncology, Biology, Physics*, vol. 14, no. 4, pp. 761–775, 1988.

[50] J. M. Slater, J. O. Archambeau, D. W. Miller, M. I. Notarus, W. Preston, and J. D. Slater, "The proton treatment center at Loma Linda University Medical Center: Rationale for and description of its development," *International Journal of Radiation Oncology, Biology, Physics*, vol. 22, pp. 383–389, jan 1992.

[51] S. Scheib, *Spot-Scanning mit Protonen experimentelle Resultate und Therapieplanung ETH Library*. PhD thesis, 1993.

[52] PTCOG, "Particle therapy co-operative group." `https://www.ptcog.ch`, 2022. Accessed: 2020-09-29.

[53] J. Seco and F. Verhaegen, *Monte Carlo Techniques in Radiation Therapy*. Imaging in medical Diagnosis A, Taylor & Francis, 2013.

[54] O. N. Vassiliev, *Monte Carlo Methods for Radiation Transport*. Biological and Medical Physics, Biomedical Engineering, Cham: Springer International Publishing, 2017.

[55] N. Metropolis and S. Ulam, "The monte carlo method," *Journal of the American statistical Association*, vol. 44, no. 247, pp. 335–341, 1949.

[56] R. Eckhardt, "Stan ulam, john von neumann, and the monte carlo method," *Los Alamos Science*, vol. 15, pp. 131–136, 1987.

[57] M. Nicholas, "The beginning of the monte carlo method," *Los Alamos Science*, Jan 1987.

[58] W. L. Dunn and J. K. Shultis, "The basis of monte carlo," in *Exploring Monte Carlo Methods* (W. L. Dunn and J. K. Shultis, eds.), pp. 21 – 46, Amsterdam: Elsevier, 2012.

[59] M. C. Cantone and C. Hoeschen, *Radiation Physics for Nuclear Medicine*, ch. Chapter 4 Principles of Monte Carlo Calculations and Codes, Alberto Fassò, Alfredo Ferrari, and Paola R.Sala, pp. 1–285. Springer Berlin Heidelberg, 2011.

[60] F. James, "A review of pseudorandom number generators," *Computer Physics Communications*, vol. 60, pp. 329–344, oct 1990.

[61] A. Ferrari, P. R. Sala, A. Fassò, and J. Ranft, "FLUKA: A Multi-Particle Transport Code," Tech. Rep. October, Stanford Linear Accelerator Center (SLAC), Menlo Park, CA, dec 2005.

[62] T. T. Böhlen, F. Cerutti, M. P. W. Chin, A. Fassó, A. Ferrari, P. G. Ortega, A. Mairani, P. R. Sala, G. Smirnov, and V. Vlachoudis, "The FLUKA Code: Developments and Challenges for High Energy and Medical Applications," *Nuclear Data Sheets*, vol. 120, pp. 211–214, jun 2014.

[63] C. Ahdida, D. Bozzato, D. Calzolari, F. Cerutti, N. Charitonidis, A. Cimmino, A. Coronetti, G. L. D'Alessandro, A. Donadon Servelle, L. S. Esposito, R. Froeschl, R. García Alía, A. Gerbershagen, S. Gilardoni, D. Horváth, G. Hugo, A. Infantino, V. Kouskoura, A. Lechner, B. Lefebvre, G. Lerner, M. Magistris, A. Manousos, G. Moryc, F. Ogallar Ruiz, F. Pozzi, D. Prelipcean, S. Roesler, R. Rossi, M. Sabaté Gilarte, F. Salvat Pujol, P. Schoofs, V. Stránský, C. Theis, A. Tsinganis, R. Versaci, V. Vlachoudis, A. Waets, and M. Widorski, "New Capabilities of the FLUKA Multi-Purpose Code," *Front. Phys.*, vol. 9, p. 788253. 14 p, 2022.

[64] S. Agostinelli, J. Allison, K. Amako, J. Apostolakis, H. Araujo, P. Arce, M. Asai, D. Axen, S. Banerjee, G. Barrand, F. Behner, L. Bellagamba, J. Boudreau, L. Broglia, A. Brunengo, H. Burkhardt, S. Chauvie, J. Chuma, R. Chytracek, G. Cooperman, G. Cosmo, P. Degtyarenko, A. Dell'Acqua, G. Depaola, D. Dietrich, R. Enami, A. Feliciello, C. Ferguson, H. Fesefeldt, G. Folger, F. Foppiano, A. Forti, S. Garelli, S. Giani, R. Giannitrapani, D. Gibin, J. J. Gomez Cadenas, I. Gonzalez, G. Gracia Abril, G. Greeniaus, W. Greiner, V. Grichine, A. Grossheim, S. Guatelli, P. Gumplinger, R. Hamatsu, K. Hashimoto, H. Hasui, A. Heikkinen, A. Howard, V. Ivanchenko, A. Johnson, F. W. Jones, J. Kallenbach, N. Kanaya, M. Kawabata, Y. Kawabata, M. Kawaguti, S. Kelner, P. Kent, A. Kimura, T. Kodama, R. Kokoulin, M. Kossov, H. Kurashige, E. Lamanna, T. Lampen, V. Lara, V. Lefebure, F. Lei, M. Liendl, W. Lockman, F. Longo, S. Magni, M. Maire, E. Medernach, K. Minamimoto, P. Mora de Freitas, Y. Morita, K. Murakami, M. Nagamatu, R. Nartallo, P. Nieminen, T. Nishimura, K. Ohtsubo, M. Okamura, S. O'Neale, Y. Oohata, K. Paech, J. Perl, A. Pfeiffer,

M. G. Pia, F. Ranjard, A. Rybin, S. Sadilov, E. di Salvo, G. Santin, T. Sasaki, N. Savvas, Y. Sawada, S. Scherer, S. Sei, V. Sirotenko, D. Smith, N. Starkov, H. Stoecker, J. Sulkimo, M. Takahata, S. Tanaka, E. Tcherniaev, E. Safai Tehrani, M. Tropeano, P. Truscott, H. Uno, L. Urban, P. Urban, M. Verderi, A. Walkden, W. Wander, H. Weber, J. P. Wellisch, T. Wenaus, D. C. Williams, D. Wright, T. Yamada, H. Yoshida, and D. Zschiesche, "GEANT4 - A simulation toolkit," *Nuclear Instruments and Methods in Physics Research, Section A: Accelerators, Spectrometers, Detectors and Associated Equipment*, vol. 506, pp. 250–303, jul 2003.

[65] J. Allison, K. Amako, J. Apostolakis, H. Araujo, P. A. Dubois, M. Asai, G. Barrand, R. Capra, S. Chauvie, R. Chytracek, G. a. P. Cirrone, G. Cooperman, G. Cosmo, G. Cuttone, G. G. Daquino, M. Donszelmann, M. Dressel, G. Folger, F. Foppiano, J. Generowicz, V. Grichine, S. Guatelli, P. Gumplinger, A. Heikkinen, I. Hrivnacova, A. Howard, S. Incerti, V. Ivanchenko, T. Johnson, F. Jones, T. Koi, R. Kokoulin, M. Kossov, H. Kurashige, V. Lara, S. Larsson, F. Lei, F. Longo, M. Maire, A. Mantero, B. Mascialino, I. McLaren, P. M. Lorenzo, K. Minamimoto, K. Murakami, P. Nieminen, L. Pandola, S. Parlati, L. Peralta, J. Perl, A. Pfeiffer, M. G. Pia, A. Ribon, P. Rodrigues, G. Russo, S. Sadilov, G. Santin, T. Sasaki, D. Smith, N. Starkov, S. Tanaka, E. Tcherniaev, B. Tomé, A. Trindade, P. Truscott, L. Urban, M. Verderi, A. Walkden, J. P. Wellisch, D. C. Williams, D. Wright, H. Yoshida, and M. Peirgentili, "Geant4 developments and applications," *IEEE Transactions on Nuclear Science*, vol. 53, no. 1, pp. 270–278, 2006.

[66] F. Salvat, J. Fernandez-Varea, and J. Sempau, "PENELOPE, A Code System for Monte Carlo Simulation of Electron and Photon Transport," in *Proceedings of a Workshop/Training Course OECD/NEA*, no. 4-7 July, 2011.

[67] D. Sarrut, M. Bardiès, N. Boussion, N. Freud, S. Jan, J.-M. Létang, G. Loudos, L. Maigne, S. Marcatili, T. Mauxion, P. Papadimitroulas, Y. Perrot, U. Pietrzyk, C. Robert, D. R. Schaart, D. Visvikis, and I. Buvat, "A review of the use and potential of the GATE Monte Carlo simulation code for radiation therapy and dosimetry applications," *Medical Physics*, vol. 41, p. 064301, may 2014.

[68] P. Arce, P. Rato, M. Canadas, and J. I. Lagares, "GAMOS: A Geant4-based easy and flexible framework for nuclear medicine applications," in *2008 IEEE Nuclear Science Symposium Conference Record*, pp. 3162–3168, IEEE, oct 2008.

[69] J. Perl, J. Shin, J. Schümann, B. A. Faddegon, and H. Paganetti, "TOPAS: An innovative proton Monte Carlo platform for research and clinical applications," *Medical Physics*, vol. 39, no. 11, pp. 6818–6837, 2012.

[70] T. Aso, Y. Maeda, G. Iwai, W. Takase, T. Sasaki, Y. Watase, T. Yamashita, T. Akagi, and Y. Nakano, "Extension of the particle therapy simulation framework to hospital information systems and multi-grid environments," *Proceedings - 15th IEEE International Conference on Computational Science and Engineering, CSE 2012 and 10th IEEE/IFIP International Conference on Embedded and Ubiquitous Computing, EUC 2012*, pp. 229–234, 2012.

[71] J. T. Goorley, M. R. James, T. E. Booth, F. B. Brown, J. S. Bull, L. J. Cox, J. W. Durkee, Jr., J. S. Elson, M. L. Fensin, R. A. Forster, III, J. S. Hendricks, H. G. Hughes, III, R. C. Johns, B. C. Kiedrowski, R. L. Martz, S. G. Mashnik, G. W. McKinney, D. B. Pelowitz, R. E. Prael, J. E. Sweezy,

L. S. Waters, T. Wilcox, and A. J. Zukaitis, "Initial MCNP6 Release Overview," *Nuclear Technology*, vol. 180, pp. 298–315, dec 2012.

[72] D. Rogers, "Fifty years of Monte Carlo simulations for medical physics," *Physics in Medicine and Biology*, vol. 51, no. 13, pp. R287–R301, 2006.

[73] A. Mairani, S. Brons, F. Cerutti, A. Fassò, A. Ferrari, M. Krämer, K. Parodi, M. Scholz, and F. Sommerer, "The FLUKA Monte Carlo code coupled with the local effect model for biological calculations in carbon ion therapy," *Physics in Medicine and Biology*, vol. 55, pp. 4273–89, aug 2010.

[74] J. Bauer, F. Sommerer, A. Mairani, D. Unholtz, R. Farook, J. Handrack, K. Frey, T. Marcelos, T. Tessonnier, S. Ecker, B. Ackermann, M. Ellerbrock, J. Debus, and K. Parodi, "Integration and evaluation of automated Monte Carlo simulations in the clinical practice of scanned proton and carbon ion beam therapy.," *Physics in medicine and biology*, vol. 59, no. 16, pp. 4635–59, 2014.

[75] A. Mirandola, S. Molinelli, G. Vilches Freixas, A. Mairani, E. Gallio, D. Panizza, S. Russo, M. Ciocca, M. Donetti, G. Magro, S. Giordanengo, and R. Orecchia, "Dosimetric commissioning and quality assurance of scanned ion beams at the Italian National Center for Oncological Hadrontherapy," *Med. Phys.*, vol. 42, pp. 5287–5300, aug 2015.

[76] "Stopping power and ranges for protons and alpha particles," *Journal of the International Commission on Radiation Units and Measurements*, vol. os25, pp. NP–NP, 04 2016.

[77] NIST, "PSTAR and ASTAR." `https://physics.nist.gov/PhysRefData/Star/Text/intro.html`, 2015.

[78] H. Bethe, "Zur Theorie des Durchgangs schneller Korpuskularstrahlen durch Materie," *Annalen der Physik*, vol. 397, no. 3, pp. 325–400, 1930.

[79] L. E. Porter, "Modified Bethe-Bloch stopping power parameters for kapton," *International Journal of Quantum Chemistry*, vol. 75, no. 4-5, pp. 943–950, 1999.

[80] "5. Recommended Values for Key Data," *Journal of the International Commission on Radiation Units and Measurements*, vol. 14, pp. 31–48, 10 2016.

[81] W. H. Barkas, J. N. Dyer, and H. H. Heckmann, "Resolution of the σ^--mass anomaly," *Phys. Rev. Lett*, vol. 11, pp. 26–28, July 1963.

[82] F. Bloch, "Zur Bremsung rasch bewegter Teilchen beim Durchgang durch Materie," *Annalen der Physik*, vol. 408, no. 3, pp. 285–320, 1933.

[83] N. F. Mott, "The scattering of fast electrons by atomic nuclei," *Proceedings of the Royal Society of London. Series A, Containing Papers of a Mathematical and Physical Character*, vol. 124, no. 794, pp. 425–442, 1929.

[84] P. Vavilov, "Ionization Losses of High-Energy Heavy Particles," *Soviet Phys. JETP*, vol. Vol: 5, no. 4, pp. 749–751, 1957.

[85] L. D. Landau, "On the energy loss of fast particles by ionization," *J. Phys*, vol. 8, no. 4, pp. 201–205, 1944.

[86] T. Bortfeld, "An analytical approximation of the Bragg curve for therapeutic proton beams.," *Medical Physics*, vol. 24, no. 12, p. 2024, 1997.

[87] U. Linz, "Ion beam therapy with ions heavier than protons: Performance and prospects," *6th International Particle Accelerator Conference, IPAC 2015*, pp. 3654–3656, 2015.

[88] G. Moliere, "Theorie der Streuung schneller geladener Teilchen II Mehrfach-und Vielfachstreuung," *Zeitschrift für Naturforschung A*, vol. 3, pp. 78–97, feb 1948.

[89] G. Molière, "Theorie der Streuung schneller geladener Teilchen," *Zeitschrift für Naturforschung A*, vol. 10, pp. 177–211, mar 1955.

[90] V. L. Highland, "Some practical remarks on multiple scattering," *Nuclear Instruments and Methods*, vol. 129, pp. 497–499, nov 1975.

[91] Y. S. Tsai, "Pair production and bremsstrahlung of charged leptons," *Reviews of Modern Physics*, vol. 46, no. 4, pp. 815–851, 1974.

[92] ICRU, "Nuclear Data for Neutron and Proton Radiotherapy and for Radiation Protection," *Radiation Research*, vol. 156, no. 2, pp. 223–224, 2001.

[93] H. Paganetti, "Nuclear interactions in proton therapy: Dose and relative biological effect distributions originating from the primary and secondary particles," *Physics in Medicine and Biology*, vol. 47, no. 5, pp. 747–764, 2002.

[94] G. Aricò, T. Gehrke, J. Jakubek, R. R. Gallas, S. Berke, O. Jäkel, A. Mairani, A. Ferrari, and M. Martišíková, "Investigation of mixed ion fields in the forward direction for 220.5 MeV/u helium ion beams: Comparison between water and PMMA targets," *Physics in Medicine and Biology*, vol. 62, no. 20, pp. 8003–8024, 2017.

[95] G. Aricò, T. Gehrke, R. R. Gallas, A. Mairani, O. Jäkel, and M. Martišíková, "Investigation of single carbon ion fragmentation in water and PMMA for hadron therapy," *Physics in Medicine and Biology*, vol. 64, no. 5, 2019.

[96] M. Durante and H. Paganetti, "Nuclear physics in particle therapy: a review," *Reports on Progress in Physics*, vol. 79, p. 096702, sep 2016.

[97] J. Alonso, "Review of ion beam therapy: present and future," *EPAC 2000. The 7th European Particle Accelerator Conference. Austria Center. Vienna, Austria*, pp. 235–239, 2000.

[98] T. W. Speer, R. Rubin, I. Rusu, I. Rusu, Y. Yu, L. Doyle, C. B. Saw, N. J. Yue, J. Classen, C. Nieder, F.-M. Kong, J. Wang, L. G. Jensen, B. S. Rose, A. J. Mundt, R. Rengan, C. R. Thomas, N. R. Patel, M. L. Wong, R. Rubin, B. J. Fisher, L. C. Daugherty, C. A. Knowlton, M. K. Mackay, I. Rusu, C. Heese, D. Lightfoot, L. T. Komarnicky-Kocher, F. Alite, C. Weiss, C. Roedel, P. Guerrieri, P. Montemaggi, T. W. Speer, L. G. Jensen, L. K. Mell, Y. Yu, L. Doyle, S. Mose, B. F. Hasson, D. Michalski, M. S. Huq, C. E. Rübe, S. Mose, C. E. Rübe, B. J. Huth, T. S. Quang, E. J. Gracely, and E. J. Gracely, "Tumor Control Probability (TCP)," in *Encyclopedia of Radiation Oncology* (L. W. Brady and T. E. Yaeger, eds.), pp. 921–922, Berlin, Heidelberg: Springer Berlin Heidelberg, 2013.

[99] M. Krämer and G. Kraft, "Track structure and DNA damage," *Advances in Space Research*, vol. 14, pp. 151–159, oct 1994.

[100] M. Krämer and G. Kraft, "Calculations of heavy-ion track structure," *Radiation and Environmental Biophysics*, vol. 33, pp. 91–109, jun 1994.

[101] C. D. Schlaff, A. Krauze, A. Belard, J. J. O'Connell, and K. A. Camphausen, "Bringing the heavy: Carbon ion therapy in the radiobiological and clinical context," *Radiation Oncology*, vol. 9, p. 88, mar 2014.

[102] M. P. Carante, S. Altieri, S. Bortolussi, I. Postuma, N. Protti, and F. Ballarini, "Modeling radiation-induced cell death: role of different levels of DNA damage clustering," *Radiation and Environmental Biophysics*, vol. 54, pp. 305–316, aug 2015.

[103] E. J. Hall, "Do No Harm&Normal Tissue Effects," *Acta Oncologica*, vol. 40, pp. 913–916, jan 2001.

[104] "2. Definitions of Basic Quantities and Terms," *Journal of the ICRU*, vol. 14, pp. 9–14, apr 2014.

[105] H. Paganetti, "Dose to water versus dose to medium in proton beam therapy Dose to water versus dose to medium in proton beam," *Physics in Medicine and Biology*, vol. 54, pp. 4399–4421, 2009.

[106] "2. Basics of Computed-Tomography Technology," *Journal of the International Commission on Radiation Units and Measurements*, vol. 12, pp. 13–23, 04 2012.

[107] U. Schneider, E. Pedroni, and A. Lomax, "The calibration of CT Hounsfield units for radiotherapy treatment planning," *Physics in Medicine and Biology*, vol. 41, pp. 111–124, jan 1996.

[108] B. Schaffner and E. Pedroni, "The precision of proton range calculations in proton radiotherapy treatment planning: Experimental verification of the relation between CT-HU and proton stopping power," *Physics in Medicine and Biology*, vol. 43, no. 6, pp. 1579–1592, 1998.

[109] W. Schneider, T. Bortfeld, and W. Schlegel, "Correlation between CT numbers and tissue parameters needed for Monte Carlo simulations of clinical dose distributions.," *Physics in medicine and biology*, vol. 45, no. 2, pp. 459–478, 2000.

[110] *Relative Biological Effectiveness in Ion Beam Therapy.* No. 461 in Technical Reports Series, Vienna: International Atomic Energy Agency, 2008.

[111] ICRU, "Report 16. Linear Energy Transfer," *Journal of the International Commission on Radiation Units and Measurements*, vol. os9, 6 1970.

[112] J. J. Wilkens and U. Oelfke, "Analytical linear energy transfer calculations for proton therapy," *Medical Physics*, vol. 30, no. 5, pp. 806–815, 2003.

[113] M. Onishi, N. Okonogi, T. Oike, Y. Yoshimoto, H. Sato, Y. Suzuki, T. Kamada, and T. Nakano, "High linear energy transfer carbon-ion irradiation increases the release of the immune mediator high mobility group box 1 from human cancer cells," *Journal of radiation research*, vol. 59, no. 5, pp. 541–546, 2018.

[114] T. Inaniwa, N. Kanematsu, K. Noda, and T. Kamada, "Treatment planning of intensity modulated composite particle therapy with dose and linear energy transfer optimization," *Physics in Medicine and Biology*, vol. 62, no. 12, pp. 5180–5197, 2017.

[115] IAEA and ICRU, "IAEA-TECDOC-1560. Dose Reporting in Ion Beam Therapy," in *Proceedings of a meeting organized jointly by IAEA and ICRU, Inc.*, no. March 2006, (Ohio, USA), pp. 18–20, 2007.

[116] J. F. Fowler, "The linear-quadratic formula and progress in fractionated radiotherapy," *The British Journal of Radiology*, vol. 62, pp. 679–694, aug 1989.

[117] A. M. Kellerer and H. H. Rossi, "RBE and the Primary Mechanism of Radiation Action," *Radiation Research*, vol. 47, p. 15, jul 1971.

[118] M. C. Joiner and A. van der Kogel, *Basic Clinical Radiobiology Fourth Edition*. London: CRC Press, 2009.

[119] S. J. McMahon, "The linear quadratic model: usage, interpretation and challenges," *Physics in Medicine and Biology*, vol. 64, p. 01TR01, dec 2018.

[120] T. Elsässer, M. Krämer, and M. Scholz, "Accuracy of the local effect model for the prediction of biologic effects of carbon ion beams in vitro and in vivo," *Int. J. Radiat. Oncol. Biol. Phys.*, vol. 71, p. 866, 2008.

[121] P. Fossati, N. Matsufuji, T. Kamada, and C. P. Karger, "Radiobiological issues in prospective carbon ion therapy trials," *Medical Physics*, vol. 45, pp. e1096–e1110, nov 2018.

[122] H. Tsujii and T. Kamada, "A review of update clinical results of carbon ion radiotherapy," *Japanese Journal of Clinical Oncology*, vol. 42, no. 8, pp. 670–685, 2012.

[123] B. S. Sørensen, J. Overgaard, and N. Bassler, "In vitro RBE-LET dependence for multiple particle types," *Acta Oncologica*, vol. 50, pp. 757–762, aug 2011.

[124] P. Peschke, C. P. Karger, M. Scholz, J. Debus, and P. E. Huber, "Relative biological effectiveness of carbon ions for local tumor control of a radioresistant prostate carcinoma in the rat," *International Journal of Radiation Oncology, Biology, Physics*, vol. 79, no. 1, pp. 239–246, 2011.

[125] *Prescribing, recording, and reporting proton-beam therapy*, vol. 7 of *ICRU Report*. Bethesda, MD: ICRU, 2007.

[126] H. Paganetti, "Relative biological effectiveness (RBE) values for proton beam therapy. Variations as a function of biological endpoint, dose, and linear energy transfer," *Physics in Medicine and Biology*, vol. 59, no. 22, pp. R419–R472, 2014.

[127] A. Lühr, C. von Neubeck, M. Krause, and E. G. Troost, "Relative biological effectiveness in proton beam therapy - Current knowledge and future challenges," *Clinical and Translational Radiation Oncology*, vol. 9, pp. 35–41, 2018.

[128] H. Paganetti, "Proton Relative Biological Effectiveness - Uncertainties and Opportunities," *International Journal of Particle Therapy*, vol. 5, pp. 2–14, aug 2018.

[129] G. Giovannini, T. T. Böhlen, G. Cabal, J. Bauer, T. Tessonnier, K. Frey, J. Debus, A. Mairani, and K. Parodi, "Variable RBE in proton therapy: comparison of different model predictions and their influence on clinical-like scenarios," *Radiation Oncology*, vol. 11, no. 1, 2016.

[130] W. Cao, A. Khabazian, P. Yepes, G. Lim, F. Poenisch, and D. Grosshans, "Linear energy transfer incorporated intensity modulated proton therapy optimization," *Physics in Medicine and Biology*, vol. 63, no. September 2017, p. 015013, 2018.

[131] J. Unkelbach, P. Botas, D. Giantsoudi, B. L. Gorissen, and H. Paganetti, "Reoptimization of Intensity Modulated Proton Therapy Plans Based on Linear Energy Transfer," *International Journal of Radiation Oncology, Biology, Physics*, vol. 96, pp. 1097–1106, dec 2016.

[132] A. Mairani, I. Dokic, G. Magro, T. Tessonnier, J. Bauer, T. T. Böhlen, M. Ciocca, A. Ferrari, P. R. Sala, O. Jäkel, J. Debus, T. Haberer, A. Abdollahi, and K. Parodi, "A phenomenological relative biological effectiveness approach for proton therapy based on an improved description of the mixed radiation field," *Physics in Medicine and Biology*, vol. 62, pp. 1378–1395, feb 2017.

[133] E. Rørvik, S. Thornqvist, C. H. Stokkevag, T. J. Dahle, L. F. Fjæra, and K. S. Ytre-Hauge, "A phenomenological biological dose model for proton therapy based on linear energy transfer spectra," *Medical Physics*, vol. 44, no. 6, pp. 2586–2594, 2017.

[134] P. Fossati, S. Molinelli, N. Matsufuji, M. Ciocca, A. Mirandola, A. Mairani, J. Mizoe, A. Hasegawa, R. Imai, T. Kamada, R. Orecchia, and H. Tsujii, "Dose prescription in carbon ion radiotherapy: A planning study to compare NIRS and LEM approaches with a clinically-oriented strategy," *Physics in Medicine and Biology*, vol. 57, no. 22, pp. 7543–7554, 2012.

[135] Christian, P. Karger, and Peschke, "RBE and related modeling in carbon-ion therapy," *Physics in Medicine and Biology*, vol. 63, pp. 1–2, 2018.

[136] A. Mairani, I. Dokic, G. Magro, T. Tessonnier, F. Kamp, D. J. Carlson, M. Ciocca, F. Cerutti, P. R. Sala, A. Ferrari, T. T. Böhlen, O. Jäkel, K. Parodi, J. Debus, A. Abdollahi, and T. Haberer, "Biologically optimized helium ion plans: calculation approach and its in vitro validation," *Physics in Medicine and Biology*, vol. 61, pp. 4283–4299, jun 2016.

[137] T. Elsässer and S. M, "Cluster effects within the local effect model," *Radiat. Res.*, vol. 167, p. 319, 2007.

[138] T. Friedrich, U. Scholz, T. Elsässer, M. Durante, and S. M, "Calculation of the biological effects of ion beams based on the microscopic spatial damage distribution pattern," *Int. J. Radiat. Biol.*, vol. 88, p. 103, 2012.

[139] J. R. Castro, "Heavy Ion Therapy: Bevalac Epoch," Tech. Rep. October, 1993.

[140] Y. Hirao, H. Ogawa, S. Yamada, Y. Sato, T. Yamada, K. Sato, A. Itano, M. Kanazawa, K. Noda, K. Kawachi, M. Endo, T. Kanai, T. Kohno, M. Sudou, S. Minohara, A. Kitagawa, F. Soga, E. Takada, S. Watanabe, K. Endo, M. Kumada, and S. Matsumoto, "Heavy ion synchrotron for medical use - HIMAC project at NIRS - Japan," *Nuclear Physics A*, vol. 538, pp. 541–550, mar 1992.

[141] K. Sato, S. Yamada, H. Ogawa, K. Kawachi, N. Araki, A. Itano, M. Kanazawa, A. Kitagawa, T. Kohno, M. Kumada, T. Murakami, M. Muramatsu, K. Noda, S. Sato, Y. Sato, E. Takada, A. Tanaka, K. Tashiro, M. Torikoshi, J. Yoshizawa, M. Endo, Y. Furusawa, T. Kanai, H. Koyama-Ito, N. Matsufuji, S. Minohara, N. Miyahara, F. Soga, M. Suzuki, H. Tomura, and Y. Hirao, "Performance of HIMAC," *Nuclear Physics, Section A*, vol. 588, no. 1, 1995.

[142] T. Kanai, Y. Furusawa, K. Fukutsu, H. Itsukaichi, K. Eguchi-Kasai, and H. Ohara, "Irradiation of mixed beam and design of spread-out bragg peak for heavy-ion radiotherapy," *Radiat. Res.*, vol. 147, p. 78, 1997.

[143] R. B. Hawkins, "A Statistical Theory of Cell Killing by Radiation of Varying Linear Energy Transfer," *Radiation Research*, vol. 140, no. 3, p. 366, 1994.

[144] H. R. B, "A microdosimetric-kinetic model for the effect of non-poisson distribution of lethal lesions on the variation of rbe with let," *Radiat. Res.*, vol. 160, p. 61, 2003.

[145] Y. Kase, T. Kanai, Y. Matsumoto, Y. Furusawa, H. Okamoto, T. Asaba, M. Sakama, and H. Shinoda, "Microdosimetric Measurements and Estimation of Human Cell Survival for Heavy-Ion Beams," *Radiation Research*, vol. 166, no. 4, pp. 629–638, 2006.

[146] T. Inaniwa, T. Furukawa, Y. Kase, N. Matsufuji, T. Toshito, Y. Matsumoto, Y. Furusawa, and K. Noda, "Treatment planning for a scanned carbon beam with a modified microdosimetric kinetic model," *Physics in Medicine and Biology*, vol. 55, no. 22, pp. 6721–6737, 2010.

[147] Y. Kase, T. Kanai, N. Matsufuji, Y. Furusawa, T. Elsässer, and M. Scholz, "Biophysical calculation of cell survival probabilities using amorphous track structure models for heavy-ion irradiation," *Physics in Medicine and Biology*, vol. 53, no. 1, pp. 37–59, 2008.

[148] T. Inaniwa, N. Kanematsu, N. Matsufuji, T. Kanai, T. Shirai, K. Noda, H. Tsuji, T. Kamada, and H. Tsujii, "Reformulation of a clinical-dose system for carbon-ion radiotherapy treatment planning at the National Institute of Radiological Sciences, Japan," *Physics in Medicine and Biology*, vol. 60, pp. 3271–3286, apr 2015.

[149] M. Scholz and Kraft, *A parameter-free track structure model for heavy ion action cross sections*. United Kingdom: Adam Hilger, 1992.

[150] M. Scholz and G. Kraft, "Track structure and the calculation of biological effects of heavy charged particles," *Advances in Space Research*, vol. 18, no. 1-2, pp. 5–14, 1996.

[151] M. Scholz, A. M. Kellerer, W. Kraft-Weyrather, and G. Kraft, "Computation of cell survival in heavy ion beams for therapy. The model and its approximation.," *Radiation and environmental biophysics*, vol. 36, pp. 59–66, feb 1997.

[152] B. Kopp, S. Meyer, A. Mairani, S. Mein, E. Blakely, J. Debus, and M. Durante, "Roadmap : helium ion therapy," 2022.

[153] F. Kamp, G. Cabal, A. Mairani, K. Parodi, J. J. Wilkens, and D. J. Carlson, "Fast Biological Modeling for Voxel-based Heavy Ion Treatment Planning Using the Mechanistic Repair-Misrepair-Fixation Model and Nuclear Fragment Spectra," *International Journal of Radiation Oncology, Biology, Physics*, vol. 93, no. 3, pp. 557–568, 2015.

[154] B. Kopp, S. B. Mein, T. Tessonnier, J. Besuglow, S. Harrabi, E. Heim, A. Abdollahi, T. Haberer, J. Debus, and A. Mairani, "Rapid effective dose calculation for raster-scanning 4He ion therapy with the modified microdosimetric kinetic model (mMKM)," *Physica Medica*, vol. 81, no. November 2020, pp. 273–284, 2021.

[155] F. Ballarini, S. Altieri, S. Bortolussi, M. P. Carante, E. Giroletti, and N. Protti, "The BIANCA model/code of radiation-induced cell death: Application to human cells exposed to different radiation types," *Radiation and Environmental Biophysics*, vol. 53, no. 3, pp. 525–533, 2014.

[156] M. P. Carante, C. Aimè, J. J. Tello Cajiao, and F. Ballarini, "BIANCA, a biophysical model of cell survival and chromosome damage by protons, C-ions and He-ions at energies and doses used in hadrontherapy," *Physics in Medicine and Biology*, vol. 63, no. 7, 2018.

[157] M. Durante, R. Orecchia, and J. S. Loeffler, "Charged-particle therapy in cancer: Clinical uses and future perspectives," *Nature Reviews Clinical Oncology*, vol. 14, no. 8, pp. 483–495, 2017.

[158] H. Fuchs, M. Alber, T. Schreiner, and D. Georg, "Implementation of spot scanning dose optimization and dose calculation for helium ions in Hyperion," *Medical Physics*, vol. 42, pp. 5157–5166, aug 2015.

[159] B. Knäusl, H. Fuchs, K. Dieckmann, and D. Georg, "Can particle beam therapy be improved using helium ions? - A planning study focusing on pediatric patients," *Acta Oncologica*, vol. 55, no. 6, pp. 751–759, 2016.

[160] T. Tessonnier, A. Mairani, W. Chen, P. R. Sala, F. Cerutti, A. Ferrari, T. Haberer, J. Debus, and K. Parodi, "Proton and Helium Ion Radiotherapy for Meningioma Tumors: A Monte Carlo-based Treatment Planning Comparison," *Radiation Oncology*, vol. 13, no. 1, pp. 1–10, 2018.

[161] U. Schneider, A. Lomax, P. Pemler, J. Besserer, D. Ross, N. Lombriser, and B. Kaser-Hotz, "The impact of IMRT and proton radiotherapy on secondary cancer incidence," *Strahlentherapie und Onkologie*, vol. 182, no. 11, pp. 647–652, 2006.

[162] M. V. Mishra, S. Aggarwal, S. M. Bentzen, N. Knight, M. P. Mehta, and W. F. Regine, "Establishing Evidence-Based Indications for Proton Therapy: An Overview of Current Clinical Trials," *International Journal of Radiation Oncology, Biology, Physics*, vol. 97, pp. 228–235, feb 2017.

[163] ASTRO, "ASTRO updates insurance coverage recommendations for proton therapy." `https://www.astro.org/uploadedFiles/_MAIN_SITE/Daily_Practice/Reimbursement/Model_Policies/Content_Pieces/ASTROPBTModelPolicy.pdf`, 2017.

[164] M. Mizumoto, Y. Oshiro, T. Yamamoto, H. Kohzuki, and H. Sakurai, "Proton Beam Therapy for Pediatric Brain Tumor," *Neurologia medico-chirurgica*, vol. 57, pp. 343–355, jul 2017.

[165] M. Durante and J. S. Loeffler, "Charged particles in radiation oncology," *Nature Reviews Clinical Oncology*, vol. 7, pp. 37–43, jan 2010.

[166] K. Hayashi, M. Koto, Y. Demizu, J.-i. Saitoh, H. Suefuji, T. Okimoto, T. Ohno, Y. Shioyama, R. Takagi, H. Ikawa, K. Nemoto, T. Nakano, and T. Kamada, "A retrospective multicenter study of carbon-ion radiotherapy for major salivary gland carcinomas: Subanalysis of J-CROS 1402 HN," *Cancer Science*, vol. 109, pp. 1576–1582, may 2018.

[167] M. Uhl, M. Mattke, T. Welzel, J. Oelmann, G. Habl, A. D. Jensen, M. Ellerbrock, T. Haberer, K. K. Herfarth, and J. Debus, "High control rate in patients with chondrosarcoma of the skull base after carbon ion therapy: First report of long-term results," *Cancer*, vol. 120, no. 10, pp. 1579–1585, 2014.

[168] S. E. Combs, T. Bruckner, J. E. Mizoe, T. Kamada, H. Tsujii, M. Kieser, and J. Debus, "Comparison of carbon ion radiotherapy to photon radiation alone or in combination with temozolomide in patients with high-grade gliomas: Explorative hypothesis-generating retrospective analysis," *Radiotherapy and Oncology*, vol. 108, no. 1, pp. 132–135, 2013.

[169] W. P. Levin, H. Kooy, J. S. Loeffler, and T. F. DeLaney, "Proton beam therapy," *British Journal of Cancer*, vol. 93, pp. 849–854, oct 2005.

[170] O. Mohamad, B. J. Sishc, J. Saha, A. Pompos, A. Rahimi, M. D. Story, A. J. Davis, and D. W. Kim, "Carbon ion radiotherapy: A review of clinical experiences and preclinical research, with an emphasis on DNA damage/repair," *Cancers*, vol. 9, no. 6, pp. 1–30, 2017.

[171] Z. Liao, J. J. Lee, R. Komaki, D. R. Gomez, M. S. O'Reilly, F. V. Fossella, G. R. Blumenschein, J. V. Heymach, A. A. Vaporciyan, S. G. Swisher, P. K. Allen, N. C. Choi, T. F. DeLaney, S. M. Hahn, J. D. Cox, C. S. Lu, and R. Mohan, "Bayesian adaptive randomization trial of passive scattering proton therapy and intensity-modulated photon radiotherapy for locally advanced non - small-cell lung cancer," *Journal of Clinical Oncology*, vol. 36, no. 18, pp. 1813–1822, 2018. PMID: 29293386.

[172] G. Palma, S. Monti, T. Xu, E. Scifoni, P. Yang, S. M. Hahn, M. Durante, R. Mohan, Z. Liao, and L. Cella, "Spatial Dose Patterns Associated With Radiation Pneumonitis in a Randomized Trial Comparing Intensity-Modulated Photon Therapy With Passive Scattering Proton Therapy for Locally Advanced Non-Small Cell Lung Cancer," *International Journal of Radiation Oncology, Biology, Physics*, vol. 104, pp. 1124–1132, aug 2019.

[173] e. b. R. Bailey, "Proceedings of the CAS - CERN Accelerator School: Accelerators for Medical Applications," in *Proceedings of the CAS - CERN Accelerator School*, vol. 1, pp. 1–5, 2015.

[174] "Advanced oncotherapy plc." `https://www.avoplc.com/en-gb/`, 2022.

[175] L. Badano, M. Benedikt, P. J. Bryant, M. Crescenti, P. Holy, A. T. Maier, M. Pullia, S. Rossi, and P. Knaus, *Proton-Ion Medical Machine Study (PIMMS), 1.* CERN, Mar 1999.

[176] P. J. Bryant, L. Badano, M. Benedikt, P. J. Bryant, M. Crescent, P. Holy, A. Maier, M. Pullia, S. Rossi, and P. Knaus, "Progress of the Proton-Ion Medical Machine Study (PIMMS)," *Strahlentherapie und Onkologie*, vol. 175, pp. 1–4, jun 1999.

[177] U. Amaldi, S. Braccini, and P. Puggioni, "High Frequency Linacs for Hadrontherapy," *Reviews of Accelerator Science and Technology*, vol. 02, pp. 111–131, jan 2009.

[178] U. Amaldi and A. Degiovanni, "Proton and Carbon Linacs for Hadron Therapy," *Linac2014*, pp. 1207–1212, 2014.

[179] A. Degiovanni, U. Amaldi, D. Bergesio, C. Cuccagna, A. L. Moro, P. Magagnin, P. Riboni, and V. Rizzoglio, "Design of a fast-cycling high-gradient rotating linac for protontherapy," *IPAC 2013: Proceedings of the 4th International Particle Accelerator Conference*, no. January 2016, pp. 3642–3644, 2013.

[180] U. Amaldi, S. Braccini, G. Magrin, P. Pearce, and R. Zennaro, "Ion acceleration system for medical and/or other applications," May 19 2010. EP Patent 2,106,678.

[181] U. Amaldi, S. Braccini, G. Magrin, P. Pearce, and R. Zennaro, "Ion acceleration system for medical and/or other applications," Mar. 26 2013. US Patent 8,405,056.

[182] A. Allisy, W. A. Jennings, A. M. Kellerer, J. W. Müller, H. H. Rossi, and S. M. Seltzer, "Report 60," *Journal of the International Commission on Radiation Units and Measurements*, vol. os31, pp. NP–NP, dec 1998.

[183] J. Hrbacek, K. K. Mishra, A. Kacperek, R. Dendale, C. Nauraye, M. Auger, J. Herault, I. K. Daftari, A. V. Trofimov, H. A. Shih, Y. L. E. Chen, A. Denker, J. Heufelder, T. Horwacik, J. Swakoń, C. Hoehr, C. Duzenli, A. Pica, F. Goudjil, A. Mazal, J. Thariat, and D. C. Weber, "Practice Patterns Analysis of Ocular Proton Therapy Centers: The International OPTIC Survey," *International Journal of Radiation Oncology, Biology, Physics*, vol. 95, no. 1, pp. 336–343, 2016.

[184] M. Ciocca, G. Magro, E. Mastella, A. Mairani, A. Mirandola, S. Molinelli, S. Russo, A. Vai, M. R. Fiore, C. Mosci, F. Valvo, R. Via, G. Baroni, and R. Orecchia, "Design and commissioning of the nonâĂŘdedicated scanning proton beamline for ocular treatment at the synchrotronâĂŘbased CNAO facility," *Medical Physics*, vol. 46, pp. 1852–1862, apr 2019.

[185] K. Bernatowicz, A. J. Lomax, and A. Knopf, "Comparative study of layered and volumetric rescanning for different scanning speeds of proton beam in liver patients," *Physics in Medicine and Biology*, vol. 58, pp. 7905–7920, nov 2013.

[186] H. Tsunemoto, S. Morita, T. Ishikawa, S. Furukawa, K. Kawachi, T. Kanai, H. Ohara, T. Kitagawa, and T. Inada, "Proton Therapy in Japan," *Radiation Research Supplement*, vol. 8, p. S235, nov 1985.

[187] E. Pedroni, R. Bacher, H. Blattmann, T. Böhringer, A. Coray, A. Lomax, S. Lin, G. Munkel, S. Scheib, U. Schneider, and A. Tourovsky, "The 200-MeV proton therapy project at the Paul Scherrer Institute: Conceptual design and practical realization," *Medical Physics*, vol. 22, no. 1, pp. 37–53, 1995.

[188] T. Haberer, W. Becher, D. Schardt, and G. Kraft, "Magnetic scanning system for heavy ion therapy," *Nuclear Instruments and Methods in Physics Research Section A: Accelerators, Spectrometers, Detectors and Associated Equipment*, vol. 330, pp. 296–305, jun 1993.

[189] S. E. Combs, O. Jäkel, T. Haberer, and J. Debus, "Particle therapy at the Heidelberg Ion Therapy Center (HIT) - Integrated research-driven university-hospital-based radiation oncology service in Heidelberg, Germany," vol. 95, pp. 41–44, apr 2010.

[190] S. Rossi, "The National Centre for Oncological Hadrontherapy (CNAO): Status and perspectives.," *Phys. Medica*, vol. 31, pp. 333–51, 6 2015.

[191] M. Stock, P. Georg, R. Mayer, T. T. Böhlen, and S. Vatnitsky, "Development of Clinical Programs for Carbon Ion Beam Therapy at MedAustron," *International Journal of Particle Therapy*, vol. 2, pp. 474–477, dec 2015.

[192] T. Furukawa, T. Inaniwa, S. Sato, T. Tomitani, S. Minohara, K. Noda, and T. Kanai, "Design study of a raster scanning system for moving target irradiation in heavy-ion radiotherapy," *Medical Physics*, vol. 34, pp. 1085–1097, feb 2007.

[193] A. Schätti, M. Zakova, D. Meer, and A. J. Lomax, "Experimental verification of motion mitigation of discrete proton spot scanning by re-scanning," *Physics in Medicine and Biology*, vol. 58, pp. 8555–8572, dec 2013.

[194] T. Kanai, M. Endo, S. Minohara, N. Miyahara, H. Koyama-Ito, H. Tomura, N. Matsufuji, Y. Futami, A. Fukumura, T. Hiraoka, Y. Furusawa, K. Ando, M. Suzuki, F. Soga, and K. Kawachi, "Biophysical characteristics of HIMAC clinical irradiation system for heavy-ion radiation therapy," *International Journal of Radiation Oncology, Biology, Physics*, vol. 44, no. 1, pp. 201–210, 1999.

[195] M. Yang, G. Virshup, J. Clayton, X. R. Zhu, R. Mohan, and L. Dong, "Theoretical variance analysis of single- and dual-energy computed tomography methods for calculating proton stopping power ratios of biological tissues," *Physics in Medicine and Biology*, vol. 55, no. 5, pp. 1343–1362, 2010.

[196] R. P. Johnson, V. A. Bashkirov, G. Coutrakon, V. Giacometti, P. Karbasi, N. T. Karonis, C. E. Ordoñez, M. Pankuch, H. F. Sadrozinski, K. E. Schubert, and R. W. Schulte, "Results from a Prototype Proton-CT Head Scanner," *Physics Procedia*, vol. 90, no. November 2016, pp. 209–214, 2017.

[197] M. Takabe, T. Masuda, M. Arimoto, J. Kataoka, K. Sueoka, T. Maruhashi, S. Tanaka, T. Nishio, T. Toshito, M. Kimura, and T. Inaniwa, "Development of simple proton CT system with novel correction methods of proton scattering," *Nuclear Instruments and Methods in Physics Research, Section A: Accelerators, Spectrometers, Detectors and Associated Equipment*, vol. 924, no. May 2018, pp. 332–338, 2019.

[198] H. Paganetti, "Range uncertainties in proton therapy and the role of Monte Carlo simulations," *Physics in Medicine and Biology*, vol. 57, no. 11, pp. 1199–11117, 2012.

[199] G. Vogin, A. Wambersie, M. Koto, T. Ohno, M. Uhl, P. Fossati, J. Balosso, R. Pötter, M. Beuve, S. E. Combs, G. Magrin, R. Mayer, U. Mock, D. Sarrut, and T. Schreiner, "A step towards international prospective trials in carbon ion radiotherapy: Investigation of factors influencing dose distribution in the facilities in operation based on a case of skull base chordoma," *Radiation Oncology*, vol. 14, no. 1, pp. 1–12, 2019.

[200] F. Albertini, A. Bolsi, A. J. Lomax, H. P. Rutz, B. Timmerman, and G. Goitein, "Sensitivity of intensity modulated proton therapy plans to changes in patient weight," *Radiotherapy and Oncology*, vol. 86, no. 2, pp. 187–194, 2008.

[201] A. J. Lomax, "Intensity modulation methods for proton radiotherapy," *Physics in Medicine and Biology*, vol. 44, pp. 185–205, jan 1999.

[202] J. Unkelbach, M. Alber, M. Bangert, R. Bokrantz, T. C. Chan, J. O. Deasy, A. Fredriksson, B. L. Gorissen, M. Van Herk, W. Liu, H. Mahmoudzadeh, O. Nohadani, J. V. Siebers, M. Witte, and H. Xu, "Robust radiotherapy planning," *Physics in Medicine and Biology*, vol. 63, no. 22, 2018.

[203] J. Saini, D. Maes, A. Egan, S. R. Bowen, S. St James, M. Janson, T. Wong, and C. Bloch, "Dosimetric evaluation of a commercial proton spot scanning Monte-Carlo dose algorithm: Comparisons against measurements and simulations," *Physics in Medicine and Biology*, vol. 62, no. 19, pp. 7659–7681, 2017.

[204] L. Lin, S. Huang, M. Kang, P. Hiltunen, R. Vanderstraeten, J. Lindberg, S. Siljamaki, T. Wareing, I. Davis, A. Barnett, J. Mcghee, C. B. Simone, T. D. Solberg, J. E. Mcdonough, and C. Ainsley, "A benchmarking method to evaluate the accuracy of a commercial proton monte carlo pencil beam scanning treatment planning system," *Journal of Applied Clinical Medical Physics*, vol. 18, no. 2, pp. 44–49, 2017.

[205] P. J. Doolan, J. Alshaikhi, I. Rosenberg, C. G. Ainsley, A. Gibson, D. D'Souza, E. H. Bentefour, and G. Royle, "A comparison of the dose distributions from three proton treatment planning systems in the planning of meningioma patients with single-field uniform dose pencil beam scanning," *Journal of Applied Clinical Medical Physics*, vol. 16, pp. 86–99, jan 2015.

[206] S. Scheib and E. Pedroni, "Dose calculation and optimization for 3D conformal voxel scanning," *Radiation and Environmental Biophysics*, vol. 31, no. 3, pp. 251–256, 1992.

[207] L. Hong, M. Goitein, M. Bucciolini, R. Comiskey, B. Gottschalk, S. Rosenthal, C. Serago, and M. Urie, "A pencil beam algorithm for proton dose calculations," *Physics in Medicine and Biology*, vol. 41, pp. 1305–1330, aug 1996.

[208] M. Soukup, M. Fippel, and M. Alber, "A pencil beam algorithm for intensity modulated proton therapy derived from Monte Carlo simulations.," *Physics in medicine and biology*, vol. 50, no. 21, pp. 5089–5104, 2005.

[209] K. Parodi, A. Mairani, and F. Sommerer, "Monte Carlo-based parametrization of the lateral dose spread for clinical treatment planning of scanned proton and carbon ion beams," *Journal of Radiation Research*, vol. 54, pp. i91–i96, jul 2013.

[210] A. Tourovsky, A. J. Lomax, U. Schneider, and E. Pedroni, "Monte Carlo dose calculations for spot scanned proton therapy.," *Physics in medicine and biology*, vol. 50, pp. 971–81, mar 2005.

[211] L. Widesott, S. Lorentini, F. Fracchiolla, P. Farace, and M. Schwarz, "Improvements in pencil beam scanning proton therapy dose calculation accuracy in brain tumor cases with a commercial Monte Carlo algorithm," *Physics in Medicine and Biology*, vol. 63, p. 145016, jul 2018.

[212] C. Grassberger, J. Daartz, S. Dowdell, T. Ruggieri, G. Sharp, and H. Paganetti, "Quantification of proton dose calculation accuracy in the lung," *International Journal of Radiation Oncology, Biology, Physics*, vol. 89, no. 2, pp. 424–430, 2014.

[213] J. Schuemann, S. J. Dowdell, C. Grassberger, C. H. Min, and H. Paganetti, "Site-specific range uncertainties caused by dose calculation algorithms for proton therapy," *Physics in Medicine and Biology*, vol. 59, no. 15, pp. 4007–4031, 2014.

[214] P. A. Taylor, S. F. Kry, and D. S. Followill, "Pencil Beam Algorithms Are Unsuitable for Proton Dose Calculations in Lung," *International Journal of Radiation Oncology, Biology, Physics*, vol. 99, no. 3, pp. 750–756, 2017.

[215] J. Saini, E. Traneus, D. Maes, R. Regmi, S. R. Bowen, C. Bloch, and T. Wong, "Advanced Proton Beam Dosimetry Part I: Review and performance evaluation of dose calculation algorithms," *Translational Lung Cancer Research*, vol. 7, no. 2, pp. 171–179, 2018.

[216] H. Paganetti, H. Jiang, K. Parodi, R. Slopsema, and M. Engelsman, "Clinical implementation of full Monte Carlo dose calculation in proton beam therapy," *Physics in Medicine and Biology*, vol. 53, pp. 4825–4853, sep 2008.

[217] C. Grassberger, A. Lomax, and H. Paganetti, "Characterizing a proton beam scanning system for Monte Carlo dose calculation in patients," *Physics in Medicine and Biology*, vol. 60, pp. 633–645, jan 2015.

[218] G. Magro, T. J. Dahle, S. Molinelli, M. Ciocca, P. Fossati, A. Ferrari, T. Inaniwa, N. Matsufuji, K. S. Ytre-Hauge, and A. Mairani, "The FLUKA Monte Carlo code coupled with the NIRS approach for clinical dose calculations in carbon ion therapy.," *Physics in Medicine and Biology*, vol. 62, pp. 3814–3827, may 2017.

[219] J. E. Johnson, C. Beltran, H. S. Wan Chan Tseung, D. W. Mundy, J. J. Kruse, T. J. Whitaker, M. G. Herman, and K. M. Furutani, "Highly efficient and sensitive patient-specific quality assurance for spot-scanned proton therapy," *PLOS ONE*, vol. 14, p. e0212412, feb 2019.

[220] A. J. Lomax, T. Böhringer, A. Bolsi, D. Coray, F. Emert, G. Goitein, M. Jermann, S. Lin, E. Pedroni, H. Rutz, O. Stadelmann, B. Timmermann, J. Verwey, and D. C. Weber, "Treatment planning and

verification of proton therapy using spot scanning: Initial experiences," *Medical Physics*, vol. 31, no. 11, pp. 3150–3157, 2004.

[221] S. Molinelli, A. Mairani, A. Mirandola, G. Vilches Freixas, T. Tessonnier, S. Giordanengo, K. Parodi, M. Ciocca, and R. Orecchia, "Dosimetric accuracy assessment of a treatment plan verification system for scanned proton beam radiotherapy: one-year experimental results and Monte Carlo analysis of the involved uncertainties," *Physics in Medicine and Biology*, vol. 58, pp. 3837–3847, jun 2013.

[222] B. Arjomandy, N. Sahoo, G. Ciangaru, R. Zhu, X. Song, and M. Gillin, "Verification of patient-specific dose distributions in proton therapy using a commercial two-dimensional ion chamber array," *Medical Physics*, vol. 37, no. 11, pp. 5831–5837, 2010.

[223] D. A. Low and J. F. Dempsey, "Evaluation of the gamma dose distribution comparison method," *Medical Physics*, vol. 30, pp. 2455–64, sep 2003.

[224] C. Winterhalter, G. Meier, D. Oxley, D. C. Weber, A. J. Lomax, and S. Safai, "Log file based Monte Carlo calculations for proton pencil beam scanning therapy," *Physics in Medicine and Biology*, vol. 64, no. 3, 2019.

[225] M. Testa, J. Schümann, H. M. Lu, J. Shin, B. Faddegon, J. Perl, and H. Paganetti, "Experimental validation of the TOPAS Monte Carlo system for passive scattering proton therapy," *Medical Physics*, vol. 40, no. 12, pp. 1–16, 2013.

[226] F. Fracchiolla, S. Lorentini, L. Widesott, and M. Schwarz, "Characterization and validation of a Monte Carlo code for independent dose calculation in proton therapy treatments with pencil beam scanning," *Physics in Medicine and Biology*, vol. 60, pp. 8601–8619, nov 2015.

[227] G. Meier, R. Besson, A. Nanz, S. Safai, and A. J. Lomax, "Independent dose calculations for commissioning, quality assurance and dose reconstruction of PBS proton therapy," *Physics in Medicine and Biology*, vol. 60, no. 7, pp. 2819–2836, 2015.

[228] H. Li, N. Sahoo, F. Poenisch, K. Suzuki, Y. Li, X. Li, X. Zhang, A. K. Lee, M. T. Gillin, and X. R. Zhu, "Use of treatment log files in spot scanning proton therapy as part of patient-specific quality assurance.," *Medical physics*, vol. 40, no. Mlc, p. 021703, 2013.

[229] K. Parodi and W. Enghardt, "Potential application of PET in quality assurance of proton therapy," *Physics in Medicine and Biology*, vol. 45, no. 11, p. N151, 2000.

[230] K. Parodi, A. Ferrari, F. Sommerer, and H. Paganetti, "Clinical CT-based calculations of dose and positron emitter distributions in proton therapy using the FLUKA Monte Carlo code," *Physics in Medicine and Biology*, vol. 52, no. 12, pp. 3369–3387, 2007.

[231] K. Parodi, H. Paganetti, H. a. Shih, S. Michaud, J. S. Loeffler, T. F. DeLaney, N. J. Liebsch, J. E. Munzenrider, A. J. Fischman, A. Knopf, and T. Bortfeld, "Patient Study of In Vivo Verification of Beam Delivery and Range, Using Positron Emission Tomography and Computed Tomography Imaging After Proton Therapy," *International Journal of Radiation Oncology, Biology, Physics*, vol. 68, no. 3, pp. 920–934, 2007.

[232] W. Enghardt, P. Crespo, F. Fiedler, R. Hinz, K. Parodi, J. Pawelke, and F. Pönisch, "Charged hadron tumour therapy monitoring by means of PET," *Nuclear Instruments and Methods in Physics Research*

Section A: Accelerators, Spectrometers, Detectors and Associated Equipment, vol. 525, no. 1, pp. 284 – 288, 2004. Proceedings of the International Conference on Imaging Techniques in Subatomic Physics, Astrophysics, Medicine, Biology and Industry.

[233] P. Crespo, G. Shakirin, and W. Enghardt, "On the detector arrangement for in-beam PET for hadron therapy monitoring," *Physics in Medicine and Biology*, vol. 51, no. 9, p. 2143, 2006.

[234] R. Dos Santos Augusto, J. Bauer, O. Bouhali, C. Cuccagna, C. Gianoli, W. S. Kozłowska, P. G. Ortega, T. Tessonnier, Y. Toufique, V. Vlachoudis, K. Parodi, and A. Ferrari, "An overview of recent developments in FLUKA PET tools.," *Physica medica*, vol. 54, pp. 189–199, oct 2018.

[235] J. M. Verburg and J. Seco, "Dosimetric accuracy of proton therapy for chordoma patients with titanium implants," *Medical Physics*, vol. 40, no. 7, p. 071727, 2013.

[236] M. Testa, C. Min, J. Verburg, J. Schümann, H. M. Lu, and H. Paganetti, "Range verification of passively scattered proton beams based on prompt gamma time patterns," *Physics in Medicine and Biology*, vol. 59, no. 15, pp. 4181–4195, 2014.

[237] E. Testa, M. Bajard, M. Chevallier, D. Dauvergne, F. L. Foulher, N. Freud, J.-M. Létang, J.-C. Poizat, C. Ray, and M. Testa, "Monitoring the bragg peak location of 73 MeVâĹţu carbon ions by means of prompt γ-ray measurements," *Applied Physics Letters*, vol. 93, no. 9, p. 093506, 2008.

[238] M. Testa, M. Bajard, M. Chevallier, D. Dauvergne, N. Freud, P. Henriquet, S. Karkar, F. Le Foulher, J. M. Létang, R. Plescak, C. Ray, M. H. Richard, D. Schardt, and E. Testa, "Real-time monitoring of the Bragg-peak position in ion therapy by means of single photon detection," *Radiation and Environmental Biophysics*, vol. 49, no. 3, pp. 337–343, 2010.

[239] J. Ranft, "Improved Monte-Carlo calculation of the nucleon-meson cascade in shielding material," *Nuclear Instruments and Methods*, vol. 48, pp. 133–140, feb 1967.

[240] V. Vlachoudis and D. Siñuela-Pastor, "Numerically robust geometry engine for compound solid geometries," p. 02502, jun 2014.

[241] V. Vlachoudis, "FLAIR: A Powerful But User Friendly Graphical Interface For FLUKA," *Proc. Int. Conf. on Mathematics, Computational*, pp. 1–11, 2009.

[242] H. A. Bethe, J. Ashkin, and E. Segré, *Experimental Nuclear Physics*, vol. 1, ch. Passage of Radiations Through Matter. Wiley, New York, 1959.

[243] E. A. Uehling, "Penetration of heavy charged particles in matter," *Annual Review of Nuclear Science*, vol. 4, no. 1, pp. 315–350, 1954.

[244] N. A. of Sciences, *Studies in penetration of charged particles in matter*. Nucl. Sci., Washington, DC: National Academy of Sciences, 1964.

[245] J. F. Ziegler, *Helium: Stopping Powers and Ranges in All Elemental Matter*, vol. 4. Pergamon Press, Elmsford, New York, 1977.

[246] J. F. Ziegler, J. Biersack, and U. Littmark, *The stopping and ranges of ions in matter*, vol. 1–5. Pergamon Press, New York, 1985.

[247] J. F. Ziegler, "Stopping of energetic light ions in elemental matter," *Journal of Applied Physics*, vol. 85, no. 3, pp. 1249–1272, 1999.

[248] R. M. Sternheimer, S. M. Seltzer, and M. J. Berger, "Density effect for the ionization loss of charged particles in various substances," *Physical Review B*, vol. 26, pp. 6067–6076, dec 1982.

[249] J. C. Ashley, R. H. Ritchie, and W. Brandt, "z_1^3 effect in the stopping power of matter for charged particles," *Physical Review B*, vol. 5, pp. 2393–2397, Apr 1972.

[250] J. C. Ashley, R. H. Ritchie, and W. Brandt, "z_1^3-dependent stopping power and range contributions," *Physical Review A*, vol. 8, pp. 2402–2408, Nov 1973.

[251] T. Lijian, H. Qing, and L. Zhengming, "Analytic fitting to the mott cross section of electrons," *Radiation Physics and Chemistry*, vol. 45, pp. 235–245, feb 1995.

[252] I. Jun, W. Kim, and R. Evans, "Electron Nonionizing Energy Loss for Device Applications," *IEEE Transactions on Nuclear Science*, vol. 56, pp. 3229–3235, dec 2009.

[253] F. Hubert, R. Bimbot, and H. Gauvin, "Semi-empirical formulae for heavy ion stopping powers in solids in the intermediate energy range," *Nuclear Instruments and Methods in Physics Research Section B: Beam Interactions with Materials and Atoms*, vol. 36, no. 4, pp. 357 – 363, 1989.

[254] A. Ferrari, J. Ranft, P. R. Sala, and A. Fassó, "New developments in FLUKA modelling of hadronic and EM interactions," no. January 1997, pp. 1–9, 1997.

[255] A. Stuart and K. J. Ord, *Kendall's advanced theory of statistics*. New York: Oxford University Press, 5th ed., 1987.

[256] A. Ferrari, P. R. Sala, R. Guaraldi, and F. Padoani, "An improved multiple scattering model for charged particle transport," *Nuclear Instruments and Methods in Physics Research Section B: Beam Interactions with Materials and Atoms*, vol. 71, pp. 412–426, sep 1992.

[257] A. Fassò, A. Ferrari, and P. R. Sala, "Electron-photon transport in FLUKA: status," in *Proc. MonteCarlo 2000 Conference, Lisbon, October 23–26 2000* (A. Kling, F. Barão, M. Nakagawa, L. Távora, and P. Vaz, eds.), pp. 159–164, Springer-Verlag Berlin, 2001.

[258] A. Fassó, A. Ferrari, P. R. Sala, and J. Ranft, "FLUKA: Status and Prospects for Hadronic Applications," in *Advanced Monte Carlo for Radiation Physics, Particle Transport Simulation and Applications* (K. Andreas, F. J. C. Barão, M. Nakagawa, L. Távora, and P. Vaz, eds.), (Berlin, Heidelberg), pp. 955–960, Springer Berlin Heidelberg, 2001.

[259] A. Fassò, A. Ferrari, J. Ranft, and P. R. Sala, "FLUKA: Performances and Applications in the Intermediate Energy Range," in *Proc. 1st AEN/NEA Specialists' Meeting on Shielding Aspects of Accelerators* (P. Dragovitsch, S. Linn, and M. Burbank, eds.), (Arlington (Texas), USA), pp. 287–304, Targets and Irradiation Facilities (SATIF 1), 1995.

[260] A. Ferrari and P. R. Sala, "The physics of high energy reactions," in *Proc. Workshop on Nuclear Reaction Data and Nuclear Reactors Physics, Design and Safety, World Scientific, Miramare-Trieste, Italy, 15 April-17 May 1996* (A. Gandini and G. Reffo, eds.), p. 424, 1998. available at http://www.fluka.org/content/publications/1996_trieste.pdf.

[261] G. Battistoni, F. Cerutti, R. Engel, A. Fassó, A. Ferrari, E. Gadioli, M. V. Garzelli, J. Ranft, S. Roesler, and P. R. Sala, "Recent Developments in the FLUKA nuclear reaction models," *Proc. 11th International Conference on Nuclear Reaction Mechanisms*, vol. 126, pp. 483–95, 2006.

[262] H. Sorge, "Flavor production in Pb(160 A GeV) on Pb collisions: Effect of color ropes and hadronic rescattering," *Physical Review C*, vol. 52, pp. 3291–3314, dec 1995.

[263] F. Cerutti, G. Battistoni, G. Capezzali, P. Colleoni, A. Ferrari, E. Gadioli, A. Mairani, and A. Pepe, "Low Energy Nucleus - Nucleus Reactions : the Bme Approach and Its Interface With Fluka," *Proc. 11th International Conference on Nuclear Reaction Mechanisms*, pp. 1–8, 2006.

[264] V. F. Weisskopf, "Statistics and Nuclear Reactions," *Physical Review*, vol. 52, pp. 295–303, aug 1937.

[265] A. Ferrari and P. R. Sala, "The Physics of High Energy Reactions," Tech. Rep. May, CERN, 1996.

[266] F. Cerutti, P. R. Sala, A. Mairani, and A. Ferrari, "New developments in FLUKA," in *Proc. 13th Int. Conf. on Nucl. Reac. Mechan., Varenna, Italy*, 2012.

[267] R. Capote, M. Herman, P. Obložinský, P. Young, S. Goriely, T. Belgya, A. Ignatyuk, A. Koning, S. Hilaire, V. Plujko, M. Avrigeanu, O. Bersillon, M. Chadwick, T. Fukahori, Z. Ge, Y. Han, S. Kailas, J. Kopecky, V. Maslov, G. Reffo, M. Sin, E. Soukhovitskii, and P. Talou, "RIPL - Reference Input Parameter Library for Calculation of Nuclear Reactions and Nuclear Data Evaluations," *Nuclear Data Sheets*, vol. 110, pp. 3107–3214, dec 2009.

[268] T. Tessonnier, T. T. Böhlen, F. Cerutti, A. Ferrari, P. R. Sala, S. Brons, T. Haberer, J. Debus, K. Parodi, and A. Mairani, "Dosimetric verification in water of a Monte Carlo treatment planning tool for proton, helium, carbon and oxygen ion beams at the Heidelberg Ion Beam Therapy Center," *Physics in Medicine and Biology*, vol. 62, no. 16, pp. 6579–6594, 2017.

[269] J. Schwaab, S. Brons, J. Fieres, and K. Parodi, "Experimental characterization of lateral profiles of scanned proton and carbon ion pencil beams for improved beam models in ion therapy treatment planning," *Physics in Medicine and Biology*, vol. 56, no. 24, pp. 7813–7827, 2011.

[270] C. Kurz, A. Mairani, and K. Parodi, "First experimental-based characterization of oxygen ion beam depth dose distributions at the Heidelberg Ion-Beam Therapy Center," *Physics in Medicine and Biology*, vol. 57, pp. 5017–5034, aug 2012.

[271] T. Tessonnier, T. Marcelos, A. Mairani, S. Brons, and K. Parodi, "Phase Space Generation for Proton and Carbon Ion Beams for External Users' Applications at the Heidelberg Ion Therapy Center," *Frontiers in Oncology*, vol. 5, 2016.

[272] M. Biaggi, F. Ballarini, W. Burkard, E. Egger, A. Ferrari, and A. Ottolenghi, "Physical and biophysical characteristics of a fully modulated 72 MeV therapeutic proton beam: model predictions and experimental data," *Nuclear Instruments and Methods in Physics Research Section B: Beam Interactions with Materials and Atoms*, vol. 159, pp. 89–100, oct 1999.

[273] M. Biaggi, F. Ballarini, A. Ferrari, A. Ottolenghi, and M. Pelliccioni, "A Monte Carlo code for a direct estimation of radiation risk.," *Physica Medica*, vol. 17 Suppl 1, pp. 103–105, 2001.

[274] F. Ballarini, M. Biaggi, A. A. Edwards, A. Ferrari, A. Ottolenghi, M. Pelliccioni, and D. A. Scannicchio, "Estimating mixed field effects: An application supporting the lack of a non-linear component for chromosome aberration induction by neutrons," *Radiation Protection Dosimetry*, vol. 103, pp. 19–27, jan 2003.

[275] F. Ballarini and A. Ottolenghi, "A Model of Chromosome Aberration Induction: Applications to Space Research," *Radiation Research*, vol. 164, pp. 567–570, oct 2005.

[276] M. Zaider and H. H. Rossi, "The Synergistic Effects of Different Radiations," *Radiation Research*, vol. 83, p. 732, sep 1980.

[277] M. H. Richard, M. Chevallier, D. Dauvergne, N. Freud, P. Henriquet, F. Le Foulher, J. M. Letang, G. Montarou, C. Ray, F. Roellinghoff, E. Testa, M. Testa, and A. H. Walenta, "Design Guidelines for a Double Scattering Compton Camera for Prompt-gamma Imaging During Ion Beam Therapy: A Monte Carlo Simulation Study," *IEEE Transactions on Nuclear Science*, vol. 58, pp. 87–94, feb 2011.

[278] H. Seo, J. H. Park, A. Ushakov, C. H. Kim, J. K. Kim, J. H. Lee, C. S. Lee, and J. S. Lee, "Experimental performance of double-scattering Compton camera with anthropomorphic phantom," vol. 6, no. 1, pp. 3–8, 2011.

[279] C. Robert, G. Dedes, G. Battistoni, T. T. Böhlen, I. Buvat, F. Cerutti, M. P. W. Chin, A. Ferrari, P. Gueth, C. Kurz, L. Lestand, A. Mairani, G. Montarou, R. Nicolini, P. G. Ortega, K. Parodi, Y. Prezado, P. R. Sala, D. Sarrut, and E. Testa, "Distributions of secondary particles in proton and carbon-ion therapy: a comparison between GATE/Geant4 and FLUKA Monte Carlo codes.," *Physics in medicine and biology*, vol. 58, pp. 2879–99, may 2013.

[280] V. Rosso, G. Battistoni, N. Belcari, N. Camarlinghi, A. Ferrari, S. Ferretti, A. C. Kraan, A. Mairani, N. Marino, J. E. Ortuño, M. Pullia, P. R. Sala, A. Santos, G. Sportelli, K. Straub, and A. Del Guerra, "A new PET prototype for proton therapy: comparison of data and Monte Carlo simulations," *Journal of Instrumentation*, vol. 8, pp. C03021–C03021, mar 2013.

[281] F. Sommerer, *Experiments and FLUKA simulations of C12 and O16 beams for therapy monitoring by means of in-beam positron emission tomography.* TU Wien, 2007. PhD thesis.

[282] T. T. Böhlen, A. Ferrari, V. Patera, and P. R. Sala, "Describing Compton scattering and two-quanta positron annihilation based on Compton profiles: Two models suited for the Monte Carlo method," *Journal of Instrumentation*, vol. 7, no. 7, 2012.

[283] H. A. Tolhoek and J. Cox, "Angular distribution and polarization of gamma radiation emitted by aligned radioactive nuclei," *Physica*, vol. 18, pp. 357–358, may 1952.

[284] Vasilis Vlachoudis, "flair." , 2020.

[285] DICOM, "Dicom standard." `https://www.dicomstandard.org/`, 2018. Accessed: 2018-09-10.

[286] D. Mason, "Pydicom: An Open Source DICOM Library," *Medical Physics*, vol. 38, no. 6, pp. 3493–3493, 2011.

[287] S. van der Walt, S. Colbert, and G. Varoquaux, "The NumPy Array: A Structure for Efficient Numerical Computation," *Computing in Science Engineering*, vol. 13, pp. 22–30, March 2011.

[288] K. Parodi, H. Paganetti, E. Cascio, J. B. Flanz, A. A. Bonab, N. M. Alpert, K. Lohmann, and T. Bortfeld, "Pet/ct imaging for treatment verification after proton therapy: A study with plastic phantoms and metallic implants," *Medical Physics*, vol. 34, no. 2, pp. 419–435, 2007.

[289] G. Shakirin, H. Braess, F. Fiedler, D. Kunath, K. Laube, K. Parodi, M. Priegnitz, and W. Enghardt, "Implementation and workflow for PET monitoring of therapeutic ion irradiation: a comparison of

in-beam, in-room, and off-line techniques," *Physics in Medicine and Biology*, vol. 56, no. 5, p. 1281, 2011.

[290] D. Stout, P. Chow, R. Silverman, R. M. Leahy, X. Lewis, S. Gambhir, and A. F. Chatziioannou, "Creating a whole body digital mouse atlas with PET, CT and cryosection images," *Molecular Imaging and Biology*, vol. 4, no. 4, p. S27, 2002.

[291] B. Dogdas, D. Stout, A. F. Chatziioannou, and R. M. Leahy, "Digimouse: a 3d whole body mouse atlas from ct and cryosection data," *Physics in Medicine and Biology*, vol. 52, no. 3, p. 577, 2007.

[292] A. E. Todd-Pokropek, T. D. Craddnuck, and F. Deconinck, "A file format for the exchange of nuclear medicine image data," *Nuclear Medicine Communications*, vol. 13, pp. 673–699, sep 1992.

[293] D. Unholtz, F. Sommerer, J. Bauer, D. van Straaten, T. Haberer, J. Debus, and K. Parodi, "Post-therapeutical $\beta+$-activity measurements in comparison to simulations towards in-vivo verification of ion beam therapy," in *2011 IEEE Nuclear Science Symposium Conference Record*, pp. 2273–2276, IEEE, oct 2011.

[294] M. Krämer and M. Scholz, "Rapid calculation of biological effects in ion radiotherapy," *Physics in Medicine and Biology*, vol. 51, pp. 1959–1970, apr 2006.

[295] H. Jiang and H. Paganetti, "Adaptation of GEANT4 to Monte Carlo dose calculations based on CT data," *Medical Physics*, vol. 31, no. 10, pp. 2811–2818, 2004.

[296] M. P. Carante and F. Ballarini, "Calculating Variations in Biological Effectiveness for a 62 MeV Proton Beam," *Frontiers in Oncology*, vol. 6, pp. 1–10, apr 2016.

[297] A. Ottolenghi, F. Ballarini, and M. Merzagora, "Modelling radiation-induced biological lesions: from initial energy depositions to chromosome aberrations," *Radiation and Environmental Biophysics*, vol. 38, no. 1, pp. 1–13, 1999.

[298] F. Ballarini and A. Ottolenghi, "A model of chromosome aberration induction and chronic myeloid leukaemia incidence at low doses," *Radiation and Environmental Biophysics*, vol. 43, no. 3, pp. 165–171, 2004.

[299] F. Ballarini, "From DNA radiation damage to cell death: Theoretical approaches," *Journal of Nucleic Acids*, vol. 2010, no. 1, 2010.

[300] F. Ballarini, S. Altieri, S. Bortolussi, E. Giroletti, and N. Protti, "A Model of Radiation-Induced Cell Killing: Insights into Mechanisms and Applications for Hadron Therapy," *Radiation Research*, vol. 180, pp. 307–315, aug 2013.

[301] T. T. Böhlen, F. Cerutti, M. P. W. Chin, A. Fassò, A. Ferrari, P. G. Ortega, A. Mairani, P. R. Sala, G. Smirnov, and V. Vlachoudis, "The FLUKA Code: Developments and Challenges for High Energy and Medical Applications," *Nuclear Data Sheets*, vol. 120, pp. 211–214, jun 2014.

[302] A. J. Van Der Kogel and G. W. Barendsen, "Late effects of spinal cord irradiation with 300 kV X rays and 15 MeV neutrons," *British Journal of Radiology*, vol. 47, pp. 393–398, may 1974.

[303] F. Ballarini, S. Altieri, S. Bortolussi, M. P. Carante, E. Giroletti, and N. Protti, "The role of DNA cluster damage and chromosome aberrations in radiation-induced cell killing: a theoretical approach," *Radiation Protection Dosimetry*, vol. 166, pp. 75–79, sep 2015.

[304] J. J. Tello Cajiao, M. P. Carante, B. Rodriguez, M. Antonio, and F. Ballarini, "Proximity effects in chromosome aberration induction by low-LET ionizing radiation," *DNA Repair*, vol. 58, pp. 38–46, oct 2017.

[305] J. J. Tello Cajiao, M. P. Carante, B. Rodriguez, M. Antonio, and F. Ballarini, "Proximity effects in chromosome aberration induction: Dependence on radiation quality, cell type and dose," *DNA Repair*, vol. 64, pp. 45–52, apr 2018.

[306] A. V. Carrano, "Chromosome aberrations and radiation-induced cell death: I. Transmission and survival parameters of aberrations," *Mutation Research/Fundamental and Molecular Mechanisms of Mutagenesis*, vol. 17, no. 3, pp. 341–353, 1973.

[307] M. N. Cornforth and J. S. Bedford, "A quantitative comparison of potentially lethal damage repair and the rejoining of interphase chromosome breaks in low passage normal human fibroblasts.," *Radiation research*, vol. 111, pp. 385–405, sep 1987.

[308] M. P. Carante and F. Ballarini, "Modelling cell death for cancer hadrontherapy," *AIMS Biophysics*, vol. 4, no. 3, pp. 465–490, 2017.

[309] A. Chatterjee and H. J. Schaefer, "Microdosimetric structure of heavy ion tracks in tissue," *Radiation and Environmental Biophysics*, vol. 13, pp. 215–227, sep 1976.

[310] FLUKA, "FLUKA manual INFN distribution." `http://www.fluka.org/`, 2020.

[311] M. Krämer and M. Scholz, "Treatment planning for heavy-ion radiotherapy: calculation and optimization of biologically effective dose," *Physics in Medicine and Biology*, vol. 45, no. 11, pp. 3319–3330, 2000.

[312] A. Rohatgi, "Webplotdigitizer." `WebPlotDigitizer`, 2019.

[313] T. A. Kato, A. Tsuda, M. Uesaka, A. Fujimori, T. Kamada, H. Tsujii, and R. Okayasu, "In vitro characterization of cells derived from chordoma cell line U-CH1 following treatment with X-rays, heavy ions and chemotherapeutic drugs," *Radiation Oncology*, vol. 6, no. 1, p. 116, 2011.

[314] H. Fujisawa, P. C. Genik, H. Kitamura, A. Fujimori, M. Uesaka, and T. A. Kato, "Comparison of human chordoma cell-kill for 290 MeV/n carbon ions versus 70 MeV protons in vitro," *Radiation Oncology*, vol. 8, no. 1, p. 91, 2013.

[315] F. C. Henderson, K. McCool, J. Seigle, W. Jean, W. Harter, and G. J. Gagnon, "Treatment of chordomas with CyberKnife: Georgetown university experience and treatment recommendations," *Neurosurgery*, vol. 64, pp. A44–A53, feb 2009.

[316] J. Debus, M. Scholz, T. Haberer, P. Peschke, O. Jäkel, C. P. Karger, and M. Wannenmacher, "Radiation Tolerance of the Rat Spinal Cord after Single and Split Doses of Photons and Carbon Ions 1," *Radiation Research*, vol. 160, pp. 536–542, nov 2003.

[317] R. Mohan and D. Grosshans, "Proton therapy - Present and future," *Advanced Drug Delivery Reviews*, vol. 109, pp. 26–44, jan 2017.

[318] M. Durante, "X-rays versus carbon ion tumor therapy: cytogenetic damage in lymphocytes," *Int. J. Radiat. Oncol. Biol. Phys.*, vol. 47, p. 793, 2000.

[319] A. Embriaco, R. Ramos, M. P. Carante, A. Ferrari, P. R. Sala, V. Vercesi, and F. Ballarini, "Healthy Tissue Damage Following Cancer Ion Therapy: A Radiobiological Database Predicting Lymphocyte Chromosome Aberrations Based on the BIANCA Biophysical Model," *Int. J. Mol. Sci.*, vol. 22, p. 10877, 2021.

[320] C. Cuccagna, V. Bencini, S. Benedetti, D. Bergesio, P. Carrio Perez, E. Felcini, A. Garonna, W. S. Kozłowska, M. Varasteh Anvar, V. Vlachoudis, and U. Amaldi, "Beam parameters optimization and characterization for a TUrning LInac for Protontherapy," *Physica Medica*, 2018.

[321] C. Cuccagna, *Dose Delivery and Image-Based Monitoring Strategies in TERA Linac Complexes for Hadron Therapy*. PhD thesis, 02/01 2021. ID: unige:149694.

[322] S. Benedetti, A. Grudiev, and A. Latina, "High gradient linac for proton therapy," *Phys. Rev. Accel. Beams*, vol. 20, no. 4, p. 40101, 2017.

[323] J. B. Farr, V. Moskvin, R. C. Lukose, W. Yao, and F. Schwamm, "Technical Note: Design and characterization of a large diameter parallel plate ionization chamber for accurate integral depth dose measurements with proton beams," *Medical Physics*, vol. 47, no. 7, pp. 3214–3224, 2020.

[324] S. Mein, C. Klein, B. Kopp, G. Magro, S. Harrabi, C. P. Karger, T. Haberer, J. Debus, A. Abdollahi, I. Dokic, and A. Mairani, "Assessment of RBE-Weighted Dose Models for Carbon Ion Therapy Toward Modernization of Clinical Practice at HIT: In Vitro, in Vivo, and in Patients," *International Journal of Radiation Oncology, Biology, Physics*, vol. 108, no. 3, pp. 779–791, 2020.

[325] U. Weber and G. Kraft, "Comparison of carbon ions versus protons," *Cancer Journal*, vol. 15, no. 4, pp. 325–332, 2009.

[326] C. P. et al, "Relative biological effectiveness variation along monoenergetic and modulated bragg peaks of a 62 mev therapeutic proton beam: preclinical assessment," *Int. J. Radiat. Oncol. Biol. Phys.*, vol. 90, p. 27, 2014.

[327] C. R. Peeler, D. Mirkovic, U. Titt, P. Blanchard, J. R. Gunther, A. Mahajan, R. Mohan, and D. R. Grosshans, "Clinical evidence of variable proton biological effectiveness in pediatric patients treated for ependymoma," *Radiotherapy and Oncology*, vol. 121, no. 3, pp. 395–401, 2016.

[328] L. Hintz, C. Glowa, M. Saager, R. Euler-Lange, P. Peschke, S. Brons, R. Grün, M. Scholz, S. Mein, A. Mairani, J. Debus, and C. P. Karger, "Relative biological effectiveness of single and split helium ion doses in the rat spinal cord increases strongly with linear energy transfer," *Radiotherapy and Oncology*, 2022.

[329] S. Mein, I. Dokic, C. Klein, T. Tessonnier, T. T. Böhlen, G. Magro, J. Bauer, A. Ferrari, K. Parodi, T. Haberer, J. Debus, A. Abdollahi, and A. Mairani, "Biophysical modeling and experimental validation of relative biological effectiveness (RBE) for 4He ion beam therapy," *Radiation Oncology*, vol. 14, no. 1, pp. 1–16, 2019.

[330] M. P. Carante, A. Embriaco, G. Aricò, A. Ferrari, A. Mairani, S. B. Mein, R. Ramos, P. R. Sala, and F. Ballarini, "Biological effectiveness of He-3 and He-4 ion beams for cancer hadrontherapy: a study based on the BIANCA biophysical model," *Physics in Medicine and Biology*, vol. 66, p. 195009, 2021.

[331] D. K. Ebner, S. J. Frank, T. Inaniwa, S. Yamada, and T. Shirai, "The Emerging Potential of Multi-Ion Radiotherapy," *Frontiers in Oncology*, vol. 11, no. February, pp. 1–8, 2021.

[332] R. dos Santos Augusto, "On the feasibility of using radioactive ion beams in hadrontherapy: dosimetric and imaging studies," Jul 2018.

Wioletta Kozłowska

Avenue de Vaudagne 49, 1217 Meyrin, Switzerland

+48 791 029 088; +41 791 027 003 • wioletta.kozlowska@protonmail.ch
www.linkedin.com/in/wkozlowska
ORCID ID: https://orcid.org/0000-0002-4899-1910

Experience

ADAM S.A. an Advanced Oncotherapy company — **Meyrin, Switzerland**
Medical Physics Scientist — *March 2020–present*

- Preparing and leading research project focused on proton and light ion system development
- Monte Carlo modelling of the linear LIGHT accelerator system for proton and light ion beam therapy including modelling of the delivery characteristic to clinical targets
- Production of the pre-comissioning synthetic beam data and continuous upgrade of the beam data model
- Biological Modelling of radiobiological endpoint prognoses including LET and RBE modelling
- Component Owner of Oncological Information System and responsible for integration with LIGHT System

European Organization for Nuclear Research (CERN) — **Geneva, Switzerland**
Medical Physics Doctoral Student/Fellow — *April 2015–February 2020*

- Front-end and back-end development of the FLUKA Particle Therapy Tool based on the FLUKA Monte Carlo code and its GUI - flair
- Treatment plan sensitivity and verification for proton and light ion therapies
- Implementation and development of the multiobjective optimization algorithms for radiobiological/LET-weighted guided treatment plans
- Sensitivity studies on different radiobiological models used in particle therapy
- Support, development and maintenance of the FLUKA - Flair medical application interfaces

European Organization for Nuclear Research (CERN) — **Geneva, Switzerland**
Master Student Researcher/Associate Research Engineer — *September 2012–March 2015*

- Performing particle transport and interaction simulations in the FLUKA Monte Carlo code
- Modeling and reviewing current state of the internal dump system of the Proton Synchrotron (PS)
- Designing a new beam dump system and adjusting a conceptual solution with respect to the planned performance
- Reviewing and analyzing solutions for the conceptual project of the CERN Neutrino Facility
- Modeling and optimizing design of the focusing devices for the Neutrino Facility

Synektik S.A. — **Warsaw, Poland**
Application and System Support Specialist — *September 2011–September 2012*

- Performing maintenance and review of applications and medical IT systems (RIS, PACS, DICOM viewers)
- Coordinating upgrades, internal adjustments and the troubleshooting for existing applications
- Preparing program documentation for supporting systems and applications
- Performing product testing
- Training and client support for new applications
- Reviewing and analyzing business needs - cooperation with users to evaluate requirements and solutions

IBM Polska Business Services Sp. z o.o — **Warsaw, Poland**
Junior IT Security Specialist — *May 2010–September 2011*

- Defining, developing and implementing tools for the IT security processes
- Performing the IT security health checking, insuring that the security services and the health checking tools are installed and executed in accordance with the contractual agreement
- Providing advice and guidance on interpretation of IT health checking results
- Coordinating the teamwork and organizing processes schedules

Education

- **Medical University of Vienna** — **Vienna, Austria**
  Doctoral Program in Medical Physics (Supervisor: Prof. Dr. DI Dietmar Georg) — *March 2015–present*
  Division Medical Radiation Physics; Department of Radiation Oncology
  Thesis: "Bridging the gaps in particle therapy using Monte Carlo Simulations Tools"
- **Warsaw University of Technology** — **Warsaw, Poland**
  Master of Science in Engineering — *February 2011–September 2013*
  Electrical and Computer Engineering with major in the Electronics and Computer Engineering in Medicine
  Thesis: "Secondary beam focusing system for CERN Neutrino Facility"
- **Warsaw University of Technology** — **Warsaw, Poland**
  Bachelor of Science in Engineering — *October 2006–February 2011*
  Electrical and Computer Engineering with major in the Electronics and Computer Engineering in Medicine
  Thesis: "Phantom for functional lung imaging in MRI"
- **Universidad Politécnica de Madrid** — **Madrid, Spain**
  International students exchange program - LLP Erasmus — *September 2009–February 2010*
  Escuela Técnica Superior de Ingenieros de Telecomunicación; Biomedical Engineering

Technical and language skills

- **Programming Languages:** Proficient in: C++, Python
  Also basic skills with: Java, R, Matlab, FORTRAN
- **Other software Skills:** FLUKA, GitLab
- **Languages:** Native: Polish
  Full professional proficiency: English
  Limited working proficiency: French, Spanish, Russian

Teaching and supervising experience

- **Research Intern - William Larsen** — **ADAM-AVO, Geneva**
  Feasibility studies for upright positioning in proton therapy — *September 2021-February 2022*
  Modification of the digital anthropomorphic phantoms for Treatment Planning exercises
  evaluating the feasibility of upright positioning in proton therapy
- **Summer Student - Magdaléna Tydrichová** — **CERN, Geneva**
  Analysis of multiobjective optimization evolutionary algorithms (MOEA) — *June-August 2017*
  Test and analysis of MultiObjective Evolutionary Algorithms
  for the scope of Monte Carlo based Treatment Planning System (MC TPS)
- **18th Basic FLUKA Course** — **CERN, Shanghai**
  Lecturer during the course organized for SPHIC — *November 2016*
  Responsible for the session dedicated to Medical Application Tools in FLUKA
- **Summer Student - Guido Arnau Antoniucci** — **CERN, Geneva**
  Development of GPU based solutions for Monte Carlo Treatment Planning Systems — *June-August 2015*
  Parallel computing solutions for MC TPS. Development of GPU based solutions for MC TPS

Publications

First application of the BIANCA biophysical model to carbon-ion patient cases — **Journal article**, *May 2022*
Physics in Medicine and Biology
W.Kozłowska, M.Carante, G.Aricò, A.Embriaco, A.Ferrari, G.Magro, A.Mairani, R. Ramos, P.Sala, D.Georg, F.Ballarini

FLUKA particle therapy tool for Monte Carlo independent calculation of scanned proton and carbon ion beam therapy — **Journal article**, *March 2019*
Physics in Medicine and Biology
W.Kozłowska, T.Böhlen, C.Cuccagna, A.Ferrari, F.Fracchiolla, G.Magro, A.Mairani, M.Schwarz, V.Vlachoudis, D.Georg

In Vivo Validation of the BIANCA Biophysical Model: Benchmarking against Rat Spinal Cord RBE Data — **Journal article**, *May 2020*
International Journal of Molecular Sciences
M.Carante, G.Aricò, A.Ferrari, C.Karger, **W.Kozłowska**, A.Mairani, P.Sala, F.Ballarini

First benchmarking of the BIANCA model for cell survival prediction in a clinical hadron therapy scenario — **Journal article**, *October 2019*
Physics in Medicine and Biology
M.Carante, G.Aricò, A.Ferrari, **W.Kozłowska**, A.Mairani, F.Ballarini

Beam characterization for the TULIP accelerator for protontherapy through full Monte Carlo simulations — **Journal article**, *October 2018*
Physica Medica
C.Cuccagna, S.Benedetti, V.Bencini, D.Bergesio, P.Carrio Perez, E.Felcini, A.Garonna, **W.Kozłowska**, M.Varasteh, V.Vlachoudis, U.Amaldi

An overview of recent developments in FLUKA PET tools — **Journal article**, *July 2018*
Physica Medica
R.S.Augusto, J.Bauer, O.Bouhali, C.Cuccagna, C.Gianoli, **W.Kozłowska**, P.G.Ortega, T.Tessonnier, Y.Toufique, V.Vlachoudis, K.Parodi, A.Ferrari

A versatile multi-objective FLUKA optimization using Genetic Algorithms — **Conference paper**, *September 2017*
EPJ Web of Conferences
V.Vlachoudis, G.A.Antoniucci, S.Mathot, **W.Kozłowska**, M.Vretenar

The FLUKA code: An accurate simulation tool for particle therapy — **Journal article**, *May 2016*
Frontiers in Oncology 6:116
G.Battistoni, J.Bauer, T.Böhlen, F.Cerutti, M.P.W.Chin, R.Dos Santos Augusto, A.Ferrari, P.G.Ortega, **W.Kozłowska**, G.Magro, A.Mairani, K.Parodi, P.Sala, P.Schoofs, T.Tessonnier, V.Vlachoudis

Conferences and Talks

- **Comparative proton therapy treatment quality between the upright and supine position for three pelvic indications** — **Poster**
  AAPM, Washington DC, USA — *July 2022*
  W.Kozłowska, A. Zemanova, W.Larsen, O.Sevela, P.Segars, J.Farr

- **Upright position for abdominal proton therapy: Evaluation study with a digital anthropomorphic phantom** — **Poster**
  PTCOG, Miami, USA — *June 2022*
  W.Kozłowska, N. Pienimäki, W.Larsen, J.Farr

- **Monte Carlo modelling methods for a proton linac beam delivery system** — **Poster**
  EPS Forum, Paris, France — *June 2022*
  W.Kozłowska, A. Kolano, N. Pienimäki, J.Farr

- **Monte Carlo Quality Assurance platform for particle therapy** — **Poster**
  ESTRO, Barcelona, Spain — *April 2018*
  W.Kozłowska, T.Böhlen, C.Cuccagna, A.Ferrari, D.Georg, A.Mairani, V.Vlachoudis

- **Towards LET-painting using FLUKA Monte Carlo Code** — **Poster**
  PTCOG, Yokohama, Japan — *May 2017*
  W.Kozłowska, T.Böhlen, C.Cuccagna, A.Ferrari, D.Georg, A.Mairani, V.Vlachoudis

- **Development of the Flair tool for FLUKA Treatment Planning Verification** — **Poster**
  ICTR-PHE, Radiotherapy and Oncology, Vol. 118, Sup. 1 (2016), Geneva, Switzerland — *February 2016*
  W.Kozłowska, T.Böhlen, A.Ferrari, D.Georg, A.Mairani, P.Sala, V.Vlachoudis

- **Recent Developments in the FLUKA tools for Treatment Planning** — **Workshop Presentation**
  Ions for Cancer Therapy, Space and Material Science, Chania, Greece — *August 2017*
  On behalf of FLUKA Collaboration

- **FLUKA applications in the medical area** — **Workshop Presentation**
  EURADOS WG 9: Radiation Dosimetry in Radiotherapy, Geneva, Switzerland — *October 2016*
  On behalf of FLUKA Collaboration